Università degli Studi di Palermo

AREA RICERCA E TRASFERIMENTO TECNOLOGICO
SETTORE DOTTORATI E CONTRATTI PER LA RICERCA
U. O. DOTTORATI DI RICERCA

Dottorato di Ricerca in Scienze Fisiche e Chimiche
Dipartimento di Fisica e Chimica – Emilio Segrè
Settore Scientifico Disciplinare CHIM/02

HALLOYSITE NANOTUBES AS VERSATILE ALUMINOSILICATE PRECURSORS FOR COMPOSITE GEOPOLYMERS: DESIGN, PREPARATION AND PHYSICO-CHEMICAL CHARACTERIZATION

IL DOTTORE
MARTINA MARIA CALVINO

IL COORDINATORE
PROF. MARCO CANNAS

IL TUTOR
PROF. GIUSEPPE LAZZARA

IL CO-TUTOR
DOTT. GIUSEPPE CAVALLARO

CICLO XXXVI
ANNO CONSEGUIMENTO TITOLO 2023

Contents

Preface

In an era characterized by an increasing demand for sustainable and eco-friendly materials, the role of nanomaterials has never been more crucial. Nanoclays, in particular, have emerged thanks to their unique properties at the nanoscale that open the doors to innovations in areas ranging from materials science to energy storage and beyond, making them a key player in the demand for greener and more efficient products. Since geopolymers are considered a practical solution for reducing CO_2 emissions in the construction industry as sustainable alternatives to traditional building materials, the inclusion of nanoclays in their formulation represents a promising way to improve their performance.

However, geopolymer research must already implement the current technologies towards new hybrid geopolymeric systems with tailored physico-chemical properties.

This doctoral thesis intends to move a step forward in developing composite halloysite-based geopolymers, giving an insight into specific characteristics of nanoclays used as aluminosilicate precursors. In this regard, following an introduction on the recent advances on nanomaterials and geopolymer technologies, in Chapter 2 a new protocol for the separation of nanoclay mixtures will be proposed, given the common presence of impurities in their natural deposits. In Chapter 3, having considered the distinct properties evidenced thanks to the different morphology of these nanoclays, NMR techniques are employed in order to investigate water diffusion and relaxation within these systems, demonstrating the existence of diverse water populations. From this examination, a specific kind of halloysite nanotube, called Patch, showed peculiar features promoting the deepening of its potential in this work. With this in mind, Chapter 4 will focus on the rheological characterization of Patch samples whose fibrous structure significantly promoted the formation of hydrogel.

Moving from this focus on the potential aluminosilicate precursors to geopolymeric materials, in Chapter 5. Relevant improvements will be shown compared to the unfilled geopolymer, due to the presence of phase change materials confined in the geopolymeric matrix.

Finally, Chapter 6 will propose on steel substrates, improving the wettability properties of its surface. The attached papers with further details about the experimental procedures and equipment employed in this thesis can be found in Chapter 8.

1. Introduction

1.1 Clay minerals and nanoclays as precursors for advanced materials

In recent decades, the world has recorded an extraordinary escalation of environmental issues arising from the constant exploitation of natural resources, escalating pollution, and the increased production of non-biodegradable materials. The scientific community is now facing the urgent need to address these pressing issues to ensure the preservation of our planet, and one crucial aspect is the pursuit of innovative and eco-friendly materials that can meet the several needs of modern society while ensuring long-term sustainability and mitigate the environmental impact of industrial activities.

In this regard, the field of nanotechnology is among the most actively researched areas in modern material science. The use of nanotechnological products and their applications are making a significant contribution towards environmental protection.

Nanomaterials are characterized by having dimensions in the nanometer scale (1-100 nm) and they gained significant attention due to their unique physicochemical properties, which make them valuable in sustainable technologies. The size-dependent properties of nanomaterials enable their potential applications in many fields. Additionally, different types of nanomaterials have been developed to enhance the properties of drugs, such as pharmacokinetics and pharmacodynamics[1]. Polymeric nanomaterials, in particular, have been widely utilized in the medical and pharmaceutical industries due to their biocompatibility, controlled release capabilities, and size compatibility with tissues and cells. Nanostructured materials possess the benefit of an exceptionally elevated surface area to volume ratio. This is crucial especially when the surface of a material contains significant active sites. Moreover, having a considerable portion of surface sites allows materials to be used more effectively for applications such as catalysis[2].

Nevertheless, a significant drawback exists with the employed materials and procedures as they can rely on finite resources and produce dangerous pollutants. Sometimes, indeed, their synthesis can involve the production of harmful byproducts or requires high levels of energy and pressure, leading to high energy consumption, especially when large-scale production is necessary.

The combination of nanotechnology and green chemistry principles and practices, known as green nanotechnology, could be crucial in creating a sustainable society. Its methods frequently exploit natural resources, safe solvents, and energy-efficient procedures to produce nanomaterials. Nanotechnology products have recently been acknowledged as highly efficient resources for environmental purification. Methods for remediation using nanomaterials involve their use for the detoxification and conversion of pollutants. One example is the utilization of titanium oxide for the photo-oxidation of organic pollutants[3]. Additionally, alternative techniques such as biodegradation, sorption, hydrolysis, photolysis, and UV irradiation can also be employed to remove pollutants[4,5].

Recently, nanoclays are receiving significant attention from researchers in various fields including chemistry, physics, engineering, biology, and materials science. This is mainly due to their unique morphological features, physico-chemical properties, and sustainable nature. Nanoclays constitute the starting point to develop innovative nanomaterials used in applications such as drug delivery, food packaging, preservation of cultural heritage, environmental cleanup, and wastewater treatment [6–8]. Moreover, different kinds of nanoclays have emerged as important resources in the environmental and bioremediation fields as adsorbent nanomaterials for pollutants[9,10].

Exploiting natural nanomaterials, such as nanoclays, represents, in fact, a way to overcome the aforementioned issues connected with nanotechnology. Chemically, nanoclays belong to the family of phyllosilicates, namely layered silicates, consisting of tetrahedral sheets of silica (T) followed by octahedral sheets of alumina (O). Clay minerals can either originate in situ or be carried and deposited elsewhere. Chemical weathering happens when rocks that are exposed to the Earth's surface interact with groundwater, which typically has low temperatures and a pH ranging from 5 to 9. This interaction leads to the dissolution of minerals in the rocks, alteration of the original rock forming minerals, transportation and elimination of soluble ions and molecules, and ultimately the creation of new minerals.

Depending on the disposition of the layers, clay minerals can be classified into 1:1 type (T–O), such as kaolinite, and 2:1 type (T–O–T), like montmorillonite and vermiculite[11]. For example, the 1:1 class is constituted by one tetrahedral layer and one octahedral layer joined together with a thickness of each TO of ca. 0.7 nm. On the other hand, 2:1 is composed of one O layer sandwiched between two T. The kaolin group of minerals belongs to the category of dioctahedral 1:1 type mineral, with a chemical composition

generally represented by the formula $Al_2Si_2O_5(OH)_4$ and lacks any layer charge. Within this class, we also find halloysite clay nanotubes that are originated from a natural process in which the flat sheets of kaolin are rolled into hollow tubular structures. The structure of halloysite can be described as a layer composed of two building blocks: silica tetrahedra and alumina octahedra that possess a unit formula of $Al_2Si_2O_5(OH)_4 \cdot nH_2O$. We can distinguish two structures: one of these is halloysite-7Å, which is the dehydrated form (n = 0) and has a layer spacing of 7.5 Å; another one is halloysite-10Å, which is the hydrated form (n = 2) and has an interlayer spacing of 10 Å. The interlayer distance in halloysite-7Å is the same as that observed in flat kaolinite, whereas the increased thickness of halloysite-10Å is due to the presence of water molecules. In particular, Ferrante et al.[12] reported a spiral geometry as a model for both the hydrated (10 Å) and anhydrous form (7 Å) of halloysite. A schematic representation of both forms is presented in Figure 1.1.

Usually, 10-15 layers of aluminosilicate form the cylinder of the halloysite tube. Their external diameter ranges from 40 to 60 nm, while the internal diameter from 10 to 15 nm. Their length can vary between 500-1500 nm[13].

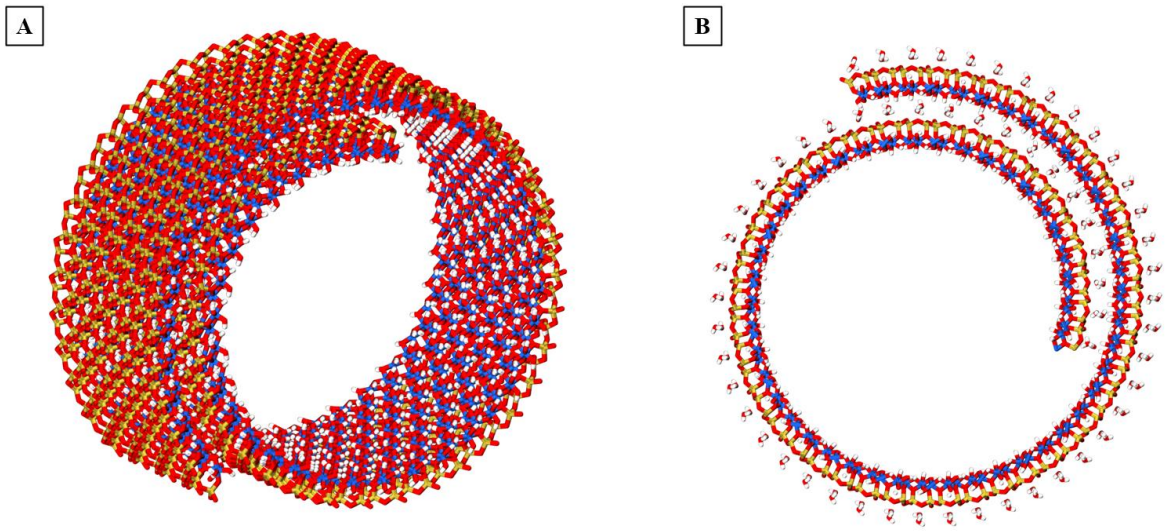

Figure 1.1. (a) Schematic representation of halloysite-7 Å.
(b) Front view of halloysite-10 Å.

Furthermore, the external and internal surfaces of halloysite have distinct chemical properties, with the former being negatively charged and the latter being positively charged

across a wide pH range from 3 to 8[14]. This characteristic is highly suitable for halloysite nanotubes as it enables the loading of negative molecules into the inner lumen[15], exploiting electrostatic interactions, that consists in the 10–15 % in volume of the pristine tubes or until 30–40 vol% after etching with sulfuric acid according to Abdullayev et al.[16].

Experimentally, the charge separation can be predicted by comparing the electrical ζ-potential values of silica and alumina surfaces in water. According to the results reported elsewhere[17], silica surfaces exhibit negative values and alumina surfaces exhibit positive values, while the overall ζ -potential of halloysite nearly corresponds with the one of silica. The surface charge of the nanotubes contributes to moderate their colloidal stability in water. However, when loaded with negatively charged drugs, the ξ-potential becomes more negative, up to values of -60 mV, resulting in colloids stable for months. Consequently, halloysite can act as an excellent carrier for various types of cargo that can be stored, transported, and subsequently released. Besides, halloysite has the advantage of not requiring long exfoliation processing, thanks to its shape and the absence of stacked platy sheets, also showing a significantly easier dispersibility, unlike platy multilayer kaolin, montmorillonite, or bentonite particles.

The inner lumen of halloysite nanotubes has a diameter capable of containing a wide range of substances, including proteins, polymers, drugs, macromolecules, and other chemically active agents[18] such as anti-corrosion, with the benefit of sustained molecular release.

Another possibility is presented by the interaction of positive active species with the outer surface of the nanotubes. In particular, the different chemistry and charges of halloysite facilitate selective functionalization with macromolecules like polymers, biopolymers, and surfactants. This allowed to overcome the performances of HNT/polymer nanocomposites that consisted of poor interfacial interactions between the polymers and the clay nanoparticles, and the agglomeration of HNTs in the polymer matrix, limiting their efficiency as filler. The siloxane groups on the outer surface of the nanotubes make the grafting difficult for organic compounds. Nevertheless, the negative surface charge enables them to be bonded, for example, with metal ions and cationic polymers. In this regard, many of the used modification methods and the roles of HNTs have been summarized by Liao et al. [19].

Compared to common carbon nanotubes, halloysite offers several advantages. These include low cost, biocompatibility, and the ability to load chemicals inside its tube

structure. Carbon nanotubes on the other hand, are known to be carcinogenic and extremely expensive. Additionally, they have a very narrow lumen diameter of approximately 1-2 nm, limiting their capacity to accommodate only the smallest molecules, such as water and certain ions.

The growing use of HNTs necessitates the evaluation of their potential toxicity to living organisms. Overall, research has revealed that halloysite is a relatively safe nanomaterial, and it is non-toxic up to a very high concentration of 5 mg/mL, which makes it suitable in biomaterials. This has been proven through various experiments involving cell cultures and animal models, ranging from microworms to piglets[20]. However, due to its the absence of biological processes of aluminosilicate degradation in the human body, halloysite cannot be considered biodegradable, making intravenous injection incompatible and not recommended[21]. Nonetheless, using modified halloysite is limited to external medical applications as an active component for the controlled release of drugs in creams, implants, or wound treatment on tissues.

Among low cost and sustainable stabilizers, clay minerals are very promising in oil-in-water emulsion stabilization. Emulsions with solid interfacially active particles, instead of common surfactants, are called Pickering emulsions. They exhibit high stability due to their resistance to coalescence and the Oswald ripening phenomena[22]. At the beginning, the limited choices of materials hindered the use of Pickering emulsions[23]. Nevertheless, advancements in material science and technology led to the creation of numerous interesting and innovative particles that can be tailored to have tuneable surface wetting properties for stabilizing Pickering emulsions[24].

Different degrees of coverage are obtained depending on the shape of the particles involved, thus playing a significant role in this process. Discs and rods nanoclays are particularly effective at maximizing coverage because they can optimally align themselves at the interface[25]. This characteristic, along with their morphology and wettability, allows anisotropic particles to greatly enhance the stability of Pickering systems. By anchoring themselves irreversibly at the oil-water interface, these particles create a physical barrier that obstructs Ostwald ripening and coalescence by providing steric hindrance[26]. The Pickering emulsion features are strongly influenced by the characteristics of the resulting droplets such as concentration, size, interactions, and charge. Nowadays, Pickering emulsions can be widely used in various applications such as food science, cosmetics, oil

recovery, and drug delivery[27,28], due to their numerous advantages compared with droplets stabilized by surfactants. The advantages include reduced or no toxicity, low production cost, easy storage, and simple recovery.

For instance, Pickering emulsions have been proposed for oil remediation technology by Owoseni et al.[29], and in their study, they demonstrated the utilization of halloysite nanotubes as active solid emulsifiers. They also investigated the factors influencing the stability of oil-in-water droplets. The findings revealed that the clay nanoparticles play a crucial role in forming a protective and rigid film at the interfaces of the two liquids, thus hindering agglomeration and sedimentation.

Pickering emulsions are also very promising for cultural heritage applications, especially for marble or stone-based artworks[30]. As a matter of fact, a recent study proposed a new method for preserving waterlogged archaeological wood using a novel protocol involving the Pickering emulsions stabilized with halloysite nanotubes and containing paraffin wax as the inner core[31]. The consolidated wood with the microparticles achieved robustness and mechanical resistance compared to the untreated sample.

A comparison between halloysite, kaolinite and attapulgite stabilized oil-in-water Pickering emulsions was also reported. It was shown that, despite having the same chemistry, halloysite is capable of stabilizing the system at higher oil fractions compared to kaolinite. This phenomenon is likely due to the higher specific area of halloysite with respect to kaolinite. Moreover, halloysite-based emulsions demonstrated a significantly higher yield stress and elastic modulus than kaolinite, with a difference of two orders of magnitude. Although kaolinite and halloysite are aluminosilicates with very similar chemical compositions, their properties are different, even at the same concentration, because of their different shapes, particle sizes, and surface properties that influence their physico-chemical features. For instance, a recent work showed the different ice nucleation properties of kaolinite compared with halloysite nanotubes. In particular, halloysites possessed higher ice nucleation activity with respect to kaolinites and more interestingly, also compared to other halloysite samples with different dimensions of the nanotube [32]. The hypothesized reason is related to the different surface areas and the stacking of layers, as the edges are recognized to be the most probable location for the ice nucleation, due to the extensive variation in their geometry.

1.1.1 Separation of nanoclays

Kaolin minerals, namely kaolinite and halloysite, are diffused throughout the Earth as clay components in soil and changed crustal rocks. During weathering, precursor aluminosilicate materials, like allophane, are believed to be created in volcaniclastic fall deposits. As the process of weathering and alteration continues, the rocks and deposits go through a transformation, losing their original texture and mineral composition, and become progressively weaker. This can sometimes lead to collapse, especially when subjected to heavy rainfall or seismic activity[33].Then, they are gradually replaced by halloysite and kaolinite, resulting in an overall increase in the clay content.

In this natural scenario, we can imagine that the composition of clays is influenced by the geological environment. For example, in certain areas, limestone (calcite) is naturally combined with raw clays and it can influence the mineralogy and reactivity of kaolinite[34].

Infrared spectroscopy (FTIR) is reported in literature as a supplementary technique for identifying clay minerals. However, it can also offer quantitative information for determining the mineral composition of clays, which is still a challenging task[35]. Currently, XRD methods, such as pattern addition, single line, or Rietveld refinement methods, are commonly used to quantitatively determine the mineralogical composition of clays. Previous studies have demonstrated the effectiveness of FTIR in quantifying kaolinite and halloysite and have highlighted the benefits of FTIR over XRD when concentrations of kaolinite and halloysite in samples are low[36]. Accordingly, a recent study proposed a way to improve the quantification of kaolinite and halloysite by implementing machine learning on mineral quantification based on spectral data[37].

The use of advanced separation methods, such as chemical treatment with magnetic separation, allows for the extraction of high-quality mineral resources. Halloysite deposits can contain impurities like muscovite, limonite, anatase, illite, iron minerals, and some organic substances, which have a negative impact on the quality of the raw material. Numerous studies have been conducted to explore cost-effective ways of removing these impurities. Coarse-grained impurities can be eliminated using screens, hydro cyclones, and magnetic separators, whereas special techniques such as centrifugation, flotation, and leaching are required for fine-grained impurities[38,39]. Following dispersion, impurities

larger than 50 μm are removed using hydro cyclones or sieves, and they are classified based on particle size in industrial production.

The use of chemical treatment combined with magnetic separation has been reported to purificate halloysite extracted from Poland[40]. The method involved crushing, hydrochloric acid absorption treatment, sedimentation, and polygradient magnetic separation in a weak magnetic field to separate aluminosilicates from iron and titanium oxides. As a result, a product with approximately 98% purity of the aluminosilicate fraction, constituted by halloysite and kaolinite, was successfully obtained.

As mentioned before, natural halloysite clay samples can contain a lot of impurities. However, besides those ones, we can also find traces of quartz phases[41] or even an approximate 10 wt% of platy kaolinite nanoparticles. This is related to the fact that halloysite and kaolinite belong to the same class of minerals, known as phyllosilicates, and they possess many similarities in terms of chemical composition except for the presence of water molecules between the unit layers of halloysite, as previously mentioned in Section 1.1. The kaolinite contamination in halloysite samples becomes significant in contexts where the utmost purity of HNTs is required. For instance, the presence of these kaolinite nanoplates can diminish the efficacy of using halloysite nanotubes as carriers for pharmaceutical and biomedical applications. In light of this, efficient separation protocols are needed, and they represent a challenging task when considering their use in pharmaceuticals and biomedicine. As documented in the literature, the way nanoparticles settle within colloidal systems is influenced by numerous factors. These include specific interactions between particles, the viscosity of the solvent, and the ionic strength of the medium [42–44]. These factors can lead to particle aggregation, which in turn diminishes the stability of the colloidal system.

Enhancing the separation of kaolinite nanoplates can be achieved by introducing inorganic flocculants [45]. Examples of such flocculants encompass aluminum and iron salts, along with environmentally friendly alternatives [46]. Additionally, the inclusion of polymers can impact on the sedimentation kinetics of kaolinite when it's dispersed in water [47].

1.2 Geopolymers

In recent times, geopolymeric materials emerged as a promising alternative with lower CO_2 emissions to classical cement concrete due to their potential for sustainable solutions. Geopolymeric materials have several advantages, such as energy conservation, environmental protection, and the ability to employ abundant raw materials like industrial wastes. Therefore, utilizing industrial byproducts and waste materials for geopolymer production is not only economically beneficial but also environmentally friendly, especially considering the growing demand for green building materials.

The term 'geopolymer' was originally introduced by Joseph Davidovits in 1978, indicating a class of solid materials synthesized by the reaction of an aluminosilicate powder with an alkaline solution[48]. In particular, the prefix ‘geo’ indicates an inorganic aluminosilicate derived from geological materials. It reacts with an alkaline solution, forming a binder through a polycondensation reaction that produces a three-dimensional tecto-aluminosilicate matrix called polysialate, which has an empirical formula of $M_n[-(SiO_2)_z-AlO_2]_n \cdot wH_2O$ where M represents a cation, n is the degree of polycondensation, and z can be 1, 2, 3, or greater. The term "sialate" refers to a building unit composed of silicon-oxoaluminate, where SiO_4 and AlO_4 tetrahedra are connected by sharing oxygen atoms. This bonding arrangement results in a negative charge on the IV-fold coordinated Al, which is balanced by cations such as Na^+, K^+, Li^+, Ca^{2+}, Ba^{2+}, NH^{4+}, and H_3O^+.

The presence of these cations is crucial for maintaining the structure's neutrality. Duxson et al.[49] proposed a polymerization method that consists of multiple steps. A schematic representation of the geopolymerization process is reported in Figure 1.2. The reaction mechanism describes the essential processes involved in converting a solid aluminosilicate source into a synthetic alkali aluminosilicate. The polymerization occurs in three stages: (1) the oxide minerals present in the source materials (usually silica and alumina) dissolve when subjected to highly alkaline conditions; (2) orientation of the dissolved oxide minerals followed by a gelation; and (3) polycondensation takes place to create a three-dimensional network of silico-aluminates structures[50]. Thus, the performance of geopolymers is significantly influenced by the levels of silica and alumina present in the source material[51]. Additionally, there is an increase in dissolution rate and the compressive strength as the alkalinity of the solution increases[52]. However, the faster reaction of the

polymer could potentially result in a significant loss of consistency during the mixing process. The alkaline activator type and curing temperature are well-known parameters that control geopolymerization and need to be optimized for producing high strength binders.

The most commonly used alkali solution for geopolymerization is a combination of sodium silicate (Na_2SiO_3) and sodium hydroxide (NaOH). The concentration of sodium hydroxide in the solution plays a significant role in determining the physical and mechanical properties of geopolymer stabilization. This solution contains hydroxide ions (OH^-) and sodium ions (Na^+), which initiate the reaction between the internal silicate and aluminate components, thus initiating the dissolving process. Moreover, with respect to K^+ cations, the smaller Na^+ ions showed increased activity in alkali reactions, leading to a higher ability to dissolve substances and effectively stabilize silicate monomers and dimers in solutions.

It has been proved that using a mixture of both sodium silicate and sodium hydroxide as an alkali activator will give better strength than using only a sodium hydroxide solution. According to previous research[53], it was clear that another factor that greatly affects the rate of geopolymer formation is the initial solid content. Increasing the solid-to-liquid ratio resulted in a significant increase in the number of precipitates. This occurrence can be attributed to the presence of a high concentration of dissolved reactant species. As the solid-to-liquid ratio increased, the level of homogeneity in the geopolymer sample decreased, mainly due to the limited availability of the alkali activator.

Water plays a crucial role in the formation, structure, and properties of geopolymers as it is an essential component of them[54]. It acts as a medium for dissolving substances, transporting dissolved ions, and facilitating the hydrolysis and polycondensation of oligomers. Additionally, water enhances the flowability of geopolymer mixtures and assists in the mixing process and ion transport. However, there has been a concern regarding the addition of excessive water during geopolymer formation, as it was previously believed that it could dilute the alkalinity of the system and lead to the transportation of ions away from the desired reaction zone. Nevertheless, the requirement for water depends on the specific characteristics of the raw materials utilized.

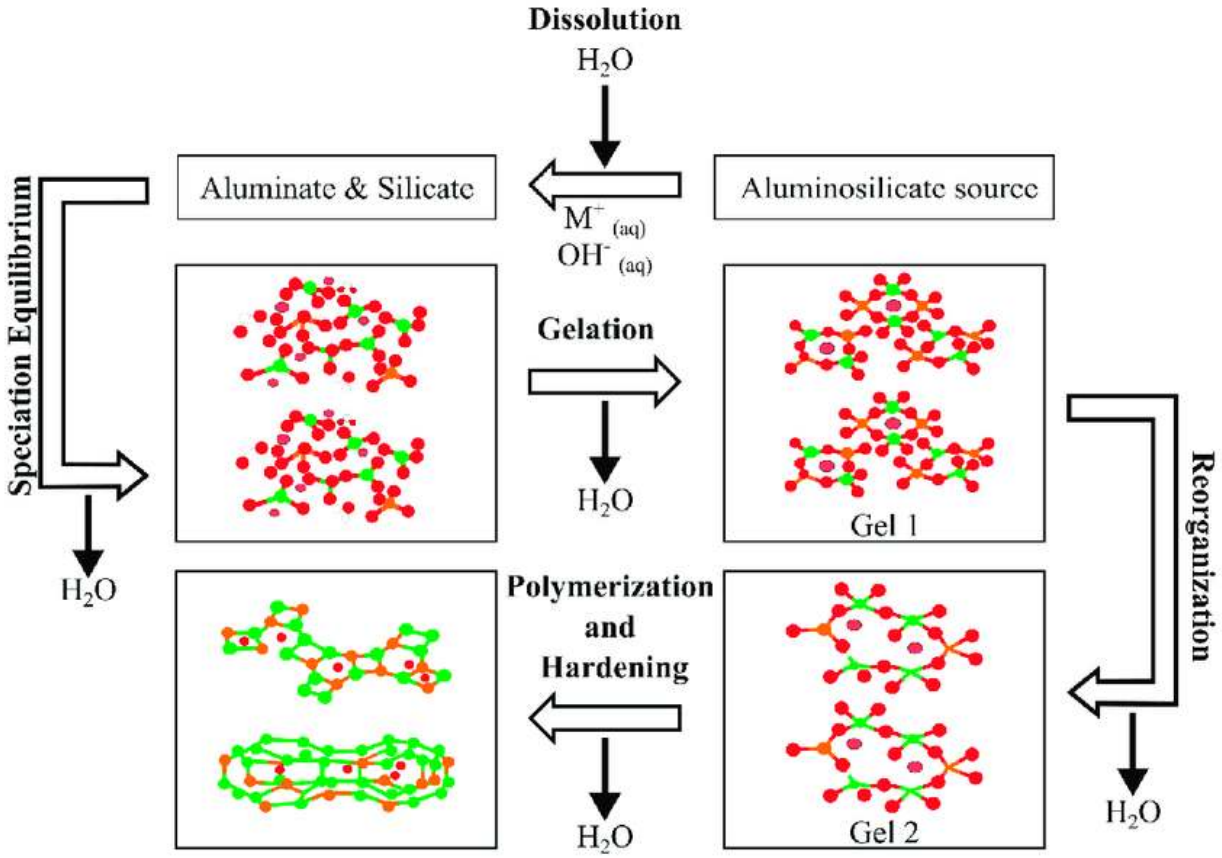

Figure 1.2. Schematic representation of geopolymerization process[55].

Thus, geopolymeric concrete is a self-compacting material that is capable of consolidating under its own weight, and it is considered one of the most revolutionary progress in concrete technology. When the precursors have completed the reaction, the resulting geopolymeric bulk structure naturally contains micro and mesopores. The extent of these porosities, usually ranging from 30 to 60 vol%, is influenced by the composition of the system and the specific Si/Al ratio. Additionally, there is growing interest in highly porous geopolymers and geopolymer foams, namely presenting porosity exceeding 70 vol%, due to their attractive physical properties such as exceptional thermal and chemical stability. These materials also have applications that go beyond the capabilities of traditional geopolymer matrices. For instance, they can be utilized as adsorbents[56,57], both for heavy metals and other substances[58], as well as for their acoustic and thermal insulating properties[59]. Moreover, it has been reported that porosities can be intentionally introduced into the micro- and mesoporous geopolymer matrix by removing a sacrificial material from its structure[60].

The advancement of new hybrid materials is driving the creation of products with multiple properties by adjusting the chemical composition of two different phases. Various studies have shown that the inclusion of additives in geopolymers can enhance their physical and chemical characteristics[61]. Over the past decade, both organic and inorganic additives, such as micro silica, microfibrils, and carbon fibers, have been successfully used to improve the mechanical strength and thermal resistance of geopolymers, as well as enhance the geopolymerization reaction for concrete applications[62,63]. For example, the addition of nano-SiO_2 has been found to enhance the microstructure, hardening properties, and compressive strength of geopolymers made from fly ash[64].

It has also been demonstrated that bio-additives can extend the durability properties of geopolymers compared to regular geopolymeric concrete[65]. It is possible to achieve materials with different properties by adjusting the chemical composition of the components, and their applications rely on this customization. While the effects of additives such as silica fume, alumina, quartz powder, fibers, and nanomaterials have mostly been explored on slag or fly ash based geopolymers[66], further research is needed to investigate their impact on clay-based geopolymers.

More recently, phase change materials (PCM) as fillers in building materials have been widely recognized as an energy-saving solution that improves the energy efficiency and sustainability of buildings. PCM are materials that are capable of absorbing and releasing thermal energy when undergoing and/or overpassing their phase change transition temperature. In Figure 1.3 a schematic illustration of this mechanism is reported. PCMs have gained attention for their potential use in thermal energy storage and have found applications in various areas such as heat recovery, solar energy storage, intelligent building materials, air conditioning, and photovoltaic devices[67]. The main objective is to contribute to more efficient and environmentally friendly energy use. When the temperature reaches the melting temperature, the PCM absorbs heat for melting. Conversely, when the temperature drops, the PCM starts to crystallize and releases the previously stored heat. However, bulk phase change materials are not suitable for use without encapsulation. Encapsulation in a shell material offers advantages such as protecting the PCM from the external environment and increasing the specific surface area for improved heat transfer[68]. PCMs can be classified into many categories according to the specific phase transitions they undergo. Solid-liquid PCMs are the most practical choice

for heat storage devices due to their high latent heat capacity and easy design. In contrast, solid-solid PCMs have a low latent heat of fusion and are not suitable for practical applications. Solid-liquid PCMs strike a good balance between a high latent heat of fusion and manageable volume change.

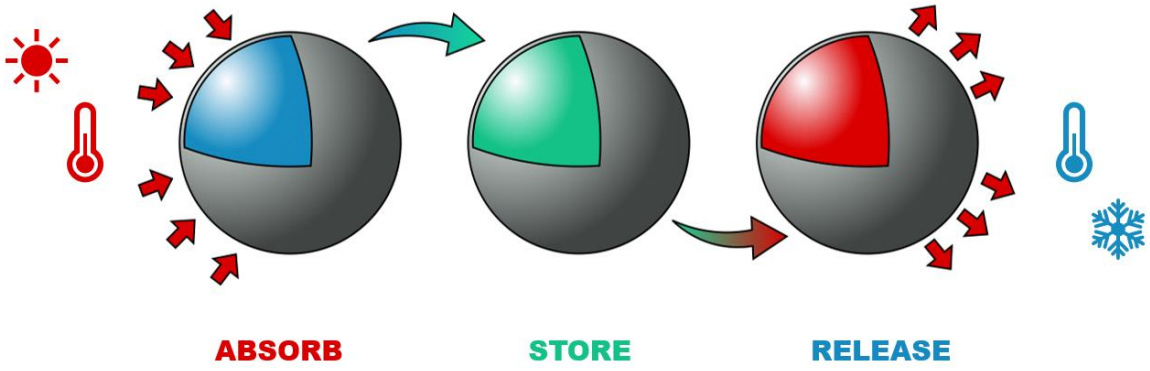

Figure 1.3. Schematic illustration of encapsulated PCM transition.

The increasing impact and attention towards eco-innovative building materials arise from their distinct features and environmental advantages. The inclusion of phase change materials is a noteworthy technology in creating new eco-sustainable composite materials. In this regard, in the latest years, many research works have been reported highlighting how useful could be combining geopolymeric materials together with PCM, creating a hybrid eco-sustainable material with high thermal savings and namely, reducing the consumption of energy for cooling and heating[69].

With this in mind, a study conducted by Hunger et al.[70] examined various experiments involving self-compacting concrete with varying amounts of microencapsulated PCM. The PCM was added to the concrete through direct mixing. The findings indicate that the inclusion of PCM results in a notable enhancement of the concrete's heat capacity and a decrease in its thermal conductivity, ultimately improving its thermal efficiency[71]. However, it is important to note that the incorporation of PCM also significantly reduced the compressive strength of the concrete[72]. Despite the reduction in compressive strength with the incorporation of phase change materials, the developed composites still satisfy the mechanical specifications for concrete applications. At the same time, they were proven to be highly effective in lowering the temperature inside enclosed spaces. Consequently, the

use of geopolymer mortar with incorporated PCM can effectively increase the thermal inertia of buildings and reduce energy consumption for cooling and heating purposes.

1.2.1 Nanoclays as functional raw materials for geopolymerization process

In recent years, natural clay minerals have been considered potential substitutes of cementitious materials because of their abundance worldwide. Using green and alternative materials instead of Portland cement is now the focus towards an efficient approach for minimizing the concrete industry's carbon footprint. Researchers are increasingly interested in the impact of carbon dioxide emissions from cement production on global warming in the construction industry [73].

As a result, there has been a growing interest in developing environmentally friendly materials from natural resources and industrial by-products[74,75]. Recycling and reutilizing industrial waste is recognized as an efficient approach to reduce power consumption across various sectors, including the cement industry. This led to a current attention to geopolymeric materials, which have the potential for environmental remediation and can be produced from industrial by-products like fly ashes[76], furnace slag[77], and natural clays[78]. In literature, it has been reported that materials with an adequate amount of reactive alumina and silica are potential sources for the synthesis of geopolymer.

The researchers discovered that nanomaterials in concrete can lead to quicker curing and generate more heat through increased hydration[79]. When combined with tricalcium silicate, nanomaterials can enhance the strength and the setting rate of concrete. The way nanomaterials disperse within the concrete also has a significant impact[80]. Accordingly, to reduce the issue of the inadequate dispersion when nanomaterials are introduced in bulk, a wide range of techniques, such as ultrasonication, mechanical stirring, and ball milling of nanoparticles have been employed[81,82]. However, the use of nanomaterials in geopolymer concrete is still under investigation in order to determine their full potential in this field.

The inclusion of nanoclay particles in geopolymer can improve its microstructure, decrease pore size and porosity, and increase the strength of the cement matrix and concrete[83,84]. Moreover, the addition of nanoclay particles improves the strength of cement paste and mortar

when it hardens[85]. According to Farzadnia et al.[86],the inclusion of 3% halloysite nanoclay in cement resulted in a significant increase in compressive strength, with up to 24% improvement in samples containing 3% halloysite, after 28 days compared to the control samples. These findings demonstrate that the enhanced strength is attributed to a denser microstructure, which can be explained by several factors such as the increased surface area, unique tubular shape of halloysite nanoclay with a high aspect ratio, the presence of SiO_2 on the surface of nanotubes, and the ability of the nanoclay to fill voids due to its swelling properties.

Geopolymer nanocomposites reinforced with nanoclay have recently garnered significant attention. Various methods can be employed to synthesize these materials, with the most common being the in situ method, where nanoclay particles are added during the geopolymer matrix synthesis. The inclusion of nanoclay particles enhances the mechanical properties of geopolymer nanocomposites, including strength, stiffness, and toughness, owing to their high aspect ratio, which acts as a physical barrier against crack propagation. Moreover, the addition of nanoclay enhances the thermal stability of the geopolymer matrix, making it suitable for high-temperature applications.

Metakaolin is extensively used in one-part alkali activated materials and it is synthesized from the calcination of kaolinite clay. This process involves heating the clay at temperatures between 450 and 800 °C and it is commonly used for precursors like kaolinite being one of the most notable. During calcination, the crystalline phase structure of the kaolinite is broken down, leading to the formation of an amorphous glassy phase that is highly reactive. The optimal temperature for calcination varies depending on the source material. In the case of kaolinite clay, it is typically calcined at temperatures ranging from 700 to 800 °C. This temperature range causes dehydroxylation, loss of long-range silica and alumina layers, and the transformation of alumina from octahedral to tetrahedral coordination [87]

As mentioned before, the most common clay used as a geopolymer raw material is kaolin, but the suitability of other clays was also investigated. For instance, clays dominated by 2:1 dioctahedral layer silicates were exploited as aluminosilicate precursors[88]. As a matter of fact, high strength geopolymers were prepared from a calcined and ground interstratified illite-smectite clay[89]. It should be considered that the quantities of clay minerals in soils can vary significantly worldwide, and it is important to comprehend how these minerals impact the reaction products in alkali activation, since clays play a dominant role in soil

composition. Marsh et al. [90] activated mixtures of kaolinite, montmorillonite, and illite precursors with sodium hydroxide solutions. They found that certain types of clays had a more significant influence on the reaction products, showing that the suitability of a particular soil for alkali activation depends not only on the total clay content but also on the types and relative quantities of clay minerals present. As a result, it has been demonstrated that secondary minerals found in kaolin will impact the reaction process and ultimate properties of geopolymer. While the inclusion of halloysite in kaolin led to a higher geopolymerization rate, enhancing the dissolution of silicon and aluminum, it did not alter the geopolymerization pathway[91]. This is why halloysite nanotubes were exploited as aluminosilicate precursors in the synthesis of geopolymers due to their high reactivity[92–94]. This improved reactivity suggests the beneficial impact of HNTs in geopolymer synthesis.

Recently, the use of halloysite as a solid precursor for geopolymer synthesis has increased and the need to establish relationships between the synthesis conditions and the final products has emerged. For instance, Kaze et al.[95] conducted a study to investigate the impact of thermal activation on geopolymer made from halloysite, with temperatures ranging from 600 to 750 °C. Their findings revealed that 750 °C was the optimal temperature for achieving the highest reactivity and mechanical properties. On this path, Zhang et al.[92] discovered that the dehydroxylation process during calcination at temperatures between 650 and 850 °C led to an increase in the amorphous content and reactivity of halloysite when reacting with an alkaline solution. This resulted in the formation of a geopolymer with a compact structure and higher compressive strength. Nevertheless, the exploration of halloysite-based geopolymers is not as extensively established as that of other precursors, like fly ash[96], kaolinite[97], and illite[88], although halloysite shows potential as an aluminosilicate precursor for their preparation.

The reactivity and mechanical performance of geopolymer binders made from blends of metakaolin and meta-halloysite were also tested. It turned out that incorporating meta-halloysite increased the rate at which aluminosilicate oligomers were released in the alkaline solution. This resulted in the development of a dense and strong matrix, which helps explain the high mechanical performances observed[98]. Thanks to the high geopolymerization reactivity of halloysite, alkali-activated halloysite-based geopolymers are sensitive to the curing conditions. According to literature[99], halloysite-based

geopolymers that are cured at room temperature possess a dense and uniform microstructure, resulting in high compressive strength. However, increasing the curing temperature led to the formation of geopolymers with more unreacted precursors and larger pores, since the polymerization occurred more rapidly. This had a negative effect on the compressive strength of the final product. Another recent paper reports the activation of halloysite with phosphoric acid instead of alkaline activator solutions[94]. The microstructure and mechanical performance have been shown to be intensely dependent on the halloysite structure and the concentration of phosphoric acid used in its preparation.

In the following chapters of this PhD thesis a preliminary focus on the specific features of the nanoclays used as aluminosilicate precursors will follow.

2. Purification of halloysite nanotubes from natural deposits

Different materials have been used in the preparation of geopolymers, with kaolinite being widely employed in the early stages of development. However, research has since expanded to include other raw materials such as natural clays, industrial waste like ashes, slag, waste glass, and copper mine tailings, as well as various natural and artificial aluminosilicates like zeolite, pure Al_2O_3–$2SiO_2$ powder, and magnesium-containing minerals. These raw materials are all aluminosilicates, rich in alumina and silica.

In the initial part of this PhD work, the main objective was to purify samples of natural halloysite nanoclay since they are often contaminated by a certain level of platy kaolinite nanoparticles, which varies depending on the geological deposit from which they were sourced.

Natural clay samples are typically composed of a mixture of various minerals, which can limit their suitability for applications in different fields. The purification of natural nanoclays involves the process of separating and removing impurities such as carbonates, iron oxides, or organic materials from raw clay materials to obtain nanoclays with improved quality and properties[100]. It is worth noting that natural halloysite may contain variable quantities of kaolinite. Consequently, the effective separation of halloysite and kaolinite becomes decisive in preparing HNTs for a wide range of applications. With this in mind, controlling the nanoclays sedimentation selectively can be an effective way to achieve this objective. The sedimentation of halloysite in water is quite unique, and a simple percolation model can explain it. It was observed that halloysite dispersions in water settle with a significant volume of sedimentation. A recent study has provided an explanation for this phenomenon based on geometric factors. In particular, by considering the contact distance between the nanotubes, it was possible to predict the volume fraction of nanotubes in the sedimentation volume[101]. On this basis, it was found that the sedimentation volume of HNTs is driven by hard-cylinder interactions, and the aqueous dispersion looks stable when the contact distance between nanoparticles is approached.

According to the literature, it is worth highlighting that introducing varying proportions of monosaccharides (like glucose) or disaccharides (such as sucrose and maltose) offers an efficient approach for regulating the stability of aqueous dispersions. This regulation is

achieved by altering water's physico-chemical properties, including its dielectric constant, refractive index, and viscosity[102]. Conversely, the incorporation of non-ionic macromolecules (such as polymers and surfactants) has the potential to influence the colloidal stability of aqueous nanoclay solutions. This influence arises from steric interactions and depletion processes, as demonstrated in studies involving kaolinite dispersions with variable amounts of biopolymer [47]. It has been reported that the sedimentation kinetics of halloysite can be perturbed by salt addition that causes a variation of ζ-potential.

With this in mind, here we decided to examine how the addition of sucrose impacts the colloidal stability of halloysite and kaolinite in aqueous media. Particularly, we studied how sucrose acts to screen the attractive interactions between clay nanotubes, using the DLVO theory. Additionally, we looked into how varying concentrations of sucrose affect the sedimentation kinetics of both nanoclays, aiming to optimize their separation efficiency in mixed halloysite/kaolinite aqueous solutions.

2.1 Impact of sucrose on the aqueous diffusion properties, surface charge and sedimentation of clay nanoparticles

Preliminary investigations were carried out on sucrose solutions to ensure accurate analysis and comprehension of the colloidal characteristics of nanoclay dispersions. The outcomes are detailed in Table 2.1. Notably, the properties under investigation influence the electrophoretic mobility, dynamic behavior in aqueous environments, and sedimentation tendencies of nanoparticles dispersed within sucrose-infused aqueous solutions.

The reported results are indeed needed to better analyse Dynamic Light Scattering experiments that helped in exploring the influence of sucrose addition on the HNTs and kaolinite’s aqueous diffusion coefficient.

Table 2.1. Refractive index, relative dielectric constant and viscosity of sucrose solutions in water at 25 °C.

Sucrose Concentration / wt%	RI	ε_r	η / mPa s
0	1.332	78.4	0.89
1.3	1.336	78.2	1.03
2.5	1.338	77.9	1.06
4.8	1.341	77.4	1.15
9.8	1.349	76.1	1.34
15.5	1.357	74.7	1.59
25.9	1.370	72.0	2.17

As a general result, kaolinite shows lower diffusion coefficients within aqueous solvents in comparison to halloysite nanotubes (Figure 2.1). This outcome is likely attributed to the larger size of kaolinite nanoparticles, which leads to decreased mobility in water with respect to HNTs. Interestingly, we noticed that the presence of sucrose does not influence the diffusion coefficient of kaolinite. On the contrary, the mobility of HNTs in aqueous environments is notably affected by the presence of sucrose.

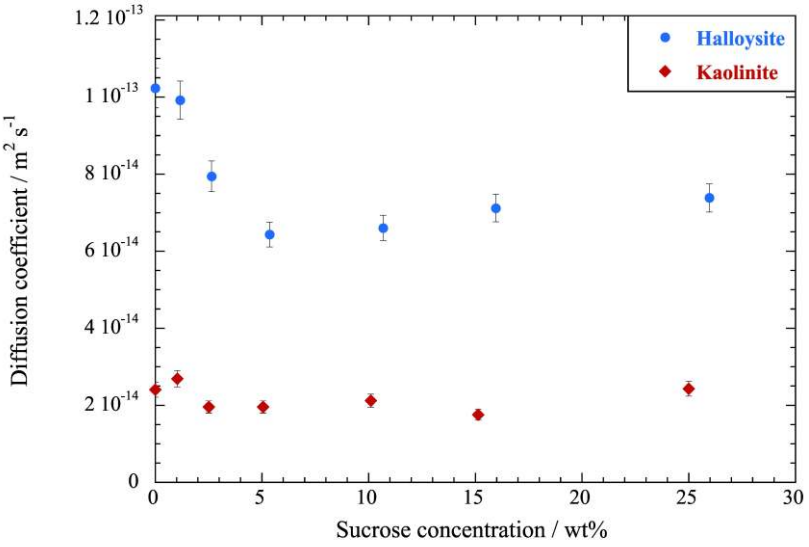

Figure 2.1. Aqueous diffusion coefficients of HNTs and kaolinite as function of the sucrose concentration.

As illustrated in Figure 2.1, adding small quantities of sucrose, up to approximately 5 wt%, led to a reduction in the diffusion coefficient of halloysite, implying a decrease in the dynamic behavior of the nanotubes. In contrast, further sucrose addition resulted in a slight increase in the diffusion coefficient, indicating enhanced diffusivity of HNTs. These trends can be linked to the influence of sucrose on the interactions between halloysite nanotubes dispersed in water.

This influence is also evidenced in the ζ-potential results (Table 2.2), where the presence of sucrose slightly alters the surface charge of both the nanoclays.

Table 2.2. ζ-potential of halloysite and kaolinite in sucrose solutions at variable concentration.

Sucrose Concentration / wt%	**ζ-potential / mV**	
	Halloysite	**Kaolinite**
0	-34.1 ± 1.5	-21.9 ± 1.1
4.8	-32.6 ± 1.1	-21.3 ± 1.5
9.8	-32.4 ± 1.4	-22.0 ± 1.2
15.5	-32.3 ± 1.3	-22.3 ± 1.2

Looking at the data in Table 2.2, it is evident that the electrostatic repulsions among kaolinite nanoparticles in sucrose solutions remain comparable to those in pure water. On the other hand, for HNTs, there is a slight reduction in the absolute ζ-potential value with the addition of sucrose. Notably, the ζ-potential values are negative across the entire range of sucrose concentrations and halloysite exhibits more negative ζ-potential values compared to kaolinite, indicating stronger repulsive interactions and hindered aggregation in the case of halloysite nanotubes.

It is worth emphasizing that the presence of sucrose can impact Van der Waals interactions among nanoparticles. This phenomenon will be thoroughly examined soon. Specifically, the addition of sucrose has the potential to diminish attractive interactions among dispersed nanoclays, thereby altering the colloidal stability of the dispersions. These effects are

influenced by the concentration of sucrose, as shown from the results regarding the aqueous diffusion coefficient of halloysite (Figure. 2.1).

As reported in Figure 2.2, dispersions of kaolinite and halloysite exhibit distinct macroscopic features, influenced by the concentration of sucrose and the time of equilibration after the preparation as well. Examining the images provided in Figure 2.2 (a), it becomes evident that the increase from 2.5 to 10 wt% of sucrose concentration leads to a lowering of the sedimentation front in halloysite dispersions.

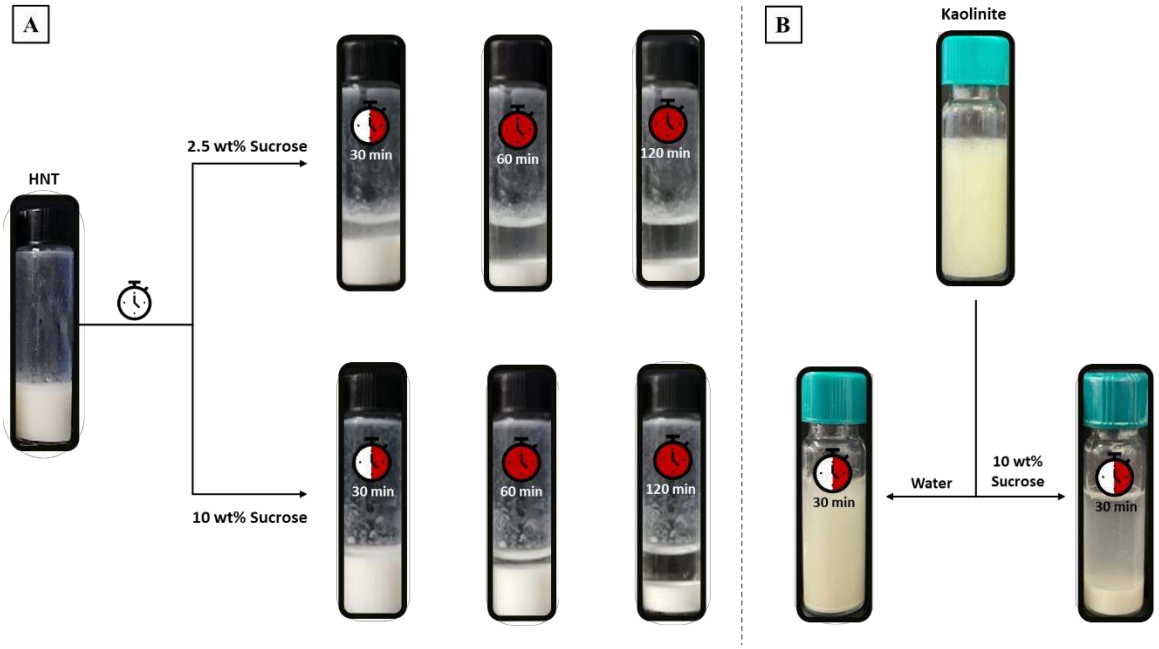

Figure 2.2. (a) HNTs dispersions in 2.5 and 10 wt% sucrose at variable times of equilibration. (b) Kaolinite dispersions in water and 10 wt% sucrose after 30 min of equilibration.

Therefore, it can be concluded that the rate of HNTs sedimentation is faster at lower sucrose concentrations. It took 2 hours to observe the complete separation between the nanoparticles and the solvent for both sucrose concentrations. After 30 minutes of equilibration, the kaolinite suspensions in water did not show a clear sedimentation front, unless the sucrose concentration was at least 10 wt%. To analyse the sedimentation kinetics, ImageJ software was used to track the time evolution of the sedimentation profiles for both HNTs and kaolinite dispersions. The sedimentation volume fraction was determined after 2 hours of equilibration, when the process was deemed complete. The

settling velocity was estimated from the slope of the sedimentation front vs. time plot, based on a previous work on the effect of ionic strength on the colloidal stability of halloysites[42]. From the macroscopic observations, the settling velocity for kaolinite could only be determined in aqueous media with sucrose concentrations of 10 wt% or higher.

Figure 2.3 (a) illustrates that the sedimentation volume fraction values for kaolinite are lower compared to halloysite, and they remain relatively constant across the range of sucrose concentrations studied. This suggests that the sedimentation of kaolinite occurs at a faster rate compared to halloysite when the sucrose concentration is 10 wt% or higher, as supported by the settling velocity data shown in Figure 2.3 (b).

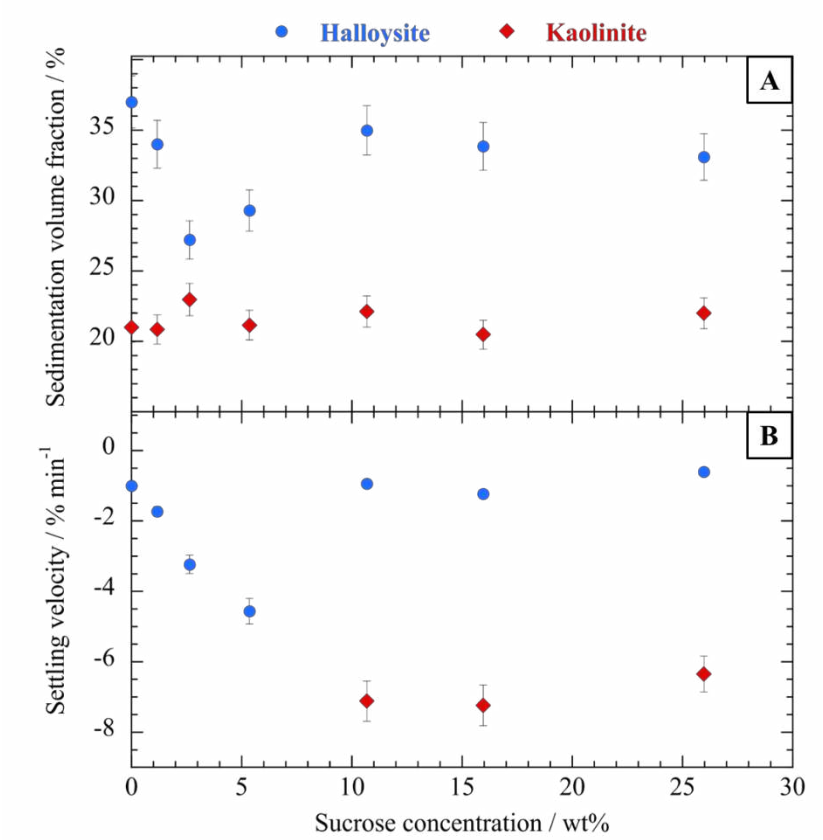

Figure 2.3. Sedimentation volume fraction (a) and settling velocity (b) of halloysite and kaolinite as function of the sucrose concentration.

Notably, this distinct sedimentation behavior could be advantageous for effectively separating kaolinite and halloysite in natural samples containing both types of nanoclays. The inclusion of the carbohydrate did not have any impact on the sedimentation volume

fraction or settling velocity (for sucrose ≥ 10 wt%) of kaolinite dispersions. Conversely, the presence of sucrose influenced the sedimentation kinetics of halloysite nanotubes dispersed in water. Our observations revealed that the sedimentation velocity of HNTs is enhanced when the sucrose concentration is up to 5 wt%, but further addition of sucrose resulted in the opposite effect. Similarly, the sedimentation volume fraction displayed a minimum value at 5 wt%. These findings regarding the relationship between the sedimentation parameters and sucrose concentration, as depicted in Figure 2.3, align with the data obtained from DLS, which demonstrated reduced diffusion of HNTs in water at low sugar concentrations and a minimum value at 5 wt%.

The impact of sucrose concentration on sedimentation parameters can be explained in terms of the balance between Van der Waals forces and repulsive interactions between nanoparticles, as described by the DLVO theory. However, this approach is not suitable for describing the sedimentation of kaolinite due to the large size of the nanoparticles. DLS experiments demonstrated that the hydrodynamic diameter of kaolinite ranged from 1828 ± 146 nm to 2796 ± 223 nm at sucrose concentrations of 1.27 and 15.5 wt%, respectively. The addition of sucrose resulted in slight changes in the surface charge of HNTs (Table 2.2), indicating that repulsive interactions between halloysite nanotubes were not affected. However, it can be predicted that sucrose does influence the Van der Waals attractive forces. The Hamaker constant was indeed calculated as a function of sucrose concentration for HNTs dispersions using the equation provided here:

$$A_H = \frac{3}{4} k_B T \cdot \left(\frac{\varepsilon_1 - \varepsilon_2}{\varepsilon_1 + \varepsilon_2}\right)^2 + \frac{3h\upsilon_e}{8\sqrt{2}} \cdot \frac{(n_1^2 - n_2^2)}{(n_1^2 + n_2^2) \cdot \left(2 \cdot \sqrt{n_1^2 + n_2^2}\right)} \quad (2.1)$$

where k_B is the Boltzmann constant, T is the absolute temperature, ε is the dielectric constant, n is the refractive index and υ_e is the mean ionization frequency of the material and it is $\approx 3 \cdot 10^{15}$ Hz. Here, the subscripts 1 and 2 refer to halloysite and sucrose solution, respectively.

Figure 2.4 shows the normalized Hamaker constant for halloysite nanotubes dispersed in aqueous solvent with varying sucrose amounts.

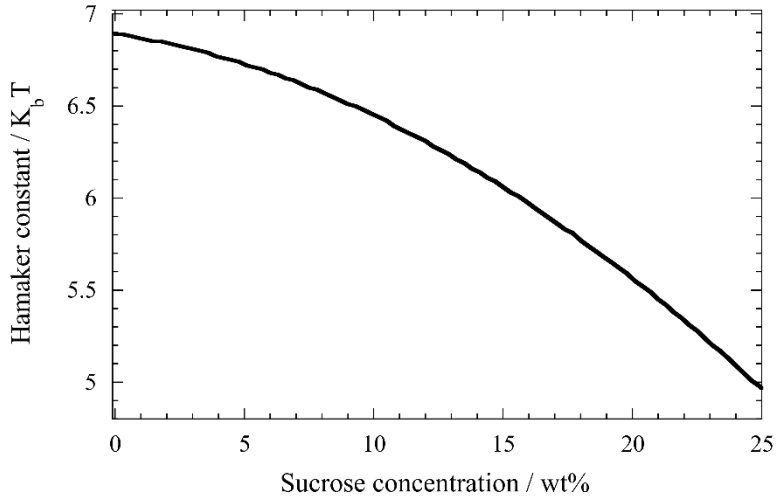

Figure 2.4. Dependence of the Hamaker constant on the sucrose concentration for halloysite, determined by using Equation 2.1.

According to Figure 2.4, the Hamaker constant is positive for all sucrose concentrations, indicating that the Van der Waals forces are attractive. We observed a decrease in the attractive forces between the nanotubes dispersed in water by adding sucrose. This decrease in the Hamaker constant aligns with the reduction in Van der Waals interactions between the dispersed nanotubes, which is further enhanced by increasing the amount of sucrose in the aqueous medium.

The decreasing trend of the Hamaker constant as a function of the sucrose concentration (Figure 2.4) can be described by a binomial equation across the entire range of investigation. Interestingly, there is a linear region where the Hamaker constant only slightly varies for sucrose concentrations up to ca. 5 wt%. Specifically, we estimated that the reduction in the Hamaker constant is less than 2%, indicating that the effect of sucrose on the attractions between nanoparticles is negligible for sugar concentrations up to approximately 5 wt%. Based on these findings, we can hypothesize that the attractive forces are significantly more predominant than the repulsive forces in the presence of small amounts of sucrose, promoting the clustering of HNTs. Consequently, the diffusion coefficient in water decreased (Figure 2.1), and sedimentation kinetics increased (Figure 2.3 (b)). These results are also consistent with the minor reduction in the surface charge of HNTs (Table 2.2).

On the other hand, for sucrose concentrations equal to or greater than 10 wt%, the difference between attractive and repulsive forces decreased, explaining both the sedimentation parameters and the data from dynamic light scattering (DLS). In other words, the attractive forces are substantially screened by sucrose, resulting in increased mobility in water and improved colloidal stability of the nanotubes.

2.2 Separation of halloysite ad kaolinite mixtures in sucrose solutions

In this study, we exploited the sedimentation kinetics of the nanoclays in sucrose solutions to achieve a successful separation of the halloysite and kaolinite components in mixtures.
Separation experiments were conducted on them according to the following procedure. Initially, we created mixtures of halloysite and kaolinite with a 1:1 mass ratio in sucrose aqueous solution at 10 wt%. The concentration of both nanoclays was maintained at 2 wt%. The dispersion was then subjected to sonication for 15 minutes, magnetic stirring for 2 hours, and 30 minutes of equilibration, which didn't guarantee the complete sedimentation of the nanoparticles. Afterward, it was removed the 30% of the total volume from the upper part of the dispersion. The recovered suspension was subsequently dried at 50°C. To eliminate the sucrose, the dried powder was washed five times with water, and then stored in a desiccator at 25°C and 75% relative humidity. In order to make a comparison, the separation experiment was also conducted using water as the solvent (Attached Manuscript I).
Few kaolinite nanoplates and a large quantity of halloysite nanotubes were observed through scanning electron microscopy in the sample obtained from a 10 wt% sucrose solution (Figure 2.5).

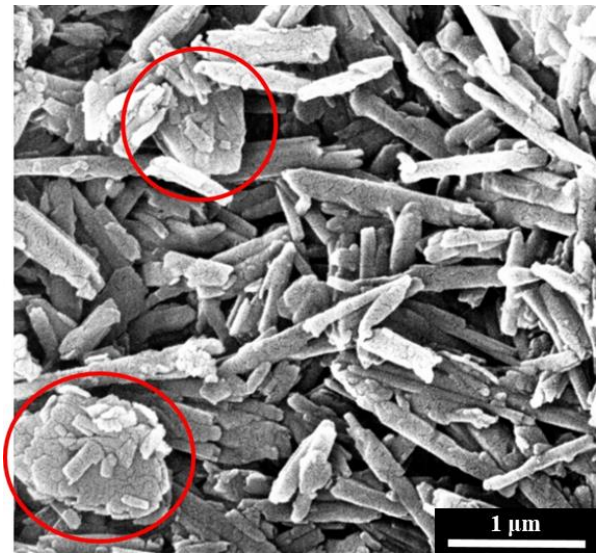

Figure 2.5. SEM image of the sample obtained from the separation in 10 wt% sucrose solution. The circular red lines highlight the kaolinite nanoplates.

The separation procedure's efficiency was further evaluated using thermogravimetry, a valuable technique for analysing multicomponent materials quantitatively and qualitatively[103,104]. Figure 2.6 presents a comparison of the differential thermogravimetric curves of the pristine nanoclays and their mixture (HNT/Kaolinite 50:50) with the curves of the materials obtained by the separation using both water and a 10 wt% sucrose solution.

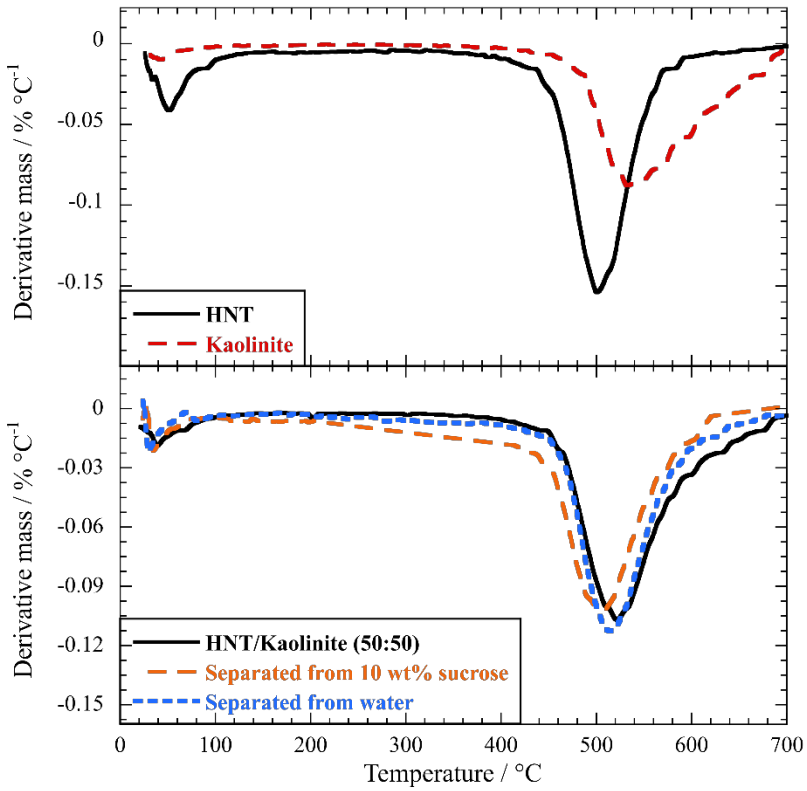

Figure 2.6. DTG curves of HNT, Kaolinite, HNT/Kaolinite mixture (50:50) and the samples obtained from the separation in water and 10 wt% sucrose.

Literature suggests that pure halloysite displayed its main mass loss between temperatures of 400 and 600 °C due to the dehydroxylation and elimination of interlayer water molecules, while kaolinite showed a more significant reduction in mass over a broader range, between 480 and 700 °C [105,106].

Based on this information, the analysis of the separated materials focused on the differential thermogravimetric curves within the range of 400–700 °C. Initially, the peak temperatures (T_{peak}) for the different samples were determined from the minimum points on the differential thermogravimetric curves. Figure 2.7 shows that a linear relationship was found between T_{peak} and the composition of the halloysite/kaolinite mixtures.

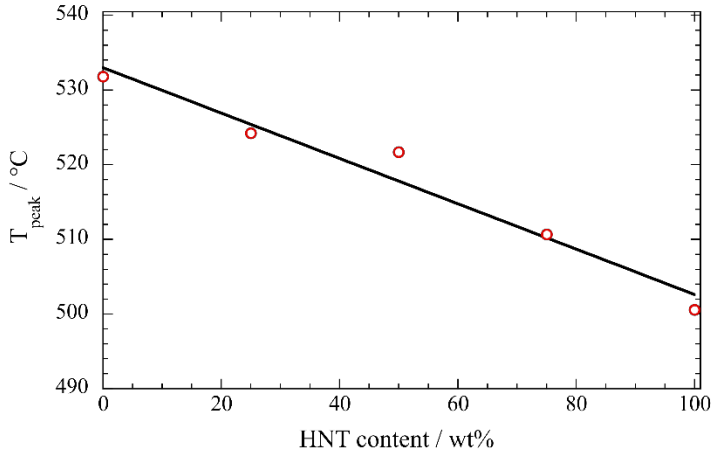

Figure 2.7. Dependence of the peak temperature with variable HNT composition for halloysite/kaolinite mixtures. The red circle points are the experimental data, while the black line represents the linear fitting.

Using the linear fitting of this trend, the mass percentage of halloysite in the separated materials was calculated based on the corresponding T_{peak} values obtained from the sucrose solution (503.8 °C) and water (514.8 °C). The results indicated that the halloysite content was 97 ± 3 wt% for the materials obtained from the separation in a 10 wt% sucrose solution, while it was 59 ± 3 wt% for the materials obtained through water.

The DTG curves of both pristine kaolinite and halloysite were analysed more accurately by fitting them using Fityk software[107]. The analysis exploited a split Gaussian function as a model, and it was employed to fit the DTG curves. It can be expressed as follows:

$$\frac{dm}{dT} = \left(\frac{dm}{dT}\right) * \exp\left[-ln2\ \left(\frac{T-T_C}{\Delta T_L}\right)^2\right] \quad for\ T \leq T_C \tag{2.2}$$

and

$$\frac{dm}{dT} = \left(\frac{dm}{dT}\right) * \exp\left[-ln2\ \left(\frac{T-T_C}{\Delta T_R}\right)^2\right] \quad for\ T \geq T_C \tag{2.3}$$

where T_C is the temperature at the centre of the function, ΔT_L and ΔT_R are the left and right widths indicated as temperature ranges, while *(dm/dT)* is the common value for the left and right sides.

The parameters obtained from fitting the DTG curves of kaolinite and halloysite are listed in Table 2.3.

Table 2.3. Fitting parameters obtained by applying the split Gaussian equations of halloysite and kaolinite DTG curves.

Fitting Parameters	Halloysite	Kaolinite
$\mathbf{T_C}$ **/ °C**	502.9	533.2
$\mathbf{\Delta T_L}$	33.2	24.0
$\mathbf{\Delta T_R}$	36.7	80.1
(dm/dT) / % °C^{-1}	-0.148	-0.066

The DTG curves of mixtures containing both the nanoclays were successfully fitted by combining the split Gaussian equations of halloysite and kaolinite. The fitting parameter considered was the rate of weight loss (dm/dT) for halloysite and kaolinite contributions. At the same time, T_C, ΔT_L, and ΔT_R were fixed (determined by fitting the DTG curves of pristine HNT and kaolinite). For example, Figure 2.8 (a) compares the experimental and calculated DTG curves for a mixture containing 50 wt% halloysite.

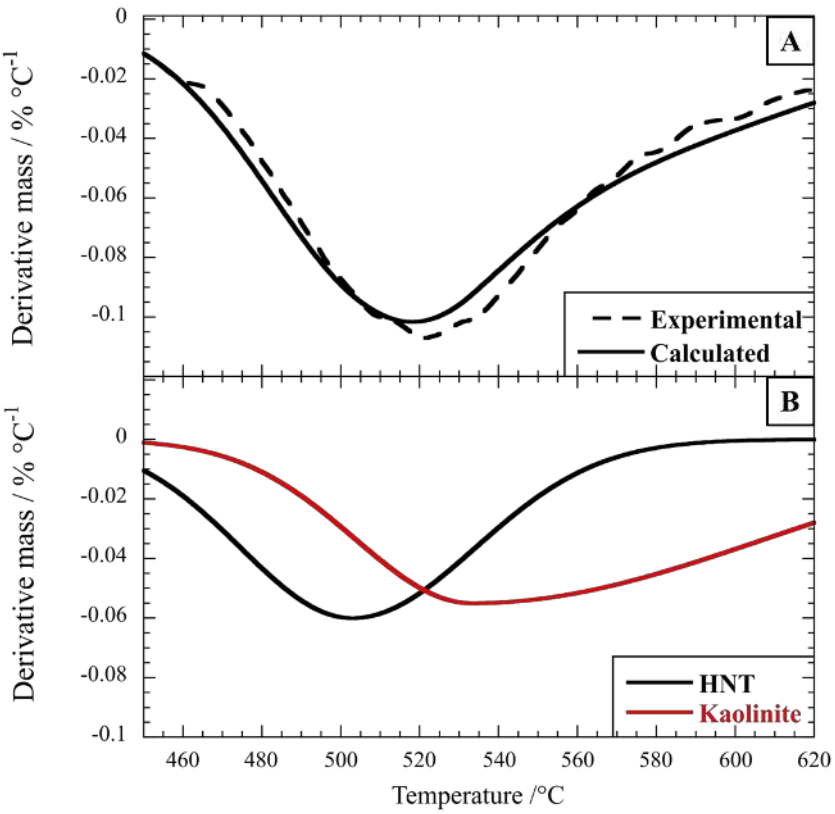

Figure 2.8. (a) Experimental and fitted DTG curves for the mixture containing 50 wt% of halloysite. (b). Split Gaussian functions of halloysite and kaolinite used in the fitting analysis.

Additionally, Figure 2.8 (b) separately displays the split Gaussian functions used in the fitting analysis. Using the fitted DTG curves, the mass percent of halloysite in the mixture can be estimated from the following equation:

$$\mathrm{HNT(wt\%)}_{SGE} = 100 \cdot (A(SGE)_{HNT}/(A(SGE)_{M} \qquad (2.4)$$

being $A(SGE)_M$ the area obtained by the integration of the split Gaussian function of the mixture, while $A(SGE)_{HNT}$ is the integral area for the single contribution of halloysite used in the fitting analysis.

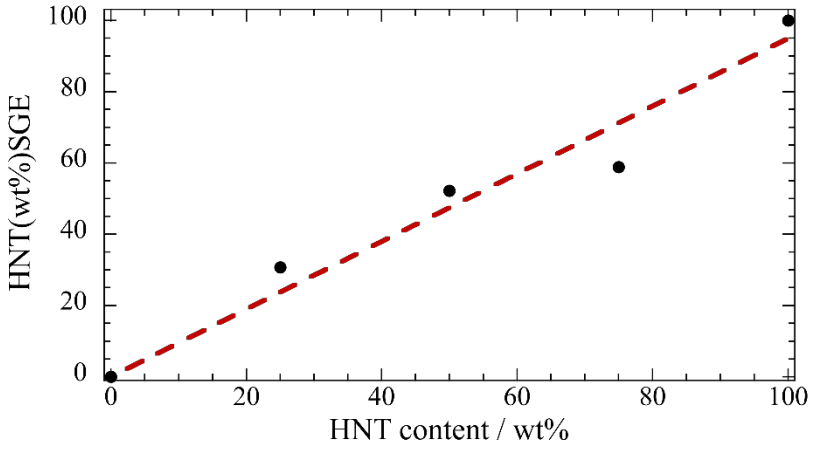

Figure 2.9. Dependence of the halloysite content determined by the fitting on the HNT concentration used to prepare the mixture with variable composition.

A linear relationship between the calculated $HNT(wt\%)_{SGE}$ values and the halloysite mass percent used to prepare the mixtures is observed in Figure 2.9. The linear regression presents R^2 equal to 0.985, while the relative error for the fitting parameter is 6%. Through the linear fitting of the data presented in Figure 2.9, we were able to determine a calibration curve that can be used to calculate the HNT content in halloysite/kaolinite composite samples with unknown compositions, including the separated material obtained using the protocol previously described.

As shown in Figure 2.10 (a), the DTG curve of the sample separated from the sucrose solution, can be analysed using a combination of split Gaussian equations for halloysite and kaolinite. In Figure 2.10 (b), it can be evidenced that the contribution of halloysite to the fitting analysis is significantly higher than that of kaolinite. By using the corresponding $HNT(wt\%)_{SGE}$ value (84.3 wt%) and the calibration curve shown in Figure 2.9 , we were able to determine that the halloysite content in the separated material is 89 ± 5 wt%, confirming the high efficiency of the separation procedure in sucrose aqueous solution.

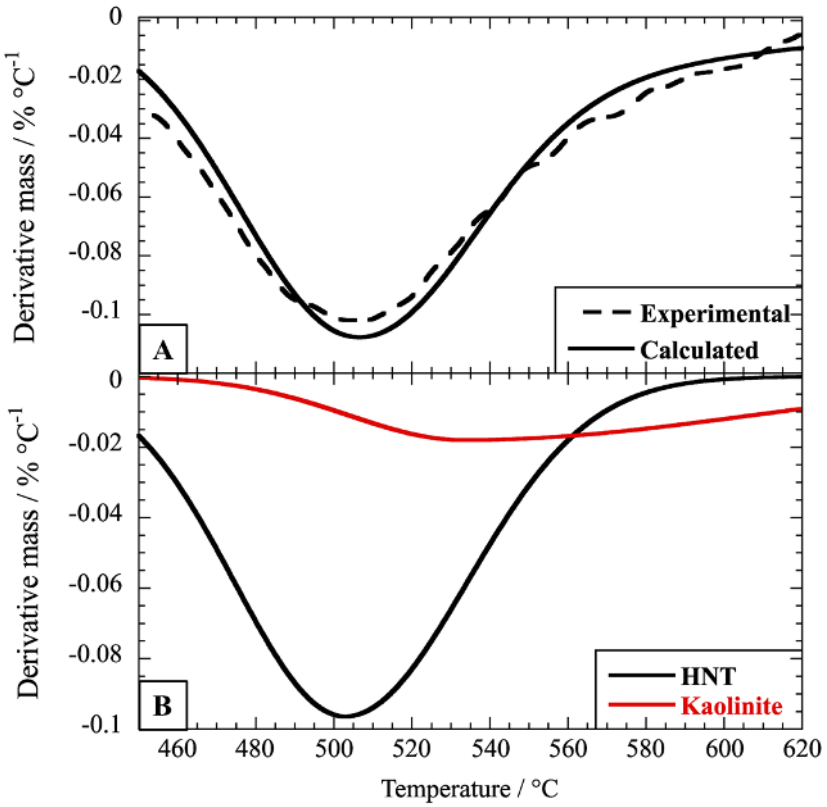

Figure 2.10. (a) Experimental and fitted DTG curves of the material obtained by the separation in 10 wt% sucrose solution. (b) Split Gaussian functions of halloysite and kaolinite contributions employed in the fitting analysis.

On the other hand, the sample separated from water has an HNT(wt%)$_{SGE}$ value of 51.6 wt%. Using this information, we calculated a HNT content of 53 ± 4 wt%, which is significantly lower than that detected for the material separated in the 10 wt% sucrose solution. These results indicate that the addition of sucrose in the aqueous solvent promotes the separation between the nanoclays. This finding is consistent with the macroscopic observations of the dispersions (Figure 2.2) and the sedimentation kinetics (Figure 2.3), which showed that the addition of 10 wt% sucrose reduces the colloidal stability of kaolinite. At the same time, the settling velocity of halloysite was only slightly affected.

The objective of this study was to develop a new method for separating mixtures of halloysite and kaolinite by using the effects of sucrose on the stability of both nanoclays in water.

It is crucial to control the sedimentation of the nanoclays in order to purify natural halloysite samples. Based on the results of Dynamic Light Scattering (DLS), we found that the effect of sucrose on the diffusion of halloysite nanotubes in water depends on the concentration of sucrose, while no effects were observed for kaolinite nanoplates. The presence of sucrose slightly affected the surface charge of the nanoclays. We observed that small amounts of sucrose (<10 wt%) improved the sedimentation kinetics of halloysite nanotubes. However, this effect was eliminated by increasing the sucrose concentration (≥10 wt%) due to the significant screening of attractive interactions between the clay nanotubes. Interestingly, the dispersibility of kaolinite was greatly reduced in the presence of sucrose concentrations exceeding 10 wt%. Therefore, we concluded that the optimal separation efficiency for halloysite/kaolinite mixtures can be achieved in a 10 wt% sucrose solution. We used thermogravimetry to determine the composition of the separated materials in both water and 10 wt% sucrose solution. We found that the presence of 10 wt% sucrose significantly increased the halloysite content (89 ± 5 wt%) compared to separation in water (53 ± 4 wt%). In summary, this study demonstrated that the addition of sucrose to aqueous solvents can successfully separate halloysite and kaolinite. The separation efficiency can be controlled by the concentration of sucrose, which affects the stability and sedimentation kinetics of both nanoclays. This protocol can be used to purify natural halloysite samples. For future investigations it would be useful to understand if the same consideration about the effect of sucrose on sedimentation behavior of these nanoclays is the same by taking into consideration other disaccharides.

3. Role of water in nanoclays from different resources

The interactions between water and clay minerals play a crucial role in a wide range of fields like materials science, soil science, and geotechnical engineering. The significance of this interaction arises from the fact that water is an essential structural component of numerous clay minerals. Consequently, the interaction between water and clay minerals has garnered significant interest for over a century. In this regard, halloysite is an attractive clay mineral known for its distinct structural characteristics related to water. The interlayer space of halloysite (10 Å) consists of two separate surfaces, between which the interlayer water is confined in an electrically neutral space.

It is possible to distinguish two forms of halloysite depending on the presence of water in the interlayer: halloysite 10 Å and halloysite 7 Å. The first one is very susceptible to irreversible dehydration, generating the collapse of the interlayer with a reduction in d-spacing from 1.1 nm to 0.72–0.74 nm, so called halloysite 7 Å. As a matter of facts, it was suggested that halloysite 10 Å is a metastable species towards the only stable form of 7 Å, since once the water is lost, it is not restored by any water treatments[108]. The existence of water in the interlayer leads to distortion between the octahedral and tetrahedral sheets, resulting in a tubular shape that is partially or completely filled with water, known as "lumen water". It should be noted that a certain amount of external water is also present outside the halloysite nanotubes. This is referred to as unconfined water. Thus, three types of water can be distinguished in halloysite (10 Å), namely interlayer, lumen, and unconfined water. Conversely, the more common form halloysite is 7 Å, with two types of water (Figure 3.1). On the other hand, as mentioned before, in platy kaolinite there is not any structural water.

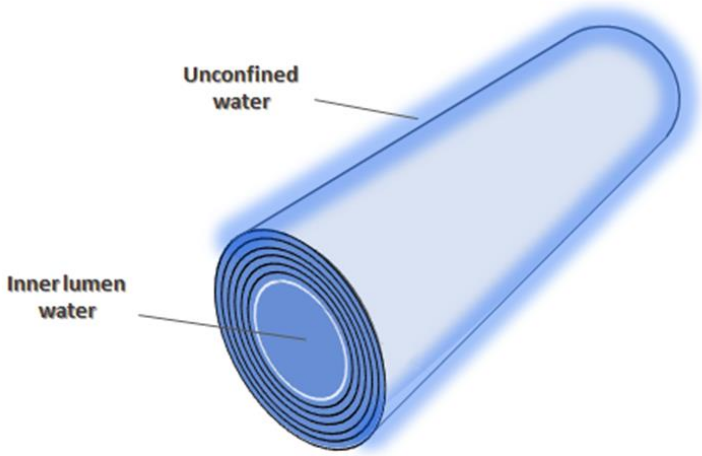

Figure 3.1. Illustration of water populations in halloysite nanotube 7 Å.

As previously reported by Lisuzzo et al.[109], the water confinement within the cavity of halloysite nanotubes was demonstrated by exploiting Knudsen thermogravimetry. It was discovered that the water vapor pressure within the nanotube's cavity is higher than that of bulk water. This finding can be attributed to the confinement of water inside the nanotube, which is in agreement with the Gibbs-Thomson effect. Because of the higher vapor pressure, the water confined within the nanotube's cavity can evaporate more quickly than bulk water. This difference in evaporation rates serves as the main driving force in filling the nanotube's cavity through aqueous dispersions. In contrast to halloysite nanotubes, experiments with kaolinite dispersions showed that the flat structure of the nanoparticles did not offer any confinement sites for the aqueous solvent. Therefore, the confinement of water is directly related to the geometrical properties of the nanoclay particles.

With this in mind, in this section, a detailed study of water in nanoclay systems will be showed. In particular, three different nanoclays have been under investigation: platy kaolinite, halloysite nanotubes (HNT) and Patch halloysite nanotubes (Patch HNT).

To this purpose, NMR techniques have been employed. Firstly, results from magic angle spinning (MAS) solid-state NMR will be presented. In order to determine molecular structures, the sample was positioned in an air-turbine tool at an angle of 54.7° in relation to the primary magnetic field. Additionally, in our case, it was rotated at a speed of 5000 Hz. This strategic positioning and spinning effectively nullify dipole-dipole couplings, enabling a clearer examination of NMR spectrum characteristics. This allows for a more

accurate identification of features like secondary quadripolar couplings and chemical shift anisotropies.

In Figure 3.2, solid state ^{1}H MAS NMR spectra of HNT, Patch halloysite and Kaolinite are reported. Before starting the experiments, the samples were equilibrated in a desiccator at a controlled relative humidity of 94% for 24 hours.

The first thing that is easily shown is that the three nanoclay presents one main peak at 4.2 ppm. It assumes different aspects in the three cases under investigation. As a matter of fact, the primary evidence is the different intensity recorded for the water signal, as it is much higher for both the halloysite samples with respect to kaolinite. This effect is related to the fact that halloysite nanotubes have more water, which contributes to the intensity of the peak. Indeed, together with the physically absorbed water, we should consider also the one in the inner lumen.

We should emphasize that the contribution to that peak is not only referred to water molecules, but it can also be related to the hydrogens from –OH groups. This is the reason why it was also measured the spectra after leaving the nanoclay at 200 °C. The obtained spectra were the same for the three samples and it presented a broad signal around 4 ppm. As a matter of fact, the NMR signal of hydrogen atoms from free-rotating water molecules is usually a sharp peak, such as those shown in Figure 3.2. On the contrary, the hydrogen atoms belonging to –OH groups are more stacked, and the resulting signal is broad like that observed for water blocked in crystal structures. This is because the crystal lattice causes the hydrogen nuclei in the water molecules to experience slightly different magnetic environments, leading to a distribution of resonance frequencies. Therefore, typically, the signal appears as a broad peak rather than a sharp peak.

Moreover, the interesting observation that can be made by looking at Figure 3.2 is related to the Patch HNT sample. Among the investigated nanoclays, it is the only one that shows the presence of separated spinning sidebands in the obtained ^{1}H MAS NMR spectra.

In solid-state NMR, the spinning sidebands appear in the spectrum as a set of spectral lines that are caused by the spinning motion of the sample and the presence of anisotropic local magnetic environments. This effect is known as "chemical shift anisotropy" (CSA) and is caused by the interaction of the nuclear magnetic moment with the local electronic environment, which can vary in different directions relative to the applied magnetic field.

In our case, the mechanism that gives rise to this phenomenon came from water undergoing rapid anisotropic reorientation. It means that water is in an anisotropic geometry, like inside a cylinder and it changes its orientation not in an isotropic way, namely having a preference for a certain orientation. On the other hand, HNT did not show any spinning sidebands. This can be explained by the longer and thinner tubes of Patch halloysite with respect to HNT, with an inner diameter between 10 and 20 nm. Moreover, the presence of higher defined anisotropic channels in Patch HNT, together with the fact that they are more monodispersed, explains this unique behavior.

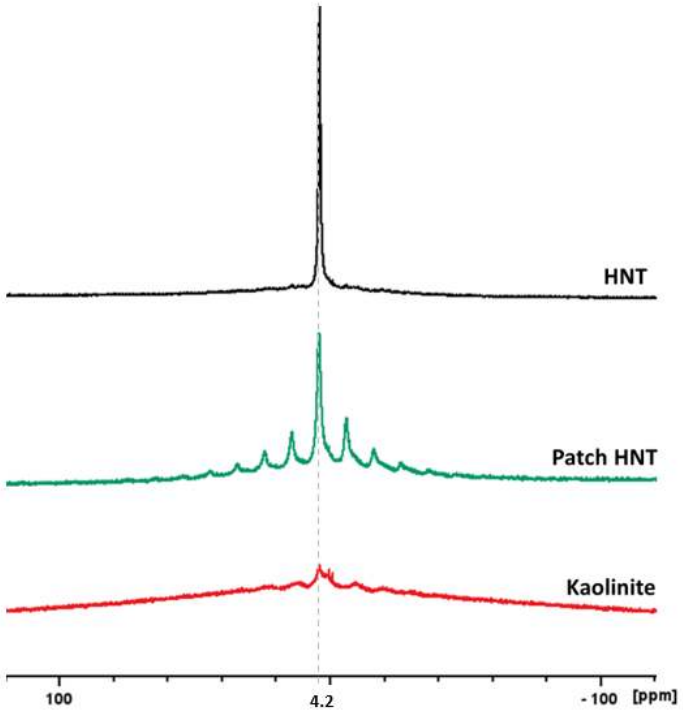

Figure 3.2. ^{1}H MAS NMR spectra of HNT, Patch halloysite and Kaolinite.

Furthermore, water sorption experiments were conducted on HNT, Kaolinite and Patch HNT in order to understand the contribution of the physically absorbed water to each sample. In Figure 3.3 is reported the variation of mass as a function of time at four different steps of relative humidities: 33, 53, 75 and 94 %.

It can be observed that the step related to higher water absorption is that at RH 94%. By the way, at each step of humidity, the variations of mass occurred in ca. 20 minutes after which a plateau was reached.

It should be noted that kaolinite showed a maximum mass variation of 2% at RH 94%. Interestingly, this value is much lower with respect to the data acquired for both the halloysite nanotube samples. They exhibited mass variations up to 18 and 19 % for Patch and HNT at RH 94%, respectively. The same behavior was also observed at lower relative humidities. The higher water absorption capacities can be significantly affected by the nanoclay morphologies. As a matter of fact, the tubular structure of halloysite provides a greater surface area compared to platy kaolinite, which allows for more water molecules to adhere to the surfaces and within the lumen of the nanotubes.

Moreover, halloysite nanotubes have higher porosity that can further increase their capacity to trap and store water. Platy kaolinite lacks such well-defined internal pore structures. Considering the different water absorption behavior of the nanoclays, the solid state signals are affected by these factors.

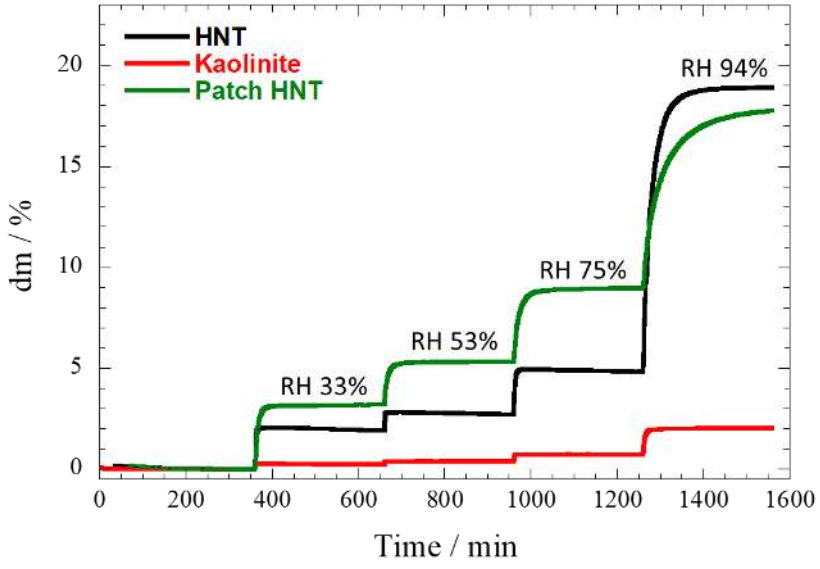

Figure 3.3. Mass variation as a function of time for HNT, Kaolinite and Patch HNT.

3.1. Diffusion of water in nanoclays

Going further with the investigation of water in nanoclay systems, self-diffusion and transverse relaxation T_2 were also studied. In nuclear magnetic resonance measurements, the diffusion and T_2 relaxation of water are two distinct phenomena that can provide different types of information about the properties of water molecules.

Diffusion refers to the random motion of water molecules due to thermal energy. In NMR, diffusion can be measured by observing the change in the intensity of the NMR signal as a function of time under a magnetic field gradient. The rate at which the signal decay provides information about the diffusion coefficient, which is related to the size and shape of the water molecules and the viscosity of the surrounding medium. It has been widely reported that diffusion measurements can be used to characterize tissue microstructure, blood flow, and fluid dynamics, among other things[110].

For diffusion experiments, a pulsed gradient stimulated echo (PGSTE) NMR sequence was employed. The molecular motions of the studied nuclei in the PGSTE result in the attenuation of the measured spin-echo signal. These motions occur during the diffusion time Δ and cause phase-encoded echo signals. The equation that describes the relationship between the attenuated signal and the experimental parameters is the following[111]:

$$\frac{S}{S_0} = \exp\left[-\gamma^2\delta^2 g^2 D\left(\nabla - \frac{\delta}{3}\right)\right] \tag{3.1}$$

where S and S_0 are echo signal intensities, with and without magnetic field gradient pulse applied, respectively, γ is the gyromagnetic ratio, δ is the gradient pulse duration, and D is the self-diffusion coefficient. The measurements were carried out as a function of the magnetic field gradient strength G, which changed in 32 steps with a maximum value of 294 G/cm. The parameters δ and Δ were equal to 0.5 ms and 50 ms, respectively, and remained unchanged during the measurements. The Equation 3.1 can be rewritten considering $b = (\gamma G\delta)^2 (\Delta - \delta/3)$:

$$\frac{S}{S_0} = \exp[-Db] \tag{3.2}$$

The b value is a measure of the strength of the diffusion weighting gradients and is proportional to the gradient amplitude and duration. Higher b values result in stronger diffusion weighting and are more sensitive to smaller and more restrictive tissue structures. In contrast, lower b-values result in weaker diffusion weighting and are more sensitive to larger and more isotropic tissue structures.

It should be mentioned that having a sufficient T_2 relaxation time is essential for successful diffusion measurements. Short T_2 times, as it happens at low temperatures, lead to rapid signal decay and reduced signal strength, making it difficult to accurately measure and characterize water diffusion data. This is why the presented data refer to the experiments carried out at 25 °C and not at a temperature lower 0 °C. The samples were measured with two different hydration levels, indicating an excess of free water. The decay curves representing the normalized echo signal intensity as a function of the b value for the sample at high hydration are shown in Figure 3.4.

In a homogeneous sample, the decay of the echo signal can be accurately described by Equation 3.2. However, in an inhomogeneous system such as, for example, wood tissue containing cavities and pores of different sizes, there may be a wide range of self-diffusion coefficients (D), resulting in a distribution[112]. We should consider that the investigated nanoclays, especially halloysite nanotubes, have different water populations and the tubular morphology affects the diffusion results. Therefore, the best fit equation for the obtained decays of the echo signal has been proved to be the combination of two components, represented by the following biexponential decay equation[110]:

$$\frac{S}{S_0} = f\exp[-bD_A] + (1-f)\exp[-bD_B] \tag{3.3}$$

with D_A and D_B the diffusion coefficient of confined and bulk water, respectively and *f* and *1-f* the fraction of the two water species. By looking at the curves in Figure 3.4, the three samples appear to have close behavior, but some differences arise by considering the self-diffusion coefficients, resulting by the fitting Equation 3.3. The obtained values are reported in Table 3.1

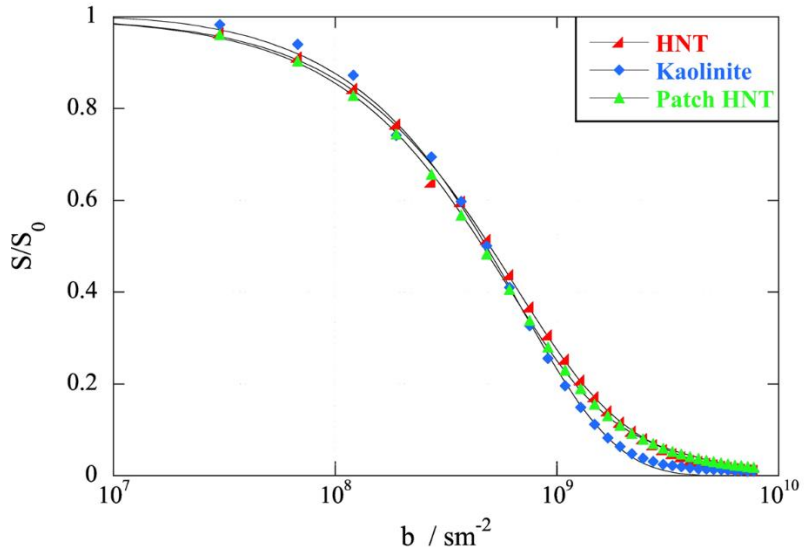

Figure 3.4. Experimental echo attenuation curves for HNT, Kaolinite and Patch Halloysite as a function of b. The black lines refer to the fitting curves.

As a general result, we can state that diffusion is slower in presence of less bulk water, namely with a low hydration level (Table 3.1). As a matter of fact, when the amount of bulk water is limited, the self-diffusion coefficient of water may decrease. The limited volume and presence of obstacles can hinder the free movement of water molecules, leading to slower diffusion. On the contrary, the self-diffusion of bulk water D_B, is nearly constant between the observed clays.

Interestingly, considering the diffusion of water confined inside the lumen of the nanotubes, namely D_A, it showed values reduced by one order of magnitude with respect to D_B. This is because the available space for water molecules to move is restricted, leading to hindered diffusion. It was previously reported that the diffusion of water in hydrophilic confinement in mesoporous silica MCM-41 was found to be considerably lower[113].

Surface interactions can also slow down the motion of water molecules as they interact with the nanotube's walls. This is particularly pronounced in narrow nanotubes and, indeed, the diffusion of Patch HNT showed lower values (D_A = 3.0 10^{-10} m^2 s^{-1}), due to its peculiar tube morphology, compared with common HNT (D_A = 4.4 10^{-10} m^2 s^{-1}). The presence of a bird nest structure in Patch HNT, where nanotubes are entangled and bent, can restrict the diffusion of free water between the nanotubes.

Moreover, it was tried to fit the decay curves of Kaolinite samples with Equation 3.3, but it turned out that the best fit could be obtained by considering only one component. The reason behind this characteristic is connected again with the morphology of the clay. It possesses layered platy sheets with limited anisotropy along the diffusion direction. This means that water molecules in platy clays do not experience significant hindrance or confinement along any particular direction. On the contrary, for halloysite nanotubes, a single component did not fit the experimental data properly.

Table 3.1. Diffusion coefficients obtained by fitting the decay intensity curves with Equation 3.3.

Sample	D_A / m^2 s^{-1}	D_B / m^2 s^{-1}
HNT High Hydration	$4.4\ 10^{-10} \pm 0.5\ 10^{-10}$	$1.75\ 10^{-9} \pm 0.07\ 10^{-9}$
HNT Low Hydration	$3.2\ 10^{-11} \pm 1.2\ 10^{-11}$	$1.26\ 10^{-9} \pm 0.03\ 10^{-9}$
Kaolinite High Hydration	/	$1.49\ 10^{-9} \pm 0.02\ 10^{-9}$
Kaolinite Low Hydration	/	$1.01\ 10^{-9} \pm 0.06\ 10^{-9}$
Patch HNT High Hydration	$3.0\ 10^{-10} \pm 0.1\ 10^{-10}$	$1.79\ 10^{-9} \pm 0.02\ 10^{-9}$
Patch HNT Low Hydration	$1.3\ 10^{-10} \pm 0.2\ 10^{-10}$	$7.9\ 10^{-10} \pm 0.3\ 10^{-10}$

3.2. T_2 relaxation of water in nanoclays

T_2 relaxation, on the other hand, refers to the decay of the NMR signal due to interactions between the water molecules and their surroundings, such as other water molecules, macromolecules, or magnetic field inhomogeneities. T_2 relaxation is characterized by a time constant T_2, which depends on factor like the molecular motion and the chemical environment.

In particular, it can be influenced by the molecular environment, such as the presence of confinement or interaction with surrounding surfaces. In Figure 3.5 the experimental decay curves of the nanoclays are shown. They exhibited biexponential decay, demonstrating the existence of two water populations and it can be expressed as:

$$\frac{S}{S_0} = f\exp\left[-t/T_{2f}\right] + (1-f)\exp[-t/T_{2s}] \quad (3.4)$$

where S is the total water signal intensity, t is the time, f is the fraction of the fast component and T_{2f} and T_{2s} are the transverse relaxation time of the slow and fast component, respectively. As example, the T_{2f} and T_{2s} values of the water in nanoclays at high hydration, obtained by fitting the curves with Equation 3.4, are reported in Table 3.2.

Table 3.2. T_2 relaxation data obtained by fitting the decay intensity curves with Equation 3.4.

Sample	**T_{2s} / ms**	**T_{2f} / ms**
HNT	$0.960 \pm 6.5\ 10^{-3}$	$0.281 \pm 8.4\ 10^{-3}$
Kaolinite	36.3 ± 3.5	$0.764 \pm 6.7\ 10^{-3}$
Patch HNT	$1.68 \pm 3.5\ 10^{-2}$	$0.49 \pm 1.2\ 10^{-2}$

It is clear observing Figure 3.5 that there is a fast and a slow water component in each one of the three analysed systems. Accordingly, it can be observed that the amount of confined water, namely the fast component, is much higher in the two halloysite nanotubes. Nevertheless, we should distinguish different explanations of this behavior in the case of halloysite nanotubes and platy kaolinite.

In the case of water confined in a nanotube, the T_2 relaxation time is generally observed to be faster than that of bulk water. When water molecules are confined in a nanotube, their motion is restricted in all directions, compared to the more free and unrestricted motion in bulk water. Since the water molecules experience more frequent collisions with their neighbouring molecules and surfaces, it can lead to faster T_2 relaxation times. Moreover, being in close proximity to the surface of the nanotube, water molecules increase their interactions, leading to faster relaxation times.

On the other hand, platy kaolinite also showed a fast component, even though its fraction is much lower than the one observed with nanotubes. This fast component is related to the interactions of water molecules that are in between the blocks of stacked layers of kaolinite. Both the T_2 values related to the fast and slow components are higher than

halloysite nanotubes, meaning that the relaxation is slower and that the water molecules are experiencing weak or few interactions.

Another result that should be noted is longer T_{2f} and T_{2s} of Patch halloysite with respect to HNT. This can be explained if we consider that in thinner tubes, water molecules may experience more significant obstruction to their diffusion along the tube's diameter, which can contribute to longer T2 relaxation times. Moreover, the interactions of water molecules inside the confined space are restricted along the inner diameter dimension while allowing relatively free movement along the length of the nanotube. However, the water interactions are more in the larger tubes of HNT, allowing faster relaxation times.

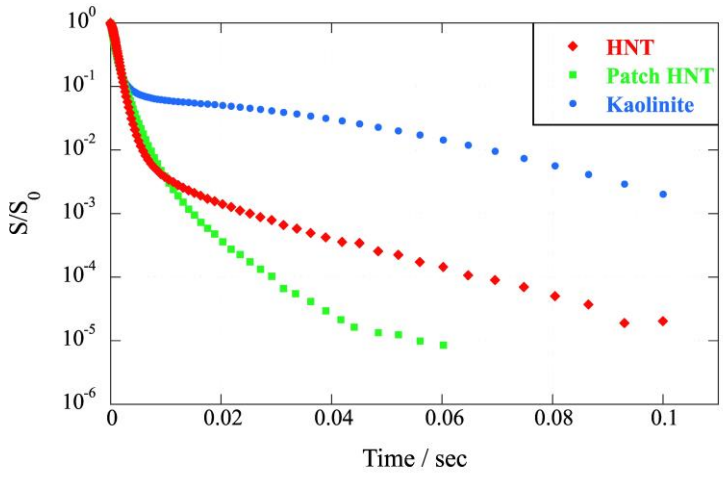

Figure 3.5. Experimental decay curves for HNT, Kaolinite and Patch Halloysite as a function of time.

Figure 3.6 reported the normalized experimental decay curves for Patch HNT, as example, at three different levels of hydration. In particular, from right to left, we observe the sample with an excess of water, then low hydrated and finally only equilibrated at 94 % of relative humidity. It can be noted that, decreasing the bulk water content, the slow component disappears and, at the end, we only see the fast component, related to the confined water inside the nanotubes. This characteristic was also shown in the other investigated clays. Additionally, a very similar behavior can be detected if we decrease the temperature below 0 °C. In that case, the interactions between the water molecules are “freezed” and only one

component will be shown in the decay curves that will appear like those presented in Figure 3.6.

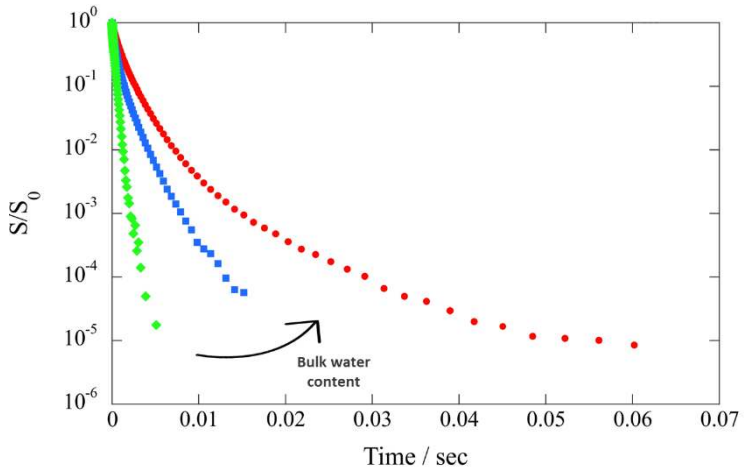

Figure 3.6. Experimental decay curves for Patch HNT at three hydration levels. The bulk water content increase from left to right.

3.3. Probing water diffusion and relaxation in geopolymers

The geopolymerization process changes the intrinsic chemical characteristics of clays. With this in mind, Figure 3.7 compares the decays of the echo signal of HNT and GP. As a matter of fact, the morphology of the resulting material after the geopolymerization is different and its diffusion behavior as well. However, the best fit equation for the echo attenuation curves has been demonstrated to be the combination of two components also for the geopolymer (Equation 3.3). The obtained diffusion coefficients are $D_A = 5.1\ 10^{-11}$ $m^2\ s^{-1}$ and $D_B = 1.67\ 10^{-9}$ $m^2\ s^{-1}$. In particular, the self-diffusion of bulk water D_B, is very close to the value observed for HNT and the nanoclays in general.

On the other hand, the diffusion related to the confined water (D_A) showed a lower value than halloysite. The finding of two different water populations, such as the halloysite sample, is connected to the porous matrix of the geopolymer. This allows the presence of water confined in the porosities. Notwithstanding, halloysite nanotubes provide a more regular confinement with fewer obstacles or complex geometry that might hinder water diffusion.

The porous structure in the geopolymer matrix can introduce more barriers and variations in the confinement environment, potentially inhibiting water diffusion and leading to a lower D value. Nevertheless, the most influencing factor to explain this phenomenon is the amount of confined water that is different in the two analysed systems. A relatively more significant amount of water is confined within the nanotubes compared to the geopolymer porosities, leading to a faster diffusion coefficient.

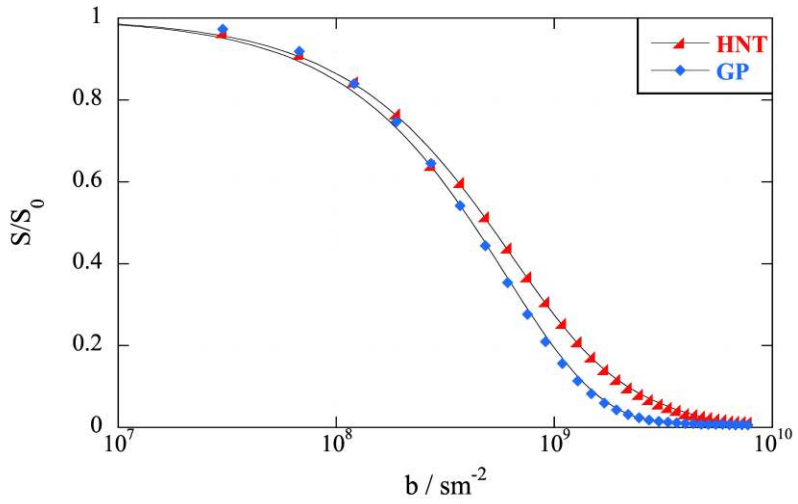

Figure 3.7. Experimental echo attenuation curves for GP and HNT as a function of b value. The black lines refer to the fitting curves.

Finally, observing the Figure 3.8, referring to the T_2 relaxation curves of water in GP and HNT samples, it is evident that GP possesses a fast and a slow component as well as halloysite (T_{2s} =1.4 ms T_{2f} = 20 μs). Additionally, it should be pointed out that the amount of the fast component in the geopolymer is much lower than that of halloysite, meaning that the confined water is less. Nevertheless, GP showed faster T_{2f} relaxation, indicating more interaction between the water molecules. The observed behavior can be explained by the quick exchange of water molecules between a perturbed surface layer with fast relaxation and a bulk water fraction with slow relaxation. This is based on a modified version of the Brownstein-Tarr model for relaxation in porous media, where T2 is directly proportional to the ratio of volume to surface area.

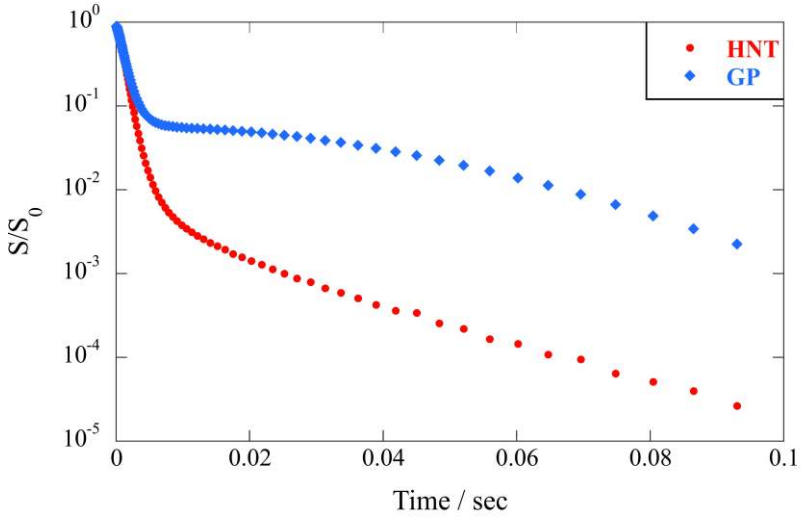

Figure 3.8. Comparison between the experimental decay curves for HNT and GP.

4. Rheological behavior of halloysite-based hydrogel

The properties and characteristics of halloysite nanotubes, such as the sizes, specific surface and polydispersity are influenced by the geological deposit from which they are sourced[114]. One of the varieties of halloysite, commonly known as Patch halloysite (PT_Hal), is widely recognized for its high purity level of approximately 96%, sourced from Western Australia[13]. These nanotubes possess thinner tubes and can reach an exceptional length up to 30 μm. Additionally, they exhibit a unique fibrous structure that forms clusters resembling patches.

Existing research studies on the use of halloysite nanotubes as nanomaterials have primarily focused on halloysite sourced from New Zealand or the USA. However, it is essential to note that the properties of halloysite can vary depending on its origin, which is influenced by local conditions during its formation. For instance, Makaremi et al.[115] demonstrated that shorter nanotubes have a higher capacity for encapsulating salicylic acid compared to patchy and longer halloysite nanotubes, which require more time and energy for loading the active molecule in their lumen. On the other hand, it is known that halloysite does not form gels on its own. Actually, Luo et al. [116] showed that the sol-gel transition occurs at approximately 40 wt% concentration, and the addition of hydrochloric acid causes a pH-induced gelation in the aqueous dispersion due to reduced repulsive electrostatic forces between the nanotubes.

Thus, in this chapter, our aim is to highlight that Patch halloysite, with its unique fibrous structure, exhibits different rheological characteristics compared to halloysite from other natural sources. Consequently, a rheological analysis of Patch halloysite samples at various concentrations is presented here.

4.1 Characterization of Patch halloysite before and after purification procedure

Patch halloysite (PT_Hal) from Western Australia was subjected to a purification process by dispersing the grounded powder in water at a pH of 7.5. After several cycles of

sonication and washing in water the dispersion was filtered by a peristaltic pump to exclude coarse residuals.

Figure 4.1 displays the thermogravimetric curves of PT_Hal, both the purified (PT_Hal_P) and not purified (PT_Hal_NP) samples. The curves exhibit two distinct mass losses, occurring up to 100 °C and within the range of 400 to 500 °C, respectively. These losses are attributed to the presence of physically adsorbed water molecules and the dehydroxylation of aluminum inner sheets.

However, the primary difference between the two samples lies in the percentage of the initial mass loss and, subsequently, the residual mass at 800 °C. Specifically, the purified PT_Hal exhibits an 82% residual mass, whereas the not purified PT_Hal displays a residual mass of 79%. This discrepancy can be attributed to the elimination of impurities through the purification procedure, resulting in a decrease in residual mass for PT_Hal_P.

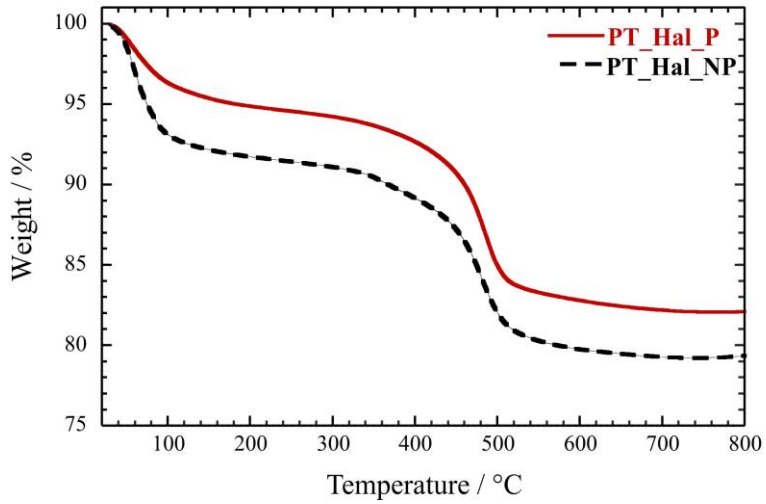

Figure 4.1. Thermogravimetric curves of PT_Hal_NP and PT_Hal_P.

The chemical composition of PT_Hal was determined using XRF measurements, before and after purification. Table 4.1 shows that the silicon content is lower in the unpurified sample (PT_Hal_NP) compared to the purified one (PT_Hal_P), which has an enrichment of 6% in silicon. Additionally, PT_Hal_P exhibits a decrease in the amount of Ti, Mg, Cr, and Mn. However, the iron content remains relatively constant after purification, although in minimal amounts.

Previous studies[13,117] have reported that patch halloysite samples typically contain less than 1% iron. Surprisingly, we found a value of 2.52% iron in PT_Hal_NP, which can be attributed to different levels of iron oxide contamination. It has been suggested that even though iron is not structurally part of halloysite, it can affect the size of the particles by inhibiting the crystal growth. The substitution of the smaller Al^{3+} ion with the larger Fe^{3+} ion in the octahedral sheet of halloysite can occur, especially at higher levels of Fe_2O_3 (approximately 4%), resulting in more planar layers, similar to kaolinite. This explains why halloysite with long tubular particles generally has low iron content, while shorter and flatter particles tend to have higher levels of structural iron.

Overall, these XRF results align with the existing literature data[118] regarding the composition of patch halloysite samples.

Table 4.1. Chemical composition of PT_Hal_P and PT_Hal_NP.

Sample	Al%	Si%	Mg%	Fe%	Ti%	Cr%	Mn%
PT_Hal_P	41.1±0.3	53.5±0.3	1.2±0.4	2.99±0.06	0.47±0.09	0.18±0.02	ND
PT_Hal_NP	41.05±0.4	46.8±0.4	2.2±0.6	2.52±0.07	6.7±0.2	0.20±0.03	0.07±0.01

4.2 Comparison between Patch and UltraPure halloysite nanotubes

Prior to conducting a thorough analysis of the rheological properties of these unique clays, we focused our attention on examining the differences between them. The X-ray diffraction patterns of both UP_Hal and PT_Hal showed the typical diffraction pattern of dehydrated halloysite (refer to Fig. S1 from Attached Manuscript II). It was previously reported that Patch undergoes dehydration, as observed through the continuous collection of XRD patterns during in situ heating. This dehydration results in irregular d-spacings, likely due to the interference between the regular flattened tubes with a d-spacing of ca. 8 Å. Specifically, we observed peaks at 2θ = 12.0, 19.9, 24.7, 35.0, 38.3, 54.9, and 62.4 corresponded to the (001), (100), (002), (110), (003), (210), and (300) planes, respectively. The (001) plane corresponds to a basal spacing of 0.72 nm, which indicates that these

samples are halloysite-(7 Å). Only the PT_Hal sample showed traces of quartz, with sharp peaks observed at 2θ= 26° and 60°.

In Figure 4.2, a morphological characterization of PT_Hal and UP_Hal is also provided. Looking at the micrographs obtained from scanning electron microscopy, PT_Hal displays significantly longer and thinner tubes. These tubes have outer diameters ranging from 40 to 55 nm, inner diameters between 12 and 22 nm, and lengths ranging from 200 to 30.000 nm. Additionally, PT_Hal nanotubes appear entangled and bent, forming a structure similar to a bird nest. Due to their thin walls, these tubes can be subjected to breaking into shorter fragments, yet intact tubes can still be observed as bundles of closely packed parallel tubes. Conversely, UP_Hal exhibits shorter and stubbier tubes, with lengths ranging from 100 nm to 2 μm (Figure 4.2 (d)).

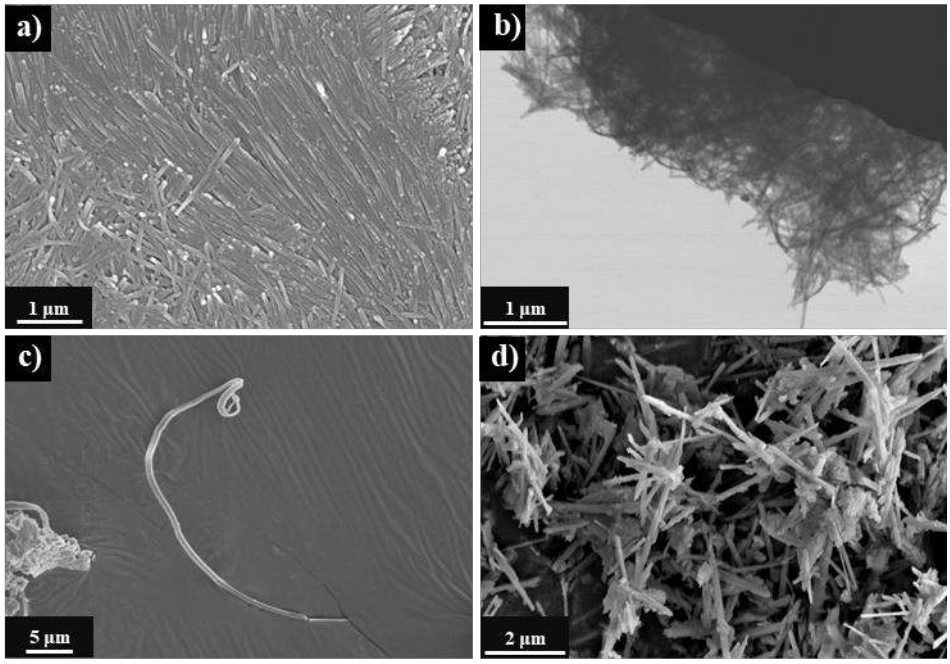

Figure 4.2. SEM micrograph showing the morphological features of Patch (a,c) and UltraPure halloysite nanotubes (d). STEM micrograph showing entangled patch halloysite nanotubes (b).

Figure 4.3 illustrates a qualitative estimation of the gel formation regarding PT_Hal and UP_Hal at a 1 wt % concentration before and after the inversion. Although PT_Hal has the same concentration, it exhibits stability to the tube inversion test, highlighting a gel-like

structure. In contrast, this is not observed in the same or even higher concentrations of UP_Hal.

Figure 4.3. Inversion test of PT_Hal and UP_Hal 1 wt%.

4.3 Rheological characterization of Patch halloysite

To characterize the clay's viscoelastic behavior, amplitude sweep tests were conducted to measure the dependence of the storage and loss moduli (G', G") on strain amplitude. The results presented in Figure 4.4 represent two examples of the more comprehensive concentration range investigated in this study, chosen to illustrate the linear viscoelastic regions. Specifically, for both PT_Hal at 1 and 2 wt %, G' is higher than G" below a strain of 10%, indicating a gel-like structure. In this region, both moduli remain constant, indicating the presence of a linear viscoelastic region. The points at which G' equals G" were determined as the crossover strain points and are clearly showed after 10 % strain. Increasing the clay concentration, the crossover points are shifted to higher oscillation strain, with values of 16.30% and 45.52% for PT_Hal at 1 and 2 wt %, respectively.

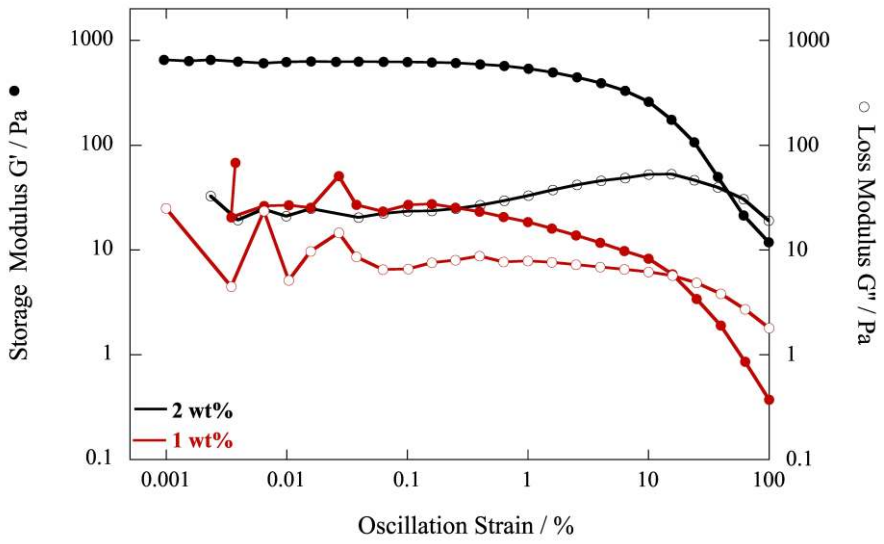

Figure 4.4. Amplitude sweep tests of PT-Hal. Storage modulus (G') and Loss modulus (G") are indicated by full and empty symbols respectively**.**

After identifying the linear viscoelastic areas, angular frequency sweep tests were conducted in which a constant strain on the systems at different frequencies was imposed. Generally, these tests provide information on the rheological behavior of the product during storage and application[119–121]. The rheological data that were obtained are displayed in Figure 4.5. In general, the storage modulus (G') is larger than the loss modulus (G") across entire the frequency range. This indicates that PT_Hal acts like a solid, or more precisely a gel-like material, suggesting a high level of structure from a concentration of 0.75 wt%. The gel-like structure of PT_Hal is time-independent, with higher frequencies representing shorter time scales and lower frequencies representing longer time scales[122,123]. This demonstrates the stability of the gel-like structure over time. Additionally, Figure 4.5 reveals that the increase of concentration results in an increase in both moduli, with the G' values consistently higher than G" within the investigated range of angular frequency from 0.005 wt%.

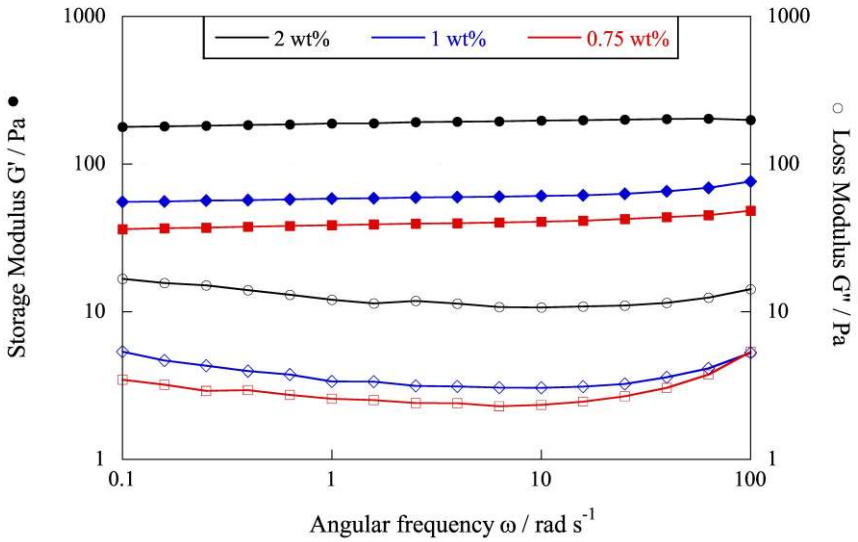

Figure 4.5. Angular frequency sweep tests for PT_Hal 2, 1 and 0.75 wt%. Full and empty symbols indicate the Storage modulus (G') and Loss modulus (G"), respectively.

The rheological behavior of the system can be further investigated by analysing the viscosity as a function of the shear rate, which provides valuable information about its performance and processing. Flow curves, shown in Figure 4.6, illustrate that as the concentration of clay increases, the viscosity also increases, with the most remarkable difference observed between PT_Hal 2 wt% and 1 wt%, where there is an order of magnitude increase. This highlights the significant impact of microstructure on the rheological behavior of Patch halloysite.

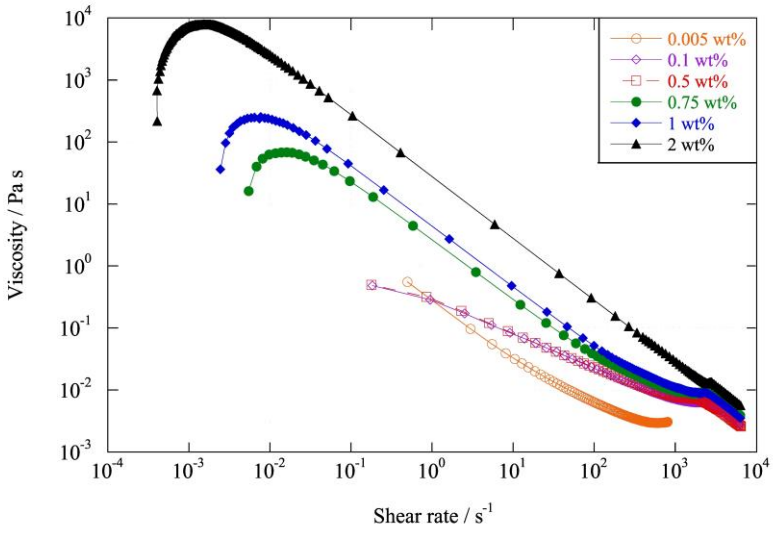

Figure 4.6. Flow ramp tests showing the viscosity as a function of the shear rate.

As a matter of fact, two phenomena should be considered to explain the rheology of Patch halloysite. Firstly, as the concentration of clay increases, the interactions between nanotubes are enhanced, leading to a higher viscosity. Secondly, an additional important factor is the presence of a bird nest structure in PT_Hal, where nanotubes are entangled and bent. In light of this, geometrical considerations can provide a broader understanding of the influence of tube morphology on rheology. This can be further analyzed by considering the average length of the nanotubes and a simple cubic model that allows to calculate the critical overlapping volume fraction φ* as follows:

$$\varphi^* = \pi R^2 / L^2 \qquad (4.1)$$

where *R* and *L* are the external radius and the length of the nanotubes, respectively.
Previous works have reported volume fraction values of approximately 4–10% for aqueous dispersions of halloysite from Dragon Mine[101,124]. In this study, we calculated the volume fractions for UP_Hal and PT_Hal, that are 3.1% and 0.03%, respectively, by considering average values for the radius and length. This suggests that PT_Hal requires 100 times less volume to generate the nanotube entanglement compared to UP_Hal. Consequently, the

critical concentration at which the hydrogel is formed will be much lower for PT_Hal samples with shorter and stubbier halloysite nanotubes.

Furthermore, the presence of network-like structures in PT_Hal reduces fluid flow, contributing to the higher viscosity of the system[125,126]. Conversely, viscosity at concentrations below 0.75 wt% shows lower values, indicating that the network is not as structured as in 1 wt%. This transition causes the material to change from a solid-like state to a liquid state, allowing it to flow easily.

All the samples showed shear thinning behavior with increasing shear rate, starting from a shear stress of 0.1 s^{-1}. As reported in literature, this is advisable for hydrogels used in biomedical applications, as they should exhibit viscous flow under shear stress and self-healing properties[127,128].

It is important to note that PT_Hal at concentrations of 0.75, 1, and 2 wt% exhibited an increase in viscosity up to a critical value at very low shear rates, beyond which it decreases. This indicates the presence of a yield stress, which is further illustrated in Figure 4.7, where the shear stress is plotted against the shear rate.

The yield stress indicates the sample structure's resistance to deformation or breakage, and it becomes detectable starting from a concentration of PT_Hal 0.75 wt%. When the applied stress is strong enough to disturb the gel-like structure of the material, the flow begins, leading to a significant decrease in viscosity, as previously shown in Figure 4.6. This change is more evident by looking at the inset in Figure 4.7, where the absence of yield stress can be observed up to a concentration of 0.5 wt%, and the curves start from 0 Pa, indicating that the material flows easily, and it is well deformable. On the other hand, PT_Hal 2 wt% exhibits a remarkable yield stress, significantly higher than less concentrated samples, reaching approximately 28 Pa (Table 4.2).

Therefore, we can conclude that PT_Hal behaves as a non-Newtonian fluid. Specifically, it can be categorized as a Pseudoplastic fluid at low concentrations and as a Bingham Plastic fluid at concentrations greater than 0.5 wt%.

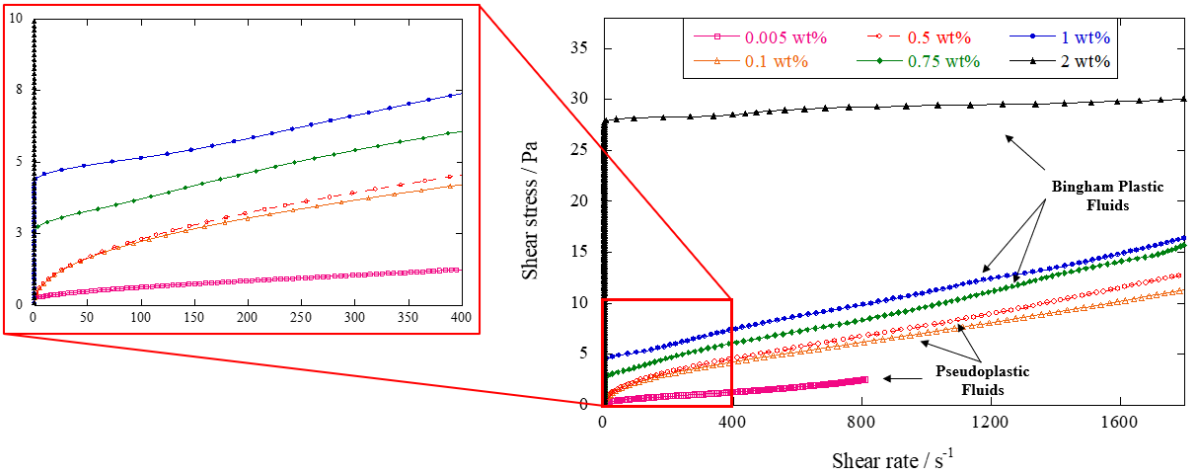

Figure 4.7. Shear stress as a function of the shear rate. A magnification highlighting different types of flow behaviour and the yield stress is presented in the inset.

Table 4.2. Yield stress values.

Sample	Yield Stress σ_0 / Pa
PT_Hal 0.005 wt %	0
PT_Hal 0.1 wt %	0
PT_Hal 0.5 wt %	0
PT_Hal 0.75 wt %	3.07
PT_Hal 1 wt %	4.69
PT_Hal 2 wt %	28.08

In order to gain a deeper understanding of the rheological properties of Patch halloysite, the Carreau and Carreau-Yasuda models were utilized to analyze the experimental flow curves.

The resulting fitting parameters obtained from Eq. 4.2 and Eq. 4.3 are documented in Table S1 in the Attached Manuscript II.

$$\frac{\eta-\eta_\infty}{\eta_0-\eta_\infty}=\frac{1}{[1+(k\dot{\gamma})^2]^{\frac{n}{2}}} \tag{4.2}$$

$$\frac{\eta-\eta_\infty}{\eta_0-\eta_\infty}=[1+(k\dot{\gamma})^a]^{\frac{n-1}{a}} \tag{4.3}$$

Here, η_0 is the viscosity at zero shear rate, η_∞ is the viscosity at infinite shear rate, k represents the consistency index or relaxation time, n and a are two dimensionless parameters.

In Figure 4.8 an increase in zero-shear rate viscosity and consistency with increasing PT_Hal concentration is detected.

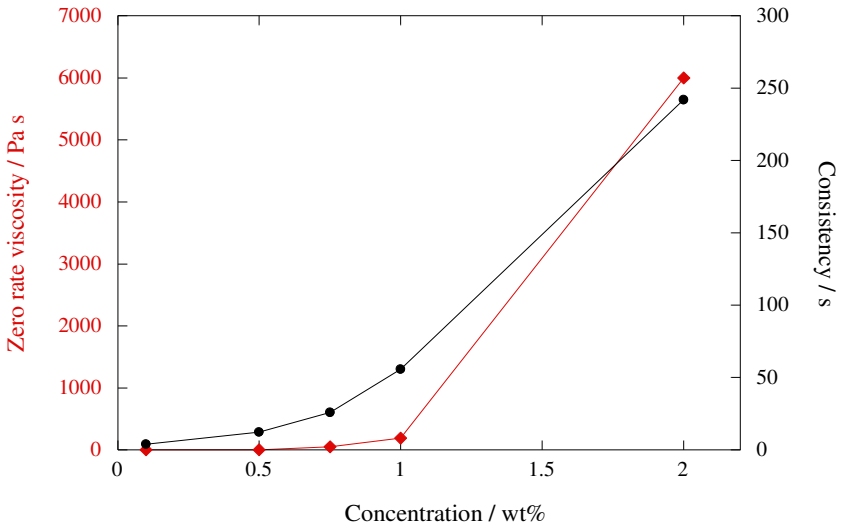

Figure 4.8. Zero-shear rate viscosity and consistency as a function of concentration.

4.4 Ionic strength influence on the Patch halloysite hydrogel

The colloidal stability of nanoclays can be influenced by several factors, including the addition of polymers[47,129] as well as the ionic strength[42]. Moreover, it has been extensively discussed in the literature[130,131] that changing the ionic strength can also have significant effects on gel-like structures[132,133], such as swelling[134], increased stability[135] or viscosity due to stronger interactions with the components of the gel[136].

For instance, studies have shown that the addition of NaCl weakens the gel structure of cellulose nanocrystal suspensions and decreases also the viscosity of the system[137]. Moreover, according to the literature, NaCl concentration affects the settling velocity of halloysite dispersions[42]. Keeping this in mind, the influence of ionic strength on the investigated hydrogels of Patch halloysite is evaluated here by adding NaCl that is a

conventional choice for such studies. Consequently, flow ramp tests were conducted on PT_Hal 1 wt% in water and at different concentrations of NaCl, as depicted in Figure 4.9. It is worth to noting that adding salt does not disrupt the gel-like network, and lower concentrations of NaCl have no significant effect on the rheological properties compared to water. In fact, the viscosity curves of PT_Hal in water and NaCl 10^{-4} M overlap. There is only a slight impact of the ionic strength, as evidenced by a minimal increase in viscosity as the NaCl concentration increases.

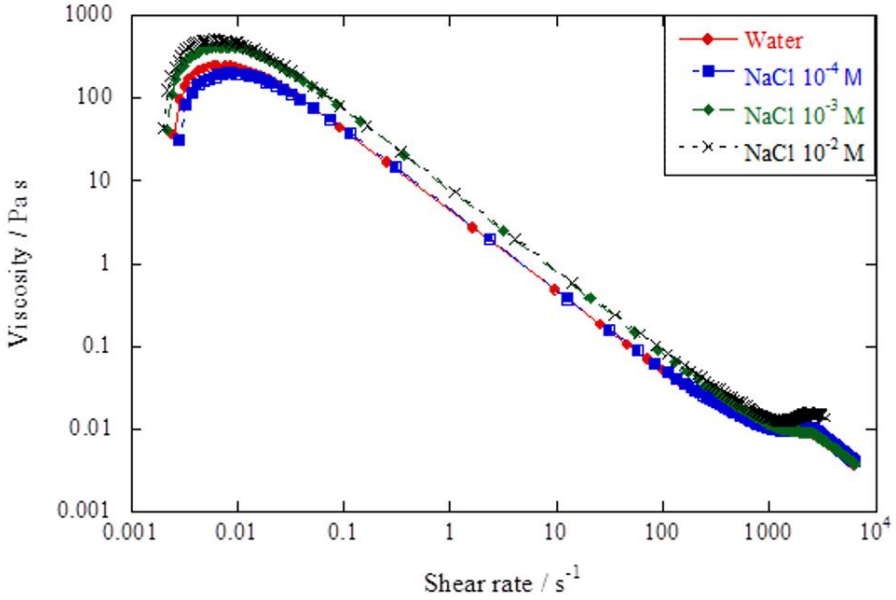

Figure 4.9. Viscosity as a function of the shear rate for PT_Hal 1 wt % in water and NaCl at different concentrations.

Measurements of ζ-potential were conducted to gather data on the surface charge of the nanotubes that was estimated by exploiting the Grahame equation, as evidenced in the Attached Manuscript II. According to Cavallaro et al.[42], while halloysites from various natural sources may exhibit comparable reactions to the addition of salt, there are differences in their effective charge that can impact their colloidal stability.

In our case, as the concentration of salt increases, the surface charge values increase. This phenomenon can be attributed to the screening effect of Na^+ ions towards the negative surface charge of PT_Hal. The introduction of electrolyte in aqueous medium resulted in a decrease of the Debye length and consequently in the ζ-potential absolute value, as stated

in Table 4.3. Additionally, the screening effect appears enhanced by increasing the ionic strength of the aqueous dispersion.

Table 4.3. ζ-potential of PT_Hal samples in water and with different NaCl concentrations.

Sample	ζ-potential / mV	Surface charge σ / C m^{-2}
Water	-17.5	/
NaCl 10^{-4} M	-15.5	$1.13 \cdot 10^{-5}$
NaCl 10^{-2} M	-14.0	$1.02 \cdot 10^{-4}$

In conclusion, once again Patch halloysite gives rise to unique features like the formation of hydrogel systems, even at low concentrations, that are not shown in other natural halloysite. Its peculiar rheological properties are related to its morphology, namely to the presence of longer nanotubes that form bird nest structures. PT_Hal exhibits solid-like characteristics, indicating a high level of structure. Interestingly, flow ramp analysis revealed two different behaviours depending on the concentration of clay. A yield stress was also observed, starting from concentrations of 0.75 wt%, indicating the clay's ability to resist deformation or breaking. We also investigated the impact of ionic strength and found that adding NaCl did not significantly affect the gel properties of this clay. For future studies it would be interesting to investigate if introducing other salts, such as bivalent cation salts, lead to the same effect as NaCl.

Based on these findings, this new hydrogel system proposed using green nanoclays can have applications in industry, biology, and for preserving cultural heritage.

5. Composite halloysite-based geopolymers filled with wax microparticles

As previously mentioned, materials that contain sufficient quantities of reactive alumina and silica are suitable for geopolymer preparation. Clay minerals, for instance, are commonly employed as precursors in the geopolymerization process due to their excellent reactivity. Halloysite, which has been utilized as an additive to enhance the cement and concrete qualities, has also started to be incorporated in geopolymer manufacturing. Nonetheless, research on halloysite-based geopolymers is far less extensively reported compared to studies on other precursors like kaolinite, illite, and fly ash. As a matter of fact, the effect of nanomaterials as additives was explored mostly on fly ash-based geopolymers. This field regarding the development of composite materials offers great relevance for the physical properties that can arise from the interactions between different species. However, a deeper investigation of hybrid clay-based geopolymers is needed.

In this chapter, we carried out two preparations of the geopolymeric materials to fill them on one side with microwax particles and on the other with beeswax (Figure 5.1). The wax microparticles of well-defined spherical shape were obtained by vacuum drying the halloysite/beeswax Pickering emulsion at room temperature. It was prepared following a similar protocol described in literature for halloysite/paraffin emulsions[31]. A detailed preparation procedure of the Pickering emulsion employed for this work is reported in the Attached Manuscript III. As illustrated in Figure 5.1 (a) the microparticles were then mixed with an equal amount of pure halloysite nanotubes and with an alkaline activating solution of NaOH. Specifically, the NaOH/HNTs ratio was set to 1 in order to balance the negative charges of four-coordinated aluminium ($[AlO_4]^-$) in the geopolymeric network with sodium cations (Na^+). After being mixed at 25 °C, a uniform slurry was obtained. It was transferred into a plastic mold and cured at 50 °C for 48 hours. A very similar procedure was exploited to prepare an unfilled conventional geopolymer and geopolymers filled with beeswax at different wax/halloysite ratios ($R_{wax/HNT}$). A list of the geopolymeric samples and their composition is reported in Table 5.1. After adding the alkaline activator solution to halloysite nanotubes, we heated the mixture at 70 °C and incorporated solid beeswax to create a uniform geopolymer slurry (Figure 5.1 (b)). The final step involved curing all the samples in a rectangular plastic mold at 50 °C for 48 hours.

Table 5.1. List of prepared geopolymeric samples and composition of each component.

Sample	$R_{wax/HNT}$	HNT / wt%	Beeswax / wt%	NaOH / wt%
GP	0	50	0	50
GP_wax	0.25	44.4	11.2	44.4
GP_wax	0.50	40	20	40
GP_wax	0.75	36.4	27.2	36.4
GP_wax	1	33.3	33.4	33.3
GP_microwax	0.07	48.3	3.4	48.3

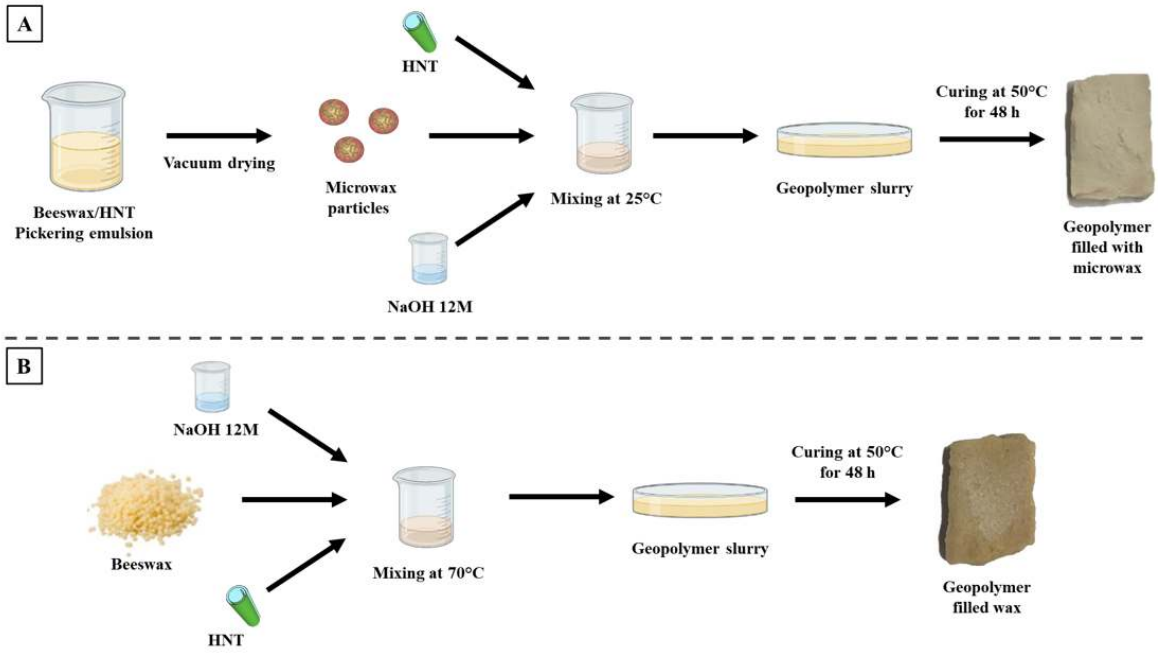

Figure 5.1. (a) Representation of the preparation protocol of geopolymer filled with wax microparticles and (b) wax.

5.1 Structural and thermal characterization of filled geopolymers

Preliminarily characterizations were performed in order to evaluate the actual formation of the geopolymeric network. To achieve this goal, both thermal analyses and spectroscopies were employed.

Figure 5.2 compares the thermogravimetric curves of geopolymers and pristine halloysite clay. It was observed a mass loss between 400 and 500 °C for the pristine halloysite clay (HNT) due to the removal of interlayer water molecules[105]. It should be noted that it was not observed in all the geopolymeric samples due to the structural changes of halloysite caused by the geopolymerization reaction. On the other hand, the geopolymers exhibited significant mass reduction, approximately of 10 wt%, from 25° to 200 °C due to the evaporation of physically adsorbed water molecules. The conventional geopolymer (GP) did not show any further mass losses within the measured temperature range. However, both GP_wax and GP_microwax displayed an evident mass change at around 350 °C due to the decomposition of the beeswax present in the geopolymeric network. Consequently, their residual masses at 700 °C (68 and 75 wt% for GP_wax and GP_microwax, respectively) were lower than that of GP sample (ca. 80 wt%).

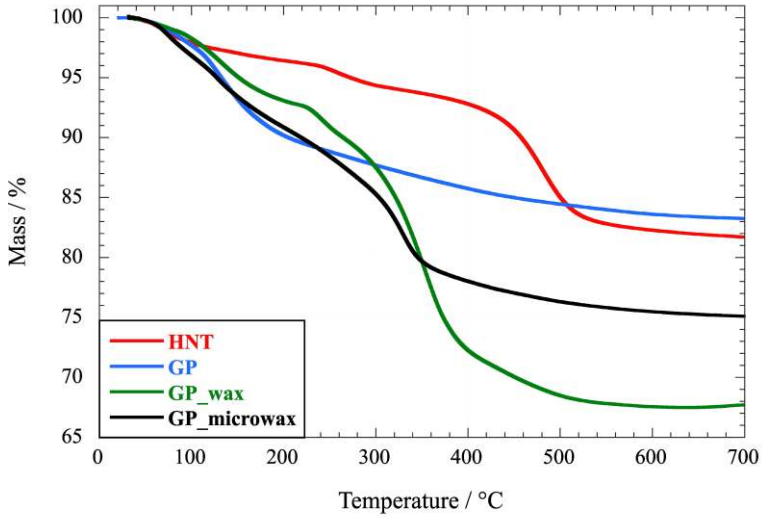

Figure 5.2. Thermograms of HNT, GP, GP_wax ($R_{wax/HNT}$ = 0.75) and GP_microwax.

Additionally, using thermogravimetric data, the weight fraction of wax (χ_w) in GP_microwax was calculated from Equation. 5.1:

$$\chi_w = \frac{MD_{700P} - MD_{700HNT}}{MD_{700W} - MD_{700HNT}} \quad (5.1)$$

where MD_{700P}, MD_{700HNT} and MD_{700w} are the degraded matters at 700 °C of wax/halloysite particles, halloysite, and beeswax, respectively. In this way, it was possible to calculate the wax/HNT mass ratio in the GP_microwax sample (Table 5.1).

The DSC measurements (see Attached Manuscript III) confirmed the presence of crystalline beeswax in the filled geopolymers. The curves exhibited endothermic peaks around 65-70 °C, which indicated the melting of the organic macromolecule. According to previous research work[138], this signal corresponds to the transition from solid to liquid, while a slight shoulder at lower temperatures, around 30-40 °C, corresponds to a transition from one solid state to another. We determined the melting temperature (T_m) of the filled beeswax by identifying the minimum point of the DSC peaks. Interestingly, the GP_microwax samples exhibited a higher T_m compared to the GP_wax samples (as shown in Table 5.2). Additionally, integrating the peaks allowed us to calculate the enthalpies (ΔH_m) of the melting process (Table 5.2) and they were expressed in J g^{-1} of beeswax, as beeswax is the component responsible for the observed melting signal. As reported by Lvov et al. [139], the presence of halloysite nanotubes partially reduces the wax crystallinity. Indeed, the obtained values indicate a decrease in enthalpy as the wax/HNT ratio increases, suggesting a reduction in the wax crystallinity within the geopolymeric network.

Table 5.2. Melting temperatures and enthalpies for beeswax and geopolymers.

Sample	$R_{wax/HNT}$	ΔH / J g^{-1}	T_m / °C
Beeswax	/	205	66.2
GP	/	/	/
GP_microwax	0.07	191	70.0
GP_wax	0.25	193	65.5
GP_wax	0.50	188	65.8
GP_wax	0.75	127	64.5
GP_wax	1	105	64.7

The FT-IR spectra for HNT, GP, and GP_wax are shown in Figure 5.3, and a comprehensive analysis of all the identified peaks can be found in Table 5.3. According to previous studies[138–140], the stretching of the hydroxyl groups in the inner and outer surfaces of halloysite nanotubes are represented by two characteristic bands at 3698 and 3608 cm^{-1}. The stretching vibrations of apical Si–O and Si–O–Si are assigned to the signals at 1093 and 1028 cm^{-1}, respectively. The peak observed at 796 cm^{-1} is attributed to the symmetric stretching of Si–O–Si, while the perpendicular stretching of Si–O–Al is related to the signals at 692 and 753 cm^{-1}. Additionally, the band at 533 cm^{-1} represents the deformation vibration of Al–O–Si. On the contrary, the process of geopolymerization affects the peak positions and leads to the disappearance of the characteristic signals of halloysite at approximately 3600 cm^{-1}.

Table 5.3. Assignment of IR peaks for geopolymers and halloysite.

Sample	Wavenumber / cm^{-1}	Band Assignment
GP	3458	OH stretching
	1658	OH bending
	1012	Si−O−T (T = tetrahedral Si or Al) asymmetric stretching
	716	Si–O–Al bending
	450	Si–O–Si in-plane stretching
GP_microwax	2920	CH_2 asymmetric stretching
	2848	CH_2 symmetric stretching
	1737	CO stretching

	1012	Si−O−T (T = tetrahedral Si or Al) asymmetric stretching
	1475	CH_2 scissor deformation
	726	CH_2 rocking deformation
	716	Si–O–Al bending
	450	Si–O–Si in-plane stretching
GP_wax $R_{wax/HNT}$=0.75	2920	CH_2 asymmetric stretching
	2848	CH_2 symmetric stretching
	1737	CO stretching
	1012	Si−O−T (T = tetrahedral Si or Al) asymmetric stretching
	1475	CH_2 scissor deformation
	726	CH_2 rocking deformation
	716	Si–O–Al bending
	450	Si–O–Si in-plane stretching
HNT	3698 – 3608	OH stretching
	1653	OH bending
	1093	Si–O stretching
	1028	Si–O–Si stretching
	796	Si–O–Si symmetric stretching
	753 – 692	Si–O–Al stretching
	533	Al–O–Si deformation

Geopolymer spectra evidenced the often called “main band” between 1025 and 1015 cm^{-1} attributed to the asymmetric stretching vibration of Si–O–T (T = tetrahedral Si or Al) and bands at 3458 and 1658 cm^{-1} assigned to stretching and bending vibrations of water’s hydration[141]. The main band, according to literature[142], depends on the Si/Al ratio and it can refer to the predominance of Si–O–Al bonds. It was noticed a shift of this band from 1044 cm^{-1} in halloysite to 1012 cm^{-1} in the geopolymeric samples that can be attributed to the degree of geopolymerization and to the increased substitution of Al in the tetrahedral silicate network[142–144]. In other words, when the Si/Al ratio is higher, the silicon content increases and the band will be shifted to higher wavenumbers thanks to the reorganization and condensation with greater Si contribution to the gel structure.

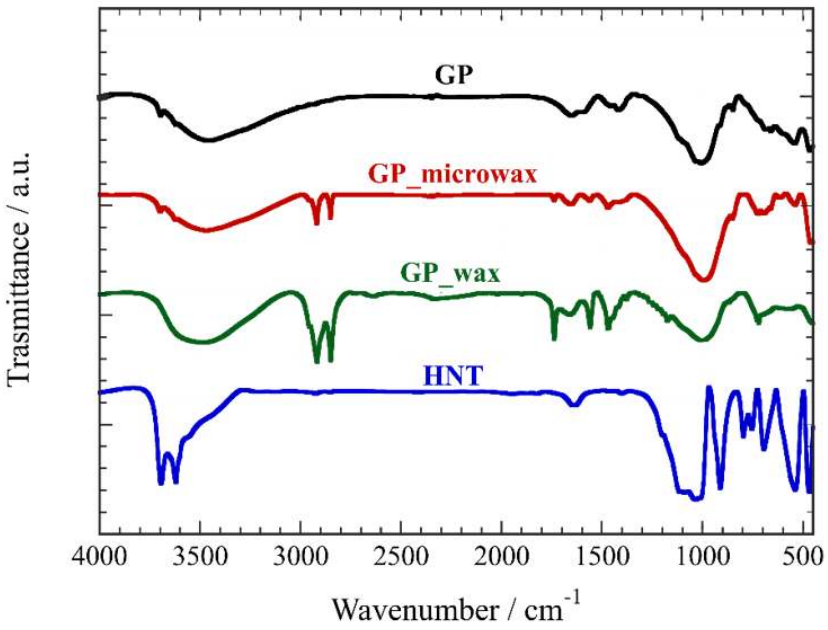

Figure 5.3. FT-IR spectra of GP, GP_microwax, GP_wax ($R_{wax/HNT}$ = 0.75) and HNT.

The filled geopolymers also showed peaks at 2920 and 2848 cm^{-1} (CH_2 asymmetric and symmetric stretching vibrations, respectively), 1737 cm^{-1} (C=O stretching vibration), as well as 1472 and 720 cm^{-1} (scissor deformation vibration and rocking vibrations of CH_2 groups, respectively). They refer to the presence of beeswax[145] and possess variable intensities depending on the wax/HNT ratio.

On the other hand, a better evaluation of the structural properties of geopolymers is given by the XRD patterns in Figure 5.4, which highlights the differences occurring after the geopolymerization.

Halloysite diffraction pattern presents the reflection at 2θ = 11.8° indicating its dehydrated form (basal spacing of 7.47 Å) and at 19.9 and 24.3° (basal spacing of 4.4 and 3.6 Å, respectively). Both the unfilled and filled geopolymers did not exhibit these signals but presented a broad reflection band from 20° to 40° (2θ), indicating the formation of an amorphous geopolymeric network.

Traces of the quartz[146,147] and the hydrosodalite phases that could appear after alkali activation[148] were also detected. GP_wax and GP_microwax samples evidenced the reflection signals (19.1, 21.2, 23.6, 29.7 and 39.9° and d equals to 4.6, 4.2, 3.8, 3.1 and 2.3 Å respectively) attributed to the orthorhombic structure of beeswax[149–151], although the intensities of these peaks are reduced compared to those of pure beeswax.

These results are consistent with the aforementioned reduction of the crystallinity of beeswax evidenced from DSC data (Table 5.2).

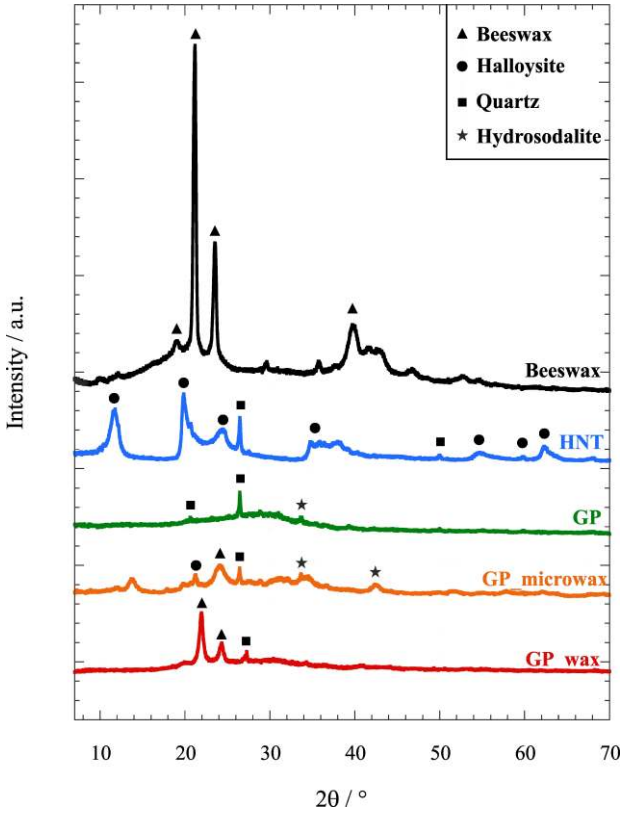

Figure 5.4. Diffractograms of Beeswax, HNT, GP, GP_microwax and GP_wax Rwax/HNT = 0.75.

5.2 Effect of wax in the morphology, wettability and mechanical performances of geopolymeric materials

The morphology of all the geopolymers was investigated by SEM analysis and the obtained images are reported in Figure 5.5. It is evident that the morphology is significantly affected by the addition of both wax and microwax particles. Compared to the filled geopolymers, the GP sample demonstrated a denser and more uniform matrix (Figure 5.5 (a)). Within the geopolymeric matrix, it was observed the presence of quartz together with a few halloysite nanotubes, which are residual precursors of the geopolymerization process. On the other hand, GP_wax exhibited an irregular morphology, with the wax

randomly distributed within the geopolymer network (Figure 5.5 (b)). In contrast, the interesting result is related to the GP_microwax sample that presents a uniform dispersion of wax microparticles with a spherical shape and a diameter ranging from 3 to 5 µm. Furthermore, Figure 5.5 (d-e) reveals that the surface of the wax microparticles was covered by spherical nanoparticles (approximately 400 nm in diameter), that probably came from halloysite, which had lost its tubular shape due to the alkaline activation. However, the presence of microparticles led to a less compact geopolymer with respect to the unfilled GP (Figure 5.5 (c)).

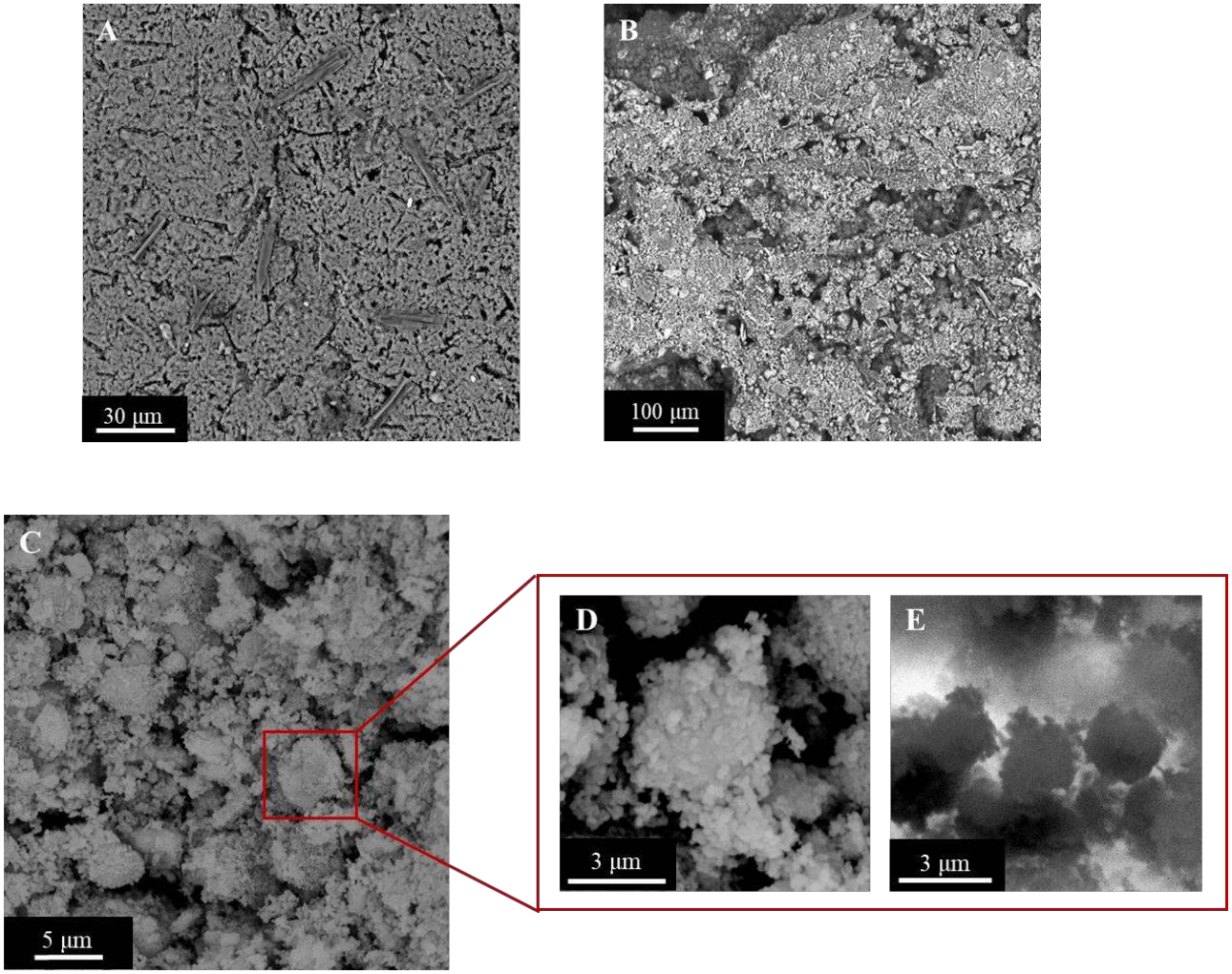

Figure 5.5. SEM images of (a) GP, (b) GP_wax ($R_{wax/HNT}$ = 1) and (c) GP_microwax. (d-e) Inset with details at the microparticles.

The increased roughness of the geopolymer surfaces, together with the different chemical compositions since we incorporated wax into the geopolymeric matrix, led to a change in the wettability properties of the prepared materials. The clay-based geopolymer GP under investigation in this study possesses a highly hydrophilic since halloysite is the aluminosilicate precursor. For this reason, it was not possible to measure the initial water contact angle of GP sample. However, after the deposition of the droplets on both GP_wax and GP_microwax materials, we were able to determine their water contact angles (Table 5.4) since wax possesses a hydrophobic nature. In particular, the reported water contact angle are the mean values of three measurements in different points of the samples. Similar findings have been observed in hydrophilic films loaded with hydrophobic coffee particles [152].

It is important to note that the surface hydrophobization caused by wax microparticles is lower than GP_wax samples, which exhibit higher contact angle values, up to 116°, as the wax content increases (Table 5.4). This indicates that the hydrophobization of the geopolymer is primarily due to changes in surface chemistry.

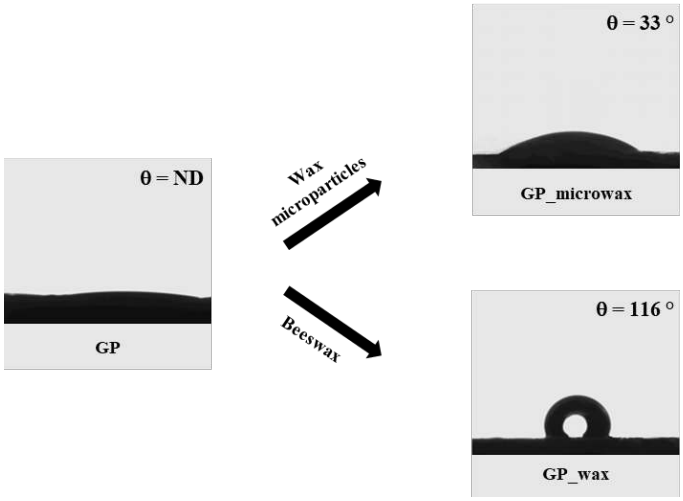

Figure 3.6. Images of the water droplets on the surfaces of GP, GP_microwax and GP_wax ($R_{wax/HNT}$ =1) just after their deposition.

The kinetic evolution of the water contact angle was evaluated exploiting Equation 5.2:

$$\theta = \theta_i \exp\left(-k_\theta t^n\right) \quad (5.2)$$

where θ_i is the initial contact angle extrapolated at zero time, k_θ estimates the process rate, and n possesses fractional values according to the presence of absorption and spreading phenomena i.e. n = 0 for pure absorption and n = 1 for pure spreading.

Table 5.4. Kinetic parameters of water contact angle measurements.

Sample	$R_{wax/HNT}$	θ_i / °	k_θ / s^{-1}	n
GP	0	ND	ND	ND
GP_wax	0.25	61.8	0.17 ± 0.01	0.22 ± 0.01
GP_wax	0.50	77.6	0.020 ± 0.003	0.67 ± 0.03
GP_wax	0.75	82.3	0.058 ± 0.003	0.34 ± 0.09
GP_wax	1	116.0	0.086 ± 0.004	0.303 ± 0.009
GP_microwax	0.07	33.4	0.018 ± 0.002	0.63 ± 0.03

As reported in literature, wax treatment did not decrease mechanical properties[153,154]. As a matter of fact, higher flexibility properties are in general observed on wax-treated specimens, leading to a positive effect on the mechanical performances. With this in mind, we investigated the effect of this addition to geopolymeric samples by comparing at first, the stress-strain curves of GP, GP_wax and GP_microwax in Figure 5.7 (a) and then by looking at different mechanical parameters, such as elastic modulus, stress at breaking point and elongation at breaking point.

Compared to the geopolymer without any fillers (GP), GP_microwax and GP_wax exhibited lower elastic modulus and stress at the breaking point values, while the elongation at the breaking point was improved (Table 5.5). This indicates that adding both wax and microwax enhanced the flexibility of the geopolymers. The elastic modulus of GP filled with wax microparticles was approximately six times lower with respect to GP sample, while the ultimate elongation was increased by a factor of six. The reason for this behavior is attributed to the uniform distribution of microwax particles within the geopolymeric matrix respect to the other filled samples. Moreover, by analyzing the stress vs strain curves, we were able to estimate the stored energy at the breaking point. Figure 5.7 (b) demonstrates that GP_wax with $R_{wax/HNT}$ =0.75 exhibited the greatest capacity for storing energy during the flexural tests. Interestingly, the energy required for the breaking

of GP_microwax was higher than that of GP_wax with $R_{wax/HNT}$ = 0.25, despite the lower amount of wax in the sample. Compared to the unfilled geopolymer, the stored energy up to breaking was improved by approximately 2.5 times for GP_wax ($R_{wax/HNT}$ = 0.25) and approximately 5 times for GP_microwax. It is worth noting that GP_microwax had a wax loading approximately three times lower than GP_wax ($R_{wax/HNT}$ = 0.25) and consequently, it represents a good compromise compared to the samples with common wax because it is important to note that GP_microwax also showed a higher stiffness.

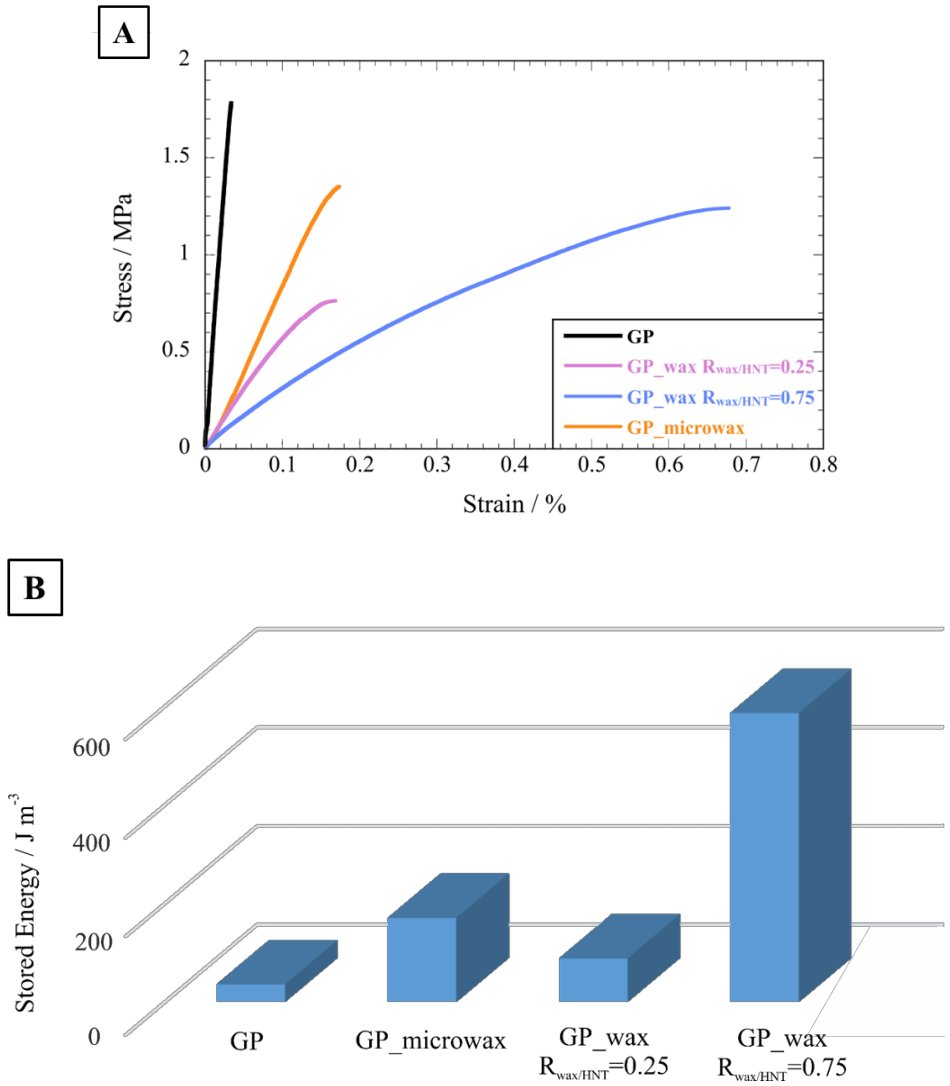

Figure 5.7. (a) Stress vs strain curves and (b) stored energies of GP, GP_microwax, GP_wax ($R_{wax/HNT}$ = 0.25 and 0.75). The relative error for the stored energies is 2%.

Table 5.5. Elastic modulus, stress at breaking point and elongation at breaking point.

Sample	$R_{wax/HNT}$	Elastic Modulus / MPa	Stress at Breaking Point / MPa	Elongation at Breaking point / %
GP	0	5425	1.8	0.03
GP_wax	0.25	603	0.8	0.17
GP_wax	0.75	261	1.2	0.69
GP_microwax	0.07	863	1.5	0.18

5.3 Heat storage capacity

As previously mentioned, wax is considered a phase change material and, indeed, an example of its use for thermal energy storage systems from Tetra Pak waste and paraffin wax was reported in literature[155], highlighting the potential of wax as phase change component.

For this reason, in this section, we examined the heat storage capacity of GP, GP_wax, and GP_microwax by using thermal images of these materials placed vertically on an electric hot plate and heated to 60 °C. Thermal images were analyzed through FLIR Tools software. This temperature ensured that the wax melting point was reached and, in this way, both the microwax particles and wax can act as phase change fillers that absorb thermal energy during phase changes.

The thermal images in Figure 5.8 (a) compare GP_microwax with GP_wax ($R_{wax/HNT}$ = 0.25) sample. Based on the analysis of these images, we determined the temperature gradient based on the distance from the support and presented the trends in Figure 5.8 (b). The temperature gradient showed negative values due to heat dissipation throughout the geopolymer material in all samples examined. Overall, we observed exponential decreasing trends. It is worth noting that GP and GP_wax ($R_{wax/HNT}$ = 0.25) exhibited similar trends, indicating that the addition of wax did not affect the heat absorption capacity of the geopolymer. Specifically, at a distance of 5 mm from the support, the

gradient temperature values were -10.99 and -11.06 °C for GP and GP_wax ($R_{wax/HNT}$ = 0.25), respectively. Conversely, the incorporation of a more considerable amount of wax into the geopolymer network (GP_wax $R_{wax/HNT}$ = 0.75) influenced the heat absorption behavior, as evidenced by the gradient temperature of -4.07°C at 5 mm. Interestingly, the addition of wax microparticles significantly reduced the gradient temperature (-7.42°C at the top of the GP_microwax sample) despite the minimal amount of wax trapped within the geopolymeric network (GP_microwax with $R_{wax/HNT}$ = 0.07, as shown in Table 5.1). This effect may be attributed to the uniform distribution of wax microparticles within the geopolymeric matrix.

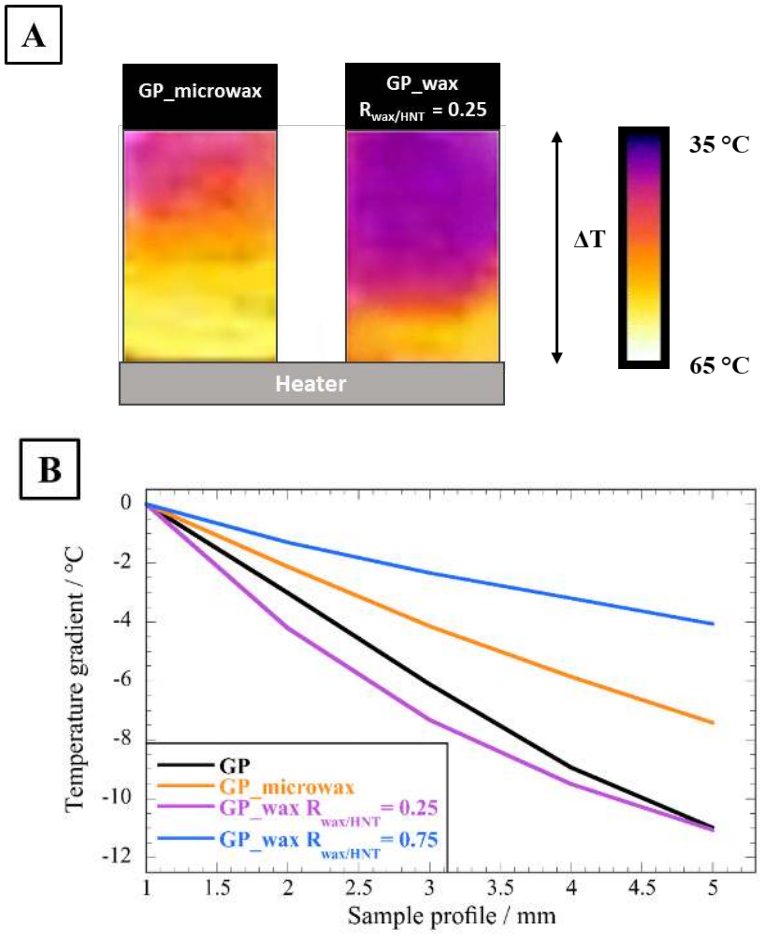

Figure 5.8. (a) Thermal images of GP_microwax and GP_wax ($R_{wax/HNT}$ = 0.25). (b) Temperature gradient as a function of the sample profile for GP, GP_microwax and GP_wax ($R_{wax/HNT}$ = 0.25 and 0.75).

5.4 Wax removal and permeability

Going further in this work, we wanted to investigate the possibility of removing wax from the geopolymers by rinsing the materials with ethanol in order to obtain materials with controlled porosity.

The removal of wax was confirmed through the qualitative essay of hydrophobicity by Nile Red and TG curves, which showed no mass loss in the temperature range of 300 to 400 °C for the washed geopolymers. Additionally, the Nile Red is used as a fluorescent probe because this molecule is highly emissive in hydrophobic environments, and it shows a red luminescence under UV light irradiation. As a matter of facts, the filled geopolymers are luminescent because of the presence of the hydrophobic. This essay demonstrated that GP_wax materials were not luminescent after being washed with ethanol beeswax. The washing procedure also affected the wettability and water vapor permeability properties of the geopolymers due to the removal of wax. The complete removal of wax was further confirmed by the very hydrophilic nature of the washed geopolymers. The water droplet image of the washed GP_wax ($R_{wax/HNT}$= 0.75) appears indeed as the unfilled geopolymer. For further details, refer to Figure 12 of the Attached Manuscript III.

On the other hand, the impact of the washing procedure on the water vapor permeability (WVP) of the filled geopolymers is shown in Figure 5.9.

The WVP tests were carried out in a desiccator with a saturated solution of calcium chloride dehydrate and bottles full of water. On the top of each bottle, the geopolymeric materials were fixed and the amount of water transferred through the materials and absorbed by the desiccant was measured by the weight loss every 24 hours for a period of 10 days. The water vapor permeability was then calculated using the Equation 5.3:

$$WVP = WVTR \left(\frac{L}{\Delta p}\right) \tag{5.3}$$

being *WVTR* the water vapor transmission rate given by:

$$WVTR = \left(\frac{\Delta m}{\Delta t}\right) A \tag{5.4}$$

where the slope of each line obtained from the weight loss of samples over time (g/h) is represented by $\Delta m/\Delta t$, A represents the exposed surface area of the sample (m^2), L represents the thickness of the sample (m), and Δp represents the difference in partial pressure (Pa) between the saturation solution at 30% relative humidity and the saturation water vapor pressure at a temperature of 28 °C.

Before rinsing with ethanol, the presence of both wax and microwax led to a decrease in the water permeability compared to the GP sample, which aligns with the hydrophobic properties observed in the water contact angle data (Table 5.4). According to literature, this decrease in water permeability can be attributed to the tortuosity effect and a decrease in available sorption sites for water molecules in the geopolymers[156]. Similar trends were indeed observed in hydroxypropylcellulose films filled with wax microparticles[157]. However, after the rinsing step, an increase in water permeability was observed due to the effective removal of wax from the geopolymeric network (Figure 5.9). Interestingly, the washed geopolymers exhibited different water permeability capacities depending on the initial wax content. The largest water vapor permeability value was found in GP_wax ($R_{wax/HNT}$ = 0.25), which displayed significantly higher water vapor permeability compared to the GP material.

The addition of wax with $R_{wax/HNT}$ =0.5 and 0.75 led to lower water vapor permeability (WVP) values after being washed with ethanol. Specifically, we can conclude that GP_wax ($R_{wax/HNT}$ = 0.25) has a higher porosity compared to GP_wax ($R_{wax/HNT}$ = 0.5 and 0.75). Regarding GP_microwax, we observed that rinsing with ethanol resulted in geopolymers with a WVP similar to the GP sample. Therefore, removing the wax microparticles leads to the formation of geopolymeric materials with a comparable porosity to the GP material. This was confirmed using a helium pycnometer, a reliable technique for investigating the skeletal density and porosity of geopolymeric materials[158]. It was found that incorporating microwax into the halloysite-based geopolymer increased the skeletal density (2.27 ± 0.03 g cm^{-3} and 2.358 ± 0.011 g cm^{-3} for GP and GP_microwax, respectively), which can be attributed to a reduction in closed pores. This discovery is in agreement with flexural experiments that showed improved stored energy up to breaking with the addition of microwax to the geopolymer (Figure 5.7). Previous literature suggests that reducing the volume of closed pores can enhance the mechanical performance of geopolymers based on kaolinite and metakaolinite[158,159]. We estimated that the porosity of GP_microwax is

significantly lower than that of GP: 24.8 % and 49.9%, respectively. The washing procedure did not affect the porosity of the unfilled geopolymer. However, an increase to 50.1% was observed for the GP_microwax sample, indicating that ethanol treatment effectively removes microwax particles from the geopolymer structure. The highest porosity of 64.4% was found in the washed GP_wax ($R_{wax/HNT}$ = 0.25) sample, consistent with its highest water vapor permeability.

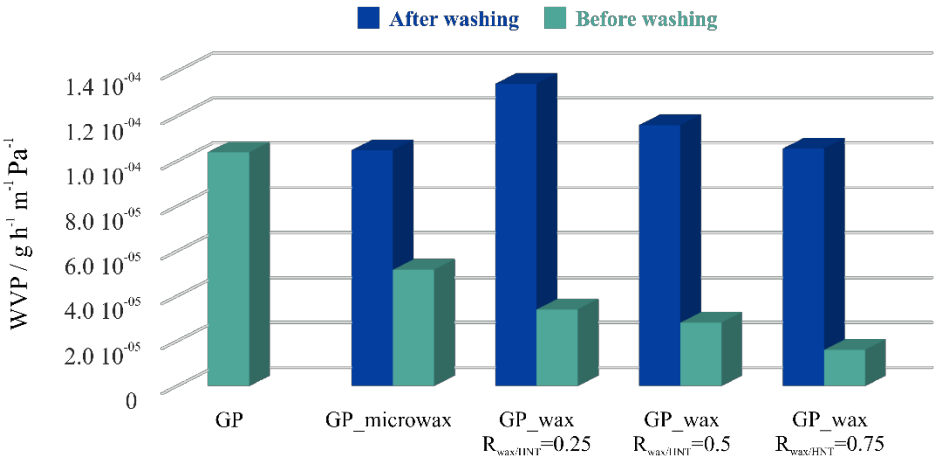

Figure 5.9. Water vapor permeability of GP sample and filled geopolymers before and after wax removal.

In this chapter, natural materials applicable for engineering purposes due to their flexibility and heat absorption capacity have been developed. In particular, halloysite nanotubes and beeswax microspheres have been used to create new hybrid geopolymers. Using thermogravimetric analysis, we estimated that our proposed method allowed to obtain halloysite-based geopolymers containing approximately 0.07 wt% of beeswax microspheres with a diameter of 3-5 μm.

Despite the small amount of beeswax, the incorporation of these microparticles into the geopolymeric network led to significant improvements in both flexural characteristics and heat storage capacity compared to the unfilled geopolymer. Specifically, the stored energy up to the breaking point increased 5 times. These improvements can be attributed to the homogeneous distribution of the beeswax microspheres within the geopolymeric matrix, as evidenced by the structural characteristics and the morphology of the filled materials.

Hybrid geopolymers filled with beeswax at variable compositions were also prepared to compare the effect of the different ways of filling on the performances and it demonstrated composition-dependent properties reflecting the random dispersion of beeswax. Improvements in flexibility and heat storage capacity were achieved only after adding a larger amount (around 40 wt%) of beeswax. Notably, compared to the microwax loading, in order to obtain composite geopolymers with similar performances, the incorporation of beeswax required an amount of approximately one order of magnitude larger. Additionally, we found that both beeswax and microwax could be easily removed by washing the hybrid geopolymers with ethanol. Interestingly, the water vapor permeability of the washed geopolymers depended on the initial amount of wax incorporated in the geopolymeric network.

This research constitutes the first step for the development of geopolymers filled with phase change materials, such as wax microspheres, which have the potential to function as smart thermal regulation systems in various engineering and biotechnology applications.

6. Application of halloysite-based geopolymers as protective layers

6.1 Treatment of the steel surface with geopolymeric protective layers

Previous studies highlighted the use of geopolymer coatings on metal substrates as effective barriers for concrete, providing protection and thermal insulation[160]. The main characteristic of these protective layers is hydrophobicity, in order to ensure reduced water adhesion and resistance to biological species growth. However, it is important to note that clay-based geopolymers are inherently hydrophilic due to their chemical characteristics.

To address this issue, microwax particles derived from Pickering emulsions can be used[161,162].

In this study, beeswax microparticles were embedded within the geopolymeric network to enhance hydrophobicity, thereby creating a new protective layer for coating applications on steel sheets. The geopolymeric samples employed here are the same as the ones presented in the previous Chapter 5 (in alternative, refer to the Attached Manuscript IV).

The coating process involved brushing the surface of the steel substrates with the geopolymeric paste, known as GP microwax. Then, the final hardening step was performed by placing the treated steel samples in an oven at 50 °C for 48 h. For comparison, the steel substrates were also treated with halloysite-based geopolymer (GP), without any beeswax addition.

The optical micrographs reported in Figure 6.1 evaluate the effect of the coating layers at a micrometric level. The steel sheet exhibited a smooth and relatively homogeneous surface after undergoing the geopolymeric coating treatments. However, there are still microdomains and particle aggregation visible on both the GP and GP microwax treated steel sheets.

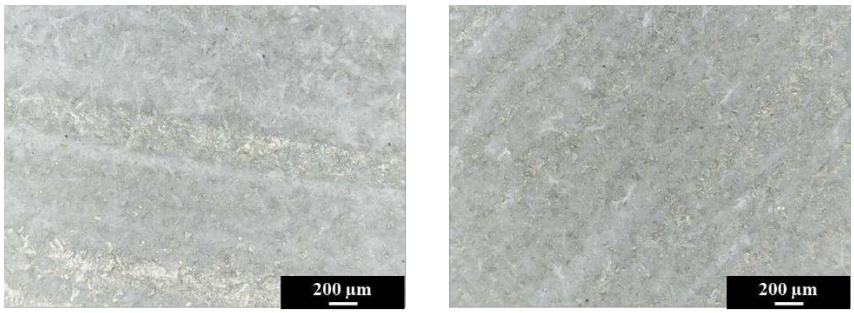

Figure 6.1. Optical micrographs of the steel surfaces treated with GP and GP microwax.

6.2 Characterization of the treated steel

The presence of the different geopolymeric treatments also influences the wettability of the steel substrates (Figure 6.2). With this in mind, we performed water contact angle measurements on both the untreated and treated surfaces. The untreated steel is hydrophilic with a contact angle of 52.3°, which remains constant over the time. When the surface is coated with the halloysite-based geopolymer GP, it becomes much more hydrophilic with a contact angle of 8.1° after the deposition of the droplet. This is likely due to the smoother surface created by the coating but especially to the high hydrophilicity of halloysite based geopolymers, which interact with water. However, when the surface is coated with GP_microwax, it remains hydrophilic with a contact angle of 49.2° that only slightly decreases to 44.3° after 60 seconds without any cleaning step carried out. Interestingly, the surface becomes more hydrophobic after washing many times with water, with the contact angle increasing to 83.6° and then slightly decreasing to 74.2° after one minute. These variations are likely due to the excess of halloysite nanotubes, which increase the hydrophilic behavior of the material. Interestingly, it is worth noting that the treatment remains stuck on the surface even after multiple washes. On the contrary, the hydrophobic contribution to the geopolymer wettability is hence enhanced when the wax microparticles can interact with the water droplet after washing away the excess of clay.

It is important to note that the addition of hydrophobic beeswax can also affect the smoothness of the micron level coating surface.

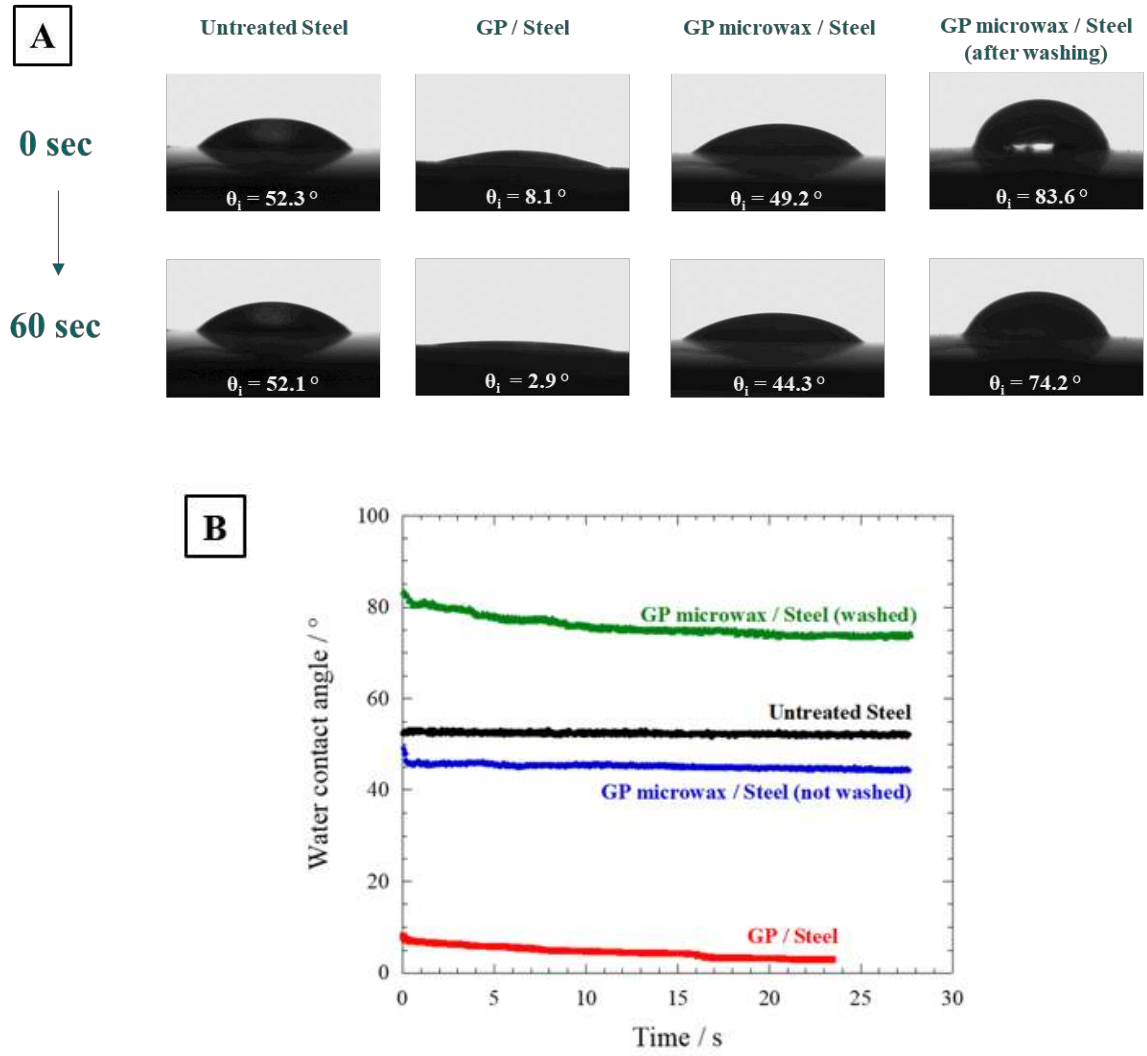

Figure 6.2. (a) Water droplets profiles at t = 0 s and t = 60 s after their deposition on the surface of the samples. (b) Water contact angle kinetics.

The droplet evolution on the surface over time was again analysed by fitting the curves with the Equation 5.2 and the water contact angle kinetics are shown in Figure 6.2 (b). The analysis reveals that the presence of microwax particles in the coating layer decreases the process rate, as indicated by the reduction of k_θ (Table 6.1). Additionally, it was observed a lower spreading contribution, as indicated by the decrease of n for the treated steel with GP_microwax compared to the pure halloysite-based geopolymeric coating.

Table 6.1. Fitting parameters of the kinetic evolution of water contact angles.

Sample	k_θ (s^{-n})	n
GP / Steel	0.121 ± 0.007	0.54 ± 0.02
GP_microwax / Steel (after washing)	0.043 ± 0.006	0.35 ± 0.04

X-ray fluorescence (XRF) studies were conducted to analyze the chemical composition of the steel sheets before and after the treatments (Figure 6.3).

It is important to note that the main peaks found in all the three tested systems were associated with the presence of Chromium, Manganese, and Iron, which are components of the bare steel sheets. However, after the treatment procedures were carried out, Silicon and Aluminum were found on the surface. Interestingly, the intensity of the Si and Al peaks was higher in the steel treated with GP compared to the steel coated with GP_microwax (inset in Figure 6.3). Iron and Chromium constitute the main components of the steel sheets, 70.85 and 18.10 wt%, respectively. However, after the treatment, although Fe and Cr are still the most abundant elements, the GP microwax treated steel contained 11.21 wt% of Al and 11.26 wt% of Si. Furthermore, the GP treated steel exhibited even higher concentrations of these elements, with 19.57 wt% of Al and 18.62 wt% of Si. It is worth noting that the Al/Si ratio is ca. 1, which is characteristic of pristine halloysite [114]. These findings also agree with the contact angle data, as a higher nanotube content in the coating layer results in a more hydrophilic surface.

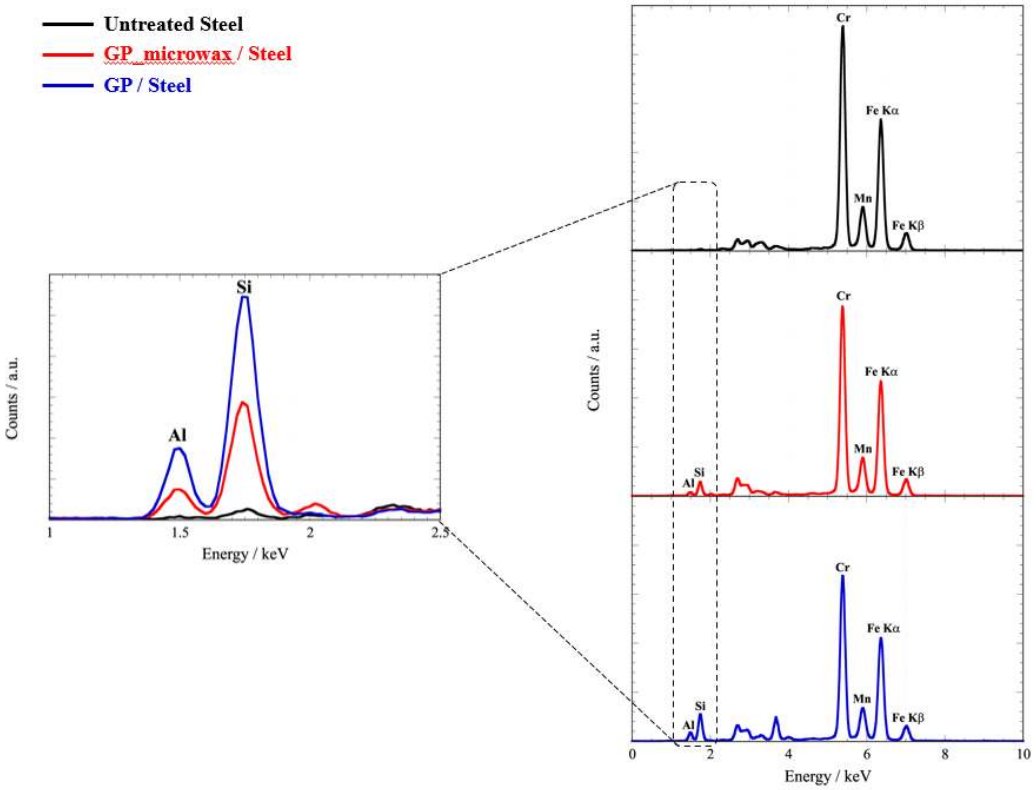

Figure 6.3. XRF spectra of untreated and treated steel.

In summary, halloysite-based geopolymers have been used for application as protective layers on steel substrates. The choice of the steel material is connected to the fact that the steel is widely used in construction and simultaneously we wanted to investigate the presence of adhesion of the prepared geopolymeric paste on smooth surfaces. On the other hand, future research studies are needed to include also other kind of surfaces.

The materials were treated with both GP and GP_microwax geopolymeric formulations and it turned out that thanks to the presence of microwax particles, the wettability properties of the steel surfaces underwent a modification. Both the untreated steel and the GP treated one showed hydrophilic features. On the contrary, the treatment with GP microwax enhanced the hydrophobicity of the material, giving new perspectives in protective coating.

7. Concluding remarks

The main objective of this PhD thesis was to prepare and characterize new composite geopolymers based on halloysite nanoclays, with a particular focus on the specific features of the nanoclays that can be used as precursors.

Firstly, a novel protocol for the separation of halloysite/kaolinite mixtures was proposed in order to purify natural samples of halloysite that often contain varying levels of platy kaolinite nanoparticles depending on their geological source. The variable effects of sucrose addition on the aqueous colloidal stability of both nanoclays were exploited.

It was observed that the diffusion of halloysite nanotubes in water is influenced by the sucrose concentration while, on the other hand, any effects were detected for kaolinite nanoplates. Results showed that amounts of sucrose less than 10 wt% enhanced the sedimentation kinetics of halloysite nanotubes, while this effect was avoided by increasing the concentration (≥ 10 wt%), in agreement with the significant screening towards the attractive interactions between the clay nanotubes. Interestingly, the dispersibility of kaolinite was strongly reduced with sucrose ≥ 10 wt%. The fitting analysis of the differential thermogravimetric curves by split Gaussian functions allowed to estimate the halloysite contents in the separated materials in water and 10 wt% of sucrose. Based on the obtained data, the separation efficiency of halloysite/kaolinite mixtures was optimized in 10 wt% sucrose aqueous solution, which influenced the aqueous colloidal stability and the sedimentation kinetics of both nanoclays.

Considering the different properties observed due to the distinct morphologies of these nanoclays, NMR techniques were used to explore the water diffusion and relaxation characteristics in platy kaolinite and two types of halloysite nanotubes. It was demonstrated the presence of different water populations and two diffusion coefficients related to the confined and bulk water were calculated for the investigated systems. Moreover, the unique structure of Patch halloysite, with longer and thinner nanotubes, influenced the water diffusion and relaxation more than the other nanoclays. Interestingly, comparing the diffusion and relaxation of HNT and halloysite-based geopolymer, it turned out that GP possesses a fast component, which is related to the confined water in its porosities, but its amount is lower compared with the one confined in the nanotubes.

Furthermore, it was also found that Patch halloysite, because of its characteristic fibrous structure, had different rheological properties compared to halloysite from other sources. A detailed rheological study on Patch samples at different concentrations was then presented showing the formation of hydrogels even at low concentrations.

Following the first part of this research project, which focused on characterizing some features of nanoclays as precursors for geopolymeric synthesis, a new method for preparing composite geopolymers was proposed. Specifically, halloysite-based geopolymers filled with beeswax microparticles were prepared. According to the morphological and structural investigations, the microwax particles were uniformly dispersed within the geopolymeric network, resulting in excellent properties for the hybrid geopolymers. Although the low amount of microwax, their loading within the geopolymeric network generated relevant improvements in the flexural characteristics and heat storage capacity with respect to the unfilled geopolymer. Comparisons were also made with halloysite-based geopolymers filled with different amounts of beeswax, showing that the properties varied depending on the composition and the random dispersion of the beeswax. Only adding a large amount of beeswax, a significant improvement in flexibility and heat storage capacity was achieved compared to filling with microwax particles alone. Namely, the filling with beeswax requires contents of ca. one order larger than the loading of microwax to obtain composite geopolymers with comparable performances. Moreover, by rinsing with ethanol, the removal of microwax and wax from the composite geopolymers has been obtained, proving that the porosity of the materials can be controlled by the initial composition of wax. The porosity of GP_microwax was estimated to be significantly lower with respect to that of unfilled GP. The washing procedure did not alter the porosity of GP, while a significant enhancement was detected for GP_microwax sample.

The presence of phase change materials confined in the geopolymeric network made this composite material suitable for various applications, particularly in terms of heat storage and flexural performance.

Finally, in the last part of this thesis, the presented halloysite-based geopolymer filled with microwax particles was employed for application as a protective coating on steel substrates by brush deposition. For comparison, geopolymeric coating without wax was also reported.

After the treatment with both geopolymeric formulations, the steel surfaces appear homogeneous and smooth. Interestingly, the presence of microwax particles altered the wettability properties of the steel surface.

As a matter of fact, both the untreated steel and the GP treated present hydrophilic values of water contact angle. Conversely, the treatment of the steel sheet with GP_microwax enhanced the hydrophobicity features of the material surface, giving new perspectives in the application of geopolymers as protective coating.

Overall, this research work has implications for the development of environmentally friendly clay-based materials and represents the starting point for the design of geopolymers filled with a phase change material that can act as smart thermal regulation systems for several applications within engineering and biotechnology.

8. Acknowledgements

I would like to express my utmost gratitude to the *Sicilia Eco Tecnologie Innovative* (S.E.T.I.) Project - Cod. 2017-NAZ-0204, PO FESR Sicilia 2014/2020, Azione 1.1.5 – that financially supported my PhD scholarship, making possible the present research work.

A special thanks goes to my tutor and mentor, Prof. Giuseppe Lazzara, whose expertise has been invaluable in shaping my *forma mentis* and this research, giving me always a different point of view and the necessary tools to enrich my scientific knowledge since my Bachelor's degree. His constant support, enthusiasm, and insightful feedback have significantly contributed to the quality and depth of this work. I am also deeply grateful to my co-tutor, Dr. Giuseppe Cavallaro, for his precious input and constructive suggestions that assisted me during these years. I would like to dedicate a special acknowledgement to Prof. Stefana Milioto, whose profound dedication and passion for the physical chemistry played an essential role in my educational and personal growth, introducing me to this world. Her influence has set the foundation for my academic and professional aspirations, and I am forever thankful for that.

I would like to express my sincere gratitude to Prof. Daniel Topgaard, who guided me during the seven months I spent at the Division of Physical Chemistry at Lund University. His expertise, inspiring point of view and critical analysis have played an instrumental role in developing my research skills and knowledge.

I would also like to thank the coauthors of my scientific collaborations for their contributions that provided new insights and perspectives, enriching my research career.

9. References

(1) Foulkes, R.; Man, E.; Thind, J.; Yeung, S.; Joy, A.; Hoskins, C. The Regulation of Nanomaterials and Nanomedicines for Clinical Application: Current and Future Perspectives. *Biomaterials Science* **2020**, *8* (17), 4653–4664. https://doi.org/10.1039/d0bm00558d.

(2) Hutton, G. A. M.; Reuillard, B.; Martindale, B. C. M.; Caputo, C. A.; Lockwood, C. W. J.; Butt, J. N.; Reisner, E. Carbon Dots as Versatile Photosensitizers for Solar-Driven Catalysis with Redox Enzymes. *Journal of the American Chemical Society* **2016**, *138* (51), 16722–16730. https://doi.org/10.1021/jacs.6b10146.

(3) Gupta, V. K.; Jain, R.; Mittal, A.; Saleh, T. A.; Nayak, A.; Agarwal, S.; Sikarwar, S. Photo-Catalytic Degradation of Toxic Dye Amaranth on TiO2/UV in Aqueous Suspensions. *Materials Science and Engineering: C* **2012**, *32* (1), 12–17. https://doi.org/10.1016/j.msec.2011.08.018.

(4) Clara, M.; Strenn, B.; Gans, O.; Martinez, E.; Kreuzinger, N.; Kroiss, H. Removal of Selected Pharmaceuticals, Fragrances and Endocrine Disrupting Compounds in a Membrane Bioreactor and Conventional Wastewater Treatment Plants. *Water Research* **2005**, *39* (19), 4797–4807. https://doi.org/10.1016/j.watres.2005.09.015.

(5) Abegglen, C.; Joss, A.; McArdell, C. S.; Fink, G.; Schlüsener, M. P.; Ternes, T. A.; Siegrist, H. The Fate of Selected Micropollutants in a Single-House MBR. *Water Research* **2009**, *43* (7), 2036–2046. https://doi.org/10.1016/j.watres.2009.02.005.

(6) Aguzzi, C.; Cerezo, P.; Viseras, C.; Caramella, C. Use of Clays as Drug Delivery Systems: Possibilities and Limitations. *Applied Clay Science* **2007**, *36* (1), 22–36. https://doi.org/10.1016/j.clay.2006.06.015.

(7) Cataldo, S.; Lazzara, G.; Massaro, M.; Muratore, N.; Pettignano, A.; Riela, S. Functionalized Halloysite Nanotubes for Enhanced Removal of Lead(II) Ions from Aqueous Solutions. *Applied Clay Science* **2018**, *156*, 87–95. https://doi.org/10.1016/j.clay.2018.01.028.

(8) Cavallaro, G.; Milioto, S.; Lazzara, G. Halloysite Nanotubes: Interfacial Properties and Applications in Cultural Heritage. *Langmuir* **2020**, *36* (14), 3677–3689. https://doi.org/10.1021/acs.langmuir.0c00573.

(9) Yuan, G. Natural and Modified Nanomaterials as Sorbents of Environmental Contaminants. *Journal of Environmental Science and Health, Part A* **2004**, *39* (10), 2661–2670. https://doi.org/10.1081/ESE-200027022.

(10) Cavallaro, G.; Lazzara, G.; Rozhina, E.; Konnova, S.; Kryuchkova, M.; Khaertdinov, N.; Fakhrullin, R. Organic-Nanoclay Composite Materials as Removal Agents for Environmental Decontamination. *RSC Adv.* **2019**, *9* (69), 40553–40564. https://doi.org/10.1039/C9RA08230A.

(11) Dana, K.; Sarkar, M. 5 - Organophilic Nature of Nanoclay. In *Clay Nanoparticles*; Cavallaro, G., Fakhrullin, R., Pasbakhsh, P., Eds.; Micro and Nano Technologies; Elsevier, 2020; pp 117–138. https://doi.org/10.1016/B978-0-12-816783-0.00005-0.

(12) Ferrante, F.; Armata, N.; Lazzara, G. Modeling of the Halloysite Spiral Nanotube. *J. Phys. Chem. C* **2015**, *119* (29), 16700–16707. https://doi.org/10.1021/acs.jpcc.5b04281.

(13) Pasbakhsh, P.; Churchman, G. J.; Keeling, J. L. Characterisation of Properties of Various Halloysites Relevant to Their Use as Nanotubes and Microfibre Fillers. *Applied Clay Science* **2013**, *74*, 47–57. https://doi.org/10.1016/j.clay.2012.06.014.

(14)Lisuzzo, L.; Cavallaro, G.; Parisi, F.; Milioto, S.; Lazzara, G. Colloidal Stability of Halloysite Clay Nanotubes. *Ceramics International* **2019**, *45* (2, Part B), 2858–2865. https://doi.org/10.1016/j.ceramint.2018.07.289.
(15)Santos, A. C.; Ferreira, C.; Veiga, F.; Ribeiro, A. J.; Panchal, A.; Lvov, Y.; Agarwal, A. Halloysite Clay Nanotubes for Life Sciences Applications: From Drug Encapsulation to Bioscaffold. *Advances in Colloid and Interface Science* **2018**, *257*, 58–70. https://doi.org/10.1016/j.cis.2018.05.007.
(16)Abdullayev, E.; Joshi, A.; Wei, W.; Zhao, Y.; Lvov, Y. Enlargement of Halloysite Clay Nanotube Lumen by Selective Etching of Aluminum Oxide. *ACS Nano* **2012**, *6* (8), 7216–7226. https://doi.org/10.1021/nn302328x.
(17)Massaro, M.; Colletti, C. G.; Lazzara, G.; Milioto, S.; Noto, R.; Riela, S. Halloysite Nanotubes as Support for Metal-Based Catalysts. *J. Mater. Chem. A* **2017**, *5* (26), 13276–13293. https://doi.org/10.1039/C7TA02996A.
(18)Lvov, Y. M.; Shchukin, D. G.; Möhwald, H.; Price, R. R. Halloysite Clay Nanotubes for Controlled Release of Protective Agents. *ACS Nano* **2008**, *2* (5), 814–820. https://doi.org/10.1021/nn800259q.
(19)Liao, J.; Wang, H.; Liu, N.; Yang, H. Functionally Modified Halloysite Nanotubes for Personalized Bioapplications. *Advances in Colloid and Interface Science* **2023**, *311*, 102812. https://doi.org/10.1016/j.cis.2022.102812.
(20)Kryuchkova, M.; Danilushkina, A.; Lvov, Y.; Fakhrullin, R. Evaluation of Toxicity of Nanoclays and Graphene Oxide: In Vivo A Paramecium Caudatum Study. *Environmental Science: Nano* **2016**, *3* (2), 442–452. https://doi.org/10.1039/c5en00201j.
(21)Massaro, M.; Lazzara, G.; Milioto, S.; Noto, R.; Riela, S. Covalently Modified Halloysite Clay Nanotubes: Synthesis, Properties, Biological and Medical Applications. *J. Mater. Chem. B* **2017**, *5* (16), 2867–2882. https://doi.org/10.1039/C7TB00316A.
(22)Cunningham, V. J.; Giakoumatos, E. C.; Ireland, P. M.; Mable, C. J.; Armes, S. P.; Wanless, E. J. Giant Pickering Droplets: Effect of Nanoparticle Size and Morphology on Stability. *Langmuir* **2017**, *33* (31), 7669–7679. https://doi.org/10.1021/acs.langmuir.7b01383.
(23)Wu, J.; Ma, G.-H. Recent Studies of Pickering Emulsions: Particles Make the Difference. *Small (Weinheim an der Bergstrasse, Germany)* **2016**, *12* (34), 4633–4648. https://doi.org/10.1002/smll.201600877.
(24)Low, L. E.; Siva, S. P.; Ho, Y. K.; Chan, E. S.; Tey, B. T. Recent Advances of Characterization Techniques for the Formation, Physical Properties and Stability of Pickering Emulsion. *Advances in Colloid and Interface Science* **2020**, *277*, 102117. https://doi.org/10.1016/j.cis.2020.102117.
(25)Ballard, N.; Law, A. D.; Bon, S. A. F. Colloidal Particles at Fluid Interfaces: Behaviour of Isolated Particles. *Soft Matter* **2019**, *15* (6), 1186–1199. https://doi.org/10.1039/C8SM02048E.
(26)Lu, T.; Gou, H.; Rao, H.; Zhao, G. Recent Progress in Nanoclay-Based Pickering Emulsion and Applications. *Journal of Environmental Chemical Engineering* **2021**, *9* (5), 105941. https://doi.org/10.1016/j.jece.2021.105941.
(27)Sharma, T.; Velmurugan, N.; Patel, P.; Chon, B. H.; Sangwai, J. S. Use of Oil-in-Water Pickering Emulsion Stabilized by Nanoparticles in Combination With Polymer Flood for Enhanced Oil Recovery. *Petroleum Science and Technology* **2015**, *33* (17–18), 1595–1604. https://doi.org/10.1080/10916466.2015.1079534.
(28)Marku, D.; Wahlgren, M.; Rayner, M.; Sjöö, M.; Timgren, A. Characterization of Starch Pickering Emulsions for Potential Applications in Topical Formulations. *International*

Journal of Pharmaceutics **2012**, *428* (1), 1–7. https://doi.org/10.1016/j.ijpharm.2012.01.031.
(29)Owoseni, O.; Nyankson, E.; Zhang, Y.; Adams, S. J.; He, J.; McPherson, G. L.; Bose, A.; Gupta, R. B.; John, V. T. Release of Surfactant Cargo from Interfacially-Active Halloysite Clay Nanotubes for Oil Spill Remediation. *Langmuir* **2014**, *30* (45), 13533–13541. https://doi.org/10.1021/la503687b.
(30)Cavallaro, G.; Milioto, S.; Nigamatzyanova, L.; Akhatova, F.; Fakhrullin, R.; Lazzara, G. Pickering Emulsion Gels Based on Halloysite Nanotubes and Ionic Biopolymers: Properties and Cleaning Action on Marble Surface. *ACS Appl. Nano Mater.* **2019**, *2* (5), 3169–3176. https://doi.org/10.1021/acsanm.9b00487.
(31)Lisuzzo, L.; Hueckel, T.; Cavallaro, G.; Sacanna, S.; Lazzara, G. Pickering Emulsions Based on Wax and Halloysite Nanotubes: An Ecofriendly Protocol for the Treatment of Archeological Woods. *ACS Appl. Mater. Interfaces* **2021**, *13* (1), 1651–1661. https://doi.org/10.1021/acsami.0c20443.
(32)Klumpp, K.; Marcolli, C.; Alonso-Hellweg, A.; Dreimol, C. H.; Peter, T. Comparing the Ice Nucleation Properties of the Kaolin Minerals Kaolinite and Halloysite. *Atmospheric Chemistry and Physics* **2023**, *23* (2), 1579–1598. https://doi.org/10.5194/acp-23-1579-2023.
(33)Dill, H. G. Kaolin: Soil, Rock and Ore: From the Mineral to the Magmatic, Sedimentary and Metamorphic Environments. *Earth-Science Reviews* **2016**, *161*, 16–129. https://doi.org/10.1016/j.earscirev.2016.07.003.
(34)Zunino, F.; Boehm-Courjault, E.; Scrivener, K. The Impact of Calcite Impurities in Clays Containing Kaolinite on Their Reactivity in Cement after Calcination. *Mater Struct* **2020**, *53* (2), 44. https://doi.org/10.1617/s11527-020-01478-9.
(35)Janik, L. J.; Keeling, J. L. FT-IR Partial Least-Squares Analysis of Tubular Halloysite in Kaolin Samples from the Mount Hope Kaolin Deposit. *Clay Minerals* **1993**, *28* (3), 365–378. https://doi.org/10.1180/claymin.1993.028.3.03.
(36)Kaufhold, S.; Hein, M.; Dohrmann, R.; Ufer, K. Quantification of the Mineralogical Composition of Clays Using FTIR Spectroscopy. *Vibrational Spectroscopy* **2012**, *59*, 29–39. https://doi.org/10.1016/j.vibspec.2011.12.012.
(37)Du Plessis, P. I.; Gazley, M. F.; Tay, S. L.; Trunfull, E. F.; Knorsch, M.; Branch, T.; Fourie, L. F. Quantification of Kaolinite and Halloysite Using Machine Learning from FTIR, XRF, and Brightness Data. *Minerals* **2021**, *11* (12), 1350. https://doi.org/10.3390/min11121350.
(38)Saklar, S.; Yorukoglu, A. Effects of Acid Leaching on Halloysite. *Physicochemical Problems of Mineral Processing* **2015**, *51* (1), 83–94. https://doi.org/10.5277/ppmp150108.
(39)Pita, F. Influence of Froth Height on Column Flotation of Kaolin Ore. *Minerals* **2017**, *7* (12). https://doi.org/10.3390/min7120235.
(40)Sakiewicz, P.; Lutynski, M.; Soltys, J.; Pytlinski, A. Purification of Halloysite by Magnetic Separation. *Physicochemical Problems of Mineral Processing* **2016**, *52* (2), 991–1001. https://doi.org/10.5277/ppmp160236.
(41)Zhao, J. M.; Chang, J. H.; Lee, Y. K.; Hwang, K. H.; Lee, J. K. Separation of Halloysite Nano Tubes (HNTs) by Homogenization of Quartz Contaminated Kaolins. *Journal of Nanoscience and Nanotechnology* **2019**, *19* (2), 984–987. https://doi.org/10.1166/jnn.2019.15931.
(42)Cavallaro, G.; Lazzara, G.; Taormina, V.; Cascio, D. Sedimentation of Halloysite Nanotubes from Different Deposits in Aqueous Media at Variable Ionic Strengths.

Colloids and Surfaces A: Physicochemical and Engineering Aspects **2019**, *576*, 22–28. https://doi.org/10.1016/j.colsurfa.2019.05.038.
(43)Tardani, F.; Casciardi, S.; Ruzicka, B.; Sennato, S. Salt Enhanced Sedimentation of Halloysite Nanotubes for Precise Determination of DNA Adsorption Isotherm. *Colloids and Surfaces A: Physicochemical and Engineering Aspects* **2020**, *605*, 125400. https://doi.org/10.1016/j.colsurfa.2020.125400.
(44)Katana, B.; Takács, D.; Csapó, E.; Szabó, T.; Jamnik, A.; Szilagyi, I. Ion Specific Effects on the Stability of Halloysite Nanotube Colloids—Inorganic Salts versus Ionic Liquids. *J. Phys. Chem. B* **2020**, *124* (43), 9757–9765. https://doi.org/10.1021/acs.jpcb.0c07885.
(45)Kang, X.; Xia, Z.; Chen, R.; Liu, P.; Yang, W. Effects of Inorganic Cations and Organic Polymers on the Physicochemical Properties and Microfabrics of Kaolinite Suspensions. *Applied Clay Science* **2019**, *176*, 38–48. https://doi.org/10.1016/j.clay.2019.04.024.
(46)Nasim, T.; Pal, A.; Bandyopadhyay, A. Flocculation of Aqueous Kaolin Suspension Using a Biodegradable Flocculant System of Poly (Vinyl Alcohol)-Acacia Nilotica Gum Blends. *Applied Clay Science* **2018**, *152*, 83–92. https://doi.org/10.1016/j.clay.2017.10.035.
(47)Cao, J.; Kang, X.; Bate, B. Microscopic and Physicochemical Studies of Polymer-Modified Kaolinite Suspensions. *Colloids and Surfaces A: Physicochemical and Engineering Aspects* **2018**, *554*, 16–26. https://doi.org/10.1016/j.colsurfa.2018.06.019.
(48)Davidovits, J. Geopolymers. *Journal of Thermal Analysis* **1991**, *37* (8), 1633–1656. https://doi.org/10.1007/BF01912193.
(49)Duxson, P.; Fernández-Jiménez, A.; Provis, J. L.; Lukey, G. C.; Palomo, A.; van Deventer, J. S. J. Geopolymer Technology: The Current State of the Art. *J Mater Sci* **2007**, *42* (9), 2917–2933. https://doi.org/10.1007/s10853-006-0637-z.
(50)Sotelo-Piña, C.; Aguilera-González, E. N.; Martínez-Luévanos, A. Geopolymers: Past, Present, and Future of Low Carbon Footprint Eco-Materials. In *Handbook of Ecomaterials*; Martínez, L. M. T., Kharissova, O. V., Kharisov, B. I., Eds.; Springer International Publishing: Cham, 2019; pp 2765–2785. https://doi.org/10.1007/978-3-319-68255-6_54.
(51)Arnoult, M.; Perronnet, M.; Autef, A.; Rossignol, S. How to Control the Geopolymer Setting Time with the Alkaline Silicate Solution. *Journal of Non-Crystalline Solids* **2018**, *495*, 59–66. https://doi.org/10.1016/j.jnoncrysol.2018.02.036.
(52)Nakum, A. V.; Arora, N. K. The Impact of Alkaline Solution to Fly Ash Ratio with Different Molarities of Sodium Hydroxide on Self-Compacted Geopolymer Concrete. *Materials Today: Proceedings* **2022**, *62*, 4168–4176. https://doi.org/10.1016/j.matpr.2022.04.688.
(53)Alonso, S.; Palomo, A. Calorimetric Study of Alkaline Activation of Calcium Hydroxide–Metakaolin Solid Mixtures. *Cement and Concrete Research* **2001**, *31* (1), 25–30. https://doi.org/10.1016/S0008-8846(00)00435-X.
(54)Aliabdo, A. A.; Abd Elmoaty, A. E. M.; Salem, H. A. Effect of Water Addition, Plasticizer and Alkaline Solution Constitution on Fly Ash Based Geopolymer Concrete Performance. *Construction and Building Materials* **2016**, *121*, 694–703. https://doi.org/10.1016/j.conbuildmat.2016.06.062.
(55)Abdila, S. R.; Abdullah, M. M. A. B.; Ahmad, R.; Burduhos Nergis, D. D.; Rahim, S. Z. A.; Omar, M. F.; Sandu, A. V.; Vizureanu, P.; Syafwandi. Potential of Soil Stabilization Using Ground Granulated Blast Furnace Slag (GGBFS) and Fly Ash via Geopolymerization Method: A Review. *Materials* **2022**, *15* (1), 375. https://doi.org/10.3390/ma15010375.

(56)Su, Q.; He, Y.; Yang, S.; Wan, H.; Chang, S.; Cui, X. Synthesis of NaA-Zeolite Microspheres by Conversion of Geopolymer and Their Performance of Pb (II) Removal. *Applied Clay Science* **2021**, *200*, 105914. https://doi.org/10.1016/j.clay.2020.105914.
(57)El Alouani, M.; Saufi, H.; Moutaoukil, G.; Alehyen, S.; Nematollahi, B.; Belmaghraoui, W.; Taibi, M. Application of Geopolymers for Treatment of Water Contaminated with Organic and Inorganic Pollutants: State-of-the-Art Review. *Journal of Environmental Chemical Engineering* **2021**, *9* (2), 105095. https://doi.org/10.1016/j.jece.2021.105095.
(58)Aghabeyk, F.; Azadmehr, A.; Hezarkhani, A. Fabrication of Feldspar-Based Geopolymers from Perlite toward Decontamination of Heavy Metals from Aqueous Solution: Hydrolysis Process, Characterizations, Kinetic and Isotherm Studies. *Journal of Environmental Chemical Engineering* **2022**, *10* (4), 108087. https://doi.org/10.1016/j.jece.2022.108087.
(59)Okada, K.; Ooyama, A.; Isobe, T.; Kameshima, Y.; Nakajima, A.; MacKenzie, K. J. D. Water Retention Properties of Porous Geopolymers for Use in Cooling Applications. *Journal of the European Ceramic Society* **2009**, *29* (10), 1917–1923. https://doi.org/10.1016/j.jeurceramsoc.2008.11.006.
(60)Bai, C.; Colombo, P. Processing, Properties and Applications of Highly Porous Geopolymers: A Review. *Ceramics International* **2018**, *44* (14), 16103–16118. https://doi.org/10.1016/j.ceramint.2018.05.219.
(61)Ferone, C.; Roviello, G.; Colangelo, F.; Cioffi, R.; Tarallo, O. Novel Hybrid Organic-Geopolymer Materials. *Applied Clay Science* **2013**, *73*, 42–50. https://doi.org/10.1016/j.clay.2012.11.001.
(62)Mustafa, R.; Shivaprasad, K. N.; Das, B. B. Effect of Various Additives on the Properties of Fly Ash Based Geopolymer Mortar. *Lecture Notes in Civil Engineering* **2019**, *25*, 707–715. https://doi.org/10.1007/978-981-13-3317-0_63.
(63)Prud'homme, E.; Michaud, P.; Rossignol, S.; Joussein, E. Mechanical Properties of Geopolymer Composite Reinforced by Organic or Inorganic Additives. In *Developments in Strategic Materials and Computational Design IV*; John Wiley & Sons, Ltd, 2013; pp 67–78. https://doi.org/10.1002/9781118807743.ch7.
(64)Han, Q.; Zhang, P.; Wu, J.; Jing, Y.; Zhang, D.; Zhang, T. Comprehensive Review of the Properties of Fly Ash-Based Geopolymer with Additive of Nano-SiO2. *Nanotechnology Reviews* **2022**, *11* (1), 1478–1498. https://doi.org/10.1515/ntrev-2022-0092.
(65)Karthik, A.; Sudalaimani, K.; Vijayakumar, C. T. Durability Study on Coal Fly Ash-Blast Furnace Slag Geopolymer Concretes with Bio-Additives. *Ceramics International* **2017**, *43* (15), 11935–11943. https://doi.org/10.1016/j.ceramint.2017.06.042.
(66)John, S. K.; Nadir, Y.; Girija, K. Effect of Source Materials, Additives on the Mechanical Properties and Durability of Fly Ash and Fly Ash-Slag Geopolymer Mortar: A Review. *Construction and Building Materials* **2021**, *280*, 122443. https://doi.org/10.1016/j.conbuildmat.2021.122443.
(67)Sharma, S.; Tahir, A.; Reddy, K. S.; Mallick, T. K. Performance Enhancement of a Building-Integrated Concentrating Photovoltaic System Using Phase Change Material. *Solar Energy Materials and Solar Cells* **2016**, *149*, 29–39. https://doi.org/10.1016/j.solmat.2015.12.035.
(68)Shchukina, E. M.; Graham, M.; Zheng, Z.; Shchukin, D. G. Nanoencapsulation of Phase Change Materials for Advanced Thermal Energy Storage Systems. *Chem. Soc. Rev.* **2018**, *47* (11), 4156–4175. https://doi.org/10.1039/C8CS00099A.
(69)Shadnia, R.; Zhang, L.; Li, P. Experimental Study of Geopolymer Mortar with Incorporated PCM. *Construction and Building Materials* **2015**, *84*, 95–102. https://doi.org/10.1016/j.conbuildmat.2015.03.066.

(70)Hunger, M.; Entrop, A. G.; Mandilaras, I.; Brouwers, H. J. H.; Founti, M. The Behavior of Self-Compacting Concrete Containing Micro-Encapsulated Phase Change Materials. *Cement and Concrete Composites* **2009**, *31* (10), 731–743. https://doi.org/10.1016/j.cemconcomp.2009.08.002.
(71)Haily, E.; Ait Ousaleh, H.; Zari, N.; Faik, A.; Bouhfid, R.; Qaiss, A. Use of a Form-Stable Phase Change Material to Improve Thermal Properties of Phosphate Sludge-Based Geopolymer Mortar. *Construction and Building Materials* **2023**, *386*. https://doi.org/10.1016/j.conbuildmat.2023.131570.
(72)Wang, Z.; Su, H.; Zhao, S.; Zhao, N. Influence of Phase Change Material on Mechanical and Thermal Properties of Clay Geopolymer Mortar. *Construction and Building Materials* **2016**, *120*, 329–334. https://doi.org/10.1016/j.conbuildmat.2016.05.091.
(73)Jankovský, O.; Lojka, M.; Lauermannová, A.-M.; Antončík, F.; Pavlíková, M.; Záleská, M.; Pavlík, Z.; Pivák, A.; Sedmidubský, D. Towards Novel Building Materials: High-Strength Nanocomposites Based on Graphene, Graphite Oxide and Magnesium Oxychloride. *Applied Materials Today* **2020**, *20*, 100766. https://doi.org/10.1016/j.apmt.2020.100766.
(74)Garlisi, C.; Trepci, E.; Li, X.; Al Sakkaf, R.; Al-Ali, K.; Nogueira, R. P.; Zheng, L.; Azar, E.; Palmisano, G. Multilayer Thin Film Structures for Multifunctional Glass: Self-Cleaning, Antireflective and Energy-Saving Properties. *Applied Energy* **2020**, *264*, 114697. https://doi.org/10.1016/j.apenergy.2020.114697.
(75)Yusuf, A.; Al Jitan, S.; Garlisi, C.; Palmisano, G. A Review of Recent and Emerging Antimicrobial Nanomaterials in Wastewater Treatment Applications. *Chemosphere* **2021**, *278*, 130440. https://doi.org/10.1016/j.chemosphere.2021.130440.
(76)Saha, S.; Rajasekaran, C. Enhancement of the Properties of Fly Ash Based Geopolymer Paste by Incorporating Ground Granulated Blast Furnace Slag. *Construction and Building Materials* **2017**, *146*, 615–620. https://doi.org/10.1016/j.conbuildmat.2017.04.139.
(77)Luna-Galiano, Y.; Leiva, C.; Villegas, R.; Arroyo, F.; Vilches, L.; Fernández-Pereira, C. Carbon Fiber Waste Incorporation in Blast Furnace Slag Geopolymer-Composites. *Materials Letters* **2018**, *233*, 1–3. https://doi.org/10.1016/j.matlet.2018.08.099.
(78)Wan, Q.; Rao, F.; Song, S.; León-Patiño, C. A. Geothermal Clay-Based Geopolymer Binders: Synthesis and Microstructural Characterization. *Applied Clay Science* **2017**, *146*, 223–229. https://doi.org/10.1016/j.clay.2017.05.047.
(79)Kishore, K.; Pandey, A.; Wagri, N. K.; Saxena, A.; Patel, J.; Al-Fakih, A. Technological Challenges in Nanoparticle-Modified Geopolymer Concrete: A Comprehensive Review on Nanomaterial Dispersion, Characterization Techniques and Its Mechanical Properties. *Case Studies in Construction Materials* **2023**, *19*, e02265. https://doi.org/10.1016/j.cscm.2023.e02265.
(80)Rambabu, D.; Sharma, S. K.; Akbar, M. A. Properties Exhibited by Nanomaterial Based Geopolymers: A Review. *Journal of Inorganic and Organometallic Polymers and Materials* **2023**, *33* (5), 1081–1118. https://doi.org/10.1007/s10904-023-02601-3.
(81)Suzuki, T. S.; Sakka, Y.; Nakano, K.; Hiraga, K. Effect of Ultrasonication on the Microstructure and Tensile Elongation of Zirconia-Dispersed Alumina Ceramics Prepared by Colloidal Processing. *Journal of the American Ceramic Society* **2001**, *84* (9), 2132–2134. https://doi.org/10.1111/j.1151-2916.2001.tb00973.x.
(82)Du, H.; Pang, S. D. Dispersion and Stability of Graphene Nanoplatelet in Water and Its Influence on Cement Composites. *Construction and Building Materials* **2018**, *167*, 403–413. https://doi.org/10.1016/j.conbuildmat.2018.02.046.

(83)Wei, J.; Meyer, C. Sisal Fiber-Reinforced Cement Composite with Portland Cement Substitution by a Combination of Metakaolin and Nanoclay. *J Mater Sci* **2014**, *49* (21), 7604–7619. https://doi.org/10.1007/s10853-014-8469-8.
(84)Hassaan, M. M.; Khater, H. M.; El-Mahllawy, M. S.; El Nagar, A. M. Production of Geopolymer Composites Enhanced by Nano-Kaolin Material. *J Adv Ceram* **2015**, *4* (4), 245–252. https://doi.org/10.1007/s40145-015-0156-y.
(85)Hakamy, A.; Shaikh, F. U. A.; Low, I. M. Characteristics of Nanoclay and Calcined Nanoclay-Cement Nanocomposites. *Composites Part B: Engineering* **2015**, *78*, 174–184. https://doi.org/10.1016/j.compositesb.2015.03.074.
(86)Farzadnia, N.; Abang Ali, A. A.; Demirboga, R.; Anwar, M. P. Effect of Halloysite Nanoclay on Mechanical Properties, Thermal Behavior and Microstructure of Cement Mortars. *Cement and Concrete Research* **2013**, *48*, 97–104. https://doi.org/10.1016/j.cemconres.2013.03.005.
(87)Kadhim, A.; Sadique, M.; Al-Mufti, R.; Hashim, K. Long-Term Performance of Novel High-Calcium One-Part Alkali-Activated Cement Developed from Thermally Activated Lime Kiln Dust. *Journal of Building Engineering* **2020**, *32*. https://doi.org/10.1016/j.jobe.2020.101766.
(88)Dietel, J.; Warr, L. N.; Bertmer, M.; Steudel, A.; Grathoff, G. H.; Emmerich, K. The Importance of Specific Surface Area in the Geopolymerization of Heated Illitic Clay. *Applied Clay Science* **2017**, *139*, 99–107. https://doi.org/10.1016/j.clay.2017.01.001.
(89)Hu, N.; Bernsmeier, D.; Grathoff, G. H.; Warr, L. N. The Influence of Alkali Activator Type, Curing Temperature and Gibbsite on the Geopolymerization of an Interstratified Illite-Smectite Rich Clay from Friedland. *Applied Clay Science* **2017**, *135*, 386–393. https://doi.org/10.1016/j.clay.2016.10.021.
(90)Marsh, A.; Heath, A.; Patureau, P.; Evernden, M.; Walker, P. Phase Formation Behaviour in Alkali Activation of Clay Mixtures. *Applied Clay Science* **2019**, *175*, 10–21. https://doi.org/10.1016/j.clay.2019.03.037.
(91)Zhang, Z.; Wang, H.; Yao, X.; Zhu, Y. Effects of Halloysite in Kaolin on the Formation and Properties of Geopolymers. *Cement and Concrete Composites* **2012**, *34* (5), 709–715. https://doi.org/10.1016/j.cemconcomp.2012.02.003.
(92)Zhang, B.; Guo, H.; Yuan, P.; Li, Y.; Wang, Q.; Deng, L.; Liu, D. Geopolymerization of Halloysite via Alkali-Activation: Dependence of Microstructures on Precalcination. *Applied Clay Science* **2020**, *185*, 105375. https://doi.org/10.1016/j.clay.2019.105375.
(93)Razzaghian Ghadikolaee, M.; Habibnejad Korayem, A.; Sharif, A.; Ming Liu, Y. The Halloysite Nanotube Effects on Workability, Mechanical Properties, Permeability and Microstructure of Cementitious Mortar. *Construction and Building Materials* **2021**, *267*, 120873. https://doi.org/10.1016/j.conbuildmat.2020.120873.
(94)Zhang, B.; Guo, H.; Yuan, P.; Deng, L.; Zhong, X.; Li, Y.; Wang, Q.; Liu, D. Novel Acid-Based Geopolymer Synthesized from Nanosized Tubular Halloysite: The Role of Precalcination Temperature and Phosphoric Acid Concentration. *Cement and Concrete Composites* **2020**, *110*, 103601. https://doi.org/10.1016/j.cemconcomp.2020.103601.
(95)Kaze, C. R.; Alomayri, T.; Hasan, A.; Tome, S.; Lecomte-Nana, G. L.; Nemaleu, J. G. D.; Tchakoute, H. K.; Kamseu, E.; Melo, U. C.; Rahier, H. Reaction Kinetics and Rheological Behaviour of Meta-Halloysite Based Geopolymer Cured at Room Temperature: Effect of Thermal Activation on Physicochemical and Microstructural Properties. *Applied Clay Science* **2020**, *196*, 105773. https://doi.org/10.1016/j.clay.2020.105773.
(96)Duan, P.; Yan, C.; Zhou, W. Compressive Strength and Microstructure of Fly Ash Based Geopolymer Blended with Silica Fume under Thermal Cycle. *Cement and Concrete Composites* **2017**, *78*, 108–119. https://doi.org/10.1016/j.cemconcomp.2017.01.009.

(97)Wan, Q.; Rao, F.; Song, S.; García, R. E.; Estrella, R. M.; Patiño, C. L.; Zhang, Y. Geopolymerization Reaction, Microstructure and Simulation of Metakaolin-Based Geopolymers at Extended Si/Al Ratios. *Cement and Concrete Composites* **2017**, *79*, 45–52. https://doi.org/10.1016/j.cemconcomp.2017.01.014.
(98)Kaze, C. R.; Jiofack, S. B. K.; Cengiz, Ö.; Alomayri, T. S.; Adesina, A.; Rahier, H. Reactivity and Mechanical Performance of Geopolymer Binders from Metakaolin/Meta-Halloysite Blends. *Construction and Building Materials* **2022**, *336*, 127546. https://doi.org/10.1016/j.conbuildmat.2022.127546.
(99)Zhang, B.; Yuan, P.; Guo, H.; Deng, L.; Li, Y.; Li, L.; Wang, Q.; Liu, D. Effect of Curing Conditions on the Microstructure and Mechanical Performance of Geopolymers Derived from Nanosized Tubular Halloysite. *Construction and Building Materials* **2021**, *268*. https://doi.org/10.1016/j.conbuildmat.2020.121186.
(100) Bergaya, F.; Lagaly, G. Chapter 7.1 - Purification of Natural Clays. In *Developments in Clay Science*; Bergaya, F., Lagaly, G., Eds.; Handbook of Clay Science; Elsevier, 2013; Vol. 5, pp 213–221. https://doi.org/10.1016/B978-0-08-098258-8.00008-0.
(101) Cavallaro, G.; Lazzara, G.; Milioto, S.; Palmisano, G.; Parisi, F. Halloysite Nanotube with Fluorinated Lumen: Non-Foaming Nanocontainer for Storage and Controlled Release of Oxygen in Aqueous Media. *Journal of Colloid and Interface Science* **2014**, *417*, 66–71. https://doi.org/10.1016/j.jcis.2013.11.026.
(102) Benítez, E. I.; Genovese, D. B.; Lozano, J. E. Effect of Typical Sugars on the Viscosity and Colloidal Stability of Apple Juice. *Food Hydrocolloids* **2009**, *23* (2), 519–525. https://doi.org/10.1016/j.foodhyd.2008.03.005.
(103) Lisuzzo, L.; Cavallaro, G.; Milioto, S.; Lazzara, G. Halloysite Nanotubes Filled with MgO for Paper Reinforcement and Deacidification. *Applied Clay Science* **2021**, *213*. https://doi.org/10.1016/j.clay.2021.106231.
(104) Cionti, C.; Taroni, T.; Sabatini, V.; Meroni, D. Nanostructured Oxide-Based Systems for the pH-Triggered Release of Cinnamaldehyde. *Materials* **2021**, *14* (6), 1536. https://doi.org/10.3390/ma14061536.
(105) Duce, C.; Vecchio Ciprioti, S.; Ghezzi, L.; Ierardi, V.; Tinè, M. R. Thermal Behavior Study of Pristine and Modified Halloysite Nanotubes: A Modern Kinetic Study. *Journal of Thermal Analysis and Calorimetry* **2015**, *121* (3), 1011–1019. https://doi.org/10.1007/s10973-015-4741-7.
(106) Cavallaro, G.; Lazzara, G.; Milioto, S. Exploiting the Colloidal Stability and Solubilization Ability of Clay Nanotubes/Ionic Surfactant Hybrid Nanomaterials. *J. Phys. Chem. C* **2012**, *116* (41), 21932–21938. https://doi.org/10.1021/jp307961q.
(107) Wojdyr, M. Fityk: A General-Purpose Peak Fitting Program. *J Appl Cryst* **2010**, *43* (5), 1126–1128. https://doi.org/10.1107/S0021889810030499.
(108) Joussein, E.; Petit, S.; Fialips, C.-I.; Vieillard, P.; Righi, D. Differences in the Dehydration-Rehydration Behavior of Halloysites: New Evidence and Interpretations. *Clays Clay Miner.* **2006**, *54* (4), 473–484. https://doi.org/10.1346/CCMN.2006.0540408.
(109) Lisuzzo, L.; Cavallaro, G.; Pasbakhsh, P.; Milioto, S.; Lazzara, G. Why Does Vacuum Drive to the Loading of Halloysite Nanotubes? The Key Role of Water Confinement. *Journal of Colloid and Interface Science* **2019**, *547*, 361–369. https://doi.org/10.1016/j.jcis.2019.04.012.
(110) Pham, Q. D.; Mojumdar, E. H.; Gooris, G. S.; Bouwstra, J. A.; Sparr, E.; Topgaard, D. Solid and Fluid Segments within the Same Molecule of Stratum Corneum Ceramide Lipid. *Quart. Rev. Biophys.* **2018**, *51*, e7. https://doi.org/10.1017/S0033583518000069.

(111) Stejskal, E. O.; Tanner, J. E. Spin Diffusion Measurements: Spin Echoes in the Presence of a Time-Dependent Field Gradient. *The Journal of Chemical Physics* **1965**, *42* (1), 288–292. https://doi.org/10.1063/1.1695690.
(112) Kowalczuk, J.; Rachocki, A.; Broda, M.; Mazela, B.; Ormondroyd, G. A.; Tritt-Goc, J. Conservation Process of Archaeological Waterlogged Wood Studied by Spectroscopy and Gradient NMR Methods. *Wood Sci Technol* **2019**, *53* (6), 1207–1222. https://doi.org/10.1007/s00226-019-01129-5.
(113) Fardis, M.; Karagianni, M.; Gkoura, L.; Papavassiliou, G. Self-Diffusion in Confined Water: A Comparison between the Dynamics of Supercooled Water in Hydrophobic Carbon Nanotubes and Hydrophilic Porous Silica. *International Journal of Molecular Sciences* **2022**, *23* (22), 14432. https://doi.org/10.3390/ijms232214432.
(114) Cavallaro, G.; Chiappisi, L.; Pasbakhsh, P.; Gradzielski, M.; Lazzara, G. A Structural Comparison of Halloysite Nanotubes of Different Origin by Small-Angle Neutron Scattering (SANS) and Electric Birefringence. *Applied Clay Science* **2018**, *160*, 71–80. https://doi.org/10.1016/j.clay.2017.12.044.
(115) Makaremi, M.; Pasbakhsh, P.; Cavallaro, G.; Lazzara, G.; Aw, Y. K.; Lee, S. M.; Milioto, S. Effect of Morphology and Size of Halloysite Nanotubes on Functional Pectin Bionanocomposites for Food Packaging Applications. *ACS Appl. Mater. Interfaces* **2017**, *9* (20), 17476–17488. https://doi.org/10.1021/acsami.7b04297.
(116) Luo, Z.; Song, H.; Feng, X.; Run, M.; Cui, H.; Wu, L.; Gao, J.; Wang, Z. Liquid Crystalline Phase Behavior and Sol–Gel Transition in Aqueous Halloysite Nanotube Dispersions. *Langmuir* **2013**, *29* (40), 12358–12366. https://doi.org/10.1021/la402836d.
(117) Churchman, G. J.; Pasbakhsh, P.; Lowe, D. J.; Theng, B. K. G. Unique but Diverse: Some Observations on the Formation, Structure and Morphology of Halloysite. *Clay Minerals* **2016**, *51* (3), 395–416. https://doi.org/10.1180/claymin.2016.051.3.14.
(118) Pramanik, A.; Sciortino, A.; Reale, M.; Pasbakhsh, P.; Cavallaro, G.; Cannas, M.; Lazzara, G.; Messina, F. Naturally Occurring Halloysite Nanotubes as Light Scatterers for Stable Random Lasing Applications. *ACS Appl. Nano Mater.* **2023**, *6* (17), 15896–15905. https://doi.org/10.1021/acsanm.3c02840.
(119) Anvari, M.; Tabarsa, M.; Cao, R.; You, S.; Joyner Melito, H. S.; Behnam, S.; Rezaei, M. Compositional Characterization and Rheological Properties of an Anionic Gum from Alyssum Homolocarpum Seeds. *Food Hydrocolloids* **2016**, *52*, 766–773. https://doi.org/10.1016/j.foodhyd.2015.07.030.
(120) Tavares, L. S.; Junqueira, L. A.; de Oliveira Guimarães, Í. C.; de Resende, J. V. Cold Extraction Method of Chia Seed Mucilage (Salvia Hispanica L.): Effect on Yield and Rheological Behavior. *Journal of Food Science and Technology* **2018**, *55* (2), 457–466. https://doi.org/10.1007/s13197-017-2954-4.
(121) Dávila, J. L.; d'Ávila, M. A. Laponite as a Rheology Modifier of Alginate Solutions: Physical Gelation and Aging Evolution. *Carbohydrate Polymers* **2017**, *157*, 1–8. https://doi.org/10.1016/j.carbpol.2016.09.057.
(122) Lawrence, P. G.; Lapitsky, Y. Ionically Cross-Linked Poly(Allylamine) as a Stimulus-Responsive Underwater Adhesive: Ionic Strength and pH Effects. *Langmuir* **2015**, *31* (4), 1564–1574. https://doi.org/10.1021/la504611x.
(123) Cunningham, G. E.; Alberini, F.; Simmons, M. J. H.; O'Sullivan, J. J. Understanding the Effects of Processing Conditions on the Formation of Lamellar Gel Networks Using a Rheological Approach. *Chemical Engineering Science* **2021**, *242*. https://doi.org/10.1016/j.ces.2021.116752.
(124) Lazzara, G.; Cavallaro, G.; Panchal, A.; Fakhrullin, R.; Stavitskaya, A.; Vinokurov, V.; Lvov, Y. An Assembly of Organic-Inorganic Composites Using Halloysite Clay

Nanotubes. *Current Opinion in Colloid & Interface Science* **2018**, *35*, 42–50. https://doi.org/10.1016/j.cocis.2018.01.002.
(125) Domenech, T.; Velankar, S. S. On the Rheology of Pendular Gels and Morphological Developments in Paste-like Ternary Systems Based on Capillary Attraction. *Soft Matter* **2015**, *11* (8), 1500–1516. https://doi.org/10.1039/c4sm02053g.
(126) Valencia, G. A.; Moraes, I. C. F.; Hilliou, L. H. G.; Lourenço, R. V.; Sobral, P. J. D. A. Nanocomposite-Forming Solutions Based on Cassava Starch and Laponite: Viscoelastic and Rheological Characterization. *Journal of Food Engineering* **2015**, *166*, 174–181. https://doi.org/10.1016/j.jfoodeng.2015.06.006.
(127) Appel, E. A.; Tibbitt, M. W.; Webber, M. J.; Mattix, B. A.; Veiseh, O.; Langer, R. Self-Assembled Hydrogels Utilizing Polymer-Nanoparticle Interactions. *Nature Communications* **2015**, *6*. https://doi.org/10.1038/ncomms7295.
(128) Zhang, Y.; Gao, W.; Chen, Y.; Escajadillo, T.; Ungerleider, J.; Fang, R. H.; Christman, K.; Nizet, V.; Zhang, L. Self-Assembled Colloidal Gel Using Cell Membrane-Coated Nanosponges as Building Blocks. *ACS Nano* **2017**, *11* (12), 11923–11930. https://doi.org/10.1021/acsnano.7b06968.
(129) Calvino, M. M.; Cavallaro, G.; Lisuzzo, L.; Milioto, S.; Lazzara, G. Separation of Halloysite/Kaolinite Mixtures in Water Controlled by Sucrose Addition: The Influence of the Attractive Forces on the Sedimentation Behavior. *Colloids and Surfaces A: Physicochemical and Engineering Aspects* **2022**, *641*, 128530. https://doi.org/10.1016/j.colsurfa.2022.128530.
(130) Wang, Y.-R.; Yang, Q.; Li-Sha, Y.-J.; Chen, H.-Q. Structural, Gelation Properties and Microstructure of Rice Glutelin/Sugar Beet Pectin Composite Gels: Effects of Ionic Strengths. *Food Chemistry* **2021**, *346*. https://doi.org/10.1016/j.foodchem.2020.128956.
(131) Drozdov, A. D.; Christiansen, J. D. The Effects of pH and Ionic Strength on the Volume Phase Transition Temperature of Thermo-Responsive Anionic Copolymer Gels. *Polymer* **2021**, *221*. https://doi.org/10.1016/j.polymer.2021.123637.
(132) Wu, H.; Xie, J.; Lattuada, M.; Kohlbrecher, J.; Morbidelli, M. Effect of Primary Particle Size and Salt Concentration on the Structure of Colloidal Gels. *Journal of Physical Chemistry C* **2011**, *115* (4), 931–936. https://doi.org/10.1021/jp103100k.
(133) Russo, J.; Fiegel, J.; Brogden, N. K. Effect of Salt Form on Gelation and Drug Delivery Properties of Diclofenac-Loaded Poloxamer Gels for Delivery to Impaired Skin. *Pharmaceutical Research* **2022**, *39* (10), 2515–2527. https://doi.org/10.1007/s11095-022-03356-1.
(134) Fernández-Nieves, A.; Fernández-Barbero, A.; De las Nieves, F. J. Salt Effects over the Swelling of Ionized Mesoscopic Gels. *Journal of Chemical Physics* **2001**, *115* (16), 7644–7649. https://doi.org/10.1063/1.1403002.
(135) Tu, Y.; Zhang, X.; Wang, L. Effect of Salt Treatment on the Stabilization of Pickering Emulsions Prepared with Rice Bran Protein. *Food Research International* **2023**, *166*. https://doi.org/10.1016/j.foodres.2023.112537.
(136) Li, J.; Zhang, W.; Tang, T.; Gu, L.; Su, Y.; Yang, Y.; Chang, C.; Han, Q. Thermal Gelation and Digestion Properties of Hen Egg White: Study on the Effect of Neutral and Alkaline Salts Addition. *Food Chemistry* **2023**, *409*, 135263. https://doi.org/10.1016/j.foodchem.2022.135263.
(137) Shafiei-Sabet, S.; Hamad, W. Y.; Hatzikiriakos, S. G. Ionic Strength Effects on the Microstructure and Shear Rheology of Cellulose Nanocrystal Suspensions. *Cellulose* **2014**, *21* (5), 3347–3359. https://doi.org/10.1007/s10570-014-0407-z.
(138) Sun, Z.; Zhang, Y.; Zheng, S.; Park, Y.; Frost, R. L. Preparation and Thermal Energy Storage Properties of Paraffin/Calcined Diatomite Composites as Form-Stable Phase

Change Materials. *Thermochimica Acta* **2013**, *558*, 16–21. https://doi.org/10.1016/j.tca.2013.02.005.
(139) Zhao, Y.; Thapa, S.; Weiss, L.; Lvov, Y. Phase Change Heat Insulation Based on Wax-Clay Nanotube Composites. *Advanced Engineering Materials* **2014**, *16* (11), 1391–1399. https://doi.org/10.1002/adem.201400094.
(140) Zhang, J.; Zhang, X.; Wan, Y.; Mei, D.; Zhang, B. Preparation and Thermal Energy Properties of Paraffin/Halloysite Nanotube Composite as Form-Stable Phase Change Material. *Solar Energy* **2012**, *86* (5), 1142–1148. https://doi.org/10.1016/j.solener.2012.01.002.
(141) Catauro, M. Thermal and Microbiological Performance of Metakaolin-Based Geopolymers Cement with Waste Glass. *Applied Clay Science* **2020**, 9.
(142) Hajimohammadi, A.; Provis, J. L.; van Deventer, J. S. J. Time-Resolved and Spatially-Resolved Infrared Spectroscopic Observation of Seeded Nucleation Controlling Geopolymer Gel Formation. *Journal of Colloid and Interface Science* **2011**, *357* (2), 384–392. https://doi.org/10.1016/j.jcis.2011.02.045.
(143) El-Naggar, M. R.; El-Dessouky, M. I. Re-Use of Waste Glass in Improving Properties of Metakaolin-Based Geopolymers: Mechanical and Microstructure Examinations. *Construction and Building Materials* **2017**, *132*, 543–555. https://doi.org/10.1016/j.conbuildmat.2016.12.023.
(144) Fernández-Jiménez, A.; Palomo, A.; Pastor, J. Y.; Martín, A. New Cementitious Materials Based on Alkali-Activated Fly Ash: Performance at High Temperatures. *Journal of the American Ceramic Society* **2008**, *91* (10), 3308–3314. https://doi.org/10.1111/j.1551-2916.2008.02625.x.
(145) Tanner, N.; Lichtenberg-Kraag, B. Identification and Quantification of Single and Multi-Adulteration of Beeswax by FTIR-ATR Spectroscopy. *Eur. J. Lipid Sci. Technol.* **2019**, *121* (12), 1900245. https://doi.org/10.1002/ejlt.201900245.
(146) Greiser, S.; Sturm, P.; Gluth, G. J. G.; Hunger, M.; Jäger, C. Differentiation of the Solid-State NMR Signals of Gel, Zeolite Phases and Water Species in Geopolymer-Zeolite Composites. *Ceramics International* **2017**, *43* (2), 2202–2208. https://doi.org/10.1016/j.ceramint.2016.11.004.
(147) Kaze, C. R.; Nana, A.; Lecomte-Nana, G. L.; Deutou, J. G. N.; Kamseu, E.; Melo, U. C.; Andreola, F.; Leonelli, C. Thermal Behaviour and Microstructural Evolution of Metakaolin and Meta-Halloysite-Based Geopolymer Binders: A Comparative Study. *J Therm Anal Calorim* **2022**, *147* (3), 2055–2071. https://doi.org/10.1007/s10973-021-10555-2.
(148) Khalifa, A. Z.; Cizer, Ö.; Pontikes, Y.; Heath, A.; Patureau, P.; Bernal, S. A.; Marsh, A. T. M. Advances in Alkali-Activation of Clay Minerals. *Cement and Concrete Research* **2020**, *132*, 106050. https://doi.org/10.1016/j.cemconres.2020.106050.
(149) Bucio, A.; Moreno-Tovar, R.; Bucio, L.; Espinosa-Dávila, J.; Anguebes-Franceschi, F. Characterization of Beeswax, Candelilla Wax and Paraffin Wax for Coating Cheeses. *Coatings* **2021**, *11* (3), 261. https://doi.org/10.3390/coatings11030261.
(150) Naderizadeh, S.; Heredia-Guerrero, J. A.; Caputo, G.; Grasselli, S.; Malchiodi, A.; Athanassiou, A.; Bayer, I. S. Superhydrophobic Coatings from Beeswax-in-Water Emulsions with Latent Heat Storage Capability. *Advanced Materials Interfaces* **2019**, *6* (5), 1801782. https://doi.org/10.1002/admi.201801782.
(151) Gaillard, Y.; Mija, A.; Burr, A.; Darque-Ceretti, E.; Felder, E.; Sbirrazzuoli, N. Green Material Composites from Renewable Resources: Polymorphic Transitions and Phase Diagram of Beeswax/Rosin Resin. *Thermochimica Acta* **2011**, *521* (1), 90–97. https://doi.org/10.1016/j.tca.2011.04.010.

(152) Cataldo, V. A.; Cavallaro, G.; Lazzara, G.; Milioto, S.; Parisi, F. Coffee Grounds as Filler for Pectin: Green Composites with Competitive Performances Dependent on the UV Irradiation. *Carbohydrate Polymers* **2017**, *170*, 198–205. https://doi.org/10.1016/j.carbpol.2017.04.092.
(153) Humar, M.; Kržišnik, D.; Lesar, B.; Thaler, N.; Ugovšek, A.; Zupančič, K.; Žlahtič, M. Thermal Modification of Wax-Impregnated Wood to Enhance Its Physical, Mechanical, and Biological Properties. *Holzforschung* **2017**, *71* (1), 57–64. https://doi.org/10.1515/hf-2016-0063.
(154) Samieadel, A.; Høgsaa, B.; Fini, E. H. Examining the Implications of Wax-Based Additives on the Sustainability of Construction Practices: Multiscale Characterization of Wax-Doped Aged Asphalt Binder. *ACS Sustainable Chem. Eng.* **2019**, *7* (3), 2943–2954. https://doi.org/10.1021/acssuschemeng.8b03842.
(155) Al-Gunaid, T.; Sobolčiak, P.; Chriaa, I.; Karkri, M.; Mrlik, M.; Ilčíková, M.; Sedláček, T.; Popelka, A.; Krupa, I. Phase Change Materials Designed from Tetra Pak Waste and Paraffin Wax as Unique Thermal Energy Storage Systems. *Journal of Energy Storage* **2023**, *64*, 107173. https://doi.org/10.1016/j.est.2023.107173.
(156) Wolf, C.; Angellier-Coussy, H.; Gontard, N.; Doghieri, F.; Guillard, V. How the Shape of Fillers Affects the Barrier Properties of Polymer/Non-Porous Particles Nanocomposites: A Review. *Journal of Membrane Science* **2018**, *556*, 393–418. https://doi.org/10.1016/j.memsci.2018.03.085.
(157) Lisuzzo, L.; Caruso, M. R.; Cavallaro, G.; Milioto, S.; Lazzara, G. Hydroxypropyl Cellulose Films Filled with Halloysite Nanotubes/Wax Hybrid Microspheres. *Ind. Eng. Chem. Res.* **2021**, *60* (4), 1656–1665. https://doi.org/10.1021/acs.iecr.0c05148.
(158) Aredes, F. G. M.; Campos, T. M. B.; Machado, J. P. B.; Sakane, K. K.; Thim, G. P.; Brunelli, D. D. Effect of Cure Temperature on the Formation of Metakaolinite-Based Geopolymer. *Ceramics International* **2015**, *41* (6), 7302–7311. https://doi.org/10.1016/j.ceramint.2015.02.022.
(159) Sornlar, W.; Wannagon, A.; Supothina, S. Stabilized Homogeneous Porous Structure and Pore Type Effects on the Properties of Lightweight Kaolinite-Based Geopolymers. *Journal of Building Engineering* **2021**, *44*, 103273. https://doi.org/10.1016/j.jobe.2021.103273.
(160) Temuujin, J.; Minjigmaa, A.; Rickard, W.; Lee, M.; Williams, I.; van Riessen, A. Fly Ash Based Geopolymer Thin Coatings on Metal Substrates and Its Thermal Evaluation. *Journal of Hazardous Materials* **2010**, *180* (1), 748–752. https://doi.org/10.1016/j.jhazmat.2010.04.121.
(161) Zhao, Y.; Kong, W.; Jin, Z.; Fu, Y.; Wang, W.; Zhang, Y.; Liu, J.; Zhang, B. Storing Solar Energy within Ag-Paraffin@Halloysite Microspheres as a Novel Self-Heating Catalyst. *Applied Energy* **2018**, *222*, 180–188. https://doi.org/10.1016/j.apenergy.2018.04.013.
(162) Lisuzzo, L.; Cavallaro, G.; Milioto, S.; Lazzara, G. Pickering Emulsions Stabilized by Halloysite Nanotubes: From General Aspects to Technological Applications. *Advanced Materials Interfaces* **2022**, 2102346–2102375. https://doi.org/10.1002/admi.202102346.

10. Attached Manuscripts

Colloids and Surfaces A: Physicochemical and Engineering Aspects 641 (2022) 128530

Contents lists available at ScienceDirect

Colloids and Surfaces A: Physicochemical and Engineering Aspects

journal homepage: www.elsevier.com/locate/colsurfa

Separation of halloysite/kaolinite mixtures in water controlled by sucrose addition: The influence of the attractive forces on the sedimentation behavior

Martina Maria Calvino, Giuseppe Cavallaro *, Lorenzo Lisuzzo, Stefana Milioto, Giuseppe Lazzara

Dipartimento di Fisica e Chimica, Università degli Studi di Palermo, Viale delle Scienze, Pad. 17, 90128 Palermo, Italy

HIGHLIGHT

- The colloidal stability of halloysite and kaolinite can be controlled by sucrose.
- The colloidal properties of both nanoclays are influenced by the sucrose concentration.
- The screening of the attractive forces affect the sedimentation kinetics of clays.
- The presence of 10 wt% sucrose favors the halloysite/kaolinite separation in water.

GRAPHICAL ABSTRACT

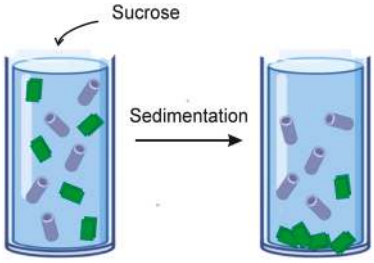

ARTICLE INFO

Keywords:
Halloysite nanotubes
Nanoclays
Aqueous colloidal stability
Separation
TGA

ABSTRACT

In this work, we propose an easy strategy for the separation of halloysite/kaolinite mixtures in sucrose aqueous solution. Preliminarily, we investigated the influence of the sucrose addition on the colloidal stability of kaolinite nanoplates and halloysite nanotubes (HNTs) dispersed in water. Dynamic Light Scattering (DLS) measurements revealed that the HNTs aqueous mobility is dependent on the sucrose concentration, while the ζ-potential is negligibly affected by the addition of the carbohydrate in the aqueous solvent. On the other hand, any variations on the surface charge and dynamic behavior of kaolinite were detected in the presence of sucrose. The obtained ζ-potential and DLS results were useful to interpret the sedimentation kinetics of kaolinite and halloysite dispersions. In particular, the peculiar sedimentation behavior of halloysite were discussed by considering the screening effect of sucrose on the attractive interactions between the nanotubes. The latter was evaluated by the calculation of the corresponding Hamaker constants. On this basis, we estimated that the optimization of the separation between kaolinite and halloysite might be achieved in 10 wt% sucrose aqueous solution. This hypothesis was confirmed by the separation experiments, which exploited the different sedimentation behavior of halloysite and kaolinite. Thermogravimetric experiments on the separated material and kaolinite/halloysite composites with variable composition allowed us to determine the efficiency of the separation protocol. To this purpose, the differential thermogravimetric curves were accurately analysed by using split Gaussian functions. In conclusion, this paper represents a further step in the purification of natural halloysite samples exploiting the ability of sucrose to control the attractive forces of the clay nanotubes as well as the colloidal stability of kaolinite nanoplates in aqueous solvent.

* Corresponding author.
E-mail address: giuseppe.cavallaro@unipa.it (G. Cavallaro).

https://doi.org/10.1016/j.colsurfa.2022.128530
Received 21 December 2021; Received in revised form 17 January 2022; Accepted 4 February 2022
Available online 7 February 2022

1. Introduction

Nowadays, nanoclays are receiving the attention of researchers in several fields, including material sciences [1–3], engineering [4–6] and biology [7–10] due to their physico-chemical properties, environmental-friendly nature and low cost [11].

Among the clay nanoparticles, halloysite nanotubes (HNTs) have attracted particular interest. They are aluminosilicates characterized by a chemical formula of $Al_2Si_2O_5(OH)_4 \cdot nH_2O$ and a hollow tubular structure with a spiral conformation [12]. Halloysite is formed by rolling-up a kaolin double layer yielding a tubular structure. Their sizes depend on the geological deposit. Averagely, the tubes' length range within 0.5–1.5 μm and the outer diameter is between 50 and 100 nm, whereas for internal diameter of the cavity is from 10 to 20 nm.

The external surface is composed of Si-O-Si groups and the internal lumen surface of Al-OH. In light of this and considering the charges of alumina and silica substrates, it is observed a charge separation in the pH range between 2 and 8 [13], in particular the inner lumen carries a positive charge, while the outer surface is negatively charged [14]. Inner and outer surfaces can be selectively modified by exploiting covalent and supramolecular interactions [15–18]. Accordingly, halloysite nanotubes have been developed as carriers for controlled release of active agents [19–32], as fillers for polymers [33–39] and for decontamination purposes [40–45]. Due to its high specific surface, halloysite was used as catalytic support for technological applications [46–54]. Recently, halloysite was successfully employed for the protective coating of hair [55,56]. The chemical composition of halloysite is similar to that of kaolinite except for the presence of water molecules between the unit layers. Similarly to halloysite, kaolinite has been exploited in many fields as inorganic support with adsorption application [57,58] or as precursor in geopolymeric materials [59,60].

Typically, halloysite samples are contaminated by a certain amount (ca. 10 wt%) of platy kaolinite nanoparticles depending on the deposit [61]. This aspect might be relevant for some applications where the high purity of halloysite is requested. As example, the presence of kaolinite nanoplates can reduce the efficiency of HNT as nanocarriers for pharmaceutical and biomedical applications. To the light of this consideration, the development of separation protocols for halloysite samples represents a challenging task for their applications in pharmaceutics and biomedicine.

According to literature, the sedimentation behavior of nanoparticles in a colloidal systems depends on several factors, including the specific interactions as well as the viscosity and the ionic strength of the solvent [62–64] that can induce aggregation decreasing the colloidal stability. The separation of kaolinite nanoplates can be favored by adding inorganic flocculants [65], such as aluminium and iron salts or other greener flocculants [66]. Moreover, the addition of polymers can influence the sedimentation kinetics of kaolinite dispersed in water [67].

In this work, we investigated the effects of sucrose addition on the colloidal stability of halloysite and kaolinite in aqueous media. Specifically, the screening effect of sucrose towards the attractive interactions between the clay nanotubes was studied according to the DLVO theory. In this regard, it should be noted that the addition of variable amounts of monosaccharides (glucose) or disaccharides (sucrose and maltose) represents an efficient strategy to control the stability of aqueous dispersions because of their influence on the physico-chemical properties (dielectric constant, refractive index and viscosity) of water [68]. The effects of sugars on the attractions between dispersed nanoparticles can be evaluated according to the Hamaker constant. On the other hand, the addition of non ionic macromolecules (such as polymers and surfactants) can be affect the aqueous colloidal stability of nanoclays due to steric interactions and depletion processes as reported for kaolinite dispersions containing variable amounts of biopolymer [67].

In conclusion, the influence of sucrose concentration on the sedimentation kinetics of both nanoclays was investigated in order to maximize the separation efficiency in halloysite/kaolinite aqueous mixtures. The obtained results can be useful to develop purification protocols for natural halloysites.

2. Materials and methods

2.1. Materials

Halloysite nanotubes (HNTs) were provided by Imerys Ceramics. They are from Matauri Bay (New Zealand). The HNTs possess a specific surface area of 28.6 $m^2\ g^{-1}$ [61]. Their length range between 100 and 3000 nm, while the intervals for the inner and outer diameters are 15–70 and 50–200 nm, respectively [33]. Compared to halloysite obtained from Dragon Mine [61], the employed HNTs do not contain impurities of kaolinite. SEM image of HNTs from Matauri Bay are presented in Fig. 1. Kaolinite (Kao) and sucrose (purity $\geq$ 99.5%) are Sigma Aldrich products. Water from reverse osmosis (Elga model Option 3) with a specific resistivity greater than 1 MΩ cm was used.

2.2. Preparation of dispersions

As concerns sedimentation experiments, halloysite nanotubes and kaolinite (concentration of 2 wt%) were separately added to 5 mL of sucrose solutions with variable concentration ranging from 1 to 35 wt%.

The obtained dispersions were sonicated for 15 min, magnetically stirred for 2 h and equilibrated for 2 h to monitor the colloidal stability of the nanoparticles.

Dynamic Light Scattering (DLS) and ζ-potential tests were conducted on HNTs or kaolinite dispersed in sucrose solutions at variable concentration. The dispersions were prepared by 15 min of sonication followed by 2 h of magnetically stirring.

2.3. Separation of halloysite/kaolinite mixtures

Separation experiments of halloysite/kaolinite mixtures were conducted as reported below. Firstly, we prepared halloysite/kaolinite mixtures with a 1:1 mass ratio in 10 wt% sucrose aqueous solution. The concentration of both nanoclays was fixed at 2 wt%. The dispersion was sonicated for 15 min, magnetically stirred for 2 h and equilibrated for 30 min, which does not guarantee the complete sedimentation of the nanoparticles. Then, we removed the upper part of the dispersion corresponding to 30% of the total volume. Then, the recovered suspension

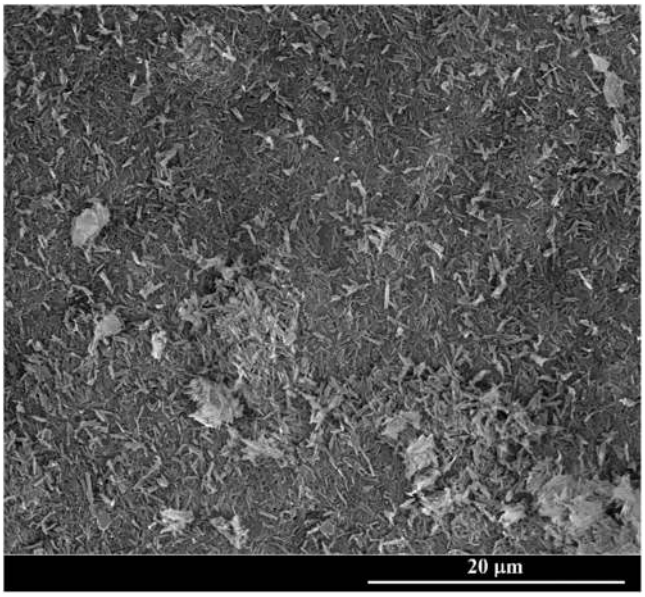

Fig. 1. SEM image of halloysite nanotubes.

was dried at 50 °C. Finally, the dried powder was washed five times with water to remove sucrose and then, stored in a desiccator at 25 °C and relative humidity of 75%. For comparison, the separation experiment was conducted using water as solvent.

2.4. Methods

The refractive indexes (RI) of the sucrose solutions were determined through an automatic refractometer (Model GPR 11-37, Index Instruments). Sample amounts were directly placed into the instrument cell where they were left to equilibrate. All measurements were performed at 25.0 ± 0.1 °C.

The viscosity experiments were carried out by using an Ubbelohde viscosimeter, which was aligned perpendicularly in a plexiglass box with circulating water (thermostatted with a Haake D8 apparatus). The absolute viscosity (η) of the sucrose solutions were estimated at 25.0 ± 0.1 °C.

The dielectric constant of sucrose solutions was determined by means of a Hewlett-Packard impedance analyzer (HP 4294 A) equipped with HP 16451B dielectric test fixtures. The experiments were conducted at 25 ± 0.1 °C.

ζ-potential and dynamic light scattering (DLS) measurements on the nanoclay aqueous dispersions were performed by a Zetasizer NANO-ZS (Malvern Instruments) at 25 ± 0.1 °C. °C. For ζ-Potential experiments a disposable folded capillary cell was used. As concerns DLS experiments, the field-time autocorrelation functions were described by a mono-exponential decay which provides the decay rate (r) of the diffusive mode. For the translational motion, the diffusion coefficient at a given concentration is $D_t = \Gamma/q^2$ where q is the scattering vector given by $4\pi n\lambda^{-1}\sin(\theta/2)$ being n the refractive index, λ the wavelength (632.8 nm) and θ the scattering angle (173°).

The sedimentation experiments were carried out in glass tubes of ca. 2 cm in diameter and length of ca. 6 cm. The kaolinite and halloysite dispersions were imaged in fixed intervals of time for 2 h. Then, the sedimentation volume and the settling velocity of the two clays in sucrose solutions were obtained from the sedimentation front, which was determined by using ImageJ software.

Thermogravimetric experiments were performed by using a Q5000 IR apparatus (TA Instruments) under inert atmosphere. To this purpose, the measurements were conducted under nitrogen flows of 25 and 10 $cm^3\ min^{-1}$ for the sample and the balance, respectively. Tests were carried out by heating the sample from room temperature to 700 °C with a heating rate of 20 °C min^{-1}. TGA analyses were conducted on the materials obtained from the separation of halloysite/kaolinite mixtures. In addition, TG experiments were performed on halloysite/kaolinite composites at variable composition and their pristine components. The temperature calibration of the apparatus was conducted on the basis of the Curie temperatures of standards as reported in literature [69,70].

Scanning electron microscopy (SEM) was conducted using a microscope ESEM FEI QUANTA 200 F. Prior to the experiment, the surface of the clays was coated with gold in argon by means of an Edwards Sputter Coater S150A to avoid charging under electron beam. The analyses were carried out in high vacuum mode (< 6 × 10–4 Pa) for simultaneous secondary electron; the energy of the beam was 25 kV and the working distance was 10 mm.

3. Results and discussion

3.1. Properties of the sucrose solutions

Preliminarily investigations on the sucrose solutions were conducted for a proper analysis and interpretation of the colloidal behavior of the nanoclay dispersions. The obtained results are presented in Table 1. It should be noted that the investigated properties affect the electrophoretic mobility, the aqueous dynamic characteristics and the sedimentation properties of the nanoparticles dispersed in the aqueous sucrose solutions.

3.2. Effects of sucrose on the aqueous diffusion behavior and surface charge of clay nanoparticles

The influence of sucrose addition on the aqueous diffusion coefficient of both HNTs and kaolinite was explored by Dynamic Light Scattering. As a general result, we detected that kaolinite possess lower diffusion coefficients in the aqueous solvents compared to those of halloysite (Fig. 2).

These findings can be related to the larger sizes of kaolinite nanoparticles and their consequent reduced mobility in water with respect to that of HNTs. We observed that the sucrose addition does not affect the diffusion coefficient of kaolinite. On the other hand, the aqueous mobility of HNTs is significantly influenced by the presence of sucrose in the medium. As shown in Fig. 2, the addition of small amounts of sucrose (concentration up to ca. 5 wt%) induced a decrease of the diffusion coefficient of halloysite indicating that the dynamic behavior of the nanotubes was reduced. Oppositely, the further addition of sucrose generated a slight increase of the diffusion coefficient highlighting that the diffusivity of HNTs was enhanced. These trends can be related to the peculiar influence of sucrose on the interactions between the halloysite nanotubes dispersed in water. As shown by ζ-potential results (Table 2), the presence of sucrose slightly alters the surface charge of HNTs as well as kaolinite.

Based on the data in Table 2, we can state that the electrostatic repulsions between the kaolinite nanoparticles in sucrose solutions are comparable to those in water. As concerns HNTs, we observed a slight decrease of the absolute ζ-potential value in the presence of sucrose. It should be noted that the ζ-potential are negative within the whole sucrose concentration range. In general, the ζ-potential values of halloysite are more negative with respect to those of kaolinite for all the investigated sucrose concentrations. Compared to kaolinite nanoplates, halloysite nanotubes exhibited stronger repulsive interactions hindering their aggregation.

It is important to evidence that the presence of sucrose can affect the Van Der Waals interactions between the nanoparticles. Specifically, the sucrose addition can reduce the attractive interactions between the dispersed nanoclays altering the colloidal stability of the dispersions. These effects are dependent on the sucrose concentration as suggested by the results on the aqueous diffusion coefficient of halloysite (Fig. 2). The influence of the sucrose concentration on the Van der Waals attractive interactions between HNTs will be extensively discussed in the paragraph 3.3.

3.3. Sedimentation of clay nanoparticles dispersed in sucrose solutions

As shown in Fig. 3, kaolinite and halloysite dispersions possess different macroscopic characteristics, which depend on the sucrose concentration as well as on the equilibration time after the preparation.

Based on the images reported in Fig. 3a, we observed that the increase of the sucrose concentration from 2.5 to 10 wt% slowed down the lowering of the sedimentation front in the halloysite dispersions. Accordingly, we can state that the kinetics of the HNTs sedimentation is

Table 1
Refractive index, relative dielectric constant and viscosity of sucrose solutions in water at 25 °C.

Sucrose concentration / wt%	RI	ε_r	η / mPa s
0	1.3325	78.4	0.8891
1.27	1.3363	78.2	1.028
2.52	1.3379	77.9	1.055
4.8	1.3405	77.4	1.146
9.88	1.3491	76.1	1.336
15.5	1.3568	74.7	1.592
25.9	1.3702	72.0	2.175

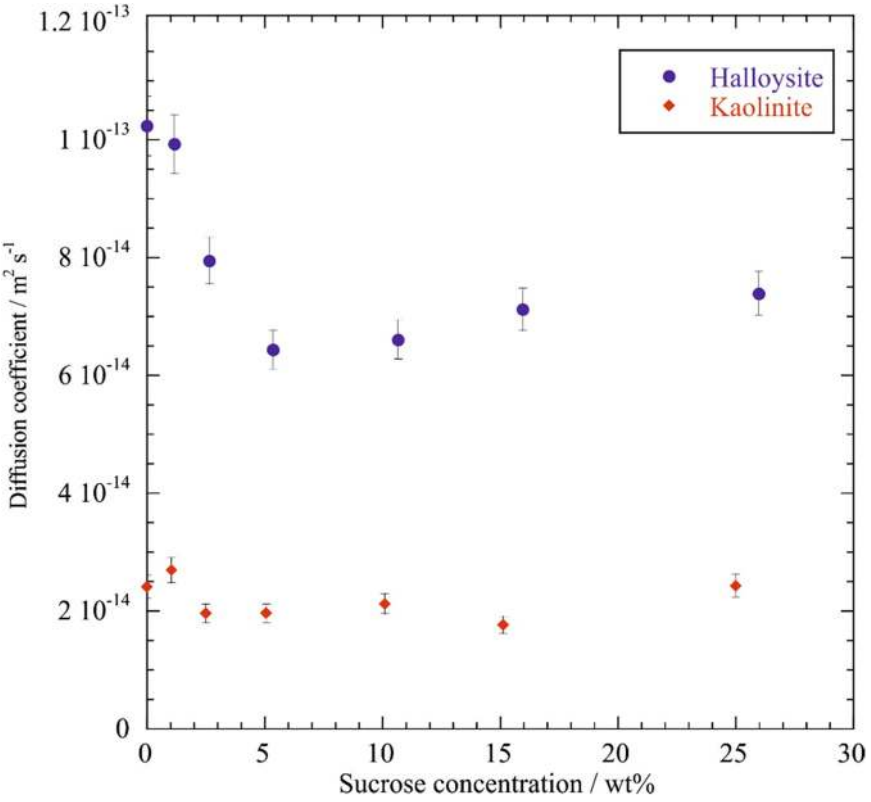

Fig. 2. Aqueous diffusion coefficients of HNTs and kaolinite as functions of sucrose concentration.

Table 2
ζ-potential of halloysite and kaolinite in sucrose solutions at variable concentration.

Sucrose concentration / wt%	ζ-potential / mV	
	Halloysite	Kaolinite
0	-34.1 ± 1.5	-21.9 ± 1.1
4.8	-32.6 ± 1.1	-21.3 ± 1.5
9.88	-32.4 ± 1.4	-22.0 ± 1.2
15.56	-32.3 ± 1.3	-22.3 ± 1.2

faster for the lower sucrose concentration. The complete separation between the dispersed nanoparticles and the solvent was detected after 2 h of equilibration for both sucrose concentrations. Fig. 3b displays the kaolinite suspensions after 30 min of equilibration. We observed that kaolinite dispersed in water does not evidence a clear sedimentation front between the sediment and the supernatant. This observation is valid for all the kaolinite dispersions with sucrose concentration lower than 10 wt%. In order to quantitatively describe the sedimentation kinetics, we analyzed the time evolution of the sedimentation profiles of HNTs and kaolinite dispersions through ImageJ software. In detail, we determined the sedimentation volume fraction after 2 h of equilibration once the process is certainly complete. Moreover, we estimated the settling velocity from the slope of the sedimentation front vs time plot as reported in our previous work regarding the effect of the ionic strength on the aqueous colloidal stability of several halloysites [62]. Based on the macroscopic observations (Fig. 4b), the settling velocity for kaolinite can be determined only in aqueous media containing sucrose with a concentration ≥ 10 wt%.

Fig. 4a shows that sedimentation volume fraction values of kaolinite are lower than those of halloysite and they are almost constant throughout the investigated sucrose concentration range. As a general result, the kaolinite sedimentation is faster compared to that of halloysite for sucrose ≥ 10 wt% as evidenced by the settling velocity data (Fig. 4b). It is remarkable to evidence that the different sedimentation kinetics could be useful for a proper separation of kaolinite and halloysite in natural samples containing both nanoclays. The addition of the carbohydrate did not alter neither the sedimentation volume fraction nor the settling velocity (for sucrose ≥ 10 wt%) of kaolinite dispersions. In contrast, the presence of sucrose affected the sedimentation kinetics of halloysite nanotubes dispersed in water. We detected that the velocity of the HNTs sedimentation is enhanced for sucrose concentration up to 5 wt%, while a further addition of sucrose generated the opposite effect. Similarly, the sedimentation volume fraction presents a minimum value at 5 wt%. The relation between the sedimentation parameters and the sucrose concentration (Fig. 4) are consistent with the DLS data, which evidenced that the HNTs diffusion in water is reduced for small concentrations of sugar reaching a minimum value at 5 wt% of carbohydrate.

3.4. Sedimentation kinetics of halloysite: the influence of sucrose addition on the Van der Waals interactions

The influence of the sucrose concentration on the sedimentation parameters can be discussed in terms of balance between Van der Waals forces and repulsive interactions between the nanoparticles (DLVO theory). It should be noted this approach is not suitable for the description of the kaolinite sedimentation because of the large sizes of the nanoparticles. Accordingly, DLS experiments at variable sucrose concentration evidenced that the hydrodynamic diameter of kaolinite ranges between 1828 ± 146 nm and 2796 ± 223 nm. These values were determined at sucrose concentrations equal to 1.27 and 15.5 wt%, respectively. As expected, the addition of sucrose generated slight variations of the surface charge of HNTs (Table 2). Therefore, we can conclude that the presence of sucrose does not affect the repulsive interactions between the halloysite nanotubes. On the other hand, we can predict that the Van der Waals attractive forces are influenced by

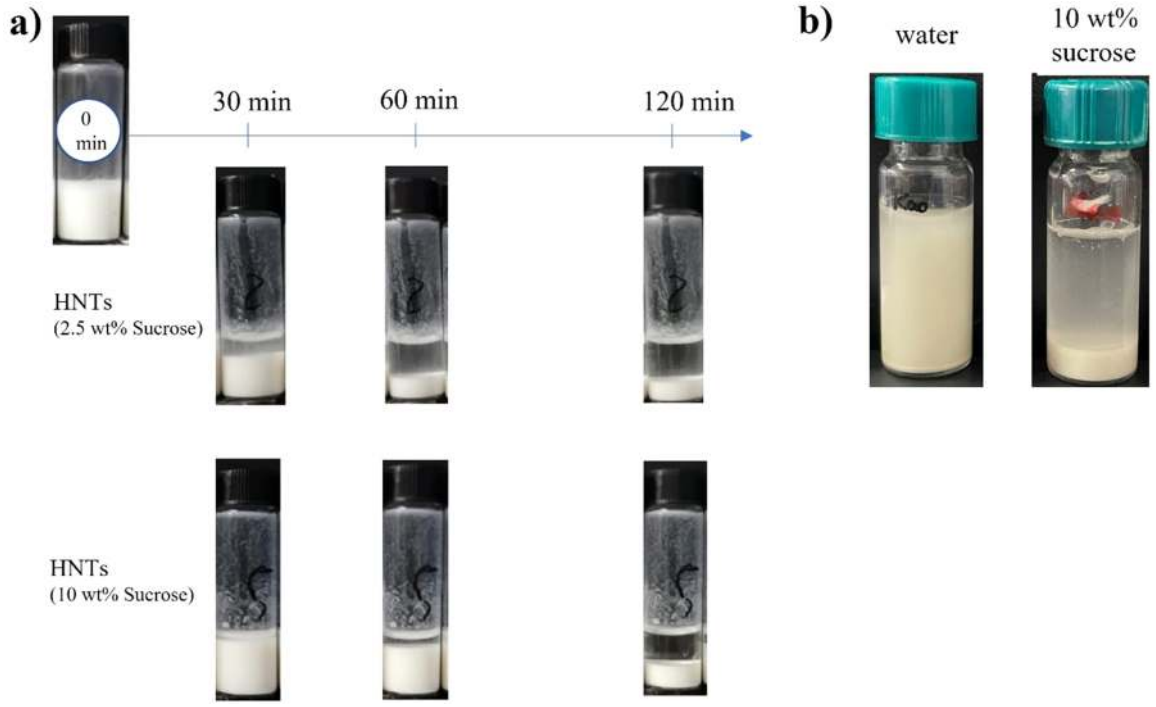

Fig. 3. (a) Images of HNTs dispersions in 2.5 and 10 wt% sucrose at variable times of equilibration. (b) Images of kaolinite dispersions in water and 10 wt% sucrose after 30 min of equilibration.

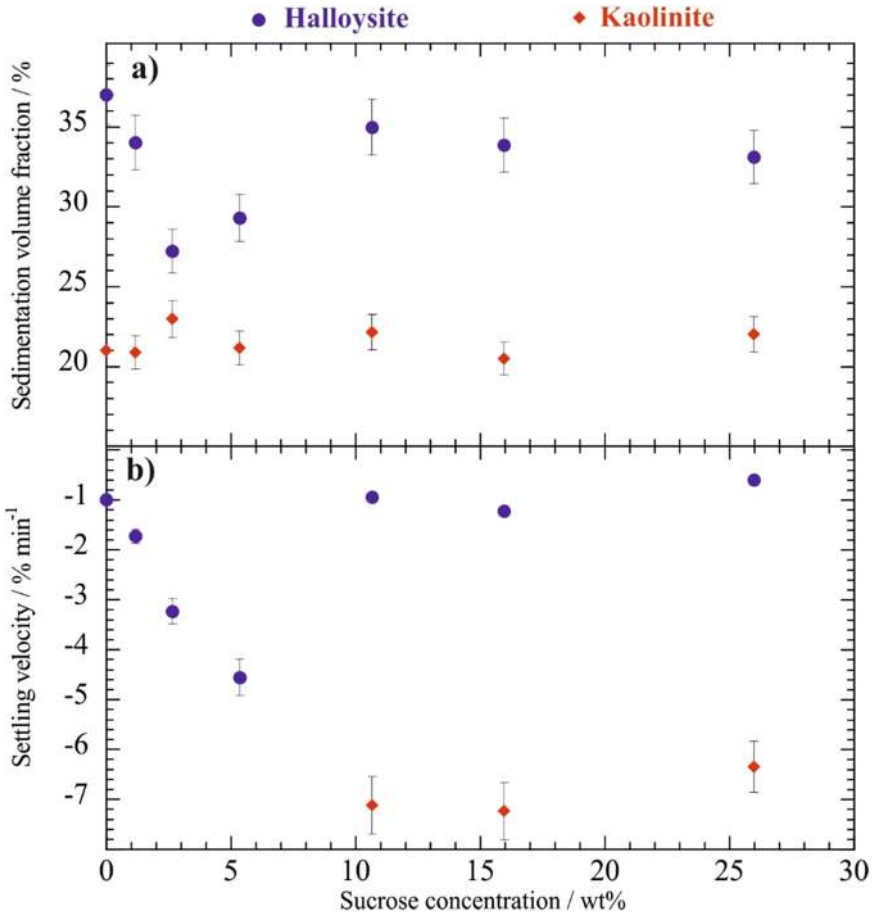

Fig. 4. Sedimentation volume fraction (a) and settling velocity (b) as functions of the sucrose concentration for halloysite and kaolinite dispersions.

sucrose. In this regard, we calculated the Hamaker constant vs sucrose concentration for HNTs dispersions by the following equation

$$A_H = \frac{3}{4}k_B T \bullet \left(\frac{\varepsilon_1 - \varepsilon_2}{\varepsilon_1 + \varepsilon_2}\right)^2 + \frac{3h\upsilon_e}{8\sqrt{2}} \bullet \frac{\left(n_1^2 - n_2^2\right)}{\left(n_1^2 + n_2^2\right) \bullet \left(2 \bullet \sqrt{n_1^2 + n_2^2}\right)} \quad (1)$$

where k_B is the Boltzmann constant, T is the absolute temperature, ε is the dielectric constant, n is the refractive index and υ_e. is the mean ionization frequency of the material and it is ≈ 3.10^{15} Hz 10^{15}. Here, the subscript 1 and 2 refer to halloysite and sucrose solution, respectively. Fig. 5 reports the Hamaker constant function normalized by the thermal energy (k_bT) for halloysite nanotubes dispersed in aqueous solvent containing variable amounts of sucrose. To this purpose, we considered the fitted curves for the dielectric constant and the refractive of index of aqueous solutions with variable sucrose concentration (see Supplementary Materials).

As shown in Fig. 5, the Hamaker constant is positive for all the sucrose concentrations indicating that the Van der Waals forces are attractive. We observed that the sucrose addition decreases the attractive forces between the nanotubes dispersed in water. In other words, the reduction of the Hamaker constant agrees with the screening of the Van der Waals interactions between the dispersed nanotubes. This effect is enhanced by increasing the sucrose amount in the aqueous medium. The decreasing trend of the Hamaker constant on the sucrose concentration (Fig. 5) can be described by a binomial equation within the whole investigated range. Interestingly, a linear region with slight variations of the Hamaker constant can be identified for sucrose ≤5 wt%. In detail, we estimated that the reduction of the Hamaker constant is lower than 2% highlighting that the influence of sucrose on the attractions between the nanoparticles is negligible for sugar concentration up to ca. 5 wt%.

Based on these considerations, we can hypothesize that the attractive forces are largely predominant with respect to the repulsions in the presence of small amounts of sucrose and, consequently, the clustering between HNTs is favored. Accordingly, the aqueous diffusion coefficient decreased (Fig. 2) and the sedimentation kinetics was enhanced (Fig. 4b). These results are also consistent with the slight reduction of the HNTs surface (Table 2). On the other hand, the discrepancy between attractions and repulsions was reduced for sucrose concentration ≥ 10 wt% explaining both DLS data and the sedimentation parameters. Namely, the attractive forces are significantly screened by sucrose determining an increase of the aqueous mobility and an improvement of the colloidal stability of the nanotubes.

3.5. Separation of halloysite and kaolinite in sucrose solution

Generally, natural clay samples are mixtures of different minerals limiting their use for several purposes. Within this, it should be noted that natural halloysites can contain variable amounts of kaolinite. Therefore, the successful separation of halloysite and kaolinite is crucial to make HNTs suitable for technological applications. Here, we exploited their sedimentation kinetics in sucrose solutions to obtain an efficient separation of the two nanoclays in halloysite/kaolinite mixtures. The protocol used for the separation of halloysite and kaolinite is described in the paragraph 2.3. Scanning electron microscopy evidenced the co-presence of few kaolinite nanoplates and a large amount of halloysite nanotubes in the sample obtained from 10 wt% sucrose solution (see Supplementary Materials). The efficiency of the separation procedure was estimated by thermogravimetry, which is a powerful technique for the quantitative and qualitative characterization of multicomponent materials [1,71]. Fig. 6 compares the differential thermogravimetric curves of pristine nanoclays and their mixture (HNT/Kaolinite 50:50) with those of the materials obtained by the separation through both water and 10 wt% sucrose solution. According to literature [72,73], pure halloysite exhibited the main mass loss in the temperature range between 400 and 600 °C due to expulsion of the interlayer water molecules, while kaolinite evidenced a significant mass reduction in a broader range (between 480 and 700 °C). On this basis, we focused the analysis of the differential thermogravimetric curves of the separated materials within the range 400–700 °C.

Firstly, we determined the peak temperatures (T_{peak}) for the different samples from the minimum of the differential thermogravimetric curves. As shown in Supplementary Materials, a linear function was detected for the dependence of T_{peak} on the composition of halloysite/kaolinite mixtures. Based on the linear fitting of this trend, we calculated the mass percent of halloysite in the separated materials from the corresponding T_{peak} values (503.8 and 514.8 °C from sucrose solution and water, respectively). We determined that the halloysite contents are 97 ± 3 wt % and 59 ± 3 wt% for the materials obtained from the separation through 10 wt% sucrose solution and water, respectively.

A more accurate analysis was conducted by the fitting of the DTG curves using Fityk software [74]. The split Gaussian function was used as model for the analysis of the DTG curves. As shown in Supplementary Materials, DTG curves of both pristine kaolinite and halloysite were fitted using the split Gaussian equation, which can be expressed as:

$$dm/dT = (dm/dT)^* \cdot \exp[-\ln(2) \cdot (T - T_C)/\Delta T_L)^2 \text{ for } T \leq T_C \quad (2)$$

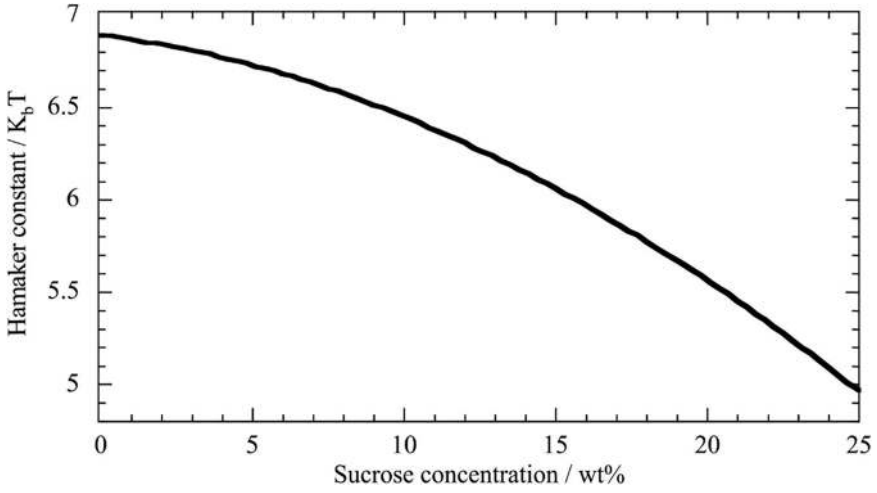

Fig. 5. Dependence of the Hamaker constant for HNTs on the sucrose concentration. The function was calculated on the basis of Eq. (1) and taking into account the fitted curved for the dielectric constant and the refractive of index of sucrose aqueous solutions (see Supplementary Materials).

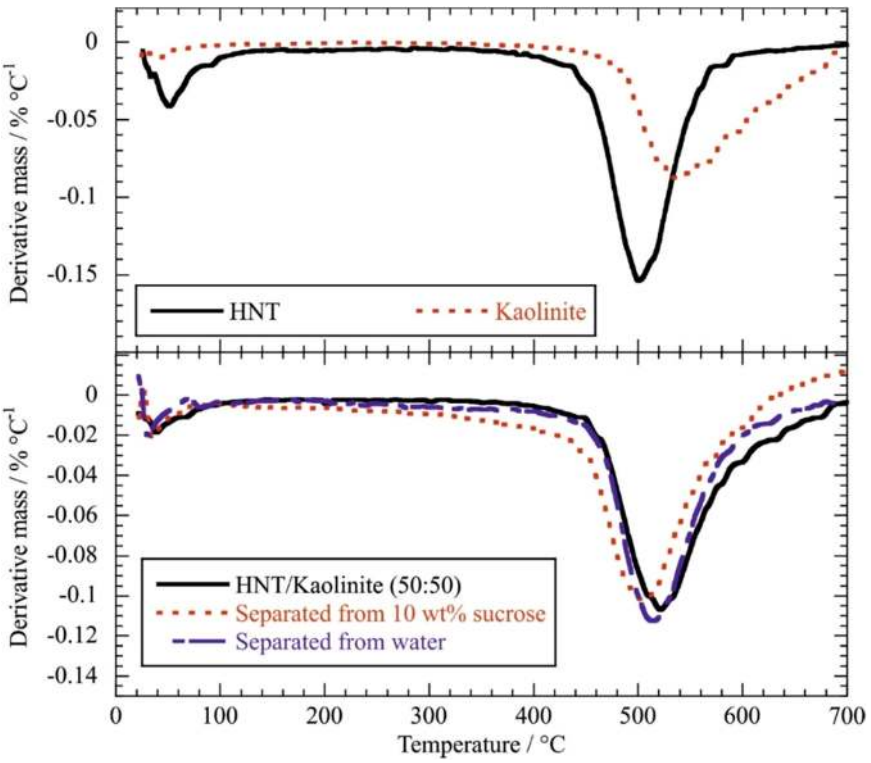

Fig. 6. Differential thermogravimetric curves of kaolinite, halloysite, kaolinite/halloysite (50:50) mixture and the materials obtained from the separation in water and 10 wt% sucrose solution.

and:

$$dm/dT = (dm/dT)^{*}\cdot[-\ln(2)\cdot(T - T_C)/\Delta T_R)^2 \text{ for } T \geq T_C \quad (3)$$

where T_C is the temperature at the center of the function, ΔT_L and ΔT_R are the left and right widths indicated as temperature ranges, while $(dm/dT)^*$ is the common value for the left and right sides.

The parameters obtained by the fitting of the DTG curves of kaolinite and halloysite are reported in Supplementary Materials. The DTG curves of halloysite/kaolinite mixtures with variable composition were successfully fitted by combining the split Gaussian equations of halloysite and kaolinite. Specifically, $(dm/dT)^*$ for halloysite and kaolinite contributions were considered as fitting parameters, while T_C, ΔT_L and ΔT_R for both nanoclays were fixed (the values determined by the fitting of the DTG curves of pristine HNT and kaolinite). As example, Fig. 7a compares the experimental and calculated DTG curves for the mixture composed by 50 wt% of halloysite. In addition, Fig. 7b shows separately the split Gaussian functions combined for the fitting analysis. Based on the fitted DTG curves, we can estimate the mass percent of halloysite in the mixture by using the following equation.

$$HNT(wt\%)_{SGE} = 100\cdot(A(SGE)_{HNT}/(A(SGE)_M) \quad (4)$$

being $A(SGE)_M$ the area obtained by the integration of the split Gaussian function of the mixture, while $A(SGE)_{HNT}$ is the integral area for the single contribution of halloysite used in the fitting analysis. Fig. 7c shows a linear trend of the calculated $HNT(wt\%)_{SGE}$ values and the halloysite mass percent employed for the preparation of the mixtures. The linear fitting of the data presented in Fig. 7c allowed us to determine a calibration curve for the calculation of the HNT content in halloysite/kaolinite composite samples with unknown composition including the separated material obtained by the protocol reported in the paragraph 2.3.

As evidenced in Fig. 8a, the DTG curve of the sample separated from sucrose solution can be analyzed by using the combination of the split Gaussian equations of halloysite and kaolinite. Fig. 8b shows that the contribution of halloysite to the fitting analysis is significantly higher compared to that of kaolinite. Based on the corresponding $HNT(wt\%)_{SGE}$ value (84.3 wt%) and the calibration curve (Fig. 7c), we determined that the halloysite content in the separated material is equal to 89 ± 5 wt%, which confirms that the separation procedure in sucrose aqueous solution was very efficient. On the other hand, we determined that the sample separated from water presents a $HNT(wt\%)_{SGE}$ value of 51.6 wt %. On this basis, we calculated a HNT content equals to 53 ± 4 wt%, which is significantly lower to that detected for the material separated from 10 wt% sucrose. According to these results, we can state that the addition of sucrose in the aqueous solvent favors the separation between the nanoclays. This finding can be related to the macroscopic observations of the dispersions (Fig. 3) and the sedimentation kinetics (Fig. 4), which highlighted that the addition of 10 wt% of sucrose decreases the kaolinite colloidal stability, while the settling velocity of halloysite was slightly affected.

4. Conclusions

This study was aimed to develop a novel protocol for the separation of halloysite/kaolinite mixtures by exploiting the variable effects of sucrose addition on the aqueous colloidal stability of both nanoclays. In this regard, it should be noted that the control of the nanoclays sedimentation is crucial for the purification of natural halloysite samples. Based on Dynamic Light Scattering (DLS) results, we observed that the influence of sucrose on the diffusion of halloysite nanotubes in water is

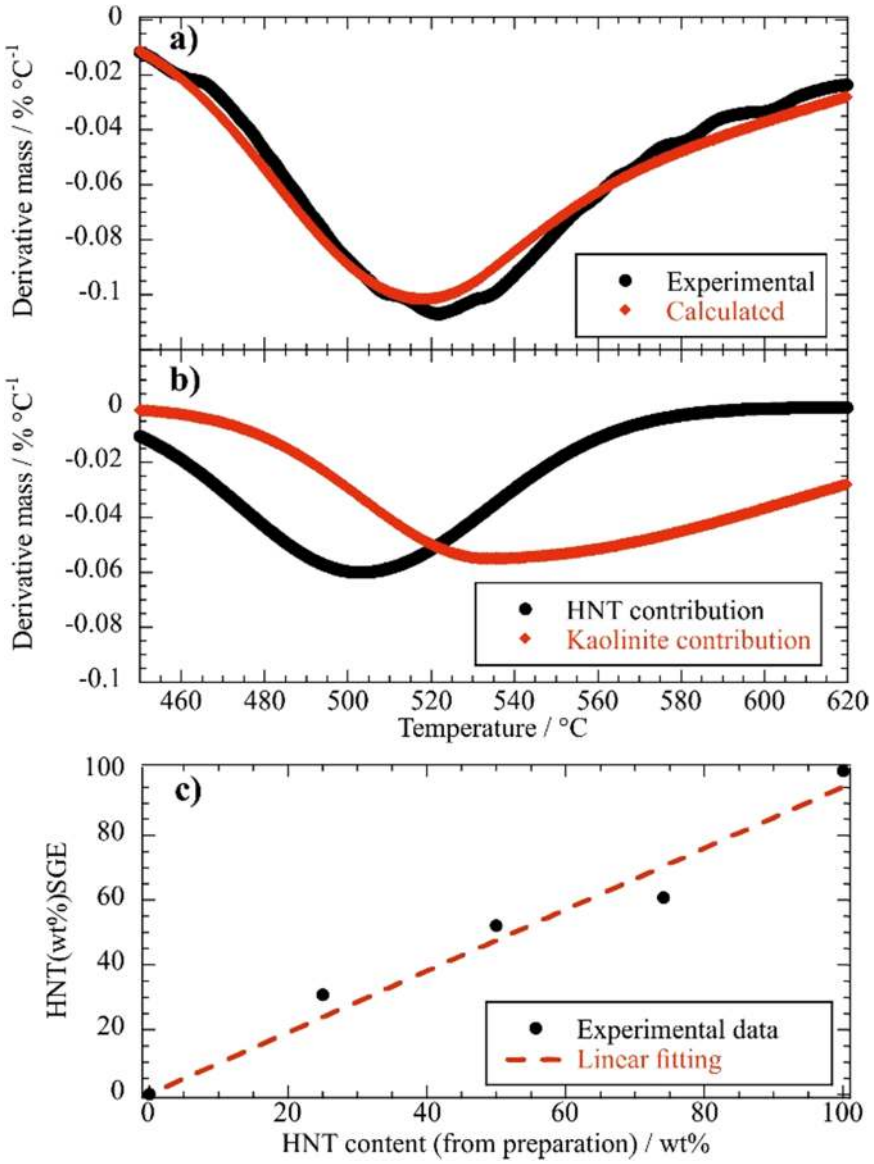

Fig. 7. (a) Experimental and fitted DTG curves for the mixture composed by 50 wt% of halloysite. (b). Split Gaussian functions of halloysite and kaolinite employed in the fitting analysis. (c) Dependence of the halloysite content determined by the fitting (Eq. 4) on the HNT concentration used for the preparation of mixture with variable composition. The linear regression presents R^2 equals to 0.985, while the relative error for the fitting parameter (the angular coefficient) is 6%.

dependent on the concentration of the carbohydrate, while any effects were detected for kaolinite nanoplates. As expected, the surface charge of the nanoclays is slightly influenced by the presence of the carbohydrate. According to the DLS and ζ-potential data, we observed that small amounts of sucrose (< 10 wt%) enhanced the sedimentation kinetics of halloysite nanotubes. This effect was avoided by increase the sucrose concentration (≥ 10 wt%) in agreement with the significant screening towards the attractive interactions between the clay nanotubes. Interestingly, the dispersibility of kaolinite was strongly reduced in the presence of sucrose with a concentration larger than 10 wt%. On this basis, we evaluated that the separation efficiency of halloysite/kaolinite mixtures can be optimized in 10 wt% sucrose aqueous solution. Thermogravimetry was employed to determine the quantitative composition of the materials separated in water as well as in 10 wt% sucrose solution. The fitting analysis of the differential thermogravimetric curves by split Gaussian functions allowed us to estimate that the halloysite contents in the separated materials. We detected that the presence of 10 wt% sucrose in the aqueous medium generated a significant increase of the halloysite content (89 ± 5 wt%) in the separated material with respect to that obtained by the separation in water (53 ± 4 wt%). In conclusion, this paper demonstrated that a successful separation between halloysite and kaolinite can be achieved by the addition of sucrose in aqueous solvents. The separation efficiency can be controlled by the sucrose concentration, which influenced the aqueous colloidal stability and sedimentation kinetics of both nanoclays. Remarkably, the proposed protocol can be exploited for the purification of natural halloysite samples.

CRediT authorship contribution statement

Martina Maria Calvino: Investigation, Data curation, Writing – original draft. **Giuseppe Cavallaro:** Writing – review & editing, Validation. **Lorenzo Lisuzzo:** Investigation, Data curation. **Stefana Milioto:** Funding acquisition, Resources. **Giuseppe Lazzara:** Conceptualization, Supervision.

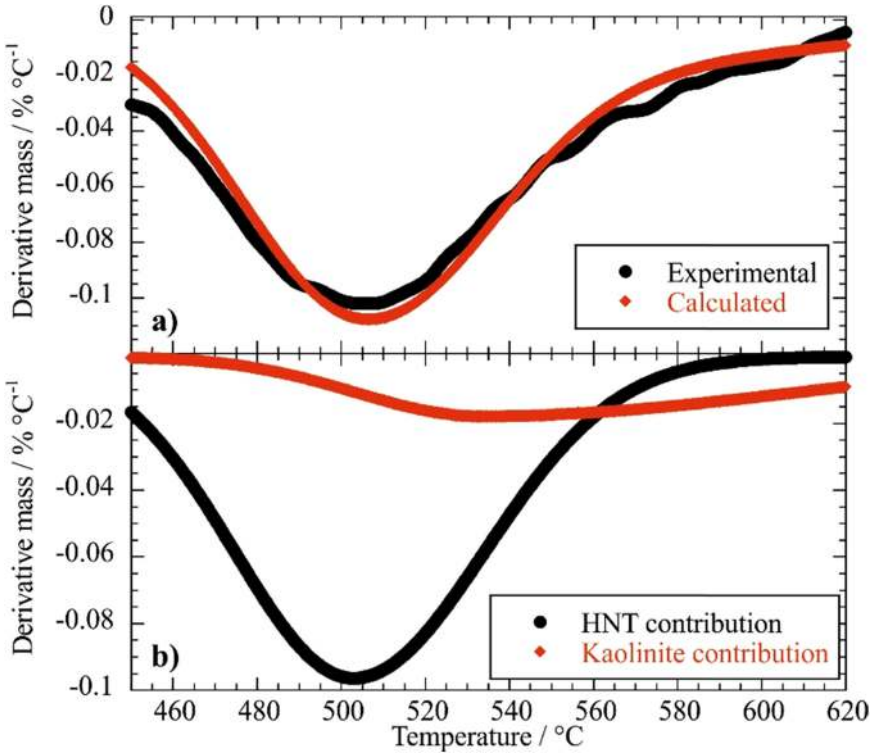

Fig. 8. (a) Experimental and fitted DTG curves for the material obtained by the separation in 10 wt% sucrose solution. (b). Split Gaussian functions of halloysite and kaolinite employed in the fitting analysis.

Declaration of Competing Interest

The authors declare that they have no known competing financial interests or personal relationships that could have appeared to influence the work reported in this paper.

Acknowledgements

The authors acknowledge the University of Palermo for the financial support. The work was funded by Progetto "SETI-Sicilia Eco Tecnologie Innovative", PO FESR Sicilia 2014/2020 – Azione 1.1.5, Codice Progetto: 2017-NAZ-0204".

Supplementary materials

Fitting curves and experimental data for refractive index and dielectric constant of aqueous solutions containing variable amounts of sucrose.

Dependence of the peak temperature (determined from the minimum of DTG curves) for halloysite/kaolinite mixtures with variable composition.

Experimental and fitted DTG curves for pristine kaolinite and halloysite.

SEM image of the sample obtained from the separation in 10 wt% sucrose solution.

Fitting parameters obtained by analysis through the split Gaussian equations of the DTG curves of halloysite and kaolinite.

Appendix A. Supporting information

Supplementary data associated with this article can be found in the online version at doi:10.1016/j.colsurfa.2022.128530.

References

[1] L. Lisuzzo, G. Cavallaro, S. Milioto, G. Lazzara, Halloysite nanotubes filled with MgO for paper reinforcement and deacidification, Appl. Clay Sci. 213 (2021), https://doi.org/10.1016/j.clay.2021.106231.
[2] B. Chen, J.R.G. Evans, Impact strength of polymer-clay nanocomposites, Soft Matter 5 (2009) 3572–3584, https://doi.org/10.1039/b902073j.
[3] A. Joshi, E. Abdullayev, A. Vasiliev, O. Volkova, Y. Lvov, Interfacial modification of clay nanotubes for the sustained release of corrosion inhibitors, Langmuir 29 (2013) 7439–7448, https://doi.org/10.1021/la3044973.
[4] E. Nyankson, O. Olasehinde, V.T. John, R.B. Gupta, Surfactant-loaded halloysite clay nanotube dispersants for crude oil spill remediation, Ind. Eng. Chem. Res. 54 (2015) 9328–9341, https://doi.org/10.1021/acs.iecr.5b02032.
[5] R.F. Fakhrullin, Y.M. Lvov, Halloysite clay nanotubes for tissue engineering, Nanomedicine 11 (2016) 2243–2246, https://doi.org/10.2217/nnm-2016-0250.
[6] Y. Feng, X. Zhou, J. Yang, X. Gao, L. Yin, Y. Zhao, B. Zhang, Encapsulation of ammonia borane in Pd/halloysite nanotubes for efficient thermal dehydrogenation, ACS Sustain. Chem. Eng. 8 (2020) 2122–2129, https://doi.org/10.1021/acssuschemeng.9b04480.
[7] E. Ruiz-Hitzky, P. Aranda, M. Darder, G. Rytwo, Hybrid materials based on clays for environmental and biomedical applications, J. Mater. Chem. 20 (2010) 9306–9321, https://doi.org/10.1039/c0jm00432d.
[8] I. Guryanov, E. Naumenko, F. Akhatova, G. Lazzara, G. Cavallaro, L. Nigamatzyanova, R. Fakhrullin, Selective cytotoxic activity of prodigiosin@halloysite nanoformulation, Front. Bioeng. Biotechnol. 8 (2020), https://doi.org/10.3389/fbioe.2020.00424.
[9] M. Liu, Y. Zhang, C. Wu, S. Xiong, C. Zhou, Chitosan/halloysite nanotubes bionanocomposites: Structure, mechanical properties and biocompatibility, Int. J. Biol. Macromol. 51 (2012) 566–575, https://doi.org/10.1016/j.ijbiomac.2012.06.022.
[10] Y. Dong, S.-S. Feng, Poly(D,L-lactide-co-glycolide)/montmorillonite nanoparticles for oral delivery of anticancer drugs, Biomaterials 26 (2005) 6068–6076, https://doi.org/10.1016/j.biomaterials.2005.03.021.
[11] M. Fizir, A. Richa, H. He, S. Touil, M. Brada, L. Fizir, A mini review on molecularly imprinted polymer based halloysite nanotubes composites: innovative materials for analytical and environmental applications, Rev. Environ. Sci. Biotechnol. 19 (2020) 241–258, https://doi.org/10.1007/s11157-020-09537-x.
[12] F. Ferrante, N. Armata, G. Lazzara, Modeling of the halloysite spiral nanotube, J. Phys. Chem. C 119 (2015) 16700–16707, https://doi.org/10.1021/acs.jpcc.5b04281.
[13] V. Vergaro, E. Abdullayev, Y.M. Lvov, A. Zeitoun, R. Cingolani, R. Rinaldi, S. Leporatti, Cytocompatibility and uptake of halloysite clay nanotubes, Biomacromolecules 11 (2010) 820–826, https://doi.org/10.1021/bm9014446.

[14] S.R. Levis, P.B. Deasy, Characterisation of halloysite for use as a microtubular drug delivery system, Int. J. Pharm. 243 (2002) 125–134, https://doi.org/10.1016/S0378-5173(02)00274-0.
[15] G. Lazzara, G. Cavallaro, A. Panchal, R. Fakhrullin, A. Stavitskaya, V. Vinokurov, Y. Lvov, An assembly of organic-inorganic composites using halloysite clay nanotubes, Curr. Opin. Colloid Interface Sci. 35 (2018) 42–50, https://doi.org/10.1016/j.cocis.2018.01.002.
[16] H. Zhang, Selective modification of inner surface of halloysite nanotubes: a review, Nanotechnol. Rev. 6 (2017) 573–581, https://doi.org/10.1515/ntrev-2017-0163.
[17] E. Tarasova, E. Naumenko, E. Rozhina, F. Akhatova, R. Fakhrullin, Cytocompatibility and uptake of polycations-modified halloysite clay nanotubes, Appl. Clay Sci. 169 (2019) 21–30, https://doi.org/10.1016/j.clay.2018.12.016.
[18] G. Cavallaro, I. Grillo, M. Gradzielski, G. Lazzara, Structure of hybrid materials based on halloysite nanotubes filled with anionic surfactants, J. Phys. Chem. C 120 (2016) 13492–13502, https://doi.org/10.1021/acs.jpcc.6b01282.
[19] Y.M. Lvov, D.G. Shchukin, H. Möhwald, R.R. Price, Halloysite clay nanotubes for controlled release of protective agents, ACS Nano 2 (2008) 814–820, https://doi.org/10.1021/nn800259q.
[20] P. Dramou, M. Fizir, A. Taleb, A. Itatahine, N.S. Dahiru, Y.A. Mehdi, L. Wei, J. Zhang, H. He, Folic acid-conjugated chitosan oligosaccharide-magnetic halloysite nanotubes as a delivery system for camptothecin, Carbohydr. Polym. 197 (2018) 117–127, https://doi.org/10.1016/j.carbpol.2018.05.071.
[21] G. Cavallaro, G. Lazzara, S. Milioto, F. Parisi, V. Evtugyn, E. Rozhina, R. Fakhrullin, Nanohydrogel formation within the halloysite lumen for triggered and sustained release, ACS Appl. Mater. Interfaces 10 (2018) 8265–8273, https://doi.org/10.1021/acsami.7b19361.
[22] C. Duce, V.D. Porta, E. Bramanti, B. Campanella, A. Spepi, M.R. Tiné, Loading of halloysite nanotubes with BSA, α -Lac and β -Lg: a Fourier transform infrared spectroscopic and thermogravimetric study, Nanotechnology 28 (2017), 055706.
[23] M. Liu, Y. Chang, J. Yang, Y. You, R. He, T. Chen, C. Zhou, Functionalized halloysite nanotube by chitosan grafting for drug delivery of curcumin to achieve enhanced anticancer efficacy, J. Mater. Chem. B 4 (2016) 2253–2263, https://doi.org/10.1039/C5TB02725J.
[24] Y.-P. Wu, J. Yang, H.-Y. Gao, Y. Shen, L. Jiang, C. Zhou, Y.-F. Li, R.-R. He, M. Liu, Folate-conjugated halloysite nanotubes, an efficient drug carrier, deliver doxorubicin for targeted therapy of breast cancer, ACS Appl. Nano Mater. 1 (2018) 595–608, https://doi.org/10.1021/acsanm.7b00087.
[25] F. Liu, L. Bai, H. Zhang, H. Song, L. Hu, Y. Wu, X. Ba, Smart H2O2-responsive drug delivery system made by halloysite nanotubes and carbohydrate polymers, ACS Appl. Mater. Interfaces 9 (2017) 31626–31633, https://doi.org/10.1021/acsami.7b10867.
[26] Y. Zhang, L. Bai, C. Cheng, Q. Zhou, Z. Zhang, Y. Wu, H. Zhang, A novel surface modification method upon halloysite nanotubes: a desirable cross-linking agent to construct hydrogels, Appl. Clay Sci. 182 (2019), 105259, https://doi.org/10.1016/j.clay.2019.105259.
[27] Y. Darrat, E. Naumenko, G. Cavallaro, G. Lazzara, Y. Lvov, R. Fakhrullin, Tubular nanocontainers for drug delivery, in: Mater. Nanoarchitectonics, Wiley-VCH Verlag GmbH & Co. KGaA, 2018, pp. 85–108, https://doi.org/10.1002/9783527808311.ch4.
[28] A. Spepi, C. Duce, A. Pedone, D. Presti, J.-G. Rivera, V. Ierardi, M.R. Tiné, Experimental and DFT characterization of halloysite nanotubes loaded with salicylic acid, J. Phys. Chem. C 120 (2016) 26759–26769, https://doi.org/10.1021/acs.jpcc.6b06964.
[29] B. Tang, H. Zhang, C. Cheng, H. Jiang, L. Bai, X. Ba, Y. Wu, Development of halloysite nanotube-based hydrogel with colorimetric H2O2-responsive character, Appl. Clay Sci. 212 (2021), 106230, https://doi.org/10.1016/j.clay.2021.106230.
[30] L. Lisuzzo, G. Cavallaro, S. Milioto, G. Lazzara, Halloysite nanotubes filled with salicylic acid and sodium diclofenac: effects of vacuum pumping on loading and release properties, J. Nanostruct. Chem. (2021), https://doi.org/10.1007/s40097-021-00391-z.
[31] M. Tonelli, I. Perini, F. Ridi, P. Baglioni, Improving the properties of antifouling hybrid composites: The use of Halloysites as nano-containers in epoxy coatings, Colloids Surf. Physicochem. Eng. Asp. 623 (2021), 126779, https://doi.org/10.1016/j.colsurfa.2021.126779.
[32] E. Boccalon, G. Viscusi, A. Sorrentino, F. Marmottini, M. Nocchetti, G. Gorrasi, Solvent-free synthesis of halloysite-layered double hydroxide composites containing salicylate as novel, active fillers, Colloids Surf. Physicochem. Eng. Asp. 627 (2021), 127135, https://doi.org/10.1016/j.colsurfa.2021.127135.
[33] P. Pasbakhsh, G.J. Churchman, J.L. Keeling, Characterisation of properties of various halloysites relevant to their use as nanotubes and microfibre fillers, Appl. Clay Sci. 74 (2013) 47–57, https://doi.org/10.1016/j.clay.2012.06.014.
[34] V. Bugatti, G. Viscusi, C. Naddeo, G. Gorrasi, Nanocomposites based on PCL and halloysite nanotubes filled with lysozyme: Effect of draw ratio on the physical properties and release analysis, Nanomaterials 7 (2017), https://doi.org/10.3390/nano7080213.
[35] G. Gorrasi, Dispersion of halloysite loaded with natural antimicrobials into pectins: characterization and controlled release analysis, Carbohydr. Polym. 127 (2015) 47–53, https://doi.org/10.1016/j.carbpol.2015.03.050.
[36] G. Gorrasi, V. Bugatti, M. Ussia, R. Mendichi, D. Zampino, C. Puglisi, S. C. Carroccio, Halloysite nanotubes and thymol as photo protectors of biobased polyamide 11, Polym. Degrad. Stab. 152 (2018) 43–51, https://doi.org/10.1016/j.polymdegradstab.2018.03.015.
[37] M. Barman, S. Mahmood, R. Augustine, A. Hasan, S. Thomas, K. Ghosal, Natural halloysite nanotubes /chitosan based bio-nanocomposite for delivering norfloxacin, an anti-microbial agent in sustained release manner, Int. J. Biol. Macromol. 162 (2020) 1849–1861, https://doi.org/10.1016/j.ijbiomac.2020.08.060.
[38] Y. Tian, Q. Qian, Y. Sheng, X. Zhang, H. Wu, L. Xu, L. Li, H. Ye, High energy density in poly(vinylidene fluoride-trifluoroethylene) composite incorporated with modified halloysite nanotubular architecture, Colloids Surf. Physicochem. Eng. Asp. 625 (2021), 126993, https://doi.org/10.1016/j.colsurfa.2021.126993.
[39] J. Raja Beryl, J.R. Xavier, Influence of silane functionalized nanoclay on the barrier, mechanical and hydrophobic properties by clay nanocomposite films in an aggressive chloride medium, Colloids Surf. Physicochem. Eng. Asp. 630 (2021), 127625, https://doi.org/10.1016/j.colsurfa.2021.127625.
[40] T. Selkälä, T. Suopajärvi, J.A. Sirviö, T. Luukkonen, P. Kinnunen, K.I. Kling, J. B. Wagner, H. Liimatainen, Efficient entrapment and separation of anionic pollutants from aqueous solutions by sequential combination of cellulose nanofibrils and halloysite nanotubes, Chem. Eng. J. 374 (2019) 1013–1024, https://doi.org/10.1016/j.cej.2019.06.008.
[41] K. Zhu, Y. Duan, F. Wang, P. Gao, H. Jia, C. Ma, C. Wang, Silane-modified halloysite/Fe3O4 nanocomposites: Simultaneous removal of Cr(VI) and Sb(V) and positive effects of Cr(VI) on Sb(V) adsorption, Chem. Eng. J. 311 (2017) 236–246, https://doi.org/10.1016/j.cej.2016.11.101.
[42] Y. Zhao, E. Abdullayev, A. Vasiliev, Y. Lvov, Halloysite nanotubule clay for efficient water purification, J. Colloid Interface Sci. 406 (2013) 121–129, https://doi.org/10.1016/j.jcis.2013.05.072.
[43] M. Omarova, L.T. Swientoniewski, I.K.M. Tsengam, A. Panchal, T. Yu, D.A. Blake, Y.M. Lvov, D. Zhang, V. John, Engineered clays as sustainable oil dispersants in the presence of model hydrocarbon degrading bacteria: the role of bacterial sequestration and biofilm formation, ACS Sustain. Chem. Eng. 6 (2018) 14143–14153, https://doi.org/10.1021/acssuschemeng.8b02744.
[44] K. Govindasamy, N.A. Dahlan, P. Janarthanan, K.L. Goh, S.-P. Chai, P. Pasbakhsh, Electrospun chitosan/polyethylene-oxide (PEO)/halloysites (HAL) membranes for bone regeneration applications, Appl. Clay Sci. 190 (2020), 105601, https://doi.org/10.1016/j.clay.2020.105601.
[45] U. Baig, M.A. Gondal, M.A. Dastageer, W.S. Falath, Rapid fabrication of textured membrane with super-wettability using simple spray-coating of Pd-doped WO3 nanoparticles for efficient oil-water separation, Colloids Surf. Physicochem. Eng. Asp. 609 (2021), 125643, https://doi.org/10.1016/j.colsurfa.2020.125643.
[46] L. Lisuzzo, G. Cavallaro, S. Milioto, G. Lazzara, Halloysite nanotubes as nanoreactors for heterogeneous micellar catalysis, J. Colloid Interface Sci. 608 (2022) 424–434, https://doi.org/10.1016/j.jcis.2021.09.146.
[47] S. Sadjadi, M.M. Heravi, M. Malmir, Pd@HNTs-CDNS-g-C3N4: a novel heterogeneous catalyst for promoting ligand and copper-free Sonogashira and Heck coupling reactions, benefits from halloysite and cyclodextrin chemistry and g-C3N4 contribution to suppress Pd leaching, Carbohydr. Polym. 186 (2018) 25–34, https://doi.org/10.1016/j.carbpol.2018.01.023.
[48] Y. Liu, J. Zhang, H. Guan, Y. Zhao, J.-H. Yang, B. Zhang, Preparation of bimetallic Cu-Co nanocatalysts on poly (diallyldimethylammonium chloride) functionalized halloysite nanotubes for hydrolytic dehydrogenation of ammonia borane, Appl. Surf. Sci. 427 (2018) 106–113, https://doi.org/10.1016/j.apsusc.2017.08.171.
[49] Y. Liu, H. Guan, J. Zhang, Y. Zhao, J.-H. Yang, B. Zhang, Polydopamine-coated halloysite nanotubes supported AgPd nanoalloy: an efficient catalyst for hydrolysis of ammonia borane, Int. J. Hydrog. Energy 43 (2018) 2754–2762, https://doi.org/10.1016/j.ijhydene.2017.12.105.
[50] S. Sadjadi, G. Lazzara, M.M. Heravi, G. Cavallaro, Pd supported on magnetic carbon coated halloysite as hydrogenation catalyst: study of the contribution of carbon layer and magnetization to the catalytic activity, Appl. Clay Sci. 182 (2019), 105299, https://doi.org/10.1016/j.clay.2019.105299.
[51] D. Jiang, H. Jing, Z. Liu, C. Jia, Q. Liu, Natural halloysite nanotube as a spatially confined nanoreactor for improving photocatalytic performance, J. Phys. Chem. C 125 (2021) 15316–15323, https://doi.org/10.1021/acs.jpcc.1c04065.
[52] A. Glotov, A. Vutolkina, A. Pimerzin, V. Vinokurov, Y. Lvov, Clay nanotube-metal core/shell catalysts for hydroprocesses, Chem. Soc. Rev. 50 (2021) 9240–9277, https://doi.org/10.1039/D1CS00502B.
[53] A. Stavitskaya, K. Mazurova, M. Kotelev, O. Eliseev, P. Gushchin, A. Glotov, R. Kazantsev, V. Vinokurov, Y. Lvov, Ruthenium-loaded halloysite nanotubes as mesocatalysts for Fischer–Tropsch synthesis, Molecules 25 (2020), https://doi.org/10.3390/molecules25081764.
[54] Y. Lvov, A. Panchal, Y. Fu, R. Fakhrullin, M. Kryuchkova, S. Batasheva, A. Stavitskaya, A. Glotov, V. Vinokurov, Interfacial self-assembly in halloysite nanotube composites, Langmuir 35 (2019) 8646–8657, https://doi.org/10.1021/acs.langmuir.8b04313.
[55] G. Cavallaro, S. Milioto, S. Konnova, G. Fakhrullina, F. Akhatova, G. Lazzara, R. Fakhrullin, Y. Lvov, Halloysite/keratin nanocomposite for human hair photoprotection coating, ACS Appl. Mater. Interfaces 12 (2020) 24348–24362, https://doi.org/10.1021/acsami.0c05252.
[56] A. Panchal, G. Fakhrullina, R. Fakhrullin, Y. Lvov, Self-assembly of clay nanotubes on hair surface for medical and cosmetic formulations, Nanoscale 10 (2018) 18205–18216, https://doi.org/10.1039/C8NR05949G.
[57] I. Fatimah, Preparation, characterization and physicochemical study of 3-amino propyl trimethoxy silane-modified kaolinite for Pb(II) adsorption, J. King Saud. Univ. Sci. 30 (2018) 250–257, https://doi.org/10.1016/j.jksus.2017.04.006.
[58] R. Duarte-Silva, M.A. Villa-García, M. Rendueles, M. Díaz, Structural, textural and protein adsorption properties of kaolinite and surface modified kaolinite adsorbents, Appl. Clay Sci. 90 (2014) 73–80, https://doi.org/10.1016/j.clay.2013.12.027.
[59] M. Catauro, Thermal and microbiological performance of metakaolin-based geopolymers cement with waste glass, Appl. Clay Sci. (2020) 9.

[60] X. Liu, J. Jiang, H. Zhang, M. Li, Y. Wu, L. Guo, W. Wang, P. Duan, W. Zhang, Z. Zhang, Thermal stability and microstructure of metakaolin-based geopolymer blended with rice husk ash, Appl. Clay Sci. 196 (2020), 105769, https://doi.org/10.1016/j.clay.2020.105769.
[61] G. Cavallaro, L. Chiappisi, P. Pasbakhsh, M. Gradzielski, G. Lazzara, A structural comparison of halloysite nanotubes of different origin by small-angle neutron scattering (SANS) and electric birefringence, Appl. Clay Sci. 160 (2018) 71–80, https://doi.org/10.1016/j.clay.2017.12.044.
[62] G. Cavallaro, G. Lazzara, V. Taormina, D. Cascio, Sedimentation of halloysite nanotubes from different deposits in aqueous media at variable ionic strengths, Colloids Surf. Physicochem. Eng. Asp. 576 (2019) 22–28, https://doi.org/10.1016/j.colsurfa.2019.05.038.
[63] F. Tardani, S. Casciardi, B. Ruzicka, S. Sennato, Salt enhanced sedimentation of halloysite nanotubes for precise determination of DNA adsorption isotherm, Colloids Surf. Physicochem. Eng. Asp. 605 (2020), 125400, https://doi.org/10.1016/j.colsurfa.2020.125400.
[64] B. Katana, D. Takács, E. Csapó, T. Szabó, A. Jamnik, I. Szilagyi, Ion specific effects on the stability of halloysite nanotube colloids—inorganic salts versus ionic liquids, J. Phys. Chem. B 124 (2020) 9757–9765, https://doi.org/10.1021/acs.jpcb.0c07885.
[65] X. Kang, Z. Xia, R. Chen, P. Liu, W. Yang, Effects of inorganic cations and organic polymers on the physicochemical properties and microfabrics of kaolinite suspensions, Appl. Clay Sci. 176 (2019) 38–48, https://doi.org/10.1016/j.clay.2019.04.024.
[66] T. Nasim, A. Pal, A. Bandyopadhyay, Flocculation of aqueous kaolin suspension using a biodegradable flocculant system of poly (vinyl alcohol)-Acacia nilotica gum blends, Appl. Clay Sci. 152 (2018) 83–92, https://doi.org/10.1016/j.clay.2017.10.035.
[67] J. Cao, X. Kang, B. Bate, Microscopic and physicochemical studies of polymer-modified kaolinite suspensions, Colloids Surf. Physicochem. Eng. Asp. 554 (2018) 16–26, https://doi.org/10.1016/j.colsurfa.2018.06.019.
[68] E.I. Benítez, D.B. Genovese, J.E. Lozano, Effect of typical sugars on the viscosity and colloidal stability of apple juice, Food Hydrocoll. 23 (2009) 519–525, https://doi.org/10.1016/j.foodhyd.2008.03.005.
[69] I. Blanco, G. Cicala, A. Latteri, G. Saccullo, A.M.M. El-Sabbagh, G. Ziegmann, Thermal characterization of a series of lignin-based polypropylene blends, J. Therm. Anal. Calorim. 127 (2017) 147–153, https://doi.org/10.1007/s10973-016-5596-2.
[70] I. Blanco, G. Cicala, C. Tosto, F.A. Bottino, Kinetic study of the thermal and thermo-oxidative degradations of polystyrene reinforced with multiple-cages POSS, Polymers 12 (2020) 2742, https://doi.org/10.3390/polym12112742.
[71] C. Cionti, T. Taroni, V. Sabatini, D. Meroni, Nanostructured oxide-based systems for the pH-triggered release of cinnamaldehyde, Materials 14 (2021), https://doi.org/10.3390/ma14061536.
[72] C. Duce, S. Vecchio Ciprioti, L. Ghezzi, V. Ierardi, M. Tinè, Thermal behavior study of pristine and modified halloysite nanotubes, J. Therm. Anal. Calorim. 121 (2015) 1011–1019, https://doi.org/10.1007/s10973-015-4741-7.
[73] G. Cavallaro, G. Lazzara, S. Milioto, Exploiting the colloidal stability and solubilization ability of clay nanotubes/ionic surfactant hybrid nanomaterials, J. Phys. Chem. C 116 (2012) 21932–21938, https://doi.org/10.1021/jp307961q.
[74] M. Wojdyr, ıt Fityk: a general-purpose peak fitting program, J. Appl. Crystallogr. 43 (2010) 1126–1128, https://doi.org/10.1107/S0021889810030499.

Journal Pre-proofs

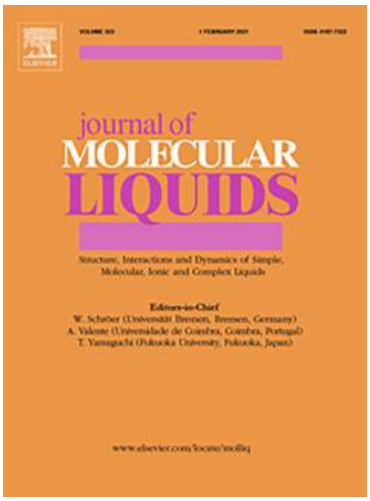

Hydrogel based on patch halloysite nanotubes: A rheological investigation

Martina Maria Calvino, Giuseppe Cavallaro, Pooria Pasbakhsh, Giuseppe Lazzara, Stefana Milioto

PII: S0167-7322(23)02528-X
DOI: https://doi.org/10.1016/j.molliq.2023.123721
Reference: MOLLIQ 123721

To appear in: *Journal of Molecular Liquids*

Received Date: 16 October 2023
Revised Date: 24 November 2023
Accepted Date: 30 November 2023

Please cite this article as: M. Maria Calvino, G. Cavallaro, P. Pasbakhsh, G. Lazzara, S. Milioto, Hydrogel based on patch halloysite nanotubes: A rheological investigation, *Journal of Molecular Liquids* (2023), doi: https://doi.org/10.1016/j.molliq.2023.123721

Hydrogel Based on Patch Halloysite Nanotubes: a Rheological Investigation

Martina Maria Calvino,[a] Giuseppe Cavallaro,[a,*] Pooria Pasbakhsh[b], Giuseppe Lazzara,[a] Stefana Milioto[a]

[a]*Dipartimento di Fisica e Chimica, Università degli Studi di Palermo, Viale delle Scienze, pad. 17, 90128 Palermo, Italy.* giuseppe.cavallaro@unipa.it

[b]*Department of Mechanical Engineering, School of Engineering, Monash University Sunway Campus, Bandar Sunway, 47500 Selangor, Malaysia*

Abstract

The rheological behaviour of Patch halloysite nanotubes (PT_Hal) was investigated here. Their peculiar morphology shows longer and thinner nanotubes and gives rise to the formation of gel-like systems that are not evidenced in halloysite from other natural sources. According to frequency sweep tests, PT_Hal possesses solid-like characteristics even at low concentrations, suggesting that the material is highly structured. Interestingly, flow ramp analysis evidenced two distinct behaviours based on the clay concentration: a yield stress was detected only from 0.75 wt%, indicating the sample's ability to resist deformation or breaking. Furthermore, the study investigated the influence of ionic strength, revealing that the addition of salt did not significantly affect the gel's properties of this clay. Accordingly, in this work we propose a new hydrogel system based on green nanoclays that can be suitable for industrial and biological applications as well as for cultural heritage.

Keywords: Halloysite nanotubes; rheology; hydrogel; patch halloysite

1. Introduction

Halloysite is a naturally occurring nanoclay with a unique hollow tubular structure. Generally, the length of halloysite nanotubes is approximately 1 μm, while the external and internal diameters vary within the ranges of 20 to 200 nm and 10 to 70 nm, respectively. Its properties and characteristics, such as the sizes, specific surface and polydispersity are influenced by the geological deposit from which they are sourced [1]. Among them, the Patch halloysite (PT_Hal), sourced from Western Australia, is acknowledged as a highly pure variety of halloysite (content of ca. 96%)[2]. These nanotubes exhibit thinner tubes and an exceptional length extending up to 30 μm. Moreover, they also stand up for their fibrous structure forming clusters that appear as patches. It is worth noting that the external and internal surfaces of halloysite have distinct chemical properties, with the former being negatively charged and the latter being positively charged across a wide pH range [3].

This characteristic enables the loading of negative molecules into the inner lumen and the interaction of positive active species with the outer surface. Halloysite also represents a versatile nanofiller that can be incorporated into biopolymeric matrices [4–6], obtaining green nanocomposite materials suitable for a wide range of applications, including medicine [7–10], cosmetics [11,12], packaging [13–15] and environmental remediation [16–25]. Moreover, halloysite nanotubes are effective as catalytic supports [26–32], additives for metal batteries [33,34] and nanocarriers for functional molecules with biological and chemical activities [35–39].

Most research studies exploring the use of halloysite nanotubes as nanomaterials have focused on halloysite derived from one of the primary sources, typically New Zealand or USA, but its properties can differ based on its origin, owing to the distinct local conditions under which it was formed [40]. For instance, Makaremi et al.[40] demonstrated that shorter nanotubes showed superior capacity in encapsulating salicylic acid within their hollow structure compared to patchy and longer halloysite nanotubes as they require additional time and energy to have the active molecule loaded in the tubes. On the other hand, it is known that halloysite does not form gel itself. Actually, Luo et al. [41] proved that the sol–gel transition occurs at a concentration of ca. 40 wt% and the aqueous dispersion exhibits a pH-induced gelation when hydrochloric acid is added, due to the reduced repulsive electrostatic forces between the nanotubes.

Thus, our study wants to point out that, thanks to its peculiar fibrous structure, Patch has different rheological features with respect to halloysite from other natural sources. Accordingly, a rheological study on patch halloysite samples at different concentrations is presented here.

In addition, literature reports that the colloidal stability of nanoclays can be influenced by several factors, including the addition of polymers [42,43] as well as the ionic strength [44]. Moreover, changing the ionic strength in a system can also have significant effects on gel-like structures [45,46], such as swelling [47], increased stability [48] or viscosity due to stronger interactions with the components of the gel [49]. Since, according to the literature, NaCl concentration affects the settling velocity of halloysite dispersions, we also investigated its influence in the PT_Hal hydrogels in this study.

2. Materials and methods

2.1 Materials

Ultra HalloPure Halloysite (UP_Hal) was a gift by I-Minerals Inc. mined in the geological deposit of Latah County

(NW Idaho, North America) and Patch Halloysite (PT_Hal) (Kalgoorie, Western Australia) is a kind donation provided by Dr. Keith Norrish from his collection and research on Patch (CSIRO Soils, Adelaide). NaCl (> 99%, CAS 7647-14-5) and NaOH pellets (≥ 98%, CAS 1310-73-2) were Sigma Aldrich products.

2.2 Patch halloysite purification

The separation of coarse impurities was performed by following a procedure reported elsewhere for PT_Hal samples [1,2]. In particular, 5 grams of PT_Hal were grounded in a mortar. The obtained powder was dispersed in deionized water and the pH was set between 7.5 and 8 by using a sodium hydroxide solution 0.1 M. Several cycles of sonication and washing in 1.5 L of water were carried out to purify the sample. After that, the dispersion was filtered by a peristaltic pump to exclude coarse residuals and dried at 50 °C for 48 hours.

2.3 Hydrogel preparation

Patch halloysite, after purification, was dispersed in deionized water at different concentrations: 0.005, 0.1, 0.5, 0.75, 1 and 2 wt%. Then, samples were sonicated for 15 minutes and stirred for 48 hours to avoid the formation of aggregates.

The same procedure was performed to prepare UP_Hal samples for comparison at 1 wt%.

Patch halloysite nanotubes were added to NaCl aqueous solutions at four different concentrations (10^{-1}, 10^{-2}, 10^{-3} and 10^{-4} M) and the obtained dispersions were sonicated for 15 min and magnetically stirred for 2 days.

2.4 Methods

2.4.1 Thermogravimetric Analysis (TGA)

Thermogravimetric experiments were carried out using a Q5000 IR apparatus (TA Instruments) under inert atmosphere using nitrogen flows of 25 and 10 cm^3 min^{-1} for the sample and the balance, respectively. Samples were heated in a platinum pan from room temperature to 800 °C with a scanning rate of 20 °C min^{-1}.

2.4.2 X-ray Fluorescence (XRF)

X-ray Fluorescence (XRF) Spectrometry was performed using an Olympus Innov X DS-2000 Delta Standard Alloy XRF Handheld Analyzer operating in the Alloy Plus analysis mode.

2.4.3 ζ-Potential

ζ-Potential measurements were performed by means of a Zetasizer NANO-ZS (Malvern Instruments) under isothermal conditions at 25.0 ± 0.1 °C. The tests were carried out by using a disposable folded capillary cell and the concentration of PT_Hal dispersion was 0.001 wt%. The ζ-potential was calculated using the Smoluchowski approximation, which is considered an accurate approximation for particles larger than 0.2 μm in aqueous solutions. All experiments were replicated three times, and the average values were reported.

2.4.4 X-ray Diffraction (XRD)

The patterns were obtained from an X-ray diffractometer (Rigaku, MiniFlex) with a CuKa radiation source including a nickel filter and working at 40 kV and 15 mA. The wavelength of the X-ray beam was 1.5406 Å, and the layer spacing of the samples was calculated by the Bragg's equation, which can be expressed as

$$n\lambda = 2d\sin\theta \quad (1)$$

where θ is the angle that the outgoing beam forms with the crystalline layer, λ is the wavelength of the radiation, d is the distance between two adjacent layers and n can be 1,2 or 3.

The angle for scanning ranged from 2 ° to 70 ° with a rate of 20 ° min^{-1} and a step of 0.02°.

2.4.5 Scanning electron microscopy

The ultra-high resolution field emission scanning electron microscope (FE-SEM, Hitachi SU8010) was used to observe the morphologies of halloysite nanotubes. A thin layer of platinum was applied to coat the samples in order to avoid electrostatic charging. Additionally, the morphology of halloysite nanotubes was also observed using the transmission mode (STEM) of the same FE-SEM instrument with a voltage of 30 kv.

2.4.6 Rheology

The rheological characterization of PT_Hal dispersions was studied using a Discovery HR-1 rheometer (TA Instruments) with a parallel plate geometry (800-1000 μm gap and 20 mm diameter). Amplitude sweep, frequency sweep and flow ramp stress tests were performed after conditioning the sample at 25 °C. The amplitude sweep tests were conducted at a constant angular frequency of 100 rad s^{-1} while increasing the oscillation strain from 0,001 % and 100 %. For frequency sweep tests, the angular frequency was ranged from 0.1 to 100 rad s^{-1} at a fixed strain amplitude of 0.1 %. Flow ramp tests were instead performed increasing the stress from 0 to 50 Pa.

3. Results and Discussion

3.1 Patch Purification

XRF measurement allowed to obtain the chemical composition of UP_Hal and PT_Hal before and after the purification. As reported in Table 1, PT_Hal not purified (PT_Hal_NP) presents lower silicon content than the same sample after purification (PT_Hal_P) which has an enrichment of 6% in silicon. Moreover, PT_Hal_P shows a decrease of the amount of Ti, Mg, Cr and Mn. On the other hand, iron content is nearly constant after purification, and it is present in a minimal amount.

It has been previously reported [2,50] that patch halloysite samples usually contain less than 1 % of iron. Actually, we found a value of 2.52% in PT_Hal_NP that can be attributed to the different levels of iron oxide contamination. As a matter of fact, Churchman et al.[50] stated that, even if iron is not part of the structure, it can influence the size of halloysite particles by restraining crystal growth. The substitution of the smaller Al^{3+} ion with the larger Fe^{3+} ion in the octahedral sheet of halloysite can also happen with high levels of Fe_2O_3 (ca. 4%) leading to more planar layers as in kaolinite. This is reflected by the fact that halloysite with long tubular particles tends to contain low Fe content whereas shorter and approximately platy particles often contain high levels of structural Fe, as demonstrated by the results reported in Table 1 for UP_Hal. Moreover, besides the amount of iron, it showed very similar chemical composition compared to PT_Hal. In general, the obtained XRF results are also in agreement with literature data reported elsewhere [51] for halloysite nanotube samples.

Table 1. Chemical composition of UP_Hal and PT_Hal samples before and after the purification.

Sample	Al/ wt%	Si/ wt%	Mg/ wt%	Fe/ wt%	Ti/ wt%	Cr/ wt%	Mn/ wt%
UP_Hal	41.7±0.4	52.1±0.4	1.4±0.6	3.89±0.09	0.8±0.1	ND	0.08±0.02
PT_Hal_P	41.1±0.3	53.5±0.3	1.2±0.4	2.99±0.06	0.47±0.09	0.18±0.02	ND
PT_Hal_NP	41.05±0.4	46.8±0.4	2.2±0.6	2.52±0.07	6.7±0.2	0.20±0.03	0.07±0.01

Thermogravimetric curves of UP_Hal, purified and not purified PT_Hal are reported in Fig. 1. All the samples exhibited the two mass losses typical of halloysite: the first one until 150 °C and the second one in the range between 350 and 550 °C, respectively related to physically adsorbed water molecules and the dehydroxylation of aluminium inner sheets. The residual mass at 800 °C and the mass losses at each step (30-150 °C and 350-550 °C) are reported in Supporting Information (Table S1). Concerning the first mass loss, UP_Hal showed the lowest value (1.17%) compared to the PT_Hal samples. Furthermore, the main difference between the two samples of Patch halloysite is related to the percentage of the first mass loss and consequently the residual mass at 800 °C. It is equal to 82% for the purified PT_Hal and 79% for the not purified PT_Hal. During the purification protocol, impurities have been washed away and consequently, we observed a lower value of residual mass in PT_Hal_P. On the other hand, the second mass loss is comparable for the three investigated samples.

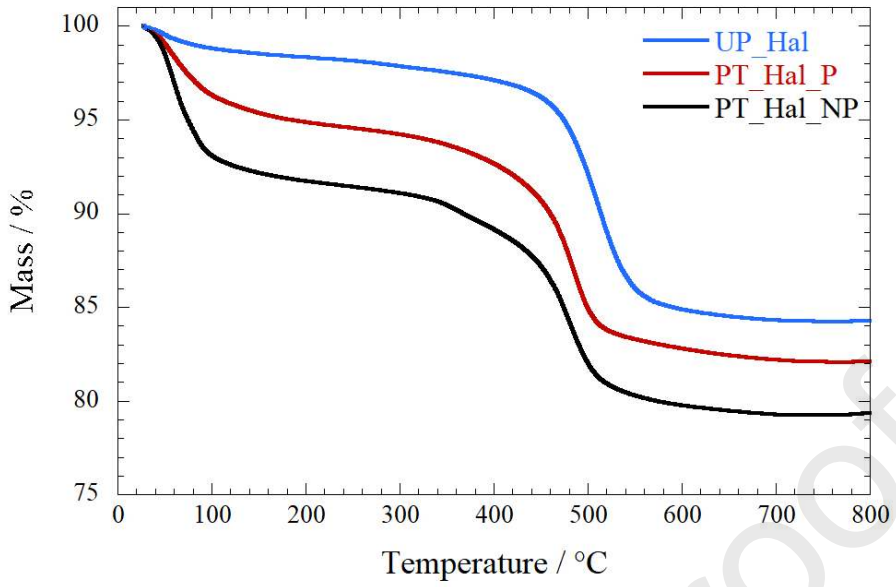

Fig. 1. Thermogravimetric curves of UP_Hal, non-purified (PT_Hal_NP) and purified (PT_Hal_P) Patch Halloysite.

3.2 Comparison between PT_Hal and UP_Hal

Before deeply analysing the rheological behavior of these peculiar clays, we focused our attention on the differences occurring between them.

A morphological characterization of PT_Hal and UP_Hal is presented in Fig. 2. SEM micrographs reveal that PT_Hal exhibits much greater length and thinness of the tubes. They are characterized by outer diameters ranging from 40 to 55 nm, inner diameters between 12 and 22 nm and lengths ranging from 200 to 30,000 nm. Moreover, PT_Hal tubes are entangled and bent, forming a structure similar to a bird nest. Since the walls are very thin, they are susceptible to breakage into shorter fragments, but still intact tubes can be observed as bundles of tightly packed parallel tubes.

On the other hand, UP_Hal, possesses shorter and stubby tubes ranging in length from 100 nm to 2 µm, while the outer diameter ranges between 100 and 200 nm and the inner diameter between 10 and 70 nm (Fig.2.(g)).

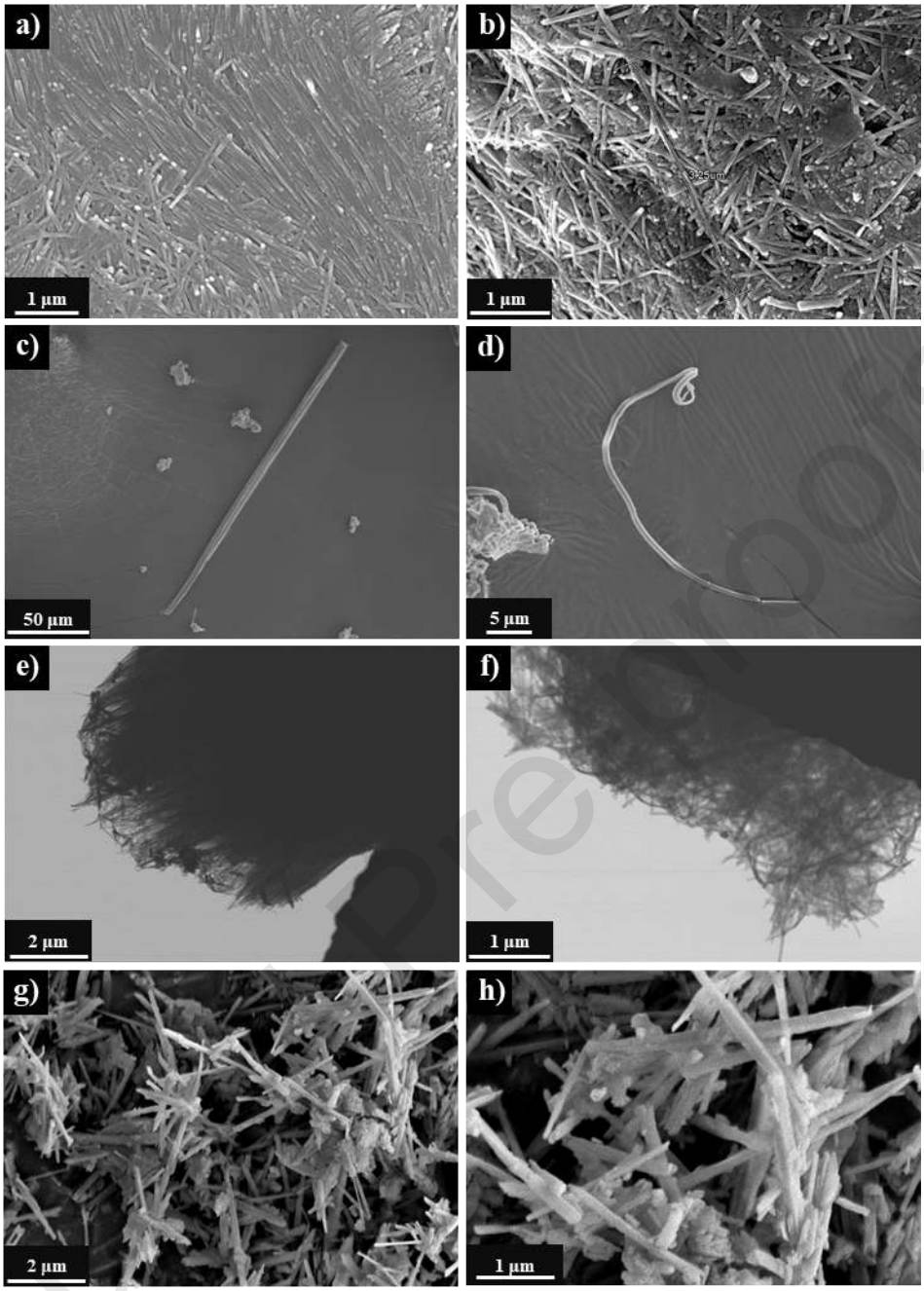

Fig.2. Morphological properties of pure Patch and UltraPure Halloysite. (a-d) Scanning electron microscopy micrographs of PT_Hal_P (e-f) Scanning transmission electron microscopy micrographs showing patchy entangled halloysite nanotubes of PT_Hal_P (g) Scanning transmission electron microscopy micrographs of UP_Hal.

X-ray diffraction patterns of both UP_Hal and PT_Hal exhibited the typical diffraction pattern of dehydrated halloysite (Fig. S1). The dehydration of Patch was previously reported [52] by following the continuous collection of XRD patterns whilst in situ heating and it was showed that the dehydration produces some irregular d-spacings probably due to the interstratification of hydrated and dehydrated halloysite layers and the interference between the regular flattened tubes with ca. 8 Å d-spacing. In particular, peaks were observed at 2θ = 12.0, 19.9, 24.7, 35.0, 38.3, 54.9 and 62.4

corresponded to (001), (100), (002), (110), (003), (210) and (300) planes, respectively [53]. The (001) plane corresponds to a basal spacing of 0.72 nm, which identifies these samples as halloysite-(7 Å).

Traces of quartz were identified only in the PT_Hal sample, corresponding to a sharp peak at 2θ= 26° and 60°.

A qualitative evaluation of the gel formation is shown in Fig 3. We reported the images of PT_Hal and UP_Hal 1 wt % before and after the inversion. Despite the same concentration of PT_Hal, it is stable to the tube inversion test showing a gel-like structure compared to the same or even higher concentrations of UP_Hal in which it is not evidenced.

Fig. 3. Inversion test of PT_Hal and UP_Hal 1 wt%.

3.3 Rheological characterization of PT_Hal

Aimed to characterize the viscoelastic behavior of the clay, amplitude sweep tests were performed by measuring the strain amplitude dependence of the storage and loss moduli (G', G").

In Fig. 4 we reported two concentrations as examples of the more comprehensive concentration range investigated in this work, just to show the linear viscoelastic regions. Namely, below 10 % strain, G' is higher than G", for both PT_Hal at 1 and 2 wt %, suggesting a gel-like structure. As a matter of fact, in this region both moduli remain constant, indicating the presence of the linear viscoelastic region. The crossover strain points are clearly displayed after 10 % strain and their values were calculated determining the point at which G'=G". As shown in Fig 4, the crossing points between G' and G" moduli are shifted to higher oscillation strain by increasing the clay concentration. Specifically, they are at 16.30 % and 45.52% for PT_Hal 1 and 2 wt %, respectively.

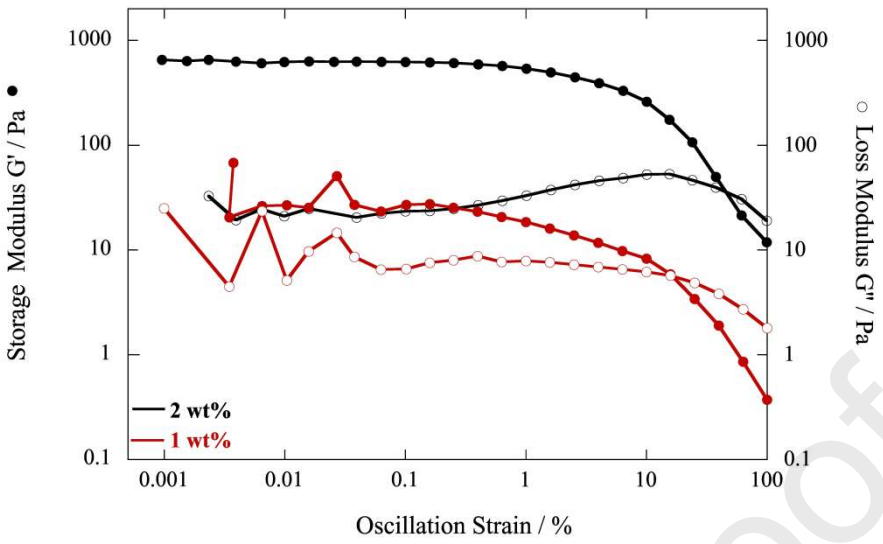

Fig. 4. Amplitude sweep tests of PT_Hal. Full and empty symbols indicate Storage modulus (G') and Loss modulus (G"), respectively**.**

Having pinpointed the linear viscoelastic regions, angular frequency sweep tests were performed, imposing a constant strain on the systems at variable frequency. Usually, frequency sweep curves give a rheological description of the product behavior during storage and application [54–56]. The obtained rheological data are displayed in Fig 5a), showing G' and G" moduli as a function of the angular frequency. As a general result, the storage modulus (G') is larger than the loss modulus (G") in the entire range of frequency. Namely, for a gel-like material G' and G" curves are constant, remarking that PT_Hal behaves like a solid and suggesting that the material is highly structured starting from a concentration of 0.75 wt%. High frequencies correspond to short time scales and low frequencies to longer time scales. This means that the gel-like structure is time-independent [57,58], highlighting their stability over time. Moreover, Fig 5b) shows that increasing the concentration both moduli increase and the G' medium values are higher than G" from 0.005 wt% along the angular frequency range investigated.

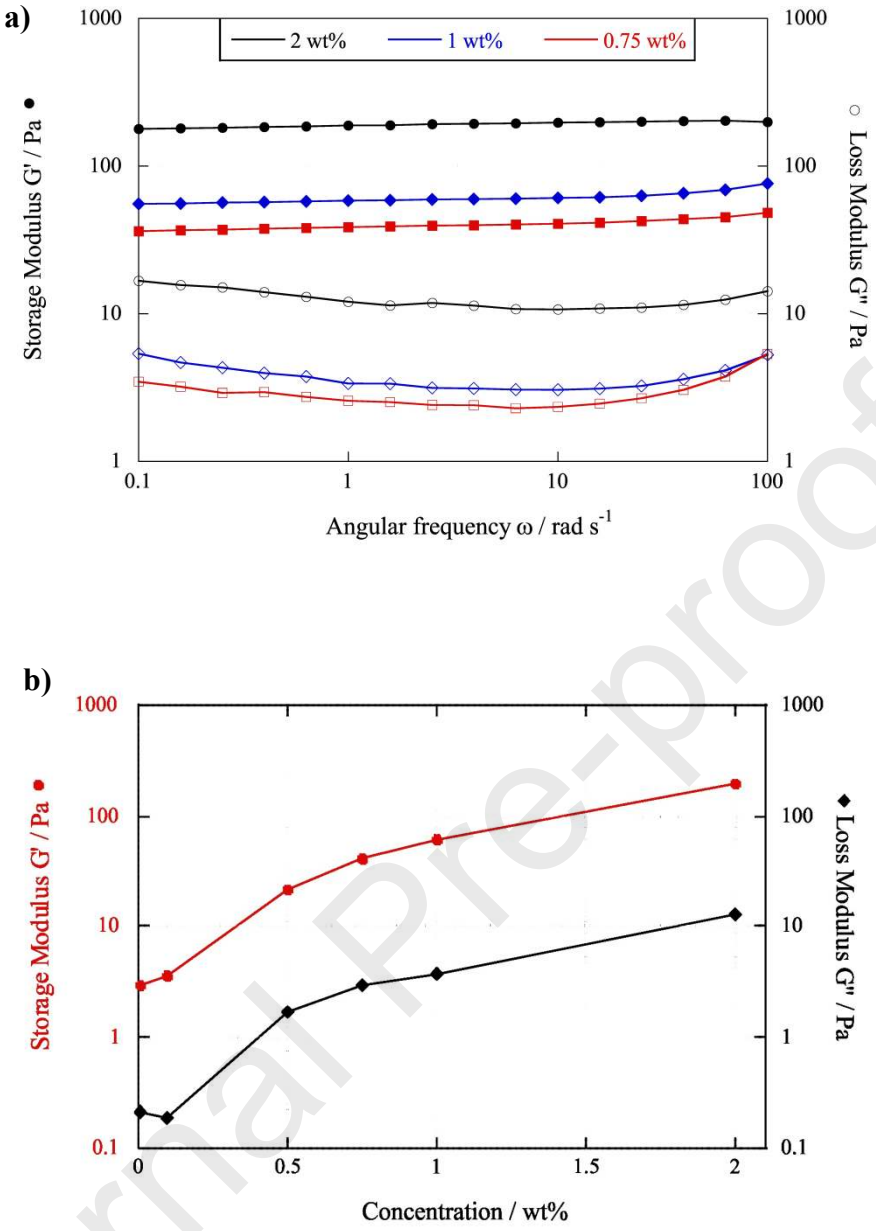

Fig. 5. a) Results of angular frequency sweep tests on PT_Hal at 2, 1 and 0.75 wt%. Full and empty symbols indicate Storage modulus (G') and Loss modulus (G"), respectively. b) Storage and Loss moduli as a function of the clay concentration.

We calculated the average tanδ values within the angular frequency range between 0.1 and 100 rad s^{-1} by G''/G' ratios. The obtained data (see Supporting Information) confirmed the solid-like behavior of the hydrogels being that tanδ is lower than 0.1 for all the investigated dispersions. We detected that tanδ is nearly constant throughout the entire concentration range highlighting the predominance of the elastic contribution.

The viscosity as a function of the shear rate can provide relevant information about its performance and processing. With this in mind, flow curves are reported in Fig 6. The viscosity displays higher values increasing the concentration of the clay. Accordingly, the most considerable difference is evidenced for PT_Hal 2 wt%, which presents an order of magnitude of increment with respect to 1 wt%. It is clear that the microstructure plays a crucial role in determining the rheological behavior of the system. In this case, two phenomena should be taken into consideration to explain the rheology of Patch halloysite.

The first is that increasing the concentration, the interactions between the nanotubes are enhanced promoting a higher viscosity of the system. Another crucial factor is represented also by the presence of a bird nest structure in PT_Hal in which the nanotubes are entangled with each other and bent[40], reducing the free water diffusion between the nanotubes. In this regard, geometrical considerations can give a more comprehensive view about the influence of the tube's morphology on the rheology. We can consider a contact distance given by the average length of the nanotubes and assume a simple cubic model to calculate the critical overlapping volume fraction φ*:

$$\varphi^* = \pi R^2 / L^2 \quad (2)$$

where R and L are the external radius and the length of the nanotubes, respectively. Volume fraction values of ca. 4–10% for aqueous dispersions of halloysite from Dragon Mine have been previously reported [3]. Here, the calculated φ*, by considering average values for R and L [2], are 3.1% for UP_Hal and 0.03% for PT_Hal. This means that the volume required to generate the nanotubes entanglement is 100 times lower for PT_Hal than UP_Hal. Namely, the critical concentration for the hydrogel formation is reached at lower concentration for PT_Hal samples with respect to shorter and stubby halloysite clay nanotubes.

Moreover, the presence of this network-like structures in PT_Hal, reduces the fluid flow, contributing to the higher viscosity of the system [59,60].

On the other hand, the viscosity below 0.75 wt% assumes low values pointing out that the network is not structured as in 1 wt%. As a result of this transition, the material undergoes a change from an apparently solid state to a liquid state, allowing it to flow easily. All the samples, starting from a shear stress of 0.1 s^{-1} exhibited shear thinning, as represented by the decrease of viscosity with increasing the shear rate. This phenomenon is requested in hydrogel for biomedical applications since they should exhibit viscous flow under shear stress and self-healing properties as reported elsewhere [61,62].

It should be noted that PT_Hal 0.75, 1 and 2 wt% at very low shear rate exhibited an increase of the viscosity up to a critical value, beyond which it decreases. Thus, this indicates the presence of yield stress that is better evidenced in Fig 7. where the shear stress as a function of the shear rate is reported.

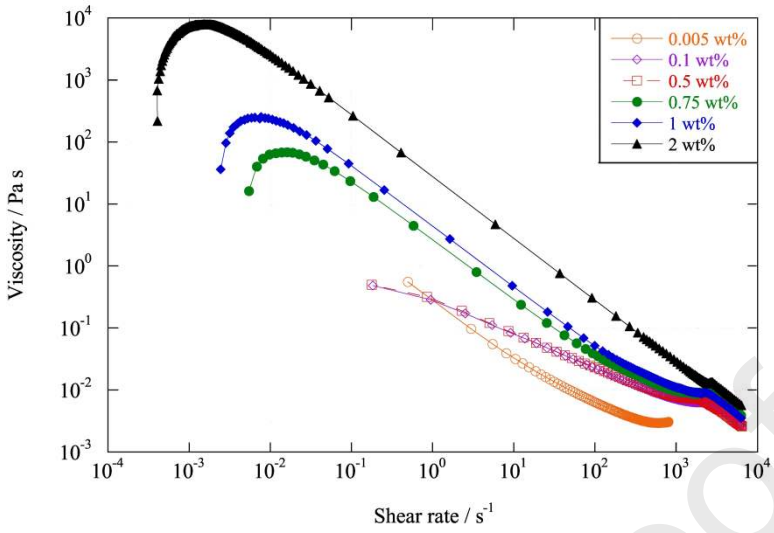

Fig. 6. Flow ramp tests showing the viscosity as a function of the shear rate.

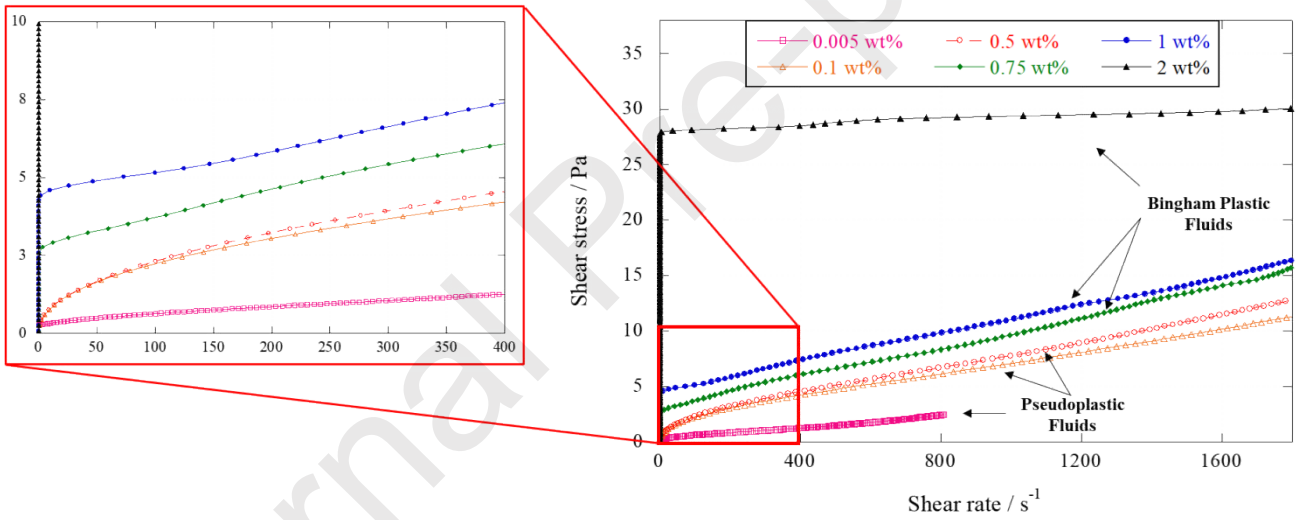

Fig. 7. Shear stress as a function of the shear rate. The inset shows a magnification highlighting different types of flow behaviour.

Accordingly, the yield stress reflects the resistance of the sample structure to deformation or break and it is detected starting from PT_Hal 0.75 wt%. The flow begins when an applied stress is strong enough to disturb the gel-like structure of the material, resulting in a significant decrease in viscosity, as previously shown in Fig 6. This is better highlighted by looking at the inset in Fig 7, where the yield stress is not evidenced up to a concentration of 0.5 wt% and these curves start from 0 Pa, meaning that the material flows and it is easily deformable. On the contrary, the yield stress of PT_Hal 2 wt% is remarkable as it is significantly higher than less concentrated samples, reaching a value of ca. 28 Pa (Table 2).

Thus, we can state that PT_Hal is a non-Newtonian fluid and specifically, it can be classified as a Pseudoplastic fluid at low concentration and as Bingham Plastic fluid at concentrations greater than 0.5 wt%.

Table 2. Yield stress values.

Sample	Yield Stress σ_0 / Pa
PT_Hal 0.005 wt %	0
PT_Hal 0.1 wt %	0
PT_Hal 0.5 wt %	0
PT_Hal 0.75 wt %	3.07
PT_Hal 1 wt %	4.69
PT_Hal 2 wt %	28.08

To better investigate the rheological properties of Patch halloysite, the Carreau (Eq. 3)) and Carreau-Yasuda models (Eq. (4)) were applied to the experimental flow curves obtaining the fitting parameters reported in Table S3.

$$\frac{\eta - \eta_\infty}{\eta_0 - \eta_\infty} = \frac{1}{[1 + (k\dot{\gamma})^2]^{\frac{n}{2}}} \quad (3)$$

$$\frac{\eta - \eta_\infty}{\eta_0 - \eta_\infty} = [1 + (k\dot{\gamma})^a]^{\frac{n-1}{a}} \quad (4)$$

Here, η_0 is the viscosity at zero shear rate, η_∞ is the viscosity at infinite shear rate, k represents the consistency index or relaxation time and n and a are two dimensionless parameters. The Carreau-Yasuda model is an extension of the Carreau model. In particular, the main difference between the two models is linked to the ability to capture shear thinning or thickening behaviours. The Carreau model is usually referred to as shear thinning, meaning that the fluid viscosity decreases as the shear rate increases. In contrast, the Carreau Yasuda model is used for both shear thinning and thickening behaviours [63]. The presence of yield stress led to the Carreau Yasuda model to better fit the analysed curves as reported in Supporting Information (Table S3).

An increase in zero-shear rate viscosity and consistency with increasing PT_Hal concentration is detected and showed in Fig. 8.

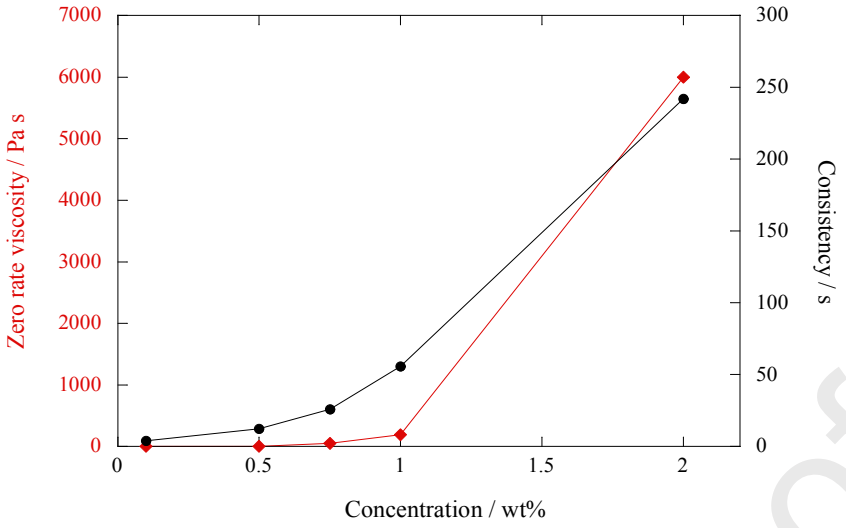

Fig. 8. Zero-shear rate viscosity and consistency as a function of concentration.

3.4 Effect of ionic strength

The ionic strength can have a strong impact on gel-like structures, and it was widely reported in literature[64,65]. For example, it has been demonstrated that the addition of NaCl can weaken the gel structure of cellulose nanocrystal suspensions and decrease the viscosity as well[66]. With this in mind, the effect of ionic strength on the investigated gels was evaluated. Accordingly, flow ramp tests performed on PT_Hal 1 wt% in water and at different NaCl concentrations are reported in Fig. 9. It can be noted that the gel-like network is not destroyed by adding the salt and with respect to water, lower concentrations of NaCl do not affect the rheology properties. As a matter of fact, the viscosity curves of PT_Hal in water and in NaCl 10^{-4} M are overlapped. There is a small effect of ionic strength increasing the NaCl concentration evidenced by a minimal increase of viscosity.

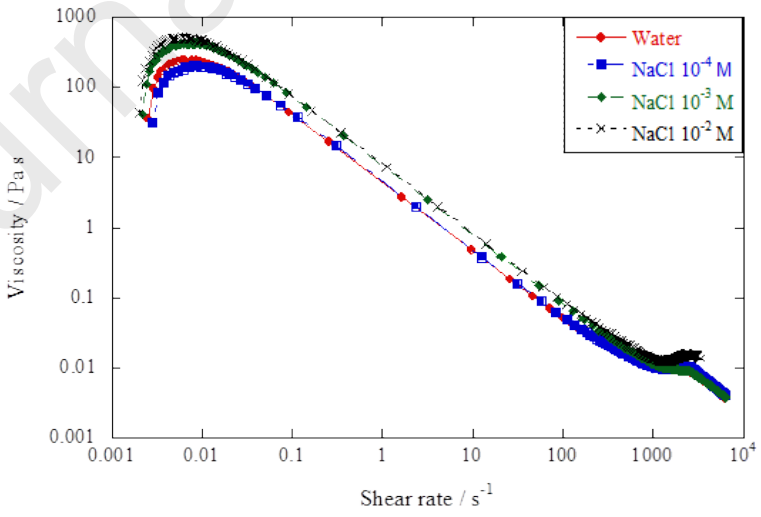

Fig. 9. Flow ramp tests. Viscosity as a function of the shear rate for PT_Hal 1 wt % in water and NaCl at different concentrations.

ζ potential measurements were carried out in order to have information about the surface charge of the nanotubes. As reported by Cavallaro et al.[44], although Hal from different natural sources can show similar responses to salt addition, they present differences in the effective charge that can influence their colloidal stability. The surface charge (σ) was estimated from the ζ potential values as established by the Grahame equation:

$$\sigma = (8\mathrm{RT}\varepsilon\varepsilon_0\mathrm{C})^{\frac{1}{2}}\sinh\left(\frac{Ze\zeta}{2k_bT}\right) \quad (5)$$

where ε is the solvent relative dielectric constant, ε_0 is the vacuum dielectric constant, C is the bulk concentration of electrolyte, e is the electron elemental charge, and Z is 1 for NaCl.

As shown in Table 3, the addition of NaCl generated a slight decrease of the absolute value of ζ potential for PT_Hal. These results can be explained by considering the screening effect of Na^+ ions towards the negative surface charge of PT_Hal. Namely, the presence of the electrolyte in the aqueous medium caused a reduction of the Debye length inducing a decrease of ζ potential absolute value. As expected, the screening effect was enhanced by increasing the ionic strength of the aqueous dispersion. Similar results were observed for halloysite nanotubes from other sources (Matauri Bay and Dragon Mine) [44].

Table 3. ζ Potential PT_Hal samples in water and NaCl.

Sample	ζ Potential / mV	Surface charge σ / mC m^{-2}
PT_Hal	-17.5	/
PT_Hal/NaCl 10^{-4} M	-15.5	$1.13\cdot10^{-5}$
PT_Hal/NaCl 10^{-2} M	-14.0	$1.02\cdot10^{-4}$

4. Conclusions

This work aims to characterize PT_Hal clay samples from a rheological point of view, highlighting that clay microstructure plays a key role on it. As a matter of facts, their different morphology led to peculiar physico-chemical properties that are not evidenced in UP_Hal. PT_Hal shows thinner and longer tubes creating a structure similar to a bird nest allowing the formation of gel-like structures. It was proved by dynamic viscoelastic tests that PT_Hal is a non-Newtonian fluid and G' is higher than G", meaning that the system is highly structured. Flow curves provided information about the viscosity related to shear rates, which is crucial in the production field where the product is subjected to stirring and pumping processes and namely different shear rates. Accordingly, two different behaviours were evidenced depending on the clay concentration: from 0.75 wt% a yield stress is

detected, reflecting the sample's ability to withstand deformation, or breaking. The effect of ionic strength was also evaluated, showing that the addition of salt doesn't affect the properties of the gel since there isn't a significant change in both ζ potential and viscosity of PT_Hal samples.

Acknowledgments. The work was financially supported by FFR 2023 and University of Palermo.

This work was funded by the European Union (NetGeneration EU) through the MUR-PNRR project SAMOTHRACE (ECS00000022).

We also thank John Keeling (EX: Geological Survey of South Australia) and Jock Churchman (University of Adelaide) for the given support to Pooria Pasbakhsh (one of the co-authors of this paper) during his research on halloysite in 2010.

References

[1] G. Cavallaro, L. Chiappisi, P. Pasbakhsh, M. Gradzielski, G. Lazzara, A structural comparison of halloysite nanotubes of different origin by Small-Angle Neutron Scattering (SANS) and Electric Birefringence, Appl. Clay Sci. 160 (2018) 71–80. https://doi.org/10.1016/j.clay.2017.12.044.

[2] P. Pasbakhsh, G.J. Churchman, J.L. Keeling, Characterisation of properties of various halloysites relevant to their use as nanotubes and microfibre fillers, Appl. Clay Sci. 74 (2013) 47–57. https://doi.org/10.1016/j.clay.2012.06.014.

[3] G. Lazzara, G. Cavallaro, A. Panchal, R. Fakhrullin, A. Stavitskaya, V. Vinokurov, Y. Lvov, An assembly of organic-inorganic composites using halloysite clay nanotubes, Curr. Opin. Colloid Interface Sci. 35 (2018) 42–50. https://doi.org/10.1016/j.cocis.2018.01.002.

[4] D.L. Francisco, L.B. Paiva, W. Aldeia, A.B. Lugão, E.A.B. Moura, Noncovalently Functionalized Halloysite Nanotubes for Use in Reinforced Polymer Composites, ACS Appl. Nano Mater. 3 (2020) 11510–11516. https://doi.org/10.1021/acsanm.0c02600.

[5] E. Abdullayev, Y. Lvov, Halloysite clay nanotubes as a ceramic "skeleton" for functional biopolymer composites with sustained drug release, J. Mater. Chem. B. 1 (2013) 2894–2903. https://doi.org/10.1039/C3TB20059K.

[6] G. Cavallaro, G. Lazzara, S. Milioto, Nanocomposites based on halloysite nanotubes and sulphated galactan from red seaweed Gloiopeltis: Properties and delivery capacity of sodium diclofenac, Int. J. Biol. Macromol. 234 (2023) 123645. https://doi.org/10.1016/j.ijbiomac.2023.123645.

[7] M.K. Pierchala, M. Makaremi, H.L. Tan, J. Pushpamalar, S. Muniyandy, A. Solouk, S.M. Lee, P. Pasbakhsh, Nanotubes in nanofibers: Antibacterial multilayered polylactic acid/halloysite/gentamicin membranes for bone regeneration application, Appl. Clay Sci. 160 (2018) 95–105. https://doi.org/10.1016/j.clay.2017.12.016.

[8] Y.M. Lvov, M.M. DeVilliers, R.F. Fakhrullin, The application of halloysite tubule nanoclay in drug delivery, Expert Opin. Drug Deliv. 13 (2016) 977–986. https://doi.org/10.1517/17425247.2016.1169271.

[9] Y. Feng, Y. He, X. Lin, M. Xie, M. Liu, Y. Lvov, Assembly of Clay Nanotubes on Cotton Fibers Mediated by Biopolymer for Robust and High-Performance Hemostatic Dressing, Adv. Healthc. Mater. 12 (2023) 2202265. https://doi.org/10.1002/adhm.202202265.

[10] R. Li, Y. Zhang, Z. Lin, Q. Lei, Y. Liu, X. Li, M. Liu, G. Wu, S. Luo, H. Wang, X. Zheng, L. Li, N. Ao, Z. Zha, Injectable halloysite-g-chitosan hydrogels as drug carriers to inhibit breast cancer recurrence, Compos. Part B Eng. 221 (2021) 109031. https://doi.org/10.1016/j.compositesb.2021.109031.

[11] A. Panchal, G. Fakhrullina, R. Fakhrullin, Y. Lvov, Self-assembly of clay nanotubes on hair surface for medical and cosmetic formulations, Nanoscale. 10 (2018) 18205–18216. https://doi.org/10.1039/c8nr05949g.

[12] A. Melnyk, O. Chyhyrynets, G. Lazzara, Encapsulation of α-Lipoic Acid in Halloysite Nanotubes, Appl. Sci. 13 (2023) 10214. https://doi.org/10.3390/app131810214.

[13] L. Ghezzi, A. Spepi, M. Agnolucci, C. Cristani, M. Giovannetti, M.R. Tiné, C. Duce, Kinetics of release and antibacterial activity of salicylic acid loaded into halloysite nanotubes, Appl. Clay Sci. 160 (2018) 88–94. https://doi.org/10.1016/j.clay.2017.11.041.

[14] G. Gorrasi, R. Pantani, M. Murariu, P. Dubois, PLA/Halloysite Nanocomposite Films: Water Vapor Barrier Properties and Specific Key Characteristics, Macromol. Mater. Eng. 299 (2014) 104–115. https://doi.org/10.1002/mame.201200424.

[15] G. Gorrasi, V. Senatore, G. Vigliotta, S. Belviso, R. Pucciariello, PET–halloysite nanotubes composites for packaging application: Preparation, characterization and analysis of physical properties, Eur. Polym. J. 61 (2014) 145–156. https://doi.org/10.1016/j.eurpolymj.2014.10.004.

[16] X. Zhao, Y. Luo, P. Tan, M. Liu, C. Zhou, Hydrophobically modified chitin/halloysite nanotubes composite sponges for high efficiency oil-water separation, Int. J. Biol. Macromol. 132 (2019) 406–415. https://doi.org/10.1016/j.ijbiomac.2019.03.219.

[17] N. Danyliuk, J. Tomaszewska, T. Tatarchuk, Halloysite nanotubes and halloysite-based composites for environmental and biomedical applications, J. Mol. Liq. 309 (2020). https://doi.org/10.1016/j.molliq.2020.113077.

[18] J. Kurczewska, M. Cegłowski, G. Schroeder, PAMAM-halloysite Dunino hybrid as an effective adsorbent of ibuprofen and naproxen from aqueous solutions, Appl. Clay Sci. 190 (2020). https://doi.org/10.1016/j.clay.2020.105603.

[19] M.M. Calvino, L. Lisuzzo, G. Cavallaro, G. Lazzara, S. Milioto, Halloysite based geopolymers filled with wax microparticles as sustainable building materials with enhanced thermo-mechanical performances, J. Environ. Chem. Eng. 10 (2022). https://doi.org/10.1016/j.jece.2022.108594.

[20] B. Micó-Vicent, F.M. Martínez-Verdú, A. Novikov, A. Stavitskaya, V. Vinokurov, E. Rozhina, R. Fakhrullin, R. Yendluri, Y. Lvov, Stabilized Dye–Pigment Formulations with

Platy and Tubular Nanoclays, Adv. Funct. Mater. 28 (2018) 1703553. https://doi.org/10.1002/adfm.201703553.

[21] O. Owoseni, Y. Su, S. Raghavan, A. Bose, V.T. John, Hydrophobically modified chitosan biopolymer connects halloysite nanotubes at the oil-water interface as complementary pair for stabilizing oil droplets, J. Colloid Interface Sci. 620 (2022) 135–143. https://doi.org/10.1016/j.jcis.2022.03.142.

[22] A. Panchal, L.T. Swientoniewski, M. Omarova, T. Yu, D. Zhang, D.A. Blake, V. John, Y.M. Lvov, Bacterial proliferation on clay nanotube Pickering emulsions for oil spill bioremediation, Colloids Surf. B Biointerfaces. 164 (2018) 27–33. https://doi.org/10.1016/j.colsurfb.2018.01.021.

[23] E. Zandi-Mehri, L. Taghavi, F. Moeinpour, I. Khosravi, S. Ghasemi, Designing of hydroxyl terminated triazine-based dendritic polymer/halloysite nanotube as an efficient nano-adsorbent for the rapid removal of Pb(II) from aqueous media, J. Mol. Liq. 360 (2022) 119407. https://doi.org/10.1016/j.molliq.2022.119407.

[24] J. Zare Pirhaji, F. Moeinpour, A. Mirhoseini Dehabadi, S.A. Yasini Ardakani, Synthesis and characterization of halloysite/graphene quantum dots magnetic nanocomposite as a new adsorbent for Pb(II) removal from water, J. Mol. Liq. 300 (2020) 112345. https://doi.org/10.1016/j.molliq.2019.112345.

[25] A. Kausar, M. Iqbal, A. Javed, K. Aftab, Z.-H. Nazli, H.N. Bhatti, S. Nouren, Dyes adsorption using clay and modified clay: A review, J. Mol. Liq. 256 (2018) 395–407. https://doi.org/10.1016/j.molliq.2018.02.034.

[26] S. Sadjadi, M.M. Heravi, M. Malmir, Pd@HNTs-CDNS-g-C3N4: A novel heterogeneous catalyst for promoting ligand and copper-free Sonogashira and Heck coupling reactions, benefits from halloysite and cyclodextrin chemistry and g-C3N4 contribution to suppress Pd leaching, Carbohydr. Polym. 186 (2018) 25–34. https://doi.org/10.1016/j.carbpol.2018.01.023.

[27] S. Sadjadi, G. Lazzara, M. Malmir, M.M. Heravi, Pd nanoparticles immobilized on the poly-dopamine decorated halloysite nanotubes hybridized with N-doped porous carbon monolayer: A versatile catalyst for promoting Pd catalyzed reactions, J. Catal. 366 (2018) 245–257. https://doi.org/10.1016/j.jcat.2018.08.013.

[28] L. Lisuzzo, G. Cavallaro, S. Milioto, G. Lazzara, Halloysite nanotubes as nanoreactors for heterogeneous micellar catalysis, J. Colloid Interface Sci. 608 (2022) 424–434. https://doi.org/10.1016/j.jcis.2021.09.146.

[29] Y. Liu, H. Guan, J. Zhang, Y. Zhao, J.-H. Yang, B. Zhang, Polydopamine-coated halloysite nanotubes supported AgPd nanoalloy: An efficient catalyst for hydrolysis of ammonia borane, Int. J. Hydrog. Energy. 43 (2018) 2754–2762. https://doi.org/10.1016/j.ijhydene.2017.12.105.

[30] Y. Liu, J. Zhang, H. Guan, Y. Zhao, J.-H. Yang, B. Zhang, Preparation of bimetallic Cu-Co nanocatalysts on poly (diallyldimethylammonium chloride) functionalized halloysite nanotubes for hydrolytic dehydrogenation of ammonia borane, Appl. Surf. Sci. 427 (2018) 106–113. https://doi.org/10.1016/j.apsusc.2017.08.171.

[31] S. Sadjadi, F. Koohestani, G. Pareras, M. Nekoomanesh-Haghighi, N. Bahri-Laleh, A. Poater, Combined experimental and computational study on the role of ionic liquid containing ligand

in the catalytic performance of halloysite-based hydrogenation catalyst, J. Mol. Liq. 331 (2021) 115740. https://doi.org/10.1016/j.molliq.2021.115740.

[32] S. Sadjadi, N. Abedian-Dehaghani, M.M. Heravi, X. Zhong, P. Yuan, J. Duran, A. Poater, N. Bahri-Laleh, Clay-supported acidic ionic liquid as an efficient catalyst for conversion of carbohydrates to 5-hydroxymethylfurfural, J. Mol. Liq. 382 (2023) 121847. https://doi.org/10.1016/j.molliq.2023.121847.

[33] L. Zhang, X. Xu, S. Jiang, L. Wei, K. Xi, Y. Lei, X. Cheng, J. Yin, Y. Gao, Halloysite nanotubes modified poly(vinylidenefluoride-co-hexafluoropropylene)-based polymer-in-salt electrolyte to achieve high-performance Li metal batteries, J. Colloid Interface Sci. 645 (2023) 45–54. https://doi.org/10.1016/j.jcis.2023.04.127.

[34] W. Wang, Y. Yang, H. Luo, J. Zhang, Design of advanced separators for high performance Li-S batteries using natural minerals with 1D to 3D microstructures, J. Colloid Interface Sci. 614 (2022) 593–602. https://doi.org/10.1016/j.jcis.2022.01.148.

[35] F. Liu, L. Bai, H. Zhang, H. Song, L. Hu, Y. Wu, X. Ba, Smart H2O2-Responsive Drug Delivery System Made by Halloysite Nanotubes and Carbohydrate Polymers, ACS Appl. Mater. Interfaces. 9 (2017) 31626–31633. https://doi.org/10.1021/acsami.7b10867.

[36] B. Tang, H. Zhang, C. Cheng, H. Jiang, L. Bai, X. Ba, Y. Wu, Development of halloysite nanotube-based hydrogel with colorimetric H2O2-responsive character, Appl. Clay Sci. 212 (2021) 106230. https://doi.org/10.1016/j.clay.2021.106230.

[37] L. Lisuzzo, G. Cavallaro, P. Pasbakhsh, S. Milioto, G. Lazzara, Why does vacuum drive to the loading of halloysite nanotubes? The key role of water confinement, J. Colloid Interface Sci. 547 (2019) 361–369. https://doi.org/10.1016/j.jcis.2019.04.012.

[38] C. Duce, V.D. Porta, E. Bramanti, B. Campanella, A. Spepi, M.R. Tiné, Loading of halloysite nanotubes with BSA, α -Lac and β -Lg: a Fourier transform infrared spectroscopic and thermogravimetric study, Nanotechnology. 28 (2017) 055706.

[39] L. Lisuzzo, G. Cavallaro, S. Milioto, G. Lazzara, Coating of silk sutures by Halloysite/wax Pickering emulsions for controlled delivery of eosin, Appl. Clay Sci. 247 (2024) 107217. https://doi.org/10.1016/j.clay.2023.107217.

[40] M. Makaremi, P. Pasbakhsh, G. Cavallaro, G. Lazzara, Y.K. Aw, S.M. Lee, S. Milioto, Effect of Morphology and Size of Halloysite Nanotubes on Functional Pectin Bionanocomposites for Food Packaging Applications, ACS Appl. Mater. Interfaces. 9 (2017) 17476–17488. https://doi.org/10.1021/acsami.7b04297.

[41] Z. Luo, H. Song, X. Feng, M. Run, H. Cui, L. Wu, J. Gao, Z. Wang, Liquid Crystalline Phase Behavior and Sol–Gel Transition in Aqueous Halloysite Nanotube Dispersions, Langmuir. 29 (2013) 12358–12366. https://doi.org/10.1021/la402836d.

[42] J. Cao, X. Kang, B. Bate, Microscopic and physicochemical studies of polymer-modified kaolinite suspensions, Colloids Surf. Physicochem. Eng. Asp. 554 (2018) 16–26. https://doi.org/10.1016/j.colsurfa.2018.06.019.

[43] M.M. Calvino, G. Cavallaro, L. Lisuzzo, S. Milioto, G. Lazzara, Separation of halloysite/kaolinite mixtures in water controlled by sucrose addition: The influence of the

attractive forces on the sedimentation behavior, Colloids Surf. Physicochem. Eng. Asp. 641 (2022) 128530. https://doi.org/10.1016/j.colsurfa.2022.128530.

[44] G. Cavallaro, G. Lazzara, V. Taormina, D. Cascio, Sedimentation of halloysite nanotubes from different deposits in aqueous media at variable ionic strengths, Colloids Surf. Physicochem. Eng. Asp. 576 (2019) 22–28. https://doi.org/10.1016/j.colsurfa.2019.05.038.

[45] H. Wu, J. Xie, M. Lattuada, J. Kohlbrecher, M. Morbidelli, Effect of primary particle size and salt concentration on the structure of colloidal gels, J. Phys. Chem. C. 115 (2011) 931–936. https://doi.org/10.1021/jp103100k.

[46] J. Russo, J. Fiegel, N.K. Brogden, Effect of Salt Form on Gelation and Drug Delivery Properties of Diclofenac-Loaded Poloxamer Gels for Delivery to Impaired Skin, Pharm. Res. 39 (2022) 2515–2527. https://doi.org/10.1007/s11095-022-03356-1.

[47] A. Fernández-Nieves, A. Fernández-Barbero, F.J. De las Nieves, Salt effects over the swelling of ionized mesoscopic gels, J. Chem. Phys. 115 (2001) 7644–7649. https://doi.org/10.1063/1.1403002.

[48] Y. Tu, X. Zhang, L. Wang, Effect of salt treatment on the stabilization of Pickering emulsions prepared with rice bran protein, Food Res. Int. 166 (2023). https://doi.org/10.1016/j.foodres.2023.112537.

[49] J. Li, W. Zhang, T. Tang, L. Gu, Y. Su, Y. Yang, C. Chang, Q. Han, Thermal gelation and digestion properties of hen egg white: Study on the effect of neutral and alkaline salts addition, Food Chem. 409 (2023) 135263. https://doi.org/10.1016/j.foodchem.2022.135263.

[50] G.J. Churchman, P. Pasbakhsh, D.J. Lowe, B.K.G. Theng, Unique but diverse: some observations on the formation, structure and morphology of halloysite, Clay Miner. 51 (2016) 395–416. https://doi.org/10.1180/claymin.2016.051.3.14.

[51] A. Pramanik, A. Sciortino, M. Reale, P. Pasbakhsh, G. Cavallaro, M. Cannas, G. Lazzara, F. Messina, Naturally Occurring Halloysite Nanotubes as Light Scatterers for Stable Random Lasing Applications, ACS Appl. Nano Mater. 6 (2023) 15896–15905. https://doi.org/10.1021/acsanm.3c02840.

[52] Mark Raven, Peter Self, Dehydration and intercalation behavior of the unique “Patch Clay” halloysite using in-situ XRD, in: 2019 EUROCLAY - Int. Conf. Clay Sci. Technol., n.d.

[53] T. Le Ba, A.Q. Alkurdi, I.E. Lukács, J. Molnár, S. Wongwises, G. Gróf, I.M. Szilágyi, A Novel Experimental Study on the Rheological Properties and Thermal Conductivity of Halloysite Nanofluids, Nanomaterials. 10 (2020) 1834. https://doi.org/10.3390/nano10091834.

[54] M. Anvari, M. Tabarsa, R. Cao, S. You, H.S. Joyner Melito, S. Behnam, M. Rezaei, Compositional characterization and rheological properties of an anionic gum from Alyssum homolocarpum seeds, Food Hydrocoll. 52 (2016) 766–773. https://doi.org/10.1016/j.foodhyd.2015.07.030.

[55] L.S. Tavares, L.A. Junqueira, Í.C. de Oliveira Guimarães, J.V. de Resende, Cold extraction method of chia seed mucilage (Salvia hispanica L.): effect on yield and rheological behavior, J. Food Sci. Technol. 55 (2018) 457–466. https://doi.org/10.1007/s13197-017-2954-4.

[56] J.L. Dávila, M.A. d'Ávila, Laponite as a rheology modifier of alginate solutions: Physical gelation and aging evolution, Carbohydr. Polym. 157 (2017) 1–8. https://doi.org/10.1016/j.carbpol.2016.09.057.

[57] P.G. Lawrence, Y. Lapitsky, Ionically cross-linked poly(allylamine) as a stimulus-responsive underwater adhesive: Ionic strength and pH effects, Langmuir. 31 (2015) 1564–1574. https://doi.org/10.1021/la504611x.

[58] G.E. Cunningham, F. Alberini, M.J.H. Simmons, J.J. O'Sullivan, Understanding the effects of processing conditions on the formation of lamellar gel networks using a rheological approach, Chem. Eng. Sci. 242 (2021). https://doi.org/10.1016/j.ces.2021.116752.

[59] T. Domenech, S.S. Velankar, On the rheology of pendular gels and morphological developments in paste-like ternary systems based on capillary attraction, Soft Matter. 11 (2015) 1500–1516. https://doi.org/10.1039/c4sm02053g.

[60] G.A. Valencia, I.C.F. Moraes, L.H.G. Hilliou, R.V. Lourenço, P.J.D.A. Sobral, Nanocomposite-forming solutions based on cassava starch and laponite: Viscoelastic and rheological characterization, J. Food Eng. 166 (2015) 174–181. https://doi.org/10.1016/j.jfoodeng.2015.06.006.

[61] E.A. Appel, M.W. Tibbitt, M.J. Webber, B.A. Mattix, O. Veiseh, R. Langer, Self-assembled hydrogels utilizing polymer-nanoparticle interactions, Nat. Commun. 6 (2015). https://doi.org/10.1038/ncomms7295.

[62] Y. Zhang, W. Gao, Y. Chen, T. Escajadillo, J. Ungerleider, R.H. Fang, K. Christman, V. Nizet, L. Zhang, Self-Assembled Colloidal Gel Using Cell Membrane-Coated Nanosponges as Building Blocks, ACS Nano. 11 (2017) 11923–11930. https://doi.org/10.1021/acsnano.7b06968.

[63] E.O. Castrejón-González, V.E. Márquez Baños, J.F. Javier Alvarado, V. Rico-Ramírez, J. Castillo-Tejas, H. Jiménez-Islas, Rheological model for micelles in solution from molecular dynamics, J. Mol. Liq. 198 (2014) 84–93. https://doi.org/10.1016/j.molliq.2014.07.016.

[64] Y.-R. Wang, Q. Yang, Y.-J. Li-Sha, H.-Q. Chen, Structural, gelation properties and microstructure of rice glutelin/sugar beet pectin composite gels: Effects of ionic strengths, Food Chem. 346 (2021). https://doi.org/10.1016/j.foodchem.2020.128956.

[65] A.D. Drozdov, J.D. Christiansen, The effects of pH and ionic strength on the volume phase transition temperature of thermo-responsive anionic copolymer gels, Polymer. 221 (2021). https://doi.org/10.1016/j.polymer.2021.123637.

[66] S. Shafiei-Sabet, W.Y. Hamad, S.G. Hatzikiriakos, Ionic strength effects on the microstructure and shear rheology of cellulose nanocrystal suspensions, Cellulose. 21 (2014) 3347–3359. https://doi.org/10.1007/s10570-014-0407-z.

Graphical Abstract

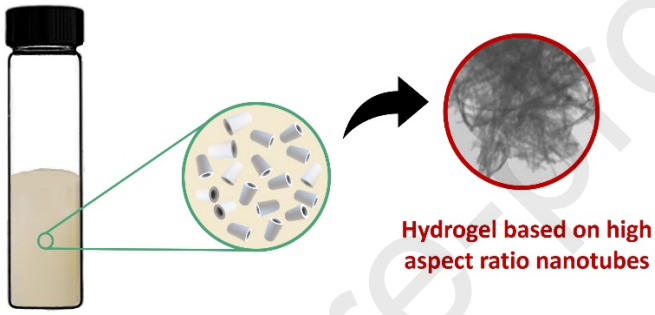

Credit Author Statement

Martina Maria Calvino: Investigation, Data curation, Writing- Original draft preparation. **Giuseppe Cavallaro:** Writing- Reviewing and Editing, Validation. **Pooria Pasbakhsh:** Data curation, Writing- Original draft preparation. **Giuseppe Lazzara:** Conceptualization, Supervision. **Stefana Milioto:** Funding acquisition, Resources.

Highlights

- Rheological behavior of several halloysite nanotubes were investigated.
- Hydrogels can be obtained by dispersing 1 wt% of patch halloysite (PT_Hal) in water.
- PT_Hal exhibits the nanotubes entanglement for volume fractions 100 times lower respect to common clay nanotubes.
- The gel formation mechanism of Patch halloysite nanotubes is not affected by the ionic strength of aqueous medium.

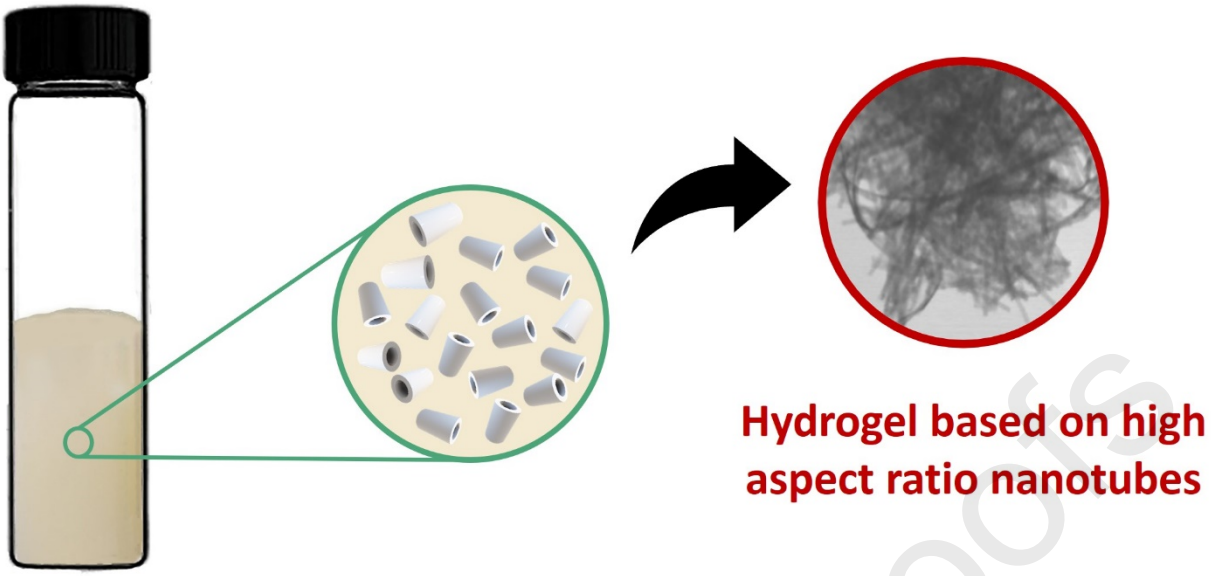

Declaration of interests

☒ The authors declare that they have no known competing financial interests or personal relationships that could have appeared to influence the work reported in this paper.

☐The authors declare the following financial interests/personal relationships which may be considered as potential competing interests:

Journal of Environmental Chemical Engineering 10 (2022) 108594

Contents lists available at ScienceDirect

Journal of Environmental Chemical Engineering

journal homepage: www.elsevier.com/locate/jece

Halloysite based geopolymers filled with wax microparticles as sustainable building materials with enhanced thermo-mechanical performances

Martina Maria Calvino [a], Lorenzo Lisuzzo [a], Giuseppe Cavallaro [a,b,*], Giuseppe Lazzara [a,b], Stefana Milioto [a,b]

[a] Dipartimento di Fisica e Chimica, Università degli Studi di Palermo, Viale delle Scienze, pad. 17, 90128 Palermo, Italy
[b] Consorzio Interuniversitario Nazionale per la Scienza e Tecnologia dei Materiali, INSTM, Via G. Giusti, 9, I-50121 Firenze, Italy

ARTICLE INFO

Editor: Dr. G. Palmisano

Keywords:
Geopolymers
Halloysite nanotubes
Pickering emulsion
Beeswax

ABSTRACT

This work proposes a novel protocol for the fabrication of halloysite based geopolymers filled with beeswax microparticles obtained from Pickering emulsions. The actual filling of the microwax into the geopolymers has been demonstrated by using several techniques, including thermal analyses, spectroscopies, microscopies and contact angle experiments. According to the morphological and structural investigations, microwax spherical particles (diameter ranging between ca. 3 and 5 μm) have been homogeneously dispersed within the geopolymeric network conferring excellent properties to the hybrid geopolymers in terms of mechanical performances and heat storage capacity although their low content in the hybrid material. For comparison, we have prepared and characterized hybrid geopolymers obtained by the loading of variable amounts of beeswax within the geopolymeric matrix. Reliable enhancements of the flexural characteristics and heat absorption capacity have been achieved only with a large content of beeswax. Moreover, the removal of microvax and wax from the hybrid geopolymers has been obtained by rinsing with ethanol. The washed geopolymers have been characterized by wettability and water vapour permeability experiments, which have been proved that the beeswax has been removed and the porosity of the materials can be controlled by the initial composition of the hybrid geopolymers.

In conclusion, this paper puts forward an easy strategy to fabricate composite geopolymers with heat storage capacity due to presence of phase change materials (microwax particles) confined in the geopolymeric network. Their enhanced flexural performances make the hybrid geoppolymers suitable as building materials.

1. Introduction

The interest in producing eco-friendly materials from natural resources or industrial by-products has increased in recent years [1,2]. In the construction field, the growing demand for cement production at a large scale further attracted researchers towards its effect on global warming by the emissions of carbon dioxide [3]. In this regard, research is currently focused on geopolymeric materials that offer new perspectives in environmental remediation technologies and can be synthesized from various industrial by-products such as fly rice husk ashes [4], furnace slag [5] and natural clays [6].

Geopolymers are inorganic polymeric materials that possess an amorphous network of aluminosilicates. They are obtained from a geopolymerization process with an alkaline activating solution leading to the formation of three-dimensional structures with Si–O–Al bonds. Poli-silicon-oxo-aluminate network is composed by SiO_4 and AlO_4 groups with a bridging oxygen between silicon and aluminum atoms and negative charges of AlO_4 groups that are typically balanced by sodium (Na^+) or potassium (K^+) cations. Geopolymers have the empirical formula $M_n[-(SiO_2)_z-AlO_2]\cdot wH_2O$ where M is a cation (Na^+, K^+ or Ca^{2+}), n is the degree of polycondensation, z is 1, 2, or 3 and w is the number of water molecules. There are three classes of geopolymers on dependence of of the Si/Al ratio: polysialate (–Si–O–Al–O), polysialate-siloxo (–Si–O–Al–O–Si–O–) and polysialate-disiloxo (–Si–O–Al–O–Si–O–Si–O) for Si/Al ratio equals to 1, 2 and 3, respectively [7]. Once the precursors have been completely reacted, the geopolymeric bulk structure is intrinsically micro and mesoporous. The amount of these porosities (ranging from 30 to 60 vol%) is related to the system's composition and to the specific Si/Al ratio. Furthermore, also highly porous geopolymers and geopolymer foams (porosity > 70 vol%) are getting attention due to their physical properties in terms of high thermal and chemical stability and other applications that cannot be pursued using

* Corresponding author at: Dipartimento di Fisica e Chimica, Università degli Studi di Palermo, Viale delle Scienze, pad. 17, 90128 Palermo, Italy.
E-mail address: giuseppe.cavallaro@unipa.it (G. Cavallaro).

https://doi.org/10.1016/j.jece.2022.108594
Received 27 June 2022; Received in revised form 18 August 2022; Accepted 11 September 2022
Available online 13 September 2022

the traditional geopolymer matrix. As examples, these materials can be employed as adsorbents [8,9], acoustic and thermal insulators [10] and adsorbents for heavy metals [11]. Porosity can be introduced on purpose into the micro- and meso-porous geopolymer matrix by removing a "sacrificial" material from its network [12].

The microstructure of geopolymer mortar can be improved by nanoparticles [13] due to their ability to be uniformly dispersed in the binder paste. Nowadays, nanoparticles are widely employed in combination with several traditional materials in order to modify and improve specific properties, developing modern multifunctional products. For instance, nanoclays are suitable as additives of cement concretes to enhance their mechanical performances because of their peculiar physical chemistry, morphology, and charge characteristics. Among clay nanoparticles, halloysite nanotubes (HNTs) are emerging natural aluminosilicates belonging to the category of phyllosilicates with the chemical formula of $Al_2Si_2O_5(OH)_4 \cdot 2\ H_2O$. These nanomaterials are widely used in for industrial and biotechnological applications because of their low cost, ecocompatibility and low toxicity [14–17]. Halloysite nanotubes have a hollow tubular structure and an inner surface consisting of octahedral gibbsite (Al–OH), while the outer surface is formed by siloxanes (Si–O–Si). The sizes of the nanotubes depend on their natural source of extraction [18]. The tube length is 1–2 μm, external diameter is between 50 and 200 nm, while the internal diameter ranges between 15 and 50 nm. The halloysite surfaces charges are influenced by pH due to the ionization equilibria of the Si–O groups (external surface) and Al-OH groups (internal surface). Consequently, the inner and the outer surfaces are positively and negatively charged, respectively, for pH ranging between 2 and 10. On this basis, ionic molecules can be used for the specific surface functionalization to improve the HNTs reactivity and selectivity and/or to drive the encapsulation of functional species within the halloysite lumen [19,20]. On this basis, halloysite can be exploited in several fields, such as adsorbent for wastewater remediation [21–26], catalytic support [21,22,27–31], drug delivery [32–37], biomedicine [38–40], cosmetics [41,42] and pharmaceutics [43,44]. Chemically, halloysite is very similar to kaolinite, which does not possess the two water molecules located between the tetrahedral layer and the octahedral one. These clays also have different morphology being that kaolinite is a platy nanoparticle with a basic unit of a two-dimensional layer of silicate groups bonded to a layer of aluminate groups. Both halloysite and kaolinite can be used as aluminosilicate precursors in geopolymer synthesis as reported in literature [45–47]. Notably, metakaolin obtained from kaolinite containing traces of halloysite was investigated [48]. It was observed that the presence of HNTs leads to a higher silicon and aluminum dissolution and, consequently, to an increase of the geopolymerization rate with respect to the pure kaolinite improving the reactivity [49]. Halloysite can also act as an interfacial active particle to stabilize the resulting Pickering emulsions [50–53].

The development of new hybrid materials drives to realize products that can have different properties by tuning the chemical composition of the two phases [54]. As reported in literature, the presence of additives in geopolymers can lead to an enhancement of their physico-chemical properties. In the last decade, both organic and inorganic additives, such as micro silica, micro fibrils and carbon fibers, were successfully employed to improve the mechanical performances and the thermal resistance of geopolymers as well to enhance the geopolymerization reaction for concrete application [55–57]. For instance, nano-SiO_2 can improve the microstructure, hardening properties and compressive strength of fly ash-based geopolymers [58]. It was demonstrated that their durability properties can be extended compared to ordinary geopolymeric concrete also by employing bio-additives [59,60]. The effect of silica fume, alumina, quartz powder, fibres and nanomaterials as additives was explored mostly on slag or fly ash based geopolymers [61] but a deeper investigation on clay based geopolymers is needed. Here, we propose new hybrid halloysite-based geopolymers with microwax particles obtained from dried Pickering emulsion. For comparison, we prepared hybrid geopolymers filled with beeswax at variable composition. Within this, it should be noted that the nanoencapsulation of phase change materials was recently explored to fabricate advanced thermal storage systems [62–64]. The final products represent the starting point for the design of hybrid and green geopolymers including confined microwax (phase change material) with a high thermal capacity that can be strategic for energy storage applications. The filled geopolymers could be employed for construction industry as a green concrete alternative to the traditional cements reducing the greenhouse gas emissions.

2. Materials and methods

2.1. Materials

Halloysite nanotubes (HNTs), beeswax, sodium hydroxide and Nile Red are Sigma Aldrich products. Ethanol (96%) is from Honeywell.

2.2. Preparation of pickering emulsions

The Pickering emulsion was prepared using a similar protocol reported elsewhere for halloysite/paraffin.[65] Firstly, 0.3 g of solid beeswax were added to 100 mL of water under magnetic stirring at 80 °C. After wax was completely dispersed, 1.2 g of halloysite nanotubes were added to the emulsion that was subjected to ultrasounds for 10 min. The obtained dispersion was magnetically stirred for 30 min at 80 °C. Then, the heating system was turned off and the emulsion was kept under stirring until the temperature of 25 °C was achieved. This strategy allowed us to obtain solid stable wax microparticles surrounded by halloysite nanotubes. According to literature [65], particles of well-defined spherical shape of about ten micrometers can be obtained using the mentioned protocol. After 24 h, the resulting Pickering emulsion was stable at room temperature, and it was dried under vacuum to obtain the powder.

2.3. Preparation of geopolymers filled with wax and microwax particles

Firstly, we dried the Pickering emulsion under vacuum at room temperature allowing us to obtain microwax spheres. Then, the microparticles were mixed with the same amount of pure halloysite nanotubes and, subsequently, with the alkaline activating solution (NaOH 12 M). Sodium cations (Na^+) balance the equal negative charges of four-coordinated Al ($[AlO_4]^-$) in the geopolymeric network. Accordingly, the NaOH/HNTs ratio was set to 1. After mixing at 25 °C, a homogeneous slurry was obtained, and it was placed into a plastic mold and cured at 50 °C for 48 h.

For comparison, a very similar procedure was carried out to prepare geopolymers filled with beeswax at different wax/halloysite ratios, $R_{wax/HNT}$ (Table 1) and an unfilled conventional geopolymer. Once added the alkaline activator solution to halloysite nanotubes, solid beeswax was incorporated under heating at 70 °C until we obtained a homogeneous geopolymer slurry (Fig. 1). The last step for all samples was curing at 50 °C for 48 h in a rectangular plastic mold.

A schematic illustration of the preparation protocol developed for the filled geopolymers is displayed in Fig. 1.

Table 1
List of the geopolymer samples with the percentages of each components.

Sample	$R_{wax/HNT}$	HNT / wt%	Beeswax / wt%	NaOH / wt%
GP	0	50	0	50
GP_wax	0.25	44.4	11.2	44.4
GP_wax	0.5	40	20	40
GP_wax	0.75	36.4	27.2	36.4
GP_wax	1	33.3	33.4	33.3
GP_microwax	0.07 *	48.3	3.4	48.3

*calculated from TGA.

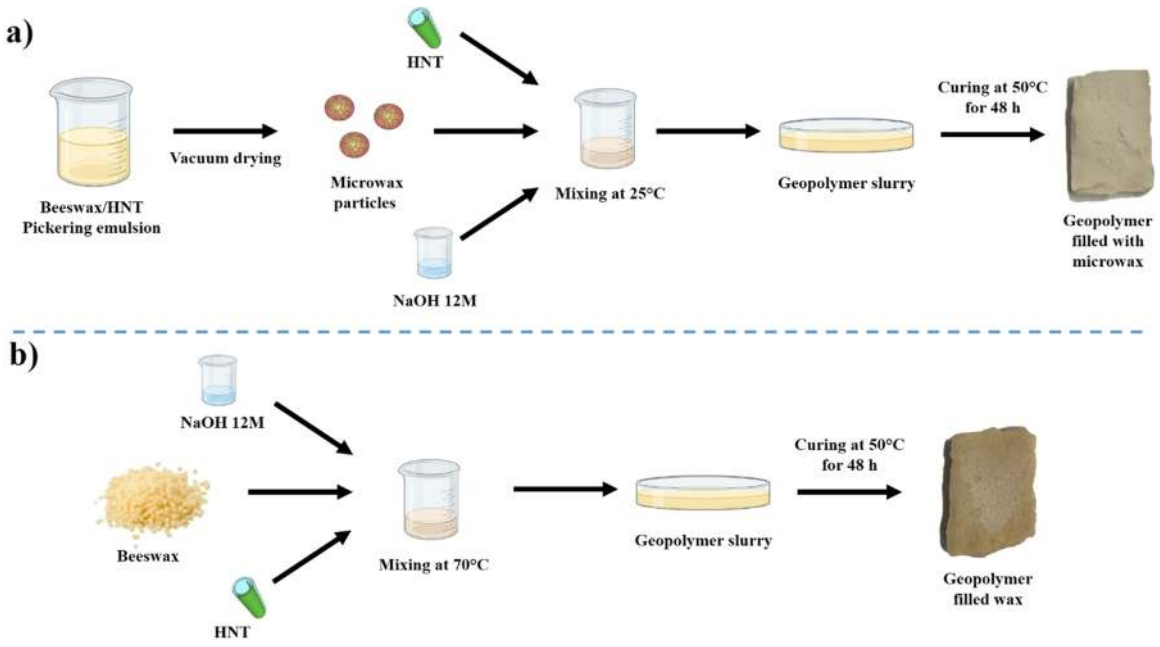

Fig. 1. Schematic representation of the preparation protocol for geopolymer filled with microwax particles (a) and wax (b).

2.4. Methods

2.4.1. Thermogravimetric analysis (TGA)

Thermogravimetric experiments were performed by means of a Q5000 IR apparatus (TA Instruments) under inert atmosphere using nitrogen flows of 25 and 10 $cm^3\ min^{-1}$ for the sample and the balance, respectively. Each sample (ca. 10 mg) was heated in a platinum pan from room temperature to 700 °C with a scanning rate of 20 °C min^{-1}.

2.4.2. Differential scanning calorimetry (DSC)

Differential scanning calorimetry (DSC) measurements were carried out with the TA Instruments DSC (2920 CE) under nitrogen flow atmosphere (flow rate of 60 $cm^3\ min^{-1}$) from − 20–110 °C with a heating rate of 10 °C min^{-1}. We used aluminum pans, while the mass sample was ca. 2 mg. The melting temperature (T_m) of beeswax in the geopolymer materials was calculated and defined as the maximum of the endothermic peak occurring in the range between 30 and 70 °C. The enthalpy of the melting process was estimated by the integration of the peaks and expressed as Joule per gram of beeswax. The calibration was performed by using the indium as standard.

2.4.3. FT-IR spectroscopy

FT-IR spectra in KBr pellets were measured using a Perkin-Elmer FT-IR Spectrum One instrument in the spectral region between 4000 and 400 cm^{-1}. An average of 30 scans per sample using a nominal resolution of 4 cm^{-1} was registered.

2.4.4. X-ray Diffraction (XRD)

The patterns were obtained from an X-ray diffractometer (Rigaku, MiniFlex) with a CuKa radiation source including a nickel filter and working at 40 kV and 15 mA. The wavelength of the X-ray beam was 1.5406 Å, and the layer spacing of the samples was calculated by the and Bragg's equation, which can be expressed as

$$n\lambda = 2d\sin\theta \quad (1)$$

where θ is the angle that the outgoing beam forms with the crystalline layer, λ is the wavelength of the radiation, d is the distance between two adjacent layers and n can be 1,2 or 3.

The angle for scanning was ranged from 2° to 70° with a rate of 20° min^{-1} and a step of 0.02°.

2.4.5. Nile Red essay

1 mg of Nile red was dissolved in 10 mL of ethanol and stirred until the compound was completely solubilized. One drop of this solution was used to cover all the samples that, after drying in the oven for 10 min, were observed under UV-lamp irradiation in a dark room.

2.4.6. Water contact angle measurements

Water contact angle measurements were carried out by using an optical contact angle apparatus (OCA 20, Data Physics Instruments, Filderstadt, Germany) implemented with a video measuring system with a high-resolution CCD camera and a high-performance digitizing adapter. Data acquisition was conducted by SCA 20 software (Data Physics Instruments, Filderstadt, Germany). The water contact angle in air was measured through the sessile drop method by gently placing a water droplet of 10 ± 0.5 μL onto the surface of the geopolymer block by a syringe pointed vertically down onto the sample. The tests were conducted at a temperature of 25.0 ± 0.1 °C. Images were collected at a rate of 25 frames per second starting from the deposition of the drop to 60 s

2.4.7. Scanning Electron Microscopy (SEM)

morphological investigations were conducted by a SEM microscope (Desktop SEM Phenom PRO X PHENOM) with magnification field 160–350.000x and voltage in the range between 4.8 and 20.5 kV. As concerns SEM analyses, each sample was preliminarily coated with gold to avoid charging effects under an electron beam.

2.4.8. Water vapour permeability analysis

Water vapor permeability tests were performed, at a temperature of 28 ± 1 °C and relative humidity of 30 ± 2% in a desiccator, which contained a saturated solution of calcium chloride dehydrate and twelve bottles (50 mL, 2 cm inner diameter) full of water. A thermohygrometer was placed inside the equipment to check the environmental parameters. Geopolymers were fixed on the top of each bottle and the water transferred through the materials, and absorbed by the desiccant, was determined from the weight loss of the bottle every 24 h for 10 days. Water vapor transmission rate (WVTR) and water vapor permeability were calculated by applying the following equations.

$$WVTR = (\Delta m/\Delta tA) \quad (2)$$

$$WVP = WVTR\ (L/\Delta p) \quad (3)$$

where Δm/Δt is the slope of each line obtained from the weight loss of samples over time (g/h), A is the exposed surface area of the sample (m^2), L is the thickness of the sample (m) and Δp is the difference of partial pressure (Pa) between saturation solution at 30% of relative humidity and saturation water vapor pressure at a temperature of 28 °C.

2.4.9. Thermal imaging

A FLIR E6-XT infrared camera (FLIR Commercial Systems Inc.) with 240 × 180 pixels and a temperature range from − 20–550 °C was employed for thermal imaging analysis. Samples were placed vertically on an electric hot plate and heated to 60 °C. Thermal images were analyzed through FLIR Tools software.

2.4.10. Dynamic mechanical analysis

Dynamic mechanical analysis was conducted with a DMA Q800 (TA Instruments) and specifically by using a three-point bending clamp at 25 °C. The ramp force was set at 0.2 N min^{-1} from 0.01 to 10 N.

2.4.11. Helium pycnometer

The Accupyc 1330 Micromeritics gas pycnometer was employed to determine the skeletal density and the porosity of the geopolymeric samples (before and after the washing by ethanol) by measuring the pressure change of helium (purity of 99.995%) in a calibrated volume. The apparatus has a 10 cm^3 cell suitable for the analysis of small specimens of the geopolymers. Standards for the volume calibration (balls purchased from Micromeritics, V_{cal} = 6.371684 cm^3) were used. The measurements were carried out at 25 °C.

3. Results and discussion

Preliminarily investigations of geopolymers were carried out by thermal analyses (TGA and DSC) and spectroscopies (XRD and FT-IR) to evaluate the actual formation of the geopolymeric network. The thermal behavior and the structural characteristics of geopolymers and their corresponding precursor (Halloysite) will be presented and discussed in the following paragraph.

3.1. Characterization of geopolymers: thermal analyses and spectroscopies

Fig. 2 compares the thermogravimetric (TG) curves of geopolymers with pristine halloysite.

We observed that pristine halloysite presents an evident mass loss in the range between 400 and 500 °C due to the expulsion of the interlayer water molecules from the HNT structure [66]. As expected, this signal was not detected in all geopolymers due to the structural changes of halloysite clay after the geopolymerization reaction. On the other hand, the geopolymer samples showed a significant mass reduction (ca. 10 wt %) from 25° to 200°C as a consequence of the evaporation process of physically adsorbed water molecules.

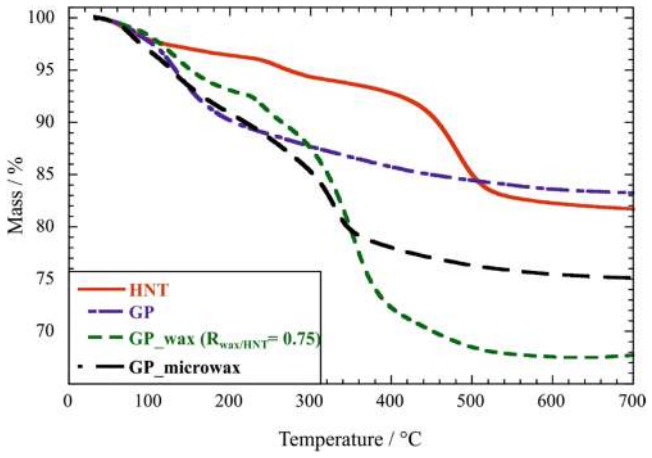

Fig. 2. Thermogravimetric curves of HNT, GP, GP_wax ($R_{wax/HNT}$ = 0.75) and GP_microwax.

The conventional geopolymer (sample GP) did not evidence any further mass losses within the investigated temperature range. On the other hand, GP_wax and GP_microwax evidenced a clear mass change at ca. 350 °C because of thermal decomposition of beeswax filled within the geopolymeric network. Accordingly, their residual masses at 700 °C (ca. 68 and 75 wt% for GP_wax and GP_microwax, respectively) are lower than the conventional geopolymer (ca. 80 wt%).

Moreover, thermogravimetric data provided the weight fraction of wax in GP_microwax calculated as follows.

$$\chi(wax) = (MD_{700\ P} - MD_{700HNT})/(MD_{700wax} - MD_{700HNT}) \quad (4)$$

where $MD_{700\ P}$, MD_{700HNT} and MD_{700wax} refer to degraded matters at 700 °C of wax/halloysite particles, halloysite and beeswax, respectively. From the calculated χ(wax) value, we determined the wax/HNT mass ratio in the GP_microwax sample (Table 1).

The presence of crystalline beeswax within the filled geopolymers was confirmed by DSC curves (see Supplementary Material),which showed endothermic peaks at ca. 65–70 °C due to the melting of the organic macromolecules. According to literature [67], this signal is related to the solid-liquid transition, while the slight shoulder occurring at a lower temperature (ca. 30–40 °C) to a solid-solid transition. We estimated the melting temperature T_m of the filled beeswax by the minimum of the DSC peaks. Interestingly, the T_m of GP_microwax is larger with respect to those of GP_wax samples (Table 2). Furthermore, the integration of the peaks provided the enthalpies (ΔH_m) of the melting process (Table 2).

The ΔH_m were expressed in J g^{-1} of beeswax, which is the component providing the melting signal. As described by Lvov et al. [68] the wax crystallinity is partially destroyed by halloysite nanotubes. As a matter of fact, the obtained values indicate a reduction of the enthalpy by increasing the wax/HNT ratio (Fig. 3) indicating a decrease of the wax crystallinity in the geopolymeric network.

FT-IR spectra for HNT, GP and GP_wax are illustrated in Fig. 4 and a detailed assignment of all the identified peaks is reported in Supplementary Material (Table 1S). According to literature [67,69], halloysite nanotubes possess two characteristic bands at 3698 and 3608 cm^{-1} representing the stretching of hydroxyl groups in the inner and outer surfaces. The signals at 1093 and 1028 cm^{-1} are assigned to the stretching vibrations of apical Si–O and Si–O–Si, respectively. The peaks at 796 cm^{-1} can be attributed to the symmetric stretching of Si–O–Si, while the signals at 692 and 753 cm^{-1} are related to the perpendicular stretching of Si–O–Al. Moreover, the band observed at 533 cm^{-1} reflects the deformation vibration of Al–O–Si.

On the other hand, geopolymerization influences the position of the peaks leading to the disappearance of the aforementioned characteristic signals of halloysite at ca. 3600 cm^{-1}. FTIR spectra of geopolymers (Fig. 4) present bands at 3458 and 1658 cm^{-1} related to the –OH

Table 2
Thermal parameters of beeswax and geopolymer samples.

Sample	$R_{wax/HNT}$	ΔH/ J g^{-1}	T_m / °C
Beeswax	/	205	66.2
GP	/	/	/
GP_wax	0.25	193	65.5
GP_wax	0.5	188	65.8
GP_wax	0.75	127	64.5
GP_wax	1	105	64.7
GP_microwax	0.07	191	70.0

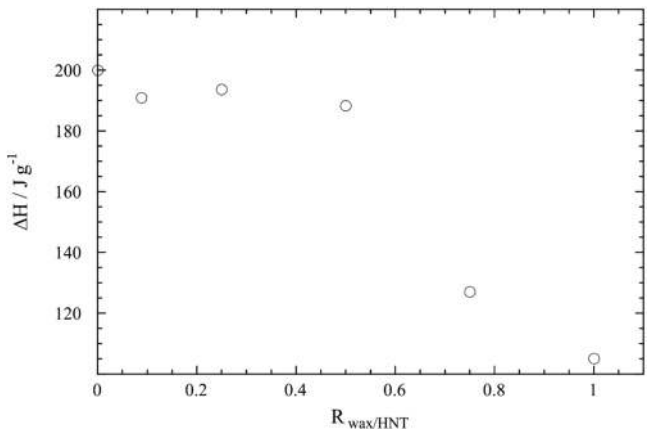

Fig. 3. Enthalpy of the wax melting process for filled geopolymers with variable wax/HNT ratio.

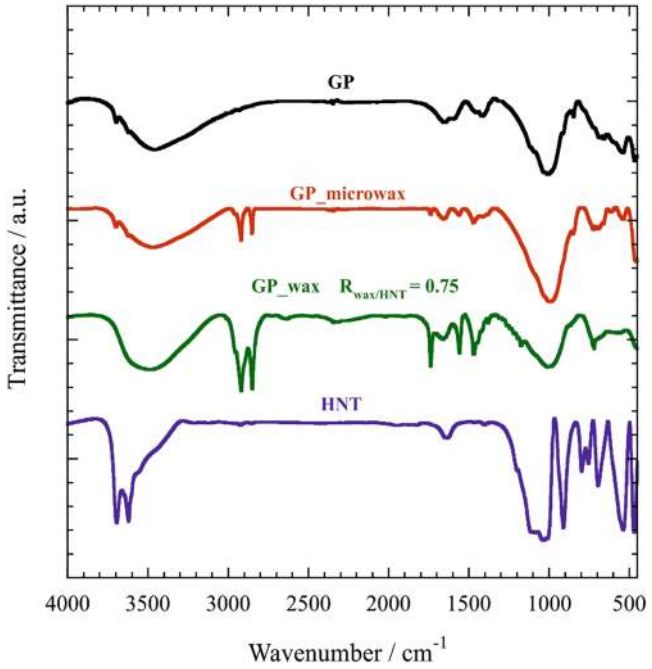

Fig. 4. FT-IR spectra of HNT, GP, GP_microwax and GP_wax ($R_{wax/HNT} = 0.75$).

stretching and bending vibrations of water's hydration.[70] Fig. 4 showed the often called "main band" between 1025 and 1015 cm^{-1} attributed to Si−O−T (T = tetrahedral Si or Al) asymmetric stretching vibration. Hajimohammadi et al.[71] stated that this band depends on connectivity and Si/Al ratio. Moreover, they revealed that it can be attributed to the presence of predominantly Si–O–Al bonds. It can be evidenced that there is a shift of this band from 1044 cm^{-1} in HNT to 1012 cm^{-1} in geopolymers that is related to the degree of geopolymerization. As reported in literature, this shift is caused by the increased substitution of Al in the tetrahedral silicate network [71–73]. Namely, the higher Si/Al ratios, the higher the silicon content and the band will be moved to higher wavenumbers as a result of reorganization and condensation with higher Si contribution to the gel structure.

The bands at 718 and 450 cm^{-1} can be associated with Si−O−Al bending vibration and in-plane Si−O−Si stretching vibration, respectively [74]. Furthermore, we observed additional FT-IR signals in the filled geopolymers with variable intensities on dependence of the wax/HNT ratio attributed to the presence of beeswax [75]. The presence of beeswax in the geopolymer structure was confirmed by the peaks at 2920 and 2848 cm^{-1} (CH_2 asymmetric and symmetric stretching vibrations, respectively), 1737 cm^{-1} (C═O stretching vibration) as well as 1472 and 720 cm^{-1} (scissor deformation vibration and rocking vibrations of CH_2 groups, respectively).

Structural differences after geopolymerization are evidenced by the diffractometer. XRD patterns of the geopolymers are illustrated in Fig. 5. The diffractogram of HNT exhibits the first reflection at 2θ = 11.8° in agreement with the dehydrated form of halloysite (basal spacing of 7.47 Å). Besides, the reflections at 19.9 and 24.3° can be related to the basal spacing of 4.4 and 3.6 Å, respectively. These signals were not detected in both the unfilled and filled geopolymers, which exhibited a broad reflection band from 20° to 40° (2θ), highlighting the formation of an amorphous geopolymeric network. In addition, all the geopolymers evidenced reflections attributed to quartz [76,77] and traces of hydrosodalite phase that could appear after alkali activation [78]. As shown in Fig. 5, both GP_wax and GP_microwax samples evidenced the reflection signals (19.1, 21.2, 23.6, 29.7 and 39.9°) attributed to the orthorhombic structure of beeswax corresponding to d equals to 4.6, 4.2, 3.8, 3.1 and 2.3 Å respectively.[79–81] It should be noted that the intensities of these peaks are reduced in the filled geopolymers compared to those of pure beeswax. These results are consistent with the reduction of the crystallinity of beeswax, as evidenced in DSC data (Table 2).

3.2. Morphology and surface properties of filled geopolymers

3.2.1. Nile red essay

The filling of geopolymers with wax and wax microparticles was demonstrated using the qualitative essay of hydrophobicity by Nile Red. It was used as a fluorescent probe because this molecule is highly

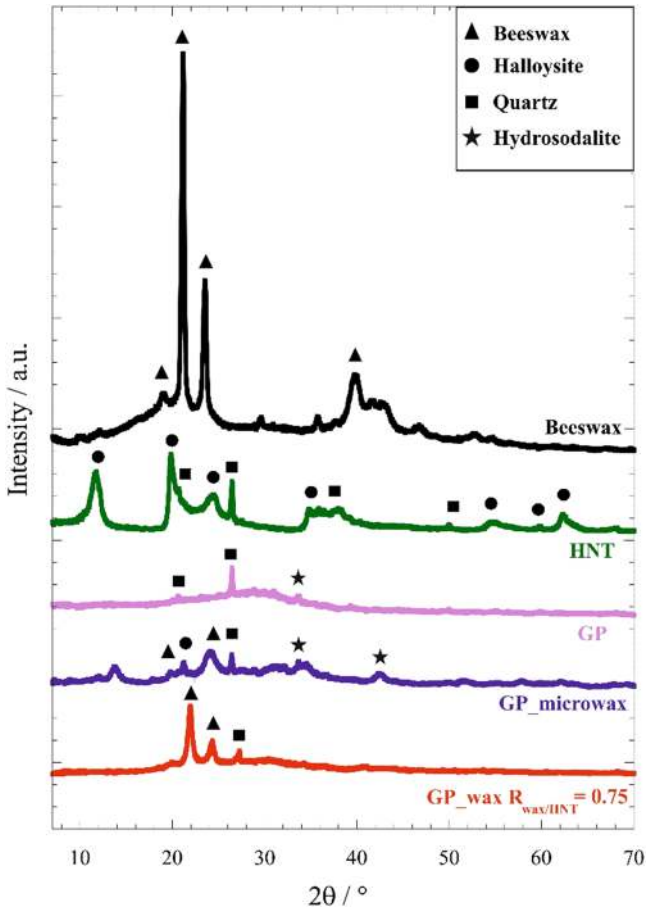

Fig. 5. Diffractograms of Beeswax, HNT, GP, GP_microwax and GP_wax $R_{wax/HNT} = 0.75$.

emissive in hydrophobic environments and it shows a red luminescence under UV light irradiation. As shown in Fig. 6, the pristine geopolymer did not evidence any luminescence in agreement with its hydrophilic character. In contrast, the filled geopolymers are luminescent because of the presence of the hydrophobic beeswax. Interestingly, GP_microwax exhibited a high luminescence although the small amount of wax entrapped within the geopolymeric network. The latter could be an indication of the high dispersibility of the wax microparticles within the geopolymeric matrix.

3.2.2. SEM analyses

SEM images of GP, GP_wax ($R_{wax/HNT}$= 1) and GP_microwax are displayed in Fig. 7. We observed that the filling with both wax and microwax particles induces significant changes in the morphology of the geopolymer. Specifically, GP showed a denser and more homogeneous matrix with respect to those of filled geopolymers (Fig. 7a). GP evidenced the presence of few halloysite nanotubes embedded within the geopolymeric matrix that can be considered as residual precursors of the geopolymerization. GP_wax exhibited an irregular morphology with the wax randomly distributed within the geopolymer network (Fig. 7b). In contrast, GP_microwax showed a uniform distribution of the wax microparticles that reduced the compactness of the geopolymer (Fig. 7c). It should be evidenced that the wax microparticles present a spherical shape with a diameter ranging between 3 and 5 μm. As shown in Fig. 7d, the surface of the wax microparticles is covered by spherical nanoparticles (diameter of ca. 400 nm) of halloysite, which lost its tubular morphology as a consequence of the alkaline activation.

3.2.3. Wettability

The filling of geopolymers with both wax and microwax induced significant changes in the wettability properties (Fig. 8). Due to its very hydrophilic character, the initial water contact angle of HNTs based geopolymer was not measureable. On the other hand, we determined the water contact angle values just after their deposition on both GP_wax and GP_microwax materials (Table 3). Accordingly, we can state that the filling of the geopolymeric network generated the hydrophobization of the surface, which can be related to the variation of its chemical composition (being wax hydrophobic) as well as to the enhancement of its roughness. The latter is consistent with SEM images (Fig. 7). Similar observations were done for hydrophilic films loaded with hydrophobic coffee particles [82].

It should be noted that the surface hydrophobization generated by wax microparticles is lower compared to that observed in GP_wax materials, which exhibited larger contact angle values by increasing the wax content (Table 3). Namely, increasing the percentage of wax causes a relevant change of θ_i values (initial contact angle) up to 116°, due to the more hydrophobic character (Table 3). These observations could indicate that the hydrophobization of the geopolymer is predominantly caused by variations of the surface chemistry.

Additionally, we investigated the kinetic evolution of the water contact angle using the following equation

$$\theta = \theta_i \exp(-k_\theta t^n) \quad (5)$$

where θ_i is the initial contact angle extrapolated at zero time, k_θ estimates the process rate, and n has fractional values according to the occurrence of absorption and spreading i.e. n = 0 for pure absorption and n = 1 for pure spreading. As example, the comparison between the experimental and calculated data for GP_wax ($R_{wax/HNT}$ = 1) is presented in Fig. 9, while the obtained fitting parameters for all the filled geopolymers are listed in Table 3.

3.3. Heat storage capacity of filled geopolymers

The heat storage capacity of GP, GP_wax and GP_microwax was studied by using thermal images of geopolymeric materials placed on a support kept at 60 °C, which guarantees that the wax melting was reached. Therefore, microwax particles and wax can act as phase change fillers absorbing thermal energy. As example, Fig. 10a shows the thermal images of GP_microwax compared to GP_wax ($R_{wax/HNT}$ = 0.25). Based on the analysis of the thermal images, we determined the temperature gradient on dependence of the distance from the support. The obtained trends are presented in Fig. 10b. As expected, the gradient temperature shows negative values because of the heat dissipation along the geopolymer material for all the investigated samples. As a general result, exponential decreasing trends were detected. It should be noted that GP and GP_wax ($R_{wax/HNT}$ = 0.25) exhibit similar trends indicating that the wax addition did not alter the heat absorption capacity of the geopolymer. Accordingly, the gradient temperature values at the top of the sample (5 mm of distance from the support) were − 10.99 and − 11.06 °C for GP and GP_wax ($R_{wax/HNT}$ = 0.25), respectively. On the other hand, larger amount of wax loaded in the geopolymeric network (GP_wax at $R_{wax/HNT}$ = 0.75) affected the heat absorption behaviour of the geopolymer being that the gradient temperature at 5 mm was - 4.07 °C. Interestingly, filling with wax microparticles significantly reduced the gradient temperature (- 7.42 °C at the top of the GP_microwax sample) despite the very low amount of wax entrapped within the geopolymeric network. In this regard, we should remind that GP_microwax presents $R_{wax/HNT}$ equals to 0.07 (Table 1). This effect could be due to the uniform distribution of wax microparticles within the geopolymeric matrix.

3.4. Mechanical performances of filled geopolymers

We investigated the effects of wax and microwax particles loadings on the flexural properties of geopolymers. Fig. 11a compares the stress vs strain curves of GP, GP_microwax and GP_wax at variable compositions ($R_{wax/HNT}$ = 0.25 and 0.75). Compared to the unfilled geopolymer, GP_microwax and GP_wax materials showed lower elastic modulus and stress at breaking point values, while the ultimate elongation was enhanced (Table 4). On this basis, we can state that the loading with

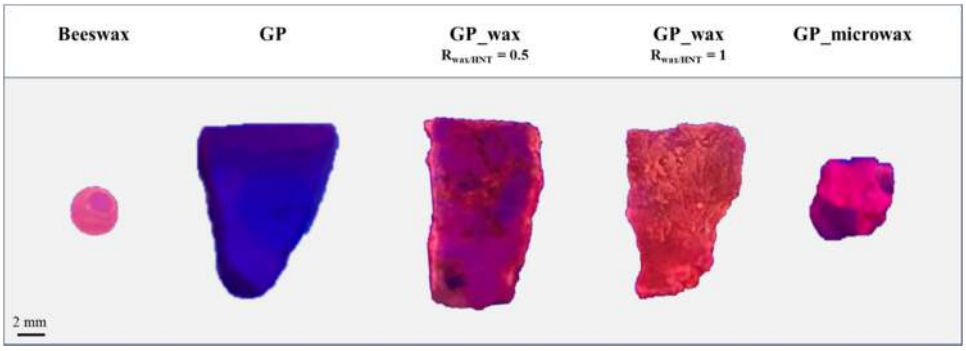

Fig. 6. Nile Red essay for Beeswax, GP, GP_wax ($R_{wax/HNT}$ = 0.5 and 1) and GP_microwax.

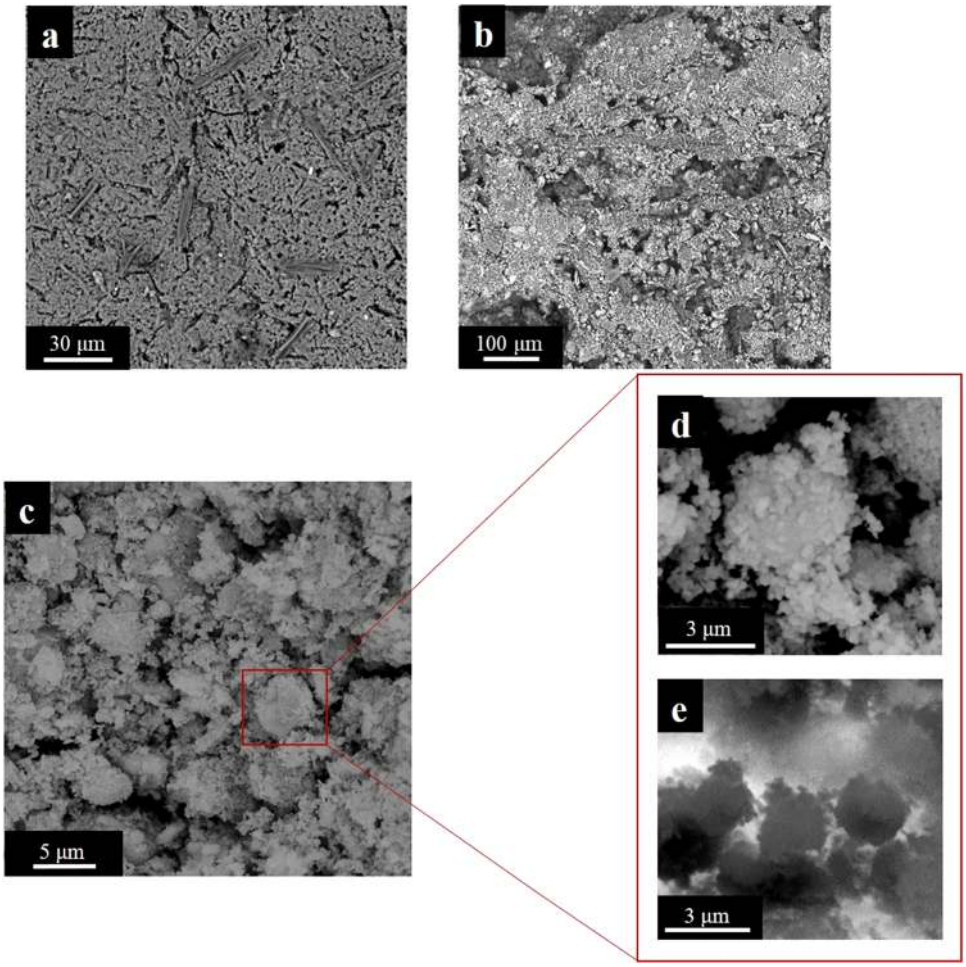

Fig. 7. SEM images of GP (a), GP_wax ($R_{wax/HNT}$ = 1) (b) and GP_microwax (c-e).

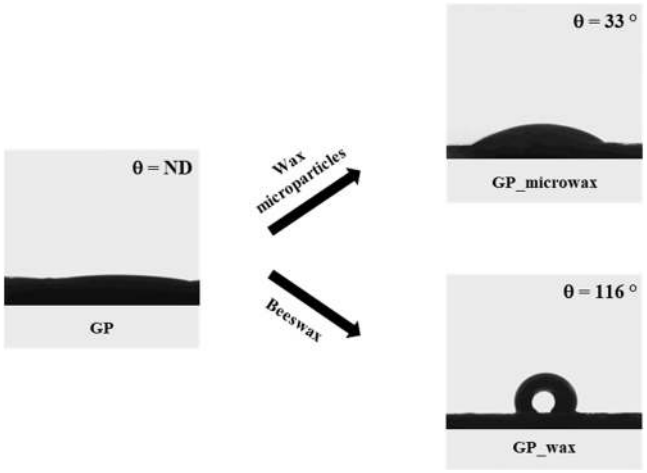

Fig. 8. Images of the water droplets contact just after their deposition on GP, GP_microwax and GP_wax ($R_{wax/HNT}$ = 1).

both wax and microwax enhanced the flexibility of the geopolymers. It should be noted that GP_microwax presents higher stiffness with low deformation due to the homogeneous distribution of microwax particles into the geopolymeric matrix. Compared to the GP material, the elastic modulus of GP filled with wax microparticles is ca. 6 times lower, while the ultimate elongation was enhanced by a factor of 6. Furthermore, the integration of stress vs strain curves allowed us to estimate the stored energy at the breaking point. As shown in Fig. 11b, GP_wax ($R_{wax/HNT}$ = 0.75) possesses the strongest capacity to store energy during the flexural tests. Interestingly, the energy requested for the breaking of GP_microwax is higher with respect to that of GP_wax ($R_{wax/HNT}$ = 0.25) despite its lower amount of wax due to the homogeneous filling of the microparticles within the geopolymeric network. Compared to the unfilled geopolymer, the stored energy up to breaking was enhanced by factors of ca. 2.5 and 5 for GP_wax ($R_{wax/HNT}$ = 0.25) and GP_microwax, respectively. It should be noted that GP_microwax presents a wax loading lower of ca. 3 times with respect to that of GP_wax ($R_{wax/HNT}$ = 0.25).

Table 3
Fitting parameters obtained from the kinetic analysis of water contact angle data.

Sample	$R_{wax/HNT}$	θ_i / °	k_θ / s^{-1}	n
GP	0	ND	ND	ND
GP_microwax	0.07	33.4	0.018 ± 0.002	0.63 ± 0.03
GP_wax	0.25	61.8	0.17 ± 0.01	0.22 ± 0.01
GP_wax	0.5	77.6	0.020 ± 0.003	0.67 ± 0.03
GP_wax	0.75	82.3	0.058 ± 0.003	0.34 ± 0.09
GP_wax	1	116.0	0.086 ± 0.004	0.303 ± 0.009

3.5. Wax removal from filled geopolymers by rinsing with ethanol

Filled geopolymers were rinsed with ethanol to remove wax from the geopolymeric network and consequently, to obtain materials with controlled porosity. The actual removal of wax was highlighted by Nile

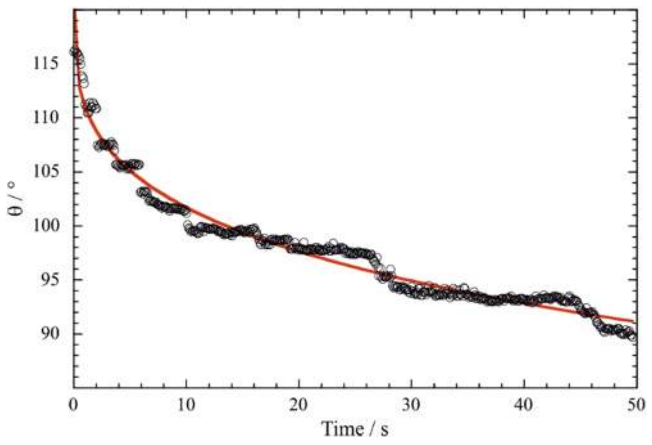

Fig. 9. Water contact angle as a function of time for GP_wax ($R_{wax/HNT}$ = 1). The red line represents the fitting according to the Eq. 5.

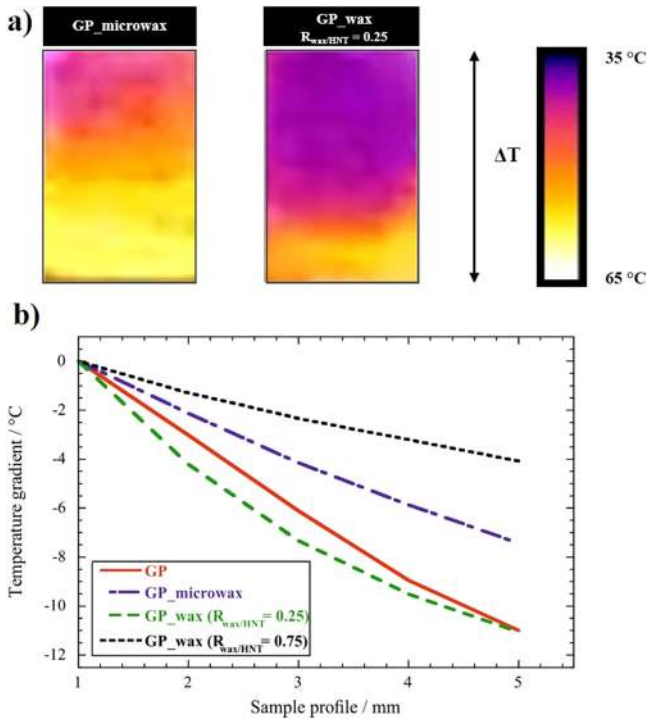

Fig. 10. Thermal images of GP_microwax and GP_wax ($R_{wax/HNT}$ = 0.25) (a). Temperature gradient as a function of the sample profile for GP, GP_microwax and GP_wax ($R_{wax/HNT}$ = 0.25 and 0.75) (b).

Red essay and TG curves, which showed that washed geopolymers did not present any mass loss in the temperature range between 300 and 400 °C (see Supplementary Material). Accordingly, Nile Red essay evidenced that GP_wax materials are not luminescent after their washing by ethanol (Fig. 12a).

As expected, the washing procedure altered the wettability and the water vapor permeability properties of the filled geopolymers due to the wax removal. The complete wax removal was proved by the very hydrophilic character of the washed geopolymers. As example, the water droplet for washed GP_wax ($R_{wax/HNT}$ = 0.75) is presented in Fig. 12b. The effect of the washing procedure on water vapor permeability of filled geopolymers are reported in Fig. 12c. Prior to the geopolymer rinsing with ethanol, the presence of both wax and microwax induced a reduction of the water permeability compared with that of GP sample, which agrees with the surface hydrophobization evidenced by the water

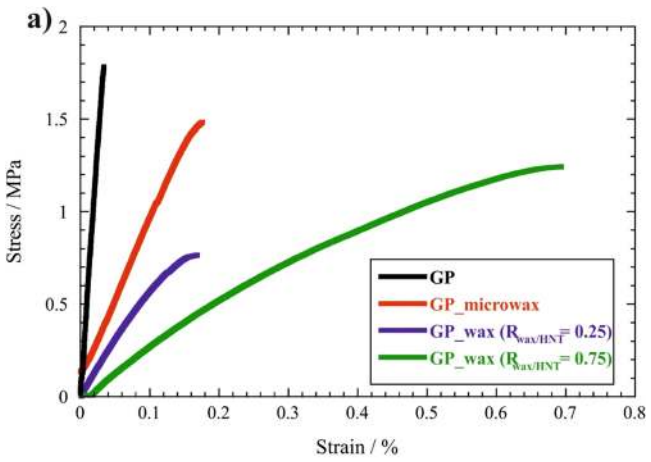

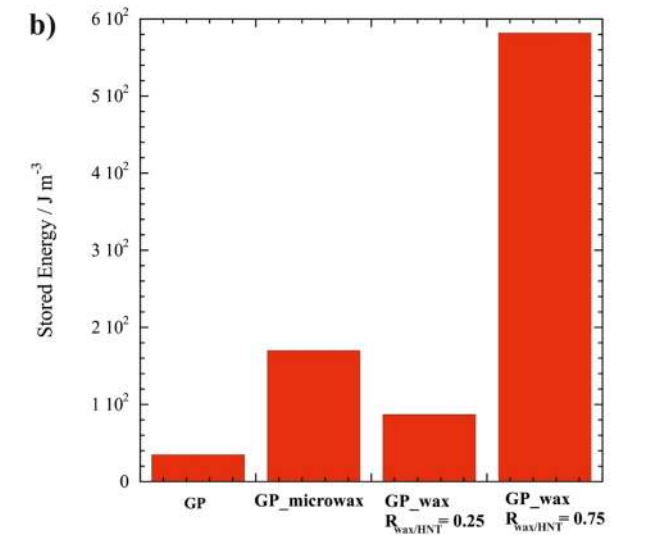

Fig. 11. Stress vs strain curves (a) and stored energies up to breaking (b) for GP, GP_microwax, GP_wax ($R_{wax/HNT}$ = 0.25 and 0.75). The relative error for stored energies up to breaking is 2%.

Table 4
Elastic modulus, stress and elongation at breaking point.[a].

Sample	Elastic Modulus / MPa	Stress at Breaking point / MPa	Elongation at Breaking point / %
GP	5425	1.8	0.03
GP_microwax	863	1.5	0.18
GP_wax ($R_{wax/HNT}$ = 0.25)	603	0.8	0.17
GP_wax ($R_{wax/HNT}$ = 0.75)	261	1.2	0.69

[a] The relative error is 2%.

contact angle data (Table 3). Specifically, the WVP results of the filled geopolymers could be attributed to the tortuosity effect as well as to decrease of geopolymer sorption sites for water molecules. Similar observations were detected for hydroxypropylcellulose films filled with wax microparticles [83]. On the other hand, an increase of the water permeability was observed after the rinsing step due to the actual removal of wax from the geopolymeric network (Fig. 12c). Interestingly, the washed geopolymers evidenced different water permeability capacity on dependence of the initial wax content. The largest WVP value was determined for GP_wax ($R_{wax/HNT}$ = 0.25), which possess a

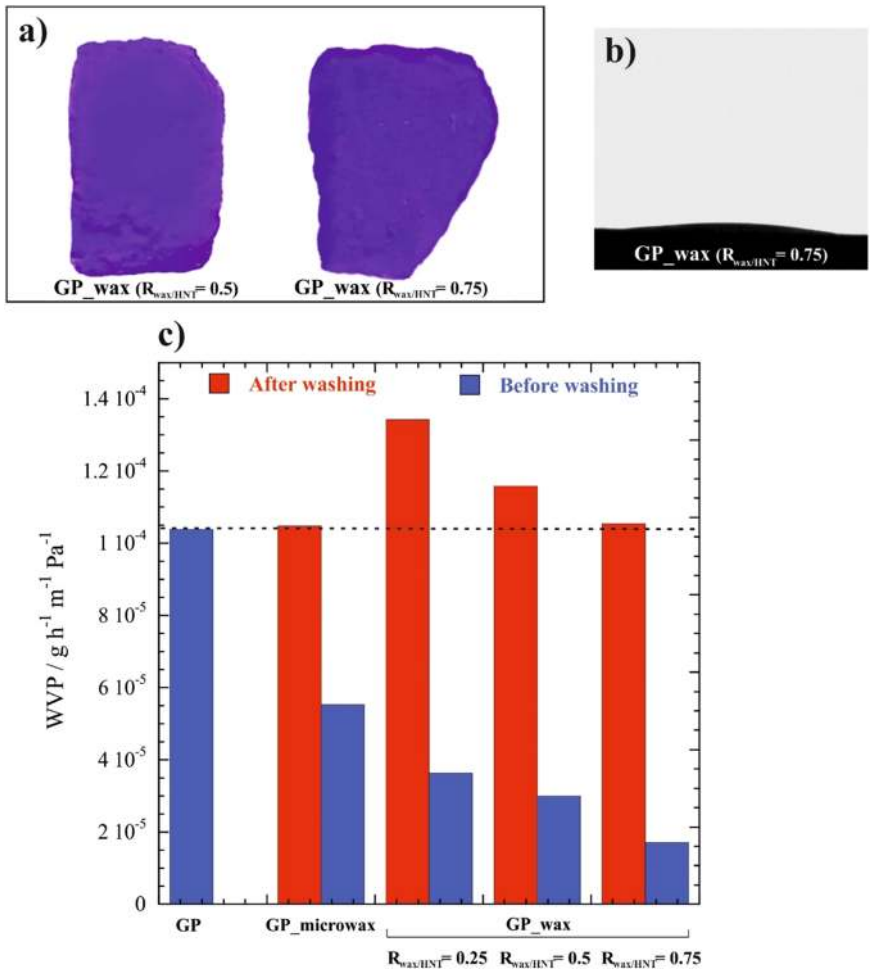

Fig. 12. Comparison of Nile Red essay for GP_wax ($R_{wax/HNT}$ = 0.5 and 0.75) after their washing with ethanol (a). Image of the water droplet after its deposition on washed GP_wax ($R_{wax/HNT}$ = 0.75) (b). Water vapor permeability of GP material and filled geopolymers before and after wax removal. Dotted line represents WVP value of GP sample.

significant higher water vapor permeability compared to that of GP material. The increase of $R_{wax/HNT}$ (0.5 and 0.75) allows us to obtain geopolymers with a lower WVP value after their washing with ethanol. Namely, we can state that GP_wax ($R_{wax/HNT}$ = 0.25) presents a higher porosity with respect to those of GP_wax ($R_{wax/HNT}$ = 0.5 and 0.75). As concerns GP_microwax, we detected that the rinsing with ethanol produced geopolymers with a water vapor permeability comparable with that of GP sample. On this basis, we can conclude that the removal of wax microparticles drives to the formation of geopolymeric materials with similar porosity respect to that of GP material. The latter was confirmed by helium pycnometer, which is a powerful technique to investigate the skeletal density and, consequently, the porosity of geopolymeric materials [74]. We observed that the incorporation of microwax within the HNT based geopolymer generates an increase of the skeletal density (2.27 ± 0.03 g cm^{-3} and 2.358 ± 0.011 g cm^{-3} for GP and GP_microwax, respectively) that can be attributed to a reduction of closed pores. This finding agrees with the flexural experiments, which evidenced that the stored energy up to breaking was enhanced by the filling of the geopolymer with microwax (Fig. 11b). In this regard, literature reports that the mechanical performances of geopolymers based on kaolinite [84] and metakaolinite [74] can be improved by decreasing the volume of closed pores. We estimated that the porosity of GP_microwax (24.8%) is significantly lower with respect to that of GP (49.9%). The washing procedure did not alter the porosity of the unfilled geopolymer, while an enhancement up to 50.1% was detected for GP_microwax sample confirming that the treatment by ethanol is effective to remove the microwax particles from the geopolymer structure. The largest porosity (64.4%) was detected for the washed GP_wax ($R_{wax/HNT}$ = 0.25) sample in agreement with its highest water vapor permeability (Fig. 12b).

4. Conclusions

Hybrid geopolymers based on halloysite nanotubes and beeswax microspheres (diameter of ca. 3 – 5 μm) have been developed as natural materials suitable for engineering applications because of their flexibility and heat absorption capacity. Based on the thermogravimetric analyses, we estimated that the proposed protocol allowed us to obtain halloysite based geopolymers containing ca. 0.06 wt% of beeswax microparticles. Although the low amount of microwax, their loading within the geopolymeric network generated relevant improvements of the flexural characteristics and heat storage capacity with respect to the unfilled geopolymer. In this regard, the stored energy up to breaking was increased by a factor of 5. These effects can be attributed to the homogeneous distribution of microwax particles (obtained from the Pickering emulsion) within the geopolymeric matrix as evidenced by the structural characteristics and the morphology of the composite geopolymers.

For comparison, halloysite based geopolymers filled with variable amounts of beeswax were fabricated. Their properties are dependent on their composition, and they reflect the random dispersion of the beeswax. Relevant improvements of the flexibility and heat storage capacity can be achieved by adding a large amount (ca. 40 wt%) of

beeswax. Namely, the filling with beeswax requires contents of ca. 1 order larger than the loading of microwax to obtain composite geopolymers with comparable performances.

Finally, we detected that both beeswax and microwax can be easily removed by washing the hybrid geopolymers with ethanol. Interestingly, the water vapour permeability of the washed geopolymers depends on the initial amount of wax incorporated in the geopolymeric network.

This work represents the starting point for the design of geopolymers filled with a phase change material (wax microparticles) that can act as smart thermal regulation systems for several applications within engineering and biotechnology.

CRediT authorship contribution statement

Martina Maria Calvino: Investigation, Data curation, Writing – original draft preparation. **Lorenzo Lisuzzo:** Data curation, Writing – original draft preparation. **Giuseppe Cavallaro:** Writing – review & editing, Validation. **Giuseppe Lazzara:** Conceptualization, Supervision. **Stefana Milioto:** Funding acquisition, Resources.

Declaration of Competing Interest

The authors declare that they have no known competing financial interests or personal relationships that could have appeared to influence the work reported in this paper.

Data Availability

Data will be made available on request.

Acknowledgments

The work was financially supported by “SETI-Sicilia Eco Tecnologie Innovative”, Cod.Progetto 2017-NAZ-0204, PO FESR Sicilia 2014/2020 – Azione 1.1.5 and the University of Palermo.

Supplementary material

DSC curves of Beeswax, GP_wax ($R_{wax/HNT} = 1$) and GP_microwax. Thermogravimetric curve of GP_wax ($R_{wax/HNT} = 1$) after washing. Assignment of IR peaks for geopolymer samples and halloysite.

Appendix A. Supporting information

Supplementary data associated with this article can be found in the online version at doi:10.1016/j.jece.2022.108594.

References

[1] C. Garlisi, E. Trepci, X. Li, R. Al Sakkaf, K. Al-Ali, R.P. Nogueira, L. Zheng, E. Azar, G. Palmisano, Multilayer thin film structures for multifunctional glass: self-cleaning, antireflective and energy-saving properties, Appl. Energy 264 (2020), 114697, https://doi.org/10.1016/j.apenergy.2020.114697.

[2] A. Yusuf, S. Al Jitan, C. Garlisi, G. Palmisano, A review of recent and emerging antimicrobial nanomaterials in wastewater treatment applications, Chemosphere 278 (2021), 130440, https://doi.org/10.1016/j.chemosphere.2021.130440.

[3] O. Jankovský, M. Lojka, A.-M. Lauermannová, F. Antončík, M. Pavlíková, M. Záleská, Z. Pavlík, A. Pivák, D. Sedmidubský, Towards novel building materials: high-strength nanocomposites based on graphene, graphite oxide and magnesium oxychloride, Appl. Mater. Today 20 (2020), 100766, https://doi.org/10.1016/j.apmt.2020.100766.

[4] S. Saha, C. Rajasekaran, Enhancement of the properties of fly ash based geopolymer paste by incorporating ground granulated blast furnace slag, Constr. Build. Mater. 146 (2017) 615–620, https://doi.org/10.1016/j.conbuildmat.2017.04.139.

[5] Y. Luna-Galiano, C. Leiva, R. Villegas, F. Arroyo, L. Vilches, C. Fernández-Pereira, Carbon fiber waste incorporation in blast furnace slag geopolymer-composites, Mater. Lett. 233 (2018) 1–3, https://doi.org/10.1016/j.matlet.2018.08.099.

[6] Q. Wan, F. Rao, S. Song, C.A. León-Patiño, Geothermal clay-based geopolymer binders: synthesis and microstructural characterization, Appl. Clay Sci. 146 (2017) 223–229, https://doi.org/10.1016/j.clay.2017.05.047.

[7] C. Ng, U.J. Alengaram, L.S. Wong, K.H. Mo, M.Z. Jumaat, S. Ramesh, A review on microstructural study and compressive strength of geopolymer mortar, paste and concrete, Constr. Build. Mater. 186 (2018) 550–576, https://doi.org/10.1016/j.conbuildmat.2018.07.075.

[8] Q. Su, Y. He, S. Yang, H. Wan, S. Chang, X. Cui, Synthesis of NaA-zeolite microspheres by conversion of geopolymer and their performance of Pb (II) removal, Appl. Clay Sci. 200 (2021), 105914, https://doi.org/10.1016/j.clay.2020.105914.

[9] M. El Alouani, H. Saufi, G. Moutaoukil, S. Alehyen, B. Nematollahi, W. Belmaghraoui, M. Taibi, Application of geopolymers for treatment of water contaminated with organic and inorganic pollutants: state-of-the-art review, J. Environ. Chem. Eng. 9 (2021), 105095, https://doi.org/10.1016/j.jece.2021.105095.

[10] K. Okada, A. Ooyama, T. Isobe, Y. Kameshima, A. Nakajima, K.J.D. MacKenzie, Water retention properties of porous geopolymers for use in cooling applications, J. Eur. Ceram. Soc. 29 (2009) 1917–1923, https://doi.org/10.1016/j.jeurceramsoc.2008.11.006.

[11] F. Aghabeyk, A. Azadmehr, A. Hezarkhani, Fabrication of feldspar-based geopolymers from perlite toward decontamination of heavy metals from aqueous solution: hydrolysis process, characterizations, kinetic and isotherm studies, J. Environ. Chem. Eng. 10 (2022), 108087, https://doi.org/10.1016/j.jece.2022.108087.

[12] C. Bai, P. Colombo, Processing, properties and applications of highly porous geopolymers: a review, Ceram. Int. 44 (2018) 16103–16118, https://doi.org/10.1016/j.ceramint.2018.05.219.

[13] B.B. Jindal, R. Sharma, The effect of nanomaterials on properties of geopolymers derived from industrial by-products: a state-of-the-art review, Constr. Build. Mater. 252 (2020), 119028, https://doi.org/10.1016/j.conbuildmat.2020.119028.

[14] G.I. Fakhrullina, F.S. Akhatova, Y.M. Lvov, R.F. Fakhrullin, Toxicity of halloysite clay nanotubes in vivo: a Caenorhabditis elegans study, Environ. Sci. Nano 2 (2015) 54–59, https://doi.org/10.1039/c4en00135d.

[15] M. Kryuchkova, A. Danilushkina, Y. Lvov, R. Fakhrullin, Evaluation of toxicity of nanoclays and graphene oxide: in vivo A Paramecium caudatum study, Environ. Sci. Nano 3 (2016) 442–452, https://doi.org/10.1039/c5en00201j.

[16] E. Rozhina, S. Batasheva, R. Miftakhova, X. Yan, A. Vikulina, D. Volodkin, R. Fakhrullin, Comparative cytotoxicity of kaolinite, halloysite, multiwalled carbon nanotubes and graphene oxide, Appl. Clay Sci. 205 (2021), 106041, https://doi.org/10.1016/j.clay.2021.106041.

[17] Z. Long, Y.-P. Wu, H.-Y. Gao, J. Zhang, X. Ou, R.-R. He, M. Liu, In vitro and in vivo toxicity evaluation of halloysite nanotubes, J. Mater. Chem. B 6 (2018) 7204–7216, https://doi.org/10.1039/C8TB01382A.

[18] L.W. Wong, P. Pasbakhsh, A.M. Arabi, J. Keeling, J.B.L. Tan, Halloysite nanotubes from various geological deposits: New insights to acid etching and their impacts on products’ characteristics, J. Environ. Chem. Eng. 9 (2021), 106235, https://doi.org/10.1016/j.jece.2021.106235.

[19] L. Lisuzzo, G. Cavallaro, S. Milioto, G. Lazzara, Halloysite nanotubes filled with MgO for paper reinforcement and deacidification, Appl. Clay Sci. 213 (2021), https://doi.org/10.1016/j.clay.2021.106231.

[20] L. Lisuzzo, G. Cavallaro, S. Milioto, G. Lazzara, Halloysite nanotubes as nanoreactors for heterogeneous micellar catalysis, J. Colloid Interface Sci. 608 (2022) 424–434, https://doi.org/10.1016/j.jcis.2021.09.146.

[21] Y. Zhao, E. Abdullayev, A. Vasiliev, Y. Lvov, Halloysite nanotubule clay for efficient water purification, J. Colloid Interface Sci. 406 (2013) 121–129, https://doi.org/10.1016/j.jcis.2013.05.072.

[22] Y. Song, P. Yuan, P. Du, L. Deng, Y. Wei, D. Liu, X. Zhong, J. Zhou, A novel halloysite–CeOx nanohybrid for efficient arsenic removal, Appl. Clay Sci. 186 (2020), https://doi.org/10.1016/j.clay.2020.105450.

[23] P. Maziarz, J. Matusik, A. Radziszewska, Halloysite-zero-valent iron nanocomposites for removal of Pb(II)/Cd(II) and As(V)/Cr(VI): Competitive effects, regeneration possibilities and mechanisms, J. Environ. Chem. Eng. 7 (2019), 103507, https://doi.org/10.1016/j.jece.2019.103507.

[24] S. Wang, D. Xiao, X. Zheng, L. Zheng, Y. Yang, H. Zhang, B. Ai, Z. Sheng, Halloysite and coconut shell biochar magnetic composites for the sorption of Pb(II) in wastewater: synthesis, characterization and mechanism investigation, J. Environ. Chem. Eng. 9 (2021), 106865, https://doi.org/10.1016/j.jece.2021.106865.

[25] M.H. Kanani-Jazi, S. Akbari, Amino-dendritic and carboxyl functionalized halloysite nanotubes for highly efficient removal of cationic and anionic dyes: kinetic, isotherm, and thermodynamic studies, J. Environ. Chem. Eng. 9 (2021), 105214, https://doi.org/10.1016/j.jece.2021.105214.

[26] M. Amid, N. Nabian, M. Delavar, Performance evaluation and modeling study of PC blended membranes incorporated with SDS-modified and unmodified halloysite nanotubes in the separation of oil from water, J. Environ. Chem. Eng. 9 (2021), 105237, https://doi.org/10.1016/j.jece.2021.105237.

[27] S. Sadjadi, M.M. Heravi, S.S. Kazemi, Ionic liquid decorated chitosan hybridized with clay: a novel support for immobilizing Pd nanoparticles, Carbohydr. Polym. 200 (2018) 183–190, https://doi.org/10.1016/j.carbpol.2018.07.093.

[28] S. Sadjadi, M. Akbari, E. Monflier, M.M. Heravi, B. Leger, Pd nanoparticles immobilized on halloysite decorated with a cyclodextrin modified melamine-based polymer: a promising heterogeneous catalyst for hydrogenation of nitroarenes, New J. Chem. 42 (2018) 15733–15742, https://doi.org/10.1039/C8NJ03014F.

[29] Y. Liu, H. Guan, J. Zhang, Y. Zhao, J.-H. Yang, B. Zhang, Polydopamine-coated halloysite nanotubes supported AgPd nanoalloy: an efficient catalyst for hydrolysis

of ammonia borane, Int. J. Hydrog. Energy 43 (2018) 2754–2762, https://doi.org/10.1016/j.ijhydene.2017.12.105.
[30] Y. Feng, X. Zhou, J. Yang, X. Gao, L. Yin, Y. Zhao, B. Zhang, Encapsulation of ammonia borane in Pd/halloysite nanotubes for efficient thermal dehydrogenation, ACS Sustain. Chem. Eng. 8 (2020) 2122–2129, https://doi.org/10.1021/acssuschemeng.9b04480.
[31] A. Glotov, A. Vutolkina, A. Pimerzin, V. Vinokurov, Y. Lvov, Clay nanotube-metal core/shell catalysts for hydroprocesses, Chem. Soc. Rev. 50 (2021) 9240–9277, https://doi.org/10.1039/D1CS00502B.
[32] M. Liu, Y. Chang, J. Yang, Y. You, R. He, T. Chen, C. Zhou, Functionalized halloysite nanotube by chitosan grafting for drug delivery of curcumin to achieve enhanced anticancer efficacy, J. Mater. Chem. B 4 (2016) 2253–2263, https://doi.org/10.1039/c5tb02725j.
[33] C. Cheng, Y. Gao, W. Song, Q. Zhao, H. Zhang, H. Zhang, Halloysite nanotube-based H2O2-responsive drug delivery system with a turn on effect on fluorescence for real-time monitoring, Chem. Eng. J. 380 (2020), 122474, https://doi.org/10.1016/j.cej.2019.122474.
[34] F. Liu, L. Bai, H. Zhang, H. Song, L. Hu, Y. Wu, X. Ba, Smart H2O2-responsive drug delivery system made by halloysite nanotubes and carbohydrate polymers, ACS Appl. Mater. Interfaces 9 (2017) 31626–31633, https://doi.org/10.1021/acsami.7b10867.
[35] Y. Zhang, L. Bai, C. Cheng, Q. Zhou, Z. Zhang, Y. Wu, H. Zhang, A novel surface modification method upon halloysite nanotubes: A desirable cross-linking agent to construct hydrogels, Appl. Clay Sci. 182 (2019), 105259, https://doi.org/10.1016/j.clay.2019.105259.
[36] A. Vikulina, D. Voronin, R. Fakhrullin, V. Vinokurov, D. Volodkin, Naturally derived nano- and micro-drug delivery vehicles: halloysite, vaterite and nanocellulose, New J. Chem. 44 (2020) 5638–5655, https://doi.org/10.1039/C9NJ06470B.
[37] G. Gorrasi, Dispersion of halloysite loaded with natural antimicrobials into pectins: characterization and controlled release analysis, Carbohydr. Polym. 127 (2015) 47–53, https://doi.org/10.1016/j.carbpol.2015.03.050.
[38] M. Liu, C. Wu, Y. Jiao, S. Xiong, C. Zhou, Chitosan-halloysite nanotubes nanocomposite scaffolds for tissue engineering, J. Mater. Chem. B 1 (2013) 2078–2089, https://doi.org/10.1039/c3tb20084a.
[39] M. Liu, R. Fakhrullin, A. Novikov, A. Panchal, Y. Lvov, Tubule nanoclay-organic heterostructures for biomedical applications, Macromol. Biosci. 19 (2019) 1800419, https://doi.org/10.1002/mabi.201800419.
[40] J. Zhang, X. Luo, Y.-P. Wu, F. Wu, Y.-F. Li, R.-R. He, M. Liu, Rod in tube: a novel nanoplatform for highly effective chemo-photothermal combination therapy toward breast cancer, ACS Appl. Mater. Interfaces 11 (2019) 3690–3703, https://doi.org/10.1021/acsami.8b17533.
[41] A. Panchal, G. Fakhrullina, R. Fakhrullin, Y. Lvov, Self-assembly of clay nanotubes on hair surface for medical and cosmetic formulations, Nanoscale 10 (2018) 18205–18216, https://doi.org/10.1039/C8NR05949G.
[42] G. Cavallaro, S. Milioto, S. Konnova, G. Fakhrullina, F. Akhatova, G. Lazzara, R. Fakhrullin, Y. Lvov, Halloysite/keratin nanocomposite for human hair photoprotection coating, ACS Appl. Mater. Interfaces 12 (2020) 24348–24362, https://doi.org/10.1021/acsami.0c05252.
[43] A. Panchal, G. Fakhrullina, R. Fakhrullin, Y. Lvov, Self-assembly of clay nanotubes on hair surface for medical and cosmetic formulations, Nanoscale 10 (2018) 18205–18216, https://doi.org/10.1039/c8nr05949g.
[44] M. Gruppuso, G. Turco, E. Marsich, D. Porrelli, Polymeric wound dressings, an insight into polysaccharide-based electrospun membranes, Appl. Mater. Today 24 (2021), 101148, https://doi.org/10.1016/j.apmt.2021.101148.
[45] B. Zhang, H. Guo, P. Yuan, Y. Li, Q. Wang, L. Deng, D. Liu, Geopolymerization of halloysite via alkali-activation: dependence of microstructures on precalcination, Appl. Clay Sci. 185 (2020), 105375, https://doi.org/10.1016/j.clay.2019.105375.
[46] M. Razzaghian Ghadikolaee, A. Habibnejad Korayem, A. Sharif, Y. Ming Liu, The halloysite nanotube effects on workability, mechanical properties, permeability and microstructure of cementitious mortar, Constr. Build. Mater. 267 (2021), 120873, https://doi.org/10.1016/j.conbuildmat.2020.120873.
[47] B. Zhang, H. Guo, P. Yuan, L. Deng, X. Zhong, Y. Li, Q. Wang, D. Liu, Novel acid-based geopolymer synthesized from nanosized tubular halloysite: the role of precalcination temperature and phosphoric acid concentration, Cem. Concr. Compos. 110 (2020), 103601, https://doi.org/10.1016/j.cemconcomp.2020.103601.
[48] M.M. Calvino, G. Cavallaro, L. Lisuzzo, S. Milioto, G. Lazzara, Separation of halloysite/kaolinite mixtures in water controlled by sucrose addition: the influence of the attractive forces on the sedimentation behavior, Coll. Surf. Physicochem. Eng. Asp. 641 (2022), 128530, https://doi.org/10.1016/j.colsurfa.2022.128530.
[49] Z. Zhang, H. Wang, X. Yao, Y. Zhu, Effects of halloysite in kaolin on the formation and properties of geopolymers, Cem. Concr. Compos. 34 (2012) 709–715, https://doi.org/10.1016/j.cemconcomp.2012.02.003.
[50] L. Lisuzzo, G. Cavallaro, S. Milioto, G. Lazzara, Pickering emulsions stabilized by halloysite nanotubes: from general aspects to technological applications, Adv. Mater. Interfaces (2022) 2102346–2102375, https://doi.org/10.1002/admi.202102346.
[51] D. Stehl, T. Skale, L. Hohl, Y. Lvov, J. Koetz, M. Kraume, A. Drews, R. Von Klitzing, Oil-in-water pickering emulsions stabilized by halloysite clay nanotubes toward efficient filterability, ACS Appl. Nano Mater. 3 (2020) 11743–11751, https://doi.org/10.1021/acsanm.0c02205.
[52] T. Yu, L.T. Swientoniewski, M. Omarova, M.-C. Li, I.I. Negulescu, N. Jiang, O. A. Darvish, A. Panchal, D.A. Blake, Q. Wu, Y.M. Lvov, V.T. John, D. Zhang, Investigation of amphiphilic polypeptoid-functionalized halloysite nanotubes as emulsion stabilizer for oil spill remediation, ACS Appl. Mater. Interfaces 11 (2019) 27944–27953, https://doi.org/10.1021/acsami.9b08623.
[53] O. Owoseni, Y. Su, S. Raghavan, A. Bose, V.T. John, Hydrophobically modified chitosan biopolymer connects halloysite nanotubes at the oil-water interface as complementary pair for stabilizing oil droplets, J. Colloid Interface Sci. 620 (2022) 135–143, https://doi.org/10.1016/j.jcis.2022.03.142.
[54] C. Ferone, G. Roviello, F. Colangelo, R. Cioffi, O. Tarallo, Novel hybrid organic-geopolymer materials, Appl. Clay Sci. 73 (2013) 42–50, https://doi.org/10.1016/j.clay.2012.11.001.
[55] R. Mustafa, K.N. Shivaprasad, B.B. Das, Effect of various additives on the properties of fly ash based geopolymer mortar, Lect. Notes Civ. Eng. 25 (2019) 707–715, https://doi.org/10.1007/978-981-13-3317-0_63.
[56] E. Prud'homme, P. Michaud, S. Rossignol, E. Joussein, Mechanical properties of geopolymer composite reinforced by organic or inorganic additives, in: 2014: pp. 67–78.
[57] P. Behera, V. Baheti, J. Militky, P. Louda, Elevated temperature properties of basalt microfibril filled geopolymer composites, Constr. Build. Mater. 163 (2018) 850–860, https://doi.org/10.1016/j.conbuildmat.2017.12.152.
[58] Q. Han, P. Zhang, J. Wu, Y. Jing, D. Zhang, T. Zhang, Comprehensive review of the properties of fly ash-based geopolymer with additive of nano-SiO2, Nanotechnol. Rev. 11 (2022) 1478–1498, https://doi.org/10.1515/ntrev-2022-0092.
[59] A. Karthik, K. Sudalaimani, C.T. Vijayakumar, Durability study on coal fly ash-blast furnace slag geopolymer concretes with bio-additives, Ceram. Int. 43 (2017) 11935–11943, https://doi.org/10.1016/j.ceramint.2017.06.042.
[60] P. Khamlue, N. Lertcumfu, P. Jaita, S. Manotham, T. Tunkasiri, P. Malasri, G. Rujijanagul, The effects of Biochar additive on the properties of Geopolymer materials, Key Eng. Mater. (2019) 273–278, https://doi.org/10.4028/www.scientific.net/KEM.798.273, 798 KEM.
[61] S.K. John, Y. Nadir, K. Girija, Effect of source materials, additives on the mechanical properties and durability of fly ash and fly ash-slag geopolymer mortar: a review, Constr. Build. Mater. 280 (2021), 122443, https://doi.org/10.1016/j.conbuildmat.2021.122443.
[62] P.F. De Castro, S. Minko, V. Vinokurov, K. Cherednichenko, D.G. Shchukin, Long-term autonomic thermoregulating fabrics based on microencapsulated phase change materials, ACS Appl. Energy Mater. 4 (2021) 12789–12797, https://doi.org/10.1021/acsaem.1c02170.
[63] E.M. Shchukina, M. Graham, Z. Zheng, D.G. Shchukin, Nanoencapsulation of phase change materials for advanced thermal energy storage systems, Chem. Soc. Rev. 47 (2018) 4156–4175, https://doi.org/10.1039/C8CS00099A.
[64] Z. Zheng, Z. Chang, G.-K. Xu, F. McBride, A. Ho, Z. Zhuola, M. Michailidis, W. Li, R. Raval, R. Akhtar, D. Shchukin, Microencapsulated phase change materials in solar-thermal conversion systems: understanding geometry-dependent heating efficiency and system reliability, ACS Nano 11 (2017) 721–729, https://doi.org/10.1021/acsnano.6b07126.
[65] L. Lisuzzo, T. Hueckel, G. Cavallaro, S. Sacanna, G. Lazzara, Pickering emulsions based on wax and halloysite nanotubes: an ecofriendly protocol for the treatment of archeological woods, ACS Appl. Mater. Interfaces 13 (2021) 1651–1661, https://doi.org/10.1021/acsami.0c20443.
[66] C. Duce, S. Vecchio Ciprioti, L. Ghezzi, V. Ierardi, M.R. Tinè, Thermal behavior study of pristine and modified halloysite nanotubes: A modern kinetic study, J. Therm. Anal. Calorim. 121 (2015) 1011–1019, https://doi.org/10.1007/s10973-015-4741-7.
[67] Z. Sun, Y. Zhang, S. Zheng, Y. Park, R.L. Frost, Preparation and thermal energy storage properties of paraffin/calcined diatomite composites as form-stable phase change materials, Thermochim. Acta 558 (2013) 16–21, https://doi.org/10.1016/j.tca.2013.02.005.
[68] Y. Zhao, S. Thapa, L. Weiss, Y. Lvov, Phase change heat insulation based on wax-clay nanotube composites, Adv. Eng. Mater. 16 (2014) 1391–1399, https://doi.org/10.1002/adem.201400094.
[69] J. Zhang, X. Zhang, Y. Wan, D. Mei, B. Zhang, Preparation and thermal energy properties of paraffin/halloysite nanotube composite as form-stable phase change material, Sol. Energy 86 (2012) 1142–1148, https://doi.org/10.1016/j.solener.2012.01.002.
[70] M. Catauro, G. Dal Poggetto, C. Sgarlata, S. Vecchio Ciprioti, S. Pacifico, C. Leonelli, Thermal and microbiological performance of metakaolin-based geopolymers cement with waste glass, Appl. Clay Sci. 197 (2020), 105763, https://doi.org/10.1016/j.clay.2020.105763.
[71] A. Hajimohammadi, J.L. Provis, J.S.J. van Deventer, Time-resolved and spatially-resolved infrared spectroscopic observation of seeded nucleation controlling geopolymer gel formation, J. Colloid Interface Sci. 357 (2011) 384–392, https://doi.org/10.1016/j.jcis.2011.02.045.
[72] M.R. El-Naggar, M.I. El-Dessouky, Re-use of waste glass in improving properties of metakaolin-based geopolymers: Mechanical and microstructure examinations, Constr. Build. Mater. 132 (2017) 543–555, https://doi.org/10.1016/j.conbuildmat.2016.12.023.
[73] A. Fernández-Jiménez, A. Palomo, J.Y. Pastor, A. Martín, New cementitious materials based on alkali-activated fly ash: performance at high temperatures, J. Am. Ceram. Soc. 91 (2008) 3308–3314, https://doi.org/10.1111/j.1551-2916.2008.02625.x.
[74] F.G.M. Aredes, T.M.B. Campos, J.P.B. Machado, K.K. Sakane, G.P. Thim, D. D. Brunelli, Effect of cure temperature on the formation of metakaolinite-based geopolymer, Ceram. Int. 41 (2015) 7302–7311, https://doi.org/10.1016/j.ceramint.2015.02.022.
[75] N. Tanner, B. Lichtenberg-Kraag, Identification and quantification of single and multi-adulteration of beeswax by FTIR-ATR spectroscopy, Eur. J. Lipid Sci. Technol. 121 (2019) 1900245, https://doi.org/10.1002/ejlt.201900245.

[76] S. Greiser, P. Sturm, G.J.G. Gluth, M. Hunger, C. Jäger, Differentiation of the solid-state NMR signals of gel, zeolite phases and water species in geopolymer-zeolite composites, Ceram. Int. 43 (2017) 2202–2208, https://doi.org/10.1016/j.ceramint.2016.11.004.

[77] C.R. Kaze, A. Nana, G.L. Lecomte-Nana, J.G.N. Deutou, E. Kamseu, U.C. Melo, F. Andreola, C. Leonelli, Thermal behaviour and microstructural evolution of metakaolin and meta-halloysite-based geopolymer binders: a comparative study, J. Therm. Anal. Calorim. 147 (2022) 2055–2071, https://doi.org/10.1007/s10973-021-10555-2.

[78] A.Z. Khalifa, Ö. Cizer, Y. Pontikes, A. Heath, P. Patureau, S.A. Bernal, A.T. M. Marsh, Advances in alkali-activation of clay minerals, Cem. Concr. Res. 132 (2020), 106050, https://doi.org/10.1016/j.cemconres.2020.106050.

[79] A. Bucio, R. Moreno-Tovar, L. Bucio, J. Espinosa-Dávila, F. Anguebes-Franceschi, Characterization of beeswax, candelilla wax and paraffin wax for coating cheeses, Coatings 11 (2021) 261, https://doi.org/10.3390/coatings11030261.

[80] S. Naderizadeh, J.A. Heredia-Guerrero, G. Caputo, S. Grasselli, A. Malchiodi, A. Athanassiou, I.S. Bayer, Superhydrophobic coatings from beeswax-in-water emulsions with latent heat storage capability, Adv. Mater. Interfaces 6 (2019) 1801782, https://doi.org/10.1002/admi.201801782.

[81] Y. Gaillard, A. Mija, A. Burr, E. Darque-Ceretti, E. Felder, N. Sbirrazzuoli, Green material composites from renewable resources: polymorphic transitions and phase diagram of beeswax/rosin resin, Thermochim. Acta 521 (2011) 90–97, https://doi.org/10.1016/j.tca.2011.04.010.

[82] V.A. Cataldo, G. Cavallaro, G. Lazzara, S. Milioto, F. Parisi, Coffee grounds as filler for pectin: green composites with competitive performances dependent on the UV irradiation, Carbohydr. Polym. 170 (2017) 198–205, https://doi.org/10.1016/j.carbpol.2017.04.092.

[83] L. Lisuzzo, M.R. Caruso, G. Cavallaro, S. Milioto, G. Lazzara, Hydroxypropyl cellulose films filled with halloysite nanotubes/wax hybrid microspheres, Ind. Eng. Chem. Res. 60 (2021) 1656–1665, https://doi.org/10.1021/acs.iecr.0c05148.

[84] W. Sornlar, A. Wannagon, S. Supothina, Stabilized homogeneous porous structure and pore type effects on the properties of lightweight kaolinite-based geopolymers, J. Build. Eng. 44 (2021), 103273, https://doi.org/10.1016/j.jobe.2021.103273.

Materials Letters 330 (2023) 133257

Contents lists available at ScienceDirect

Materials Letters

journal homepage: www.elsevier.com/locate/matlet

Beeswax/halloysite microparticles embedded within a geopolymeric layer for the protective coating of steel

Martina Maria Calvino [a], Lorenzo Lisuzzo [a], Giuseppe Cavallaro [a,*], Giuseppe Lazzara [a], Candida Pipitone [a], Francesco Giannici [a]

[a] Dipartimento di Fisica e Chimica, Università degli Studi di Palermo, Viale delle Scienze, pad. 17, 90128 Palermo, Italy

ARTICLE INFO

Keywords:
Halloysite
Geopolymer
Coating

ABSTRACT

A halloysite-based geopolymer filled with microwax particles was designed as a protective layer on steel substrates. Beeswax microparticles were obtained from the clay stabilized Pickering emulsions and they were homogeneously dispersed within the geopolymeric network, thus improving the coating physico-chemical properties. Specifically, this treatment changed the steel's wettability by increasing its hydrophobicity. Moreover, XRF analysis was conducted in order to have details on the chemical compositions.

1. Introduction

Geopolymers are an innovative and green alternative for construction materials due to the employing of industrial by-products or natural resources with the benefit of the reduction of carbon dioxide emissions [1]. They consist of cross-linked tetrahedral [AlO_4] and [SiO_4] groups with alkali metal cations, and are synthesized by activating an aluminosilicate precursor with a highly alkaline solution [2,3]. Among the precursors, clay minerals as kaolinite and halloysite nanotubes are commonly used given their low cost, eco-friendliness and biocompatibility [4–7]. Geopolymer coatings on metal substrates as protective and thermal barriers for concrete have been reported [8]. In order to guarantee low water adhesion and to reduce the growth of biological species, hydrophobicity is one of the main characteristics of the protective layers [9]. As a matter of fact, it should be noted that geopolymers are inherently hydrophilic because of the hydroxyl groups on their surface. Therefore, microwax particles obtained from Pickering emulsions has been employed [10–12]. In this work beeswax microparticles were embedded within the geopolymeric network to increase the hydrophobicity, obtaining a new protective layer on steel sheets for coating applications.

2. Experimental section

2.1. Geopolymer preparation and treatment of the steel sheets

Beeswax, Halloysite (HNTs), ethanol (≥99.5 %), acetone (≥99.5 %) and sodium hydroxide (≥98 %) are Sigma Aldrich products. Steel sheets are a gift from Puleo SpA, Italy. The beeswax/HNTs microparticles were prepared via Pickering emulsions as reported in literature [10]. Afterwards, a NaOH solution (12 M) was added to the dried beeswax/HNTs microparticles at 1:1 NaOH/HNTs ratio, resulting in a viscous and flowing paste. Prior to any treatment, the steel sheets were degreased in acetone using an ultrasonic bath and washed with deionized water and ethanol. The coating of the steel substrates was performed by brushing the surface with the geopolymeric paste (GP microwax). The final hardening step was carried out by placing the treated steel samples in an oven at 50 °C for 48 h. Then, samples were washed many times by pouring about 100 mL of water on their surface and by dipping them into 50 mL of water overnight. Finally, the treated samples were dried at room conditions for 5 days before characterization. It is worth to note that the same protocol was used for the treatment of the steel substrates with pure halloysite based geopolymer (GP), without any beeswax addition for comparison.

2.2. Characterization

Optical images of the samples were obtained by a digital microscope

* Corresponding author.
E-mail address: giuseppe.cavallaro@unipa.it (G. Cavallaro).

https://doi.org/10.1016/j.matlet.2022.133257
Received 30 June 2022; Received in revised form 6 August 2022; Accepted 25 September 2022
Available online 3 October 2022

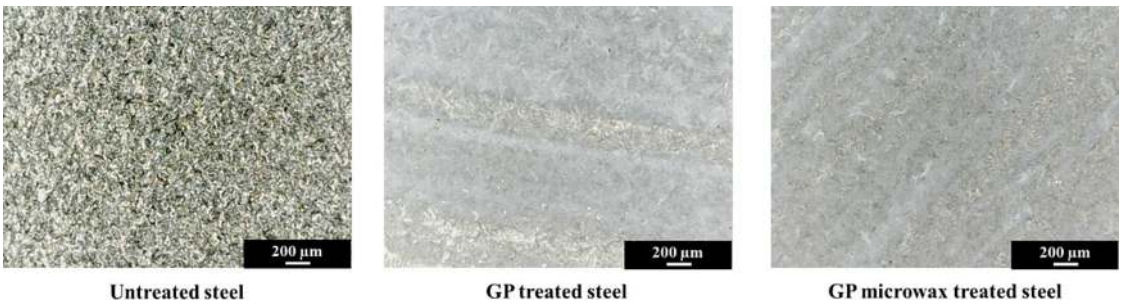

Fig. 1. Optical micrographs of untreated steel and sheets coated with HNTs based geopolymer and beeswax/HNTs microparticles based geopolymer.

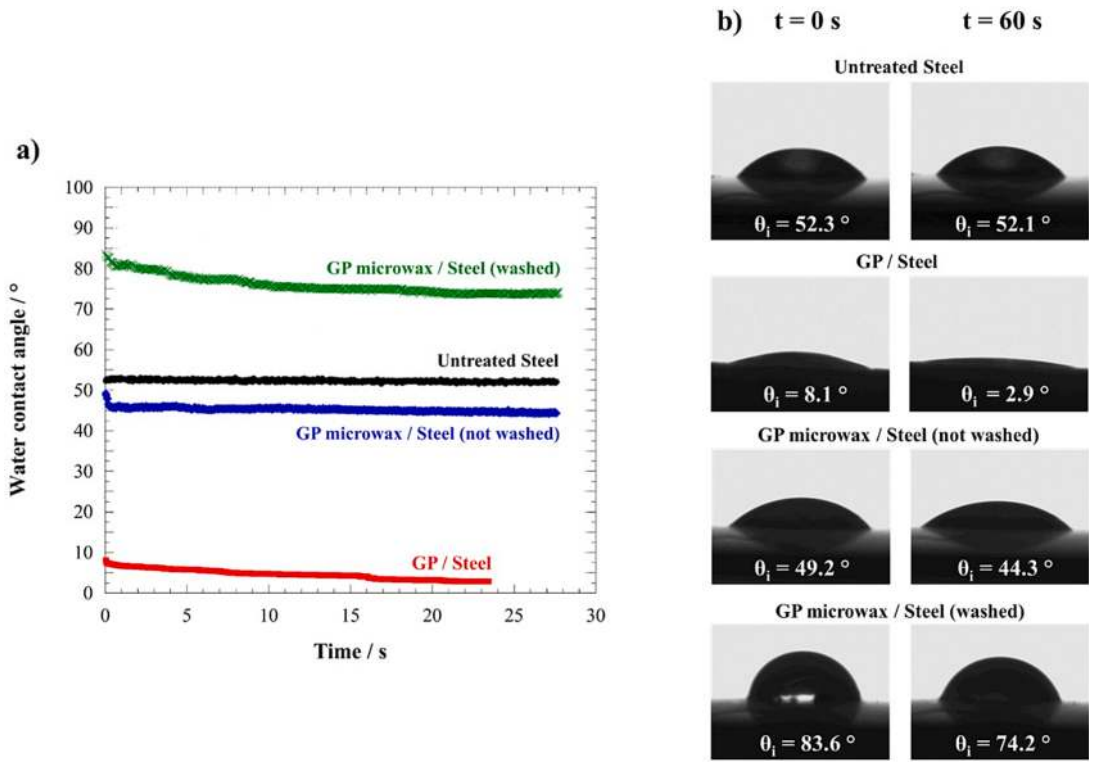

Fig. 2. (a) Water contact angle curves as a function of time, (b water droplets profiles at t = 0 s and t = 60 s after their deposition on the surface of the samples.

Table 1
Fitting parameters of the water contact angle kinetic evolution.

	K_0 (s^{-n})	n
GP/Steel	0.121 ± 0.007	0.54 ± 0.02
GP microwax/Steel (washed)	0.043 ± 0.006	0.35 ± 0.04

(CoolingTech).

The wettability was investigated through water contact angle measurements in the sessile drop method, by employing an optical apparatus (OCA 20, Data Physics Instruments) at 25.0 ± 0.1 °C. X-ray Fluorescence (XRF) Spectrometry was carried out by an Olympus Innov-X DS-2000 Delta.

3. Results and discussion

Optical microscopy was conducted to observe the morphological features of the treated and untreated steel sheets, and to evaluate the effect of the coating layers at a micrometric level (Fig. 1).

The surface of the bare steel sheets appears heterogeneous and porous, while it looks smoother and homogeneous after the treatments. This effect can be related to the filling of pores with the coating protective materials, even though some microdomains and aggregation of particles can be observed on both the GP and GP microwax treated steel sheets. Accordingly, we can state that both treatments are effective in reducing the steel porosity although GP and GP microwax are not totally incorporated within the steel structure.

Untreated sheet is hydrophilic and its contact angle is 52.3° without any variation as a function of time (Fig. 2). Once the surface is coated with the halloysite based geopolymer, it becomes much more hydrophilic and its contact angle falls to 8.1°. This effect can be related both to the high hydrophilicity of halloysite based geopolymer which can interact with the water via hydrogen bonding with the –OH groups on the surface, and to the smoother surface of the sample [13].

A different behaviour was recorded after coating with the beeswax/HNTs microparticles based geopolymer. For instance, the material is still hydrophilic with a contact angle of 49.2° that barely decreases to 44.3° after 60 s before any cleaning step is carried out. Remarkably, the treated steel becomes more hydrophobic after washing the surface with water. The value soared to 83.6° and then it slightly decreased to 74.2° after one minute.

These variations can be most likely related to the excess of halloysite

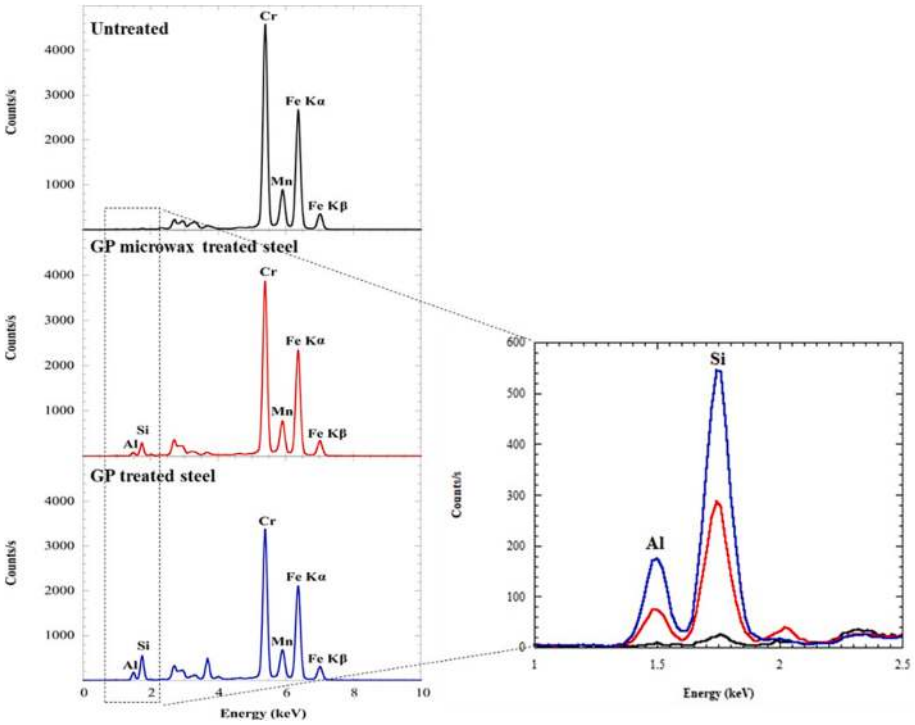

Fig. 3. XRF spectra of treated and untreated steel sheets.

nanotubes. After washing away the excess of clay, the microwax particles on the surface can interact with the water droplet thus enhancing the hydrophobic contribution to the wettability of the material. It should be noted that the addition of hydrophobic beewax can affect the micron-level coating surface structure smoothness.

In order to have more details about the droplet evolution on the surface, the data were analyzed by fitting the curves with the following equation:

$$\Theta = \theta_i \exp(-k_\theta \tau^{n}) \quad (1)$$

where θ_i is the contact angle at $t = 0$, k_θ is the constant related to the kinetics of the process and n is a coefficient which describes the mechanism of the water droplet evolution after its deposition on the solid substrate. In particular, values for n range from 0 to 1 on dependence of the absorption and spreading contributions, respectively.

It is clear that the presence of the microwax particles within the coating layer is responsible for a decrease of the process rate, as evidenced by k_θ reduction (Table 1). Similarly, the mechanism of the water droplet evolution on the treated steel sheet is affected, being the spreading contribution lower compared to the pure halloysite based geopolymeric coating, as suggested by the decrease of n (Table 1).

Aimed at characterizing the chemical composition of the protective layers on the steel sheets, XRF studies were carried out (Fig. 3). It is worth to note that, in the three investigated systems, the most significant peaks are related to the presence of Chromium, Manganese and Iron which are proper components of the bare steel sheet. After the treatment protocols are carried out, instead, Silicon and Aluminum can be detected on the surface. Most interestingly, the intensity of the Si and Al peaks is higher for GP treated steel compared to the steel coated with beeswax/HNTs microparticles based geopolymer (inset in Fig. 3).

Iron and Chromium are the main components of the steel sheets in terms of composition, with 70.85 and 18.10 wt%, respectively. After the treatment protocols, instead, Al and Si are detected significantly. Despite Fe and Cr are still the most abundant elements, the amounts of Al and Si are 11.21 and 11.26 wt%, respectively, for GP microwax treated sample. Besides, the quantities of these elements increase up to 19.57 and 18.62 wt% in the GP treated steel. It should be noted that the Al/Si ratio is ca. 1, which is typical for pristine halloysite [14]. These findings are also in agreement with the contact angle data. Indeed, the higher the amount of nanotubes in the coating layer, the more hydrophilic the surface.

4. Conclusions

Halloysite-based geopolymer with beeswax microparticles has been employed as protective layer on steel sheets by brush deposition. For comparison, geopolymeric coating without wax was also reported. After the treatment with both geopolymeric formulations, the steel surfaces appear more homogeneous and smoother. The presence of microwax particles changed the wettability properties of the steel surfaces. In fact, the untreated steel and the GP treated both present hydrophilic values of contact angle. On the other hand, the treatment of the steel sheet with GP microwax enhanced the hydrophobicity features of the material giving new perspectives in protective coating.

CRediT authorship contribution statement

Martina Maria Calvino: Investigation, Data curation, Writing – original draft. **Lorenzo Lisuzzo:** Investigation, Data curation, Writing – original draft. **Giuseppe Cavallaro:** Writing – review & editing, Validation. **Giuseppe Lazzara:** Conceptualization, Supervision. **Candida Pipitone:** Investigation. **Francesco Giannici:** Funding acquisition, Resources.

Declaration of Competing Interest

The authors declare that they have no known competing financial interests or personal relationships that could have appeared to influence the work reported in this paper.

Data availability

Data will be made available on request.

Acknowledgements

The work was financially supported by "PON I&C 2014-20, SICAM U-GOV PRJ-0514 – Ricerca Industriale", by "SETI-Sicilia Eco Tecnologie Innovative", Cod.Progetto 2017-NAZ-0204, PO FESR Sicilia 2014/2020 – Azione 1.1.5 and by the University of Palermo.

References

[1] B. Zhang, H. Guo, P. Yuan, Y. Li, Q. Wang, L. Deng, D. Liu, Geopolymerization of halloysite via alkali-activation: Dependence of microstructures on precalcination, Appl. Clay Sci. 185 (2020), 105375, https://doi.org/10.1016/j.clay.2019.105375.

[2] M. Catauro, G. Dal Poggetto, C. Sgarlata, S. Vecchio Ciprioti, S. Pacifico, C. Leonelli, Thermal and microbiological performance of metakaolin-based geopolymers cement with waste glass, Appl. Clay Sci. 197 (2020) 105763.

[3] T.T. Haw, F. Hart, A. Rashidi, P. Pasbakhsh, Sustainable cementitious composites reinforced with metakaolin and halloysite nanotubes for construction and building applications, Appl. Clay Sci. 188 (2020), 105533, https://doi.org/10.1016/j.clay.2020.105533.

[4] S. Sadjadi, M.M. Heravi, M. Malmir, Pd@HNTs-CDNS-g-C3N4: A novel heterogeneous catalyst for promoting ligand and copper-free Sonogashira and Heck coupling reactions, benefits from halloysite and cyclodextrin chemistry and g-C3N4 contribution to suppress Pd leaching, Carbohydr. Polym. 186 (2018) 25–34, https://doi.org/10.1016/j.carbpol.2018.01.023.

[5] G. Gorrasi, R. Pantani, M. Murariu, P. Dubois, PLA/Halloysite Nanocomposite Films: Water Vapor Barrier Properties and Specific Key Characteristics, Macromol. Mater. Eng. 299 (2014) 104–115, https://doi.org/10.1002/mame.201200424.

[6] E. Rozhina, S. Batasheva, R. Miftakhova, X. Yan, A. Vikulina, D. Volodkin, R. Fakhrullin, Comparative cytotoxicity of kaolinite, halloysite, multiwalled carbon nanotubes and graphene oxide, Appl. Clay Sci. 205 (2021), 106041, https://doi.org/10.1016/j.clay.2021.106041.

[7] A. Joshi, C. Montes, S. Salehi, E. Allouche, Y. Lvov, Optimization of Geopolymer Properties by Coating of Fly-Ash Microparticles with Nanoclays, J. Inorg. Organomet. Polym. 25 (2015) 282–292, https://doi.org/10.1007/s10904-014-0105-1.

[8] J. Temuujin, A. Minjigmaa, W. Rickard, M. Lee, I. Williams, A. van Riessen, Fly ash based geopolymer thin coatings on metal substrates and its thermal evaluation, J. Hazard. Mater. 180 (2010) 748–752, https://doi.org/10.1016/j.jhazmat.2010.04.121.

[9] Y. Zhang, L. Bai, C. Cheng, Q. Zhou, Z. Zhang, Y. Wu, H. Zhang, A novel surface modification method upon halloysite nanotubes: A desirable cross-linking agent to construct hydrogels, Appl. Clay Sci. 182 (2019) 105259–105267, https://doi.org/10.1016/j.clay.2019.105259.

[10] L. Lisuzzo, T. Hueckel, G. Cavallaro, S. Sacanna, G. Lazzara, Pickering Emulsions Based on Wax and Halloysite Nanotubes: An Ecofriendly Protocol for the Treatment of Archeological Woods, ACS Appl. Mater. Interfaces 13 (2021) 1651–1661, https://doi.org/10.1021/acsami.0c20443.

[11] Y. Zhao, W. Kong, Z. Jin, Y. Fu, W. Wang, Y. Zhang, J. Liu, B. Zhang, Storing solar energy within Ag-Paraffin@Halloysite microspheres as a novel self-heating catalyst, Appl. Energy 222 (2018) 180–188, https://doi.org/10.1016/j.apenergy.2018.04.013.

[12] L. Lisuzzo, G. Cavallaro, S. Milioto, G. Lazzara, Pickering Emulsions Stabilized by Halloysite Nanotubes: From General Aspects to Technological Applications, Adv. Mater.Interfaces. 2102346 (2022) 1–29, https://doi.org/10.1002/admi.202102346.

[13] L. Lisuzzo, M.R. Caruso, G. Cavallaro, S. Milioto, G. Lazzara, Hydroxypropyl Cellulose Films Filled with Halloysite Nanotubes/Wax Hybrid Microspheres, Ind. Eng. Chem. Res. 60 (2021) 1656–1665, https://doi.org/10.1021/acs.iecr.0c05148.

[14] G. Cavallaro, L. Chiappisi, P. Pasbakhsh, M. Gradzielski, G. Lazzara, A structural comparison of halloysite nanotubes of different origin by Small-Angle Neutron Scattering (SANS) and Electric Birefringence, Appl. Clay Sci. 160 (2018) 71–80, https://doi.org/10.1016/j.clay.2017.12.044.